DISS. ETH NO. 26715

The effect of air-sea interaction and moist processes on the variability of stable water isotopologues in the marine boundary layer - observations and model studies

A thesis submitted to attain the degree of
DOCTOR OF SCIENCES OF ETH ZURICH
(DR. SC. ETH ZURICH)

presented by

IRIS LIVIA THURNHERR
MSc in Atmospheric and Climate Science, ETH Zurich
born on 28 October 1988
citizen of Hubersdorf (SO)

accepted on the recommendation of

Prof. Dr. Heini Wernli, examiner
Dr. Franziska Aemisegger, co-examiner
Dr. Adriana Bailey, co-examiner

2020

Contents

Abstract

Water is essential for life on Earth and affects ecosystems and societies. The atmospheric water cycle connects many water reservoirs and plays a crucial role in the distribution of water on Earth. The atmospheric circulation shapes precipitation patterns on the surface, the occurrence of floods and droughts and the availability of water for agriculture. Stable water isotopologues (SWIs) are naturally occurring tracers of phase changes in the atmospheric water cycle and allow insight into the history of air masses. They provide a framework to analyse phase change processes in the atmosphere on a range of temporal and spatial scales from large-scale moisture transport to cloud formation, precipitation, and small-scale turbulent mixing.

The aim of this thesis is to investigate the drivers of SWI variability in the marine boundary layer (MBL) on various spatial and temporal scales. The main focus is on the effects of the large-scale atmospheric flow and moist processes during the transport of air masses on the isotopic composition of water vapour. Five-month ship-based measurements of SWIs were collected during the Antarctic Circumnavigation Expedition (ACE) in the Atlantic and Southern Ocean from November 2016 to April 2017. In combination with the isotope-enabled numerical weather prediction model $COSMO_{iso}$ and single-process air parcel models, the SWI variability in

the MBL is investigated. For the reconstruction of the air mass history, backward trajectories and a moisture sources diagnostic are applied.

In the first part of the thesis, the setup and calibration procedure of the SWI measurements in water vapour during ACE are described and assessed in detail. These SWI measurements cover a wide range of latitudes and are used to analyse meridional SWI variations. It is shown that the MBL air masses are increasingly depleted in heavy isotopes from the tropics to polar regions. The meridional distribution of the isotopic composition in the MBL depends on the climatic conditions such as air temperature, specific humidity and relative humidity with respect to sea surface temperature. The SWI variability at a given latitude is highest in the extratropics and lowest in the tropics and subtropics. In the extratropics, the high SWI variability coincides with high frequencies of extratropical cyclones and high variability in the moisture source regions. Regions with persistent anticyclones in the subtropics are associated with lower SWI variability compared to regions affected by extratropical cyclones. Furthermore, from parallel measurements of SWIs at two different heights above the ocean surface on the research vessel, vertical SWI gradients are studied. These vertical SWI gradients show a wind dependency with larger gradients at high wind speeds due to sea spray evaporation and at low wind speeds due to decreasing turbulent mixing.

In the second part of this thesis, single-process air parcel models are introduced. Three processes are studied separately and their impact on the isotopic composition of an air parcel are quantified as well as their sensitivity to the controlling environmental parameter is analysed. The three studied processes are: 1) the effect of the continuous moisture uptake from ocean evaporation when an air parcel is advected over a horizontal gradient in sea surface temperature, 2) moisture loss by dew deposition in an air parcel that is oversaturated with respect to the ocean surface, and 3) cloud

formation during a moist adiabatic ascent. These single-process models are used in the third part of this thesis to assess the importance of different moist diabatic processes for the SWI variability during cold and warm advection along the Southern Ocean storm track during ACE. The novelty of this approach using these single-process models is the Lagrangian perspective that simulates the evolution of the isotopic composition of water vapour due to the accumulated effect of a single phase change process on a particular air parcel. This simple idealised approach is complemented by simulations with $COSMO_{iso}$, which allows to assess the importance of the non-linear interaction of the processes that were studied separately with the single-process air parcel models.

In the third part, the isotopic signature of water vapour in the cold and warm sectors of extratropical cyclones is investigated using the ACE measurements and modelling of SWIs. An objective identification scheme is applied to identify regions with cold and warm temperature advection in the Southern Ocean. Opposite air-sea moisture fluxes in the cold and warm sector lead to contrasting isotopic compositions of the MBL water vapour. In the cold sector, positive deuterium excess (d) and negative $\delta^2 H$ and $\delta^{18} O$ anomalies are observed, while in the warm sector, d shows negative and $\delta^2 H$ and $\delta^{18} O$ positive anomalies. Using $COSMO_{iso}$ simulations, the evolution of the isotopic signal during cold and warm advection is analysed. In the cold sector, strong ocean evaporation within the sector is the main factor leading to high d in the MBL. In the warm sector, moisture uptake generally occurs before the air parcel enters the warm sector and the isotopic composition of the water vapour is strongly modified during transport within the warm sector, mainly due to the following three processes: 1) dew deposition on the ocean surface, 2) ocean evaporation in a nearly saturated environment and 3) cloud formation, which can affect the air parcel hundreds of km away from the measurement site. These findings

imply that the interpretation of SWI measurements relies on the knowledge of the air mass history and the processes shaping the isotopic composition during transport. The application of the single-process air parcel models shows that the different processes have distinct behaviours in the d-q-phase space that can help identifying the drivers of the SWI variability in the MBL.

In summary, this thesis presents a unique SWI dataset and illustrates how the atmospheric flow configuration during the measurements affects the SWI variability of water vapour in the MBL on various temporal and spatial scales. These findings improve our understanding of the SWI variability and give new insight into processes shaping the d of water vapour in the MBL.

Zusammenfassung

Wasser ist unverzichtbar für das Leben auf der Erde und wirkt sich auf Ökosysteme sowie Gesellschaftsstrukturen aus. Der atmosphärische Wasserkreislauf verbindet die diversen Wasserreservoire und spielt eine entscheidende Rolle bei der Wasserverteilung auf der Erde. Die Atmosphärenzirkulation prägt Niederschlagsmuster, das Auftreten von Überschwemmungen und Dürreperioden sowie die Wasserverfügbarkeit für die Landwirtschaft. Stabile Wasserisotopologe (SWI) sind natürlich vorkommende Indikatoren von Phasenübergängen im atmosphärischen Wasserkreislauf und ermöglichen Einblicke in die Geschichte von Luftmassen. SWI bieten ein Bezugssystem, um Phasenübergänge in der Atmosphäre auf verschiedenen zeitlichen und räumlichen Skalen zu analysieren: von grossskaligem Feuchtetransport zu Wolkenbildung, Niederschlag und kleinskaligem turbulentem Mischen.

Diese Dissertation hat zum Ziel, die Prozesse, welche für die SWI-Variabilität in der marinen Grenzschicht auf verschiedenen räumlichen und zeitlichen Skalen verantwortlich sind, zu identifizieren. Der Hauptfokus liegt dabei auf den Auswirkungen der grossskaligen Atmosphärenzirkulation und der Feuchteprozesse während des Transports von Luftmassen auf die Isotopenzusammensetzung des Wasserdampfs. Dafür wurden SWI im Wasserdampf während der fünfmonatigen Antarctic Circumnavigation

Expedition (ACE) im Atlantik und Südpolarmeer von November 2016 bis April 2017 gemessen. Diese Messungen werden mit der Isotopenversion des numerischen Wettermodells COSMO$_{iso}$ und Lagrangeschen Prozessmodellen kombiniert, um die SWI-Variabilität in der marinen Grenzschicht zu untersuchen. Für die Rekonstruktion der Geschichte von Luftmassen werden Rückwärtstrajektorien und eine Feuchtequellendiagnostik verwendet.

Im ersten Teil dieser Arbeit wird der Versuchsaufbau und das Kalibrationsverfahren der SWI-Messungen im Wasserdampf detailliert beschrieben und bewertet. Diese Isotopenmessungen decken eine grosse Spannbreite von Breitengraden ab und werden gebraucht, um meridionale SWI-Variationen zu analysieren. Es zeigt sich, dass die Luftmassen in der marinen Grenzschicht von den Tropen in Richtung der Polargebiete zunehmend an schweren Isotopen abgereichert werden. Die meridionale Verteilung der Isotopenzusammensetzung in der marinen Grenzschicht hängt von den klimatischen Bedingungen wie der Lufttemperatur, der spezifischen Feuchte und der relative Feuchte im Verhältnis zur Meeresoberflächentemperatur ab. Die Variabilität der SWI an einem bestimmten Breitengrad ist in den Extratropen am grössten und in den Tropen sowie Subtropen am kleinsten. In den Extratropen stimmt die hohe SWI-Variabilität mit Regionen, die eine hohe Frequenz an extratropischen Zyklonen und eine hohe Variabilität in den Feuchtequellen aufweisen, überein. Regionen mit persistenten Antizyklonen in den Subtropen sind, verglichen mit Regionen, die von extratropischen Zyklonen betroffen sind, mit tieferer SWI-Variabilität verknüpft. Desweiteren wurden auf dem Forschungsschiff gleichzeitig SWI-Messungen auf zwei verschiedenen Höhen über dem Meeresspiegel durchgeführt, welche genutzt werden, um vertikale SWI-Gradienten zu untersuchen. Diese vertikalen SWI-Gradienten zeigen eine Windabhängigkeit mit grösseren Gradienten bei hoher Windgeschwindig-

keit aufgrund der Verdunstung von Gischtpartikeln sowie bei sehr tiefer Windgeschwindigkeit wegen des geringen turbulenten Mischens.

Im zweiten Teil dieser Arbeit werden Lagrangesche Prozessmodelle, welche sich auf einzelne Prozesse fokussieren, eingeführt. Drei Prozesse werden mit diesen Modellen dargestellt und der Einfluss dieser Prozesse auf die Isotopenzusammensetzung der Luftmassen quantifiziert sowie die Sensitivität der Kontrollparameter analysiert. Die drei untersuchten Prozesse sind: 1) Der Einfluss von anhaltender Feuchteaufnahme durch Ozeanverdunstung auf ein Luftpaket, welches über einen meridionalen Gradienten der Meeresoberflächentemperatur advektiert wird, 2) Feuchteabnahme in einem relativ zur Ozeanoberfläche übersättigten Luftpaket durch Taudeposition, und 3) Wolkenbildung während des feuchtadiabatischen Aufsteigens eines Luftpakets. Diese Prozessmodelle werden im dritten Teil der Arbeit auf die Relevanz der verschiedenen feuchtdiabatischen Prozessen für die SWI-Variabilität während Warm- und Kaltadvektion im Südpolarmeer untersucht. Die Einzigartigkeit des Ansatzes der Prozessmodelle ist die Lagrangsche Perspektive, mit welcher die Entwicklung der Isotopenzusammensetzung im Wasserdampfs aufgrund des akkumulierten Einflusses von einzelnen Phasenübergängen auf ein Luftpaket untersucht wird. Dieser einfache theoretische Ansatz wird ergänzt durch $COSMO_{iso}$-Simulationen, welche es ermöglichen, die Relevanz der nichtlinearen Interaktion der Prozesse in den einzelnen Prozessmodellen zu evaluieren.

Im dritten Teil wird die Isotopenzusammensetzung des Wasserdampfs in den Kalt- und Warmsektoren von extratropischen Zyklonen mithilfe der ACE-Messungen und Isotopenmodellierungen untersucht. Kalt- und Warm-advektion im Südpolarmeer werden mit einem objektiven Identifikationsschema bestimmt. Entgegengesetzte Feuchteflüsse zwischen der Atmosphäre und dem Ozean während Kalt- und Warmadvektion führen zu kontrastierenden Isotopenzusammensetzungen im Wasserdampf der mari-

nen Grenzschicht. Im Kaltsektor werden positive Deuterium excess (d) und negative δ^2H- und δ^{18}O-Anomalien beobachtet, während d im Warmsektor negative und δ^2H und δ^{18}O positive Anomalien aufweisen. Mithilfe von COSMO$_{\text{iso}}$-Simulationen wird die Entwicklung der Isotopenzusammensetzung während Kalt- und Warmadvektion untersucht. Im Kaltsektor ist starke Ozeanverdunstung innerhalb des Sektors der Hauptfaktor, welcher zu hohem d in der marinen Grenzschicht führt. Im Warmsektor findet die Feuchteaufnahme hauptsächlich vor dem Eintritt der Luftmassen in den Warmsektor statt. Die Isotopenzusammensetzung des Wasserdampfs wird stark verändert während des Transports innerhalb des Warmsektors, hauptsächlich aufgrund der folgenden drei Prozesse: 1) Tauposition auf der Ozeanoberfläche, 2) Ozeanverdunstung in einer beinahe gesättigten Umgebung und 3) Wolkenbildung. Diese Erkenntnisse implizieren, dass die Interpretation der SWI-Messungen vom Wissen über die Geschichte eines Luftpakets und der Prozesse, welche die Isotopenzusammensetzung während des Transports beeinflussen, abhängt. Die Anwendung der Prozessmodelle zeigt, dass die verschiedenen Prozesse im d-q-Phasendiagramm ausgeprägte Verhaltensweisen aufweisen, welche benützt werden können, um die Ursache der SWI-Variabilität in der marinen Grenzschicht zu bestimmen.

Zusammenfassend präsentiert diese Dissertation einen einmaligen SWI-Datensatz und illustriert, wie die Konfiguration der Atmosphärenzirkulation während der Messungen die SWI-Variabilität im Wasserdampf der marinen Grenzschicht auf verschiedenen zeitlichen und räumlichen Skalen beeinflusst. Diese Erkenntnisse verbessern unser Verständnis der SWI-Variabilität und geben neue Einsicht in die Prozesse, welche d im Wasserdampf der marinen Grenzschicht formen.

Chapter 1

Introduction

Water is essential for life on Earth and influences many aspects of our society. There are many ways by which water affects ecosystems and societies on Earth. As outlined by Hastrup (2013), *'[w]ater irrigates, inundates, floods, dries up, and creates social tensions as well as transport systems.'* Furthermore, water creates economical and moral value and deep imaginative implications, for example the ocean as a symbol of discovery of new lands and new imaginative horizons (Hastrup, 2013). A model of the distribution of water on Earth is the hydrological cycle (Fig.1, Horton (1931)), which comprises all water reservoirs on Earth and the transport of water between and in these reservoirs. The atmospheric branch of the hydrological cycle (referred to as atmospheric water cycle in the following) describes the abundance and distribution of water in gaseous, liquid and solid form in the atmosphere. The patterns of precipitation on the surface, the occurrence of floods and droughts, and the availability of water for agriculture is strongly influenced by the cycling of water in the atmosphere, which is shaped by atmospheric dynamics. Especially, the

short term variability of the atmospheric water cycle in the extratropics is linked to our daily weather. The occurrence of precipitation as well as strong large-scale ocean evaporation is associated with extratropical cyclones (Papritz et al., 2014; Aemisegger and Papritz, 2018), their coherent air streams (Pfahl et al., 2013) and fronts (Catto et al., 2012). Furthermore, heavy precipitation can be linked to the coherent transport of water vapour from evaporation hotspots, as it was shown for evaporation hotspots in the North Atlantic caused by upper-level troughs, which led to heavy precipitation in the Southern Alpine region (Winschall et al., 2012). Therefore, a thorough understanding of the atmospheric water cycle and how it is shaped by the large-scale atmospheric flow is needed to correctly predict weather phenomena, such as heavy precipitation, which affect our daily life.

The study of stable water isopotologues (SWIs) helps in understanding the atmospheric water cycle. SWIs occur naturally and are distributed in different relative abundances across the water reservoirs of the hydrological cycle. During phase changes, the relative abundance of different SWIs changes. This leaves a characteristic fingerprint in the isotopic composition of water, which depends on the involved phase change processes and the environmental conditions. In the atmosphere, the isotopic composition of water vapour is altered, for example, by the introduction of new vapour from ocean evaporation, during moist atmospheric processes, such as liquid and ice cloud formation and mixing of air masses, and during below-cloud processes such as rain evaporation, snow sublimation and rain equilibration with the surrounding water vapour (see, e.g., reviews by Gat, 2008; Galewsky et al., 2016). Therefore, SWIs serve as natural tracers of moist processes in the atmosphere, which are difficult to identify by traditional measurements of the water vapour content in the air.
The study of SWIs in the atmospheric water cycle on a global and long-
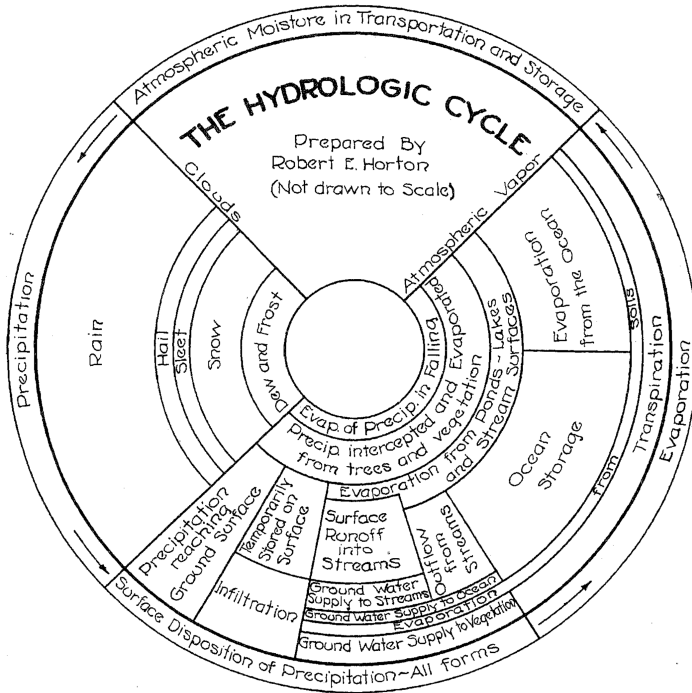
Figure 1.1: The hydrological cycle (from Horton, 1931).

term scale is possible by the Global Network of Isotopes in Precipitation (GNIP), which was initiated in 1961 by the International Atomic Energy Agency (IAEA) in cooperation with the World Meteorological Organization to collect monthly precipitation samples around the globe. The GNIP dataset provides information on the relationship of the isotopic composition of precipitation and climatic conditions (Rozanski et al., 1992). The main drivers of the climatological mean isotopic composition of precipitation are air temperature, latitude, altitude, precipitation intensity, seasonality, and distance from the coast (Dansgaard, 1964). This knowledge of the drivers of the mean isotopic composition of precipitation in the current climate is used to reconstruct the past climate from, e.g., ice cores (Epstein et al., 1970; Jouzel and Merlivat, 1984; Johnsen et al., 1989; Jouzel et al., 1997). Observational studies of SWIs in water vapour were rare (e.g. Yakir and Wang, 1996; Yepez et al., 2003; Uemura et al., 2008) before the development of laser spectrometry for SWI measurements in water vapour because these studies were laborious and error-prone using a cold trap to collect water vapour samples. The use of laser spectrometry facilitates the SWI measurements in water vapour and allows for continuous, automated measurements with high temporal resolution (e.g. Aemisegger et al., 2012; Steen-Larsen et al., 2013; Bonne et al., 2014). The high temporal resolution of such SWI measurements in water vapour allows to study short-term change in the atmospheric isotopic composition as, for example, caused by the passage of a cold front (Aemisegger et al., 2015; Graf et al., 2019). Various processes have been identified to cause short-term isotopic variations in water vapour. Amongst these processes are changing atmospheric transport pathways (Pfahl and Wernli, 2008; Steen-Larsen et al., 2013; Bailey et al., 2019), different environmental conditions at the measurement site (Steen-Larsen et al., 2014), influence from ocean evaporation and mixing at the marine boundary layer top (Benetti et al., 2018), and exchange with

precipitation and below-cloud processes (Aemisegger et al., 2015; Graf et al., 2019).

This thesis focuses on measurements and modelling of SWIs in water vapour and the linkage of SWI variability with small- to large-scale atmospheric flow. In this chapter, a few basic concepts of SWI meteorology are introduced. First, SWI notations and physics are described (Sec. 1.1). Second, isotopic fractionation processes in the atmospheric water cycle and, specifically, in the marine boundary layer and within extratropical cyclone are reviewed (Sec. 1.2.1).

1.1 Isotope physics

1.1.1 Definitions and notations

Water molecules consist of two hydrogen (H) atoms and one oxygen (O) atom. These oxygen and hydrogen atoms can be different stable isotopes generating different water isotopologues, which consist of atoms with the same atomic number but have small differences in their chemical and physical properties. The most abundant SWIs are $^1\text{H}_2^{16}\text{O}$, $^1\text{H}_2^{18}\text{O}$, $^1\text{H}_2^{17}\text{O}$ and $^1\text{H}^2\text{H}^{16}\text{O}$, of which $^1\text{H}_2^{16}\text{O}$, $^1\text{H}_2^{18}\text{O}$ and $^1\text{H}^2\text{H}^{16}\text{O}$ will be discussed in this thesis. The global mean abundance frequencies of the two heavy isotopologues $^1\text{H}_2^{18}\text{O}$ and $^1\text{H}^2\text{H}^{16}\text{O}$ are very low compared to the light isotopologue $^1\text{H}_2^{16}\text{O}$ (Tab. 1.1). The abundance of the heavy isotopologues is therefore expressed with the isotopic ratio R defined as the ratio of the concentration of the heavy to the light isotopologue:

$$^{18}R = \frac{[^1\text{H}_2^{18}\text{O}]}{[^1\text{H}_2^{16}\text{O}]}, \quad ^2R = \frac{2 \cdot [^1\text{H}^2\text{H}^{16}\text{O}]}{[^1\text{H}_2^{16}\text{O}]} \qquad (1.1)$$

To be able to compare isotopic ratios from different reservoirs, the δ-notation (Dansgaard, 1964) has been introduced, which compares the isotopic ratio of a sample to an internationally defined standard isotopic ratio

$$\delta^2 H[\permil] = (\frac{^2R_{sample}}{^2R_{\text{VSMOW2}} \cdot 2} - 1) \cdot 1000, \qquad (1.2)$$

$$\delta^{18} O[\permil] = (\frac{^{18}R_{sample}}{^{18}R_{\text{VSMOW2}}} - 1) \cdot 1000. \qquad (1.3)$$

VSMOW2 refers to the Vienna Standard Mean Ocean Water 2 defined by the IAEA. For simplicity, isotopologues will be referred to as isotopes in the following.

1.1.2 Isotopic fractionation

The relative abundance of SWIs is altered during phase change processes due to the different thermodynamical and quantum-mechanical properties of the different SWIs. The effect of the different transfer rates of SWIs from one phase to another is referred to as isotopic fractionation. Fractionation during equilibrium and non-equilibrium conditions is distinguished in the literature and they will be explained in the following.

Equilibrium fractionation

Equilibrium fractionation occurs due to different thermodynamical properties of the different SWIs. Heavy molecules have higher binding energies of the hydrogen bonds than light molecules. Therefore, heavy water molecules are more likely to stay in the phase with the higher binding energy than light water molecules. For example, during the phase transition between water vapour and liquid water, $^1H_2^{18}O$ and $^1H^2H^{16}O$ more

Table 1.1: Properties of stable water isotopologues $^1H_2^{18}O$, $^1H^2H^{16}O$ and $^1H_2^{16}O$: Natural abundance (after Sharp, 2007) and for $^1H_2^{18}O$ and $^1H^2H^{16}O$ equilibrium fractionation factor (α_e) from Majoube (1971) and Horita and Wesolowski (1994), [MA71] and [HW94] respectively, and the ratio of diffusivities ($\frac{^hD}{^lD}$) from Cappa et al. (2003) and Merlivat (1978), [CA03] and [ME78] respectively.

Isotopologue	$^1H_2^{18}O$	$^1H^2H^{16}O$	$^1H_2^{16}O$
global mean abundance [%]	0.200	0.031	99.731
$\alpha_e^{v/l}$ at 20 °C			
MA71	0.99030	0.92164	
HW94	0.99032	0.92222	
$^hD(^lD)^{-1}$			
CA03	0.969	0.984	
ME78	0.9723	0.9755	

likely stay in the liquid phase compared to $^1H_2^{16}O$. The strength of isotopic fractionation is expressed by the fractionation factor α, which compares the isotopic ratio of the two phases. The equilibrium fractionation factor between the vapour and liquid phase is defined as

$$\alpha_e^{v/l} = \frac{R^v}{R^l} \qquad (1.4)$$

where R^v and R^l are the isotopic ratios in vapour and liquid, respectively. By definition, $\alpha_e^{v/l} < 1.0$, because heavy isotopologues prefer the liquid
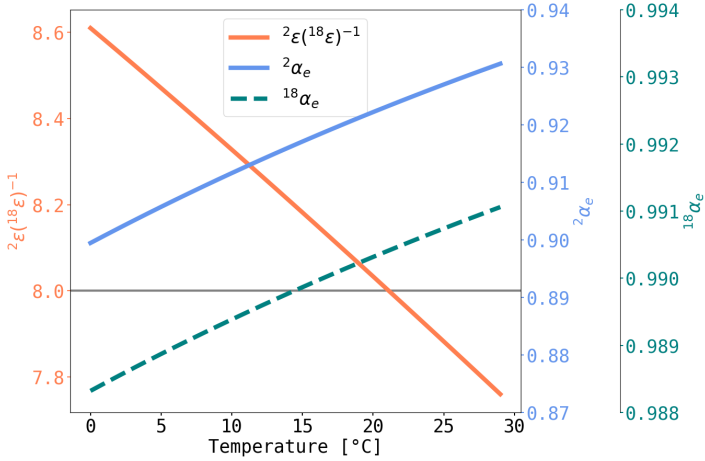
Figure 1.2: $^{2}\alpha_e$, $^{18}\alpha_e$, *and* $\frac{^{2}\epsilon}{^{18}\epsilon}$ *as a function of temperature.* $\frac{^{2}\epsilon}{^{18}\epsilon}$ *represents the ratio of δ^2H and $\delta^{18}O$ for water vapour evaporated in thermodynamic equilibrium from an ocean with the isotopic composition of 0‰ for δ^2H and $\delta^{18}O$.*

phase. Experimental values of $^{18}\alpha_e^{v/l}$ and $^{2}\alpha_e^{v/l}$ have been derived by Majoube (1971) and Horita and Wesolowski (1994) (summarised in Tab. 1.1). The changes in δ-values induced by equilibrium fractionation can be approximated by $\epsilon = (\alpha_e - 1) \cdot 1000$, because α_e is close to 1 for $^1H_2^{18}O$ and $^1H^2H^{16}O$. At 20 °C, $^{2}\alpha_e$=0.9222 and $^{18}\alpha_e$=0.9903 (Horita and Wesolowski, 1994), which means that $^{2}\epsilon$ is approximately 8 times larger than $^{18}\epsilon$.

Equilibrium fractionation is temperature dependent and stronger at low temperatures. The temperature dependency of $^{2}\alpha_e$ and $^{18}\alpha_e$ differs.

$^1H^2H^{16}O$ experience a stronger increase in strength of equilibrium fractionation with decreasing temperature relative to $^1H_2^{18}O$. Therefore, the ratio $\frac{^2\epsilon}{^{18}\epsilon}$ increases with decreasing temperature (Fig. 1.2).

Rayleigh distillation

A widely used model to describe changes in the isotopic composition due to continuous isotopic fractionation between two moisture reservoirs is the *Rayleigh distillation model*. This model has been introduced by Dansgaard (1964) to simulate the evolution of the isotopic composition of an air mass due to continuous rain formation. In an ascending air mass, temperature decreases and this eventually leads to cloud formation when the dew point temperature is reached. If this condensate is removed immediately from the air mass, the condensate is enriched in heavy isotopes by ϵ compared to the original water vapour. Due to subsequent removal of the condensate, the residual water vapour becomes increasingly depleted in heavy isotopes as distillation progresses. The isotopic ratio of the residual vapour at time t can be described as

$$R[t] = R[t_0] \cdot f^{\alpha^{l/v}-1}, \tag{1.5}$$

where $R[t_0]$ is the isotopic ratio at the start time t_0, f is the remaining mass fraction of the vapour and $\alpha^{l/v} = \frac{1}{\alpha^{v/l}} > 1$ is the fractionation factor. A detailed discussion of the Rayleigh model and the effect of the temperature dependency of α_e is given in chapter 3.1.3.

The Rayleigh model has been used by Dansgaard (1964) to explain the relationship of the mean climatological isotopic composition of precipitation and temperature, also called the *temperature effect* (Fig. 1.3). Moving from warm to cold areas, rainout leads to an increasing loss of heavy isotopes, thus causing the *latitude effect* during meridional transport and
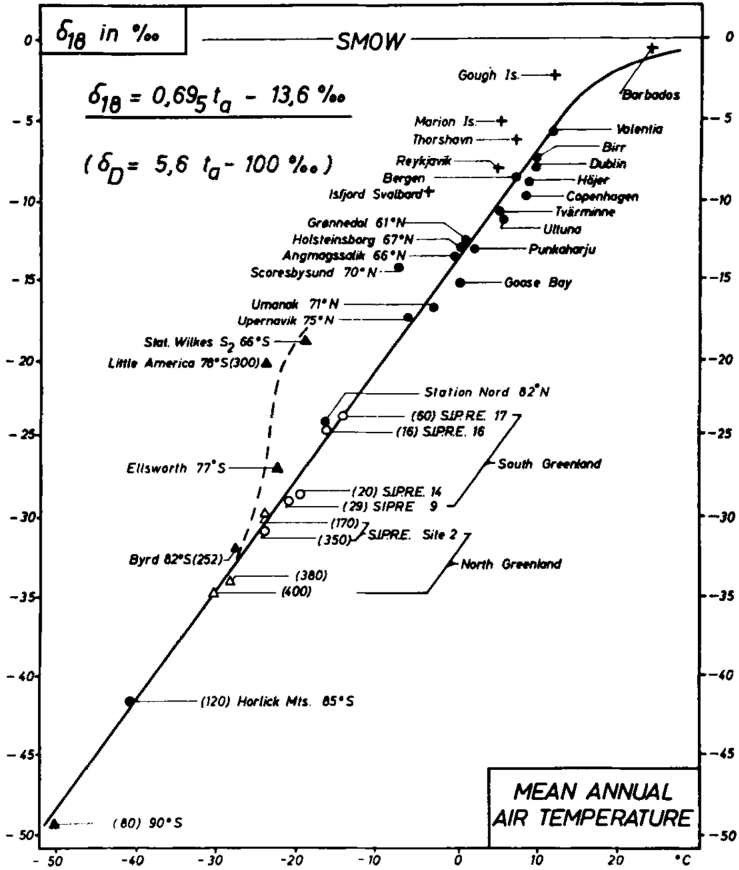
Figure 1.3: The annual mean $\delta^{18}O$ of precipitation as a function of the annual mean air temperature at the surface. The figures in parenthesis indicate the total thickness (in cm) of the investigated snow layer (from Dansgaard (1964))

the *altitude effect* during the ascent of air masses. Therefore, the isotopic composition of precipitation at high altitude and latitude has lower δ-values than precipitation at low altitude and latitude.

Non-equilibrium fractionation

The second type of isotopic fractionation is called non-equilibrium fractionation and occurs, additionally to equilibrium fractionation, during phase change processes which are not in thermodynamic equilibrium. Non-equilibrium fractionation occurs due to differences in the molecular diffusion velocity (diffusivity) of the different SWIs. Heavy molecules have lower diffusion velocities than light molecules, which leads to an additional depletion of heavy isotopes in the vapour phase during non-equilibrium fractionation, compared to equilibrium fractionation. The non-equilibrium fractionation factor α_k (where k stands for $kinetic$) can be expressed in the following way (after Cappa et al., 2003):

$$\alpha_k = (\frac{^h D}{^l D})^n \tag{1.6}$$

D is the molecular diffusivity of the heavy (^{h}) and light (^{l}) isotopes. Different values of molecular diffusivities of water vapour have been derived from experimental studies (Merlivat, 1978; Cappa et al., 2003) and are summarised in Table 1.1. The constant $0 \leq n \leq 1$ depends on the type of transport during the phase change, where $n = 0$ (i.e. $\alpha_k = 1.0$) represents situations of pure turbulent transport and $n = 1$ pure molecular diffusion. For ocean evaporation, n has been estimated to lie between 0.22-0.28 (Gat, 1996; Pfahl and Wernli, 2009; Aemisegger and Sjolte, 2018).

A measure of non-equilibrium fractionation is the deuterium excess d de-

fined as

$$d = \delta^2\text{H} - 8 \cdot \delta^{18}\text{O}. \tag{1.7}$$

d is close to zero in the absence of non-equilibrium fractionation, because $^2\epsilon$ is approximately 8 times larger than $^{18}\epsilon$ (Fig. 1.2). Due to non-equilibrium fractionation, the ratio of $\delta^{18}\text{O}$ and $\delta^2\text{H}$ is altered relative to the ratio expected from purely equilibrium fractionation, which leads to d different from zero. During ocean evaporation, $\delta^2\text{H}$ in the vapour phase increases relative to $\delta^{18}\text{O}$ due to non-equilibrium fractionation as $^2D >^{18} D$. Therefore, positive d is seen in the evaporated water vapour, while the remaining ocean surface water shows the opposite relative distribution of $\delta^{18}\text{O}$ and $\delta^2\text{H}$ and, thus, negative d.

d is not only varied by non-equilibrium processes but can also change during equilibrium conditions due to the temperature dependence of α_e and the non-linearity of the δ-scale definition (Dütsch et al., 2017). At temperatures above 20 °C, $\frac{^2\epsilon}{^{18}\epsilon}$ is larger than 8 leading to positive d in water vapour. At temperatures below 20 °C, the opposite effect occurs, which leads to negative d in water vapour. This effect will be discussed in more detail in section 3.1.3 for equilibrium fractionation during cloud formation.

A wind dependency of the non-equilibrium fractionation during ocean evaporation has been proposed by Merlivat and Jouzel (1979). They introduce a smooth wind regime for surface wind speeds below $7\,\text{m}\,\text{s}^{-1}$ with high non-equilibrium fractionation and a rough wind regime above $7\,\text{m}\,\text{s}^{-1}$ with lower non-equilibrium fractionation due to increased importance of turbulent diffusion (which corresponds to low n in equation 1.6). The discrete change in non-equilibrium fractionation as proposed by the wind regimes has not been confirmed by measurements, which showed a weak wind dependency (Pfahl and Wernli, 2009). Measured SWI values lie be-

tween the isotopic composition of evaporated water vapour in the smooth and rough regime (Uemura et al., 2008; Benetti et al., 2014; Steen-Larsen et al., 2014). In Chapter 2, the wind dependency of non-equilibrium fractionation is further discussed using near-surface vertical SWI gradients from SWI measurements.

1.2 Isotopic fractionation in the atmosphere

1.2.1 The atmospheric water cycle

The atmospheric water cycle describes the distribution and cycling of water in gaseous, liquid and solid form within the atmosphere. Phase changes in the atmospheric water cycle lead to variations in the distribution of heavy and light isotopes within the cycle. In the following, processes, which lead to changes in the isotopic composition of atmospheric water vapour, are discussed by following an air mass from the moisture sources to the moisture sinks (Fig. 1.4).

Globally, the dominant source of atmospheric water vapour is evaporation from the ocean surface (see ① in Fig. 1.4). Over land, the input from land evaporation (①) and evapotranspiration from vegetation (④) are important sources (Dütsch et al., 2016). During the evaporation of water vapour, $\delta^{18}O$ and $\delta^{2}H$ decrease relative to the ocean or land isotopic composition due to isotopic fractionation. The evaporated water vapour is, on average, approximately 80 ‰ and 10 ‰ lower for $\delta^{2}H$ and $\delta^{18}O$, respectively, compared to the source isotopic composition. The isotopic composition of the source and the environmental condition during evaporation, i.e. temperature and relative humidity, define the exact isotopic composition of evaporated water vapour. Therefore, if the isotopic composition of the

water vapour is not altered during transport in the atmosphere, $\delta^{18}O$ and δ^2H in atmospheric water vapour are directly related to the environmental conditions at the moisture source. Low $\delta^{18}O$ and δ^2H can thus be associated to strong equilibrium fractionation at low temperature and increased non-equilibrium fractionation at low relative humidity.

A further moisture source for atmospheric water vapour is sea spray evaporation (③). Sea spray is produced under high sea surface roughness, which favours wave breaking and bubble bursting. Here, sea spray evaporation refers to the nearly total evaporation of water vapour from sea spray droplets. If water vapour evaporates completely from sea spray droplets, no isotopic fractionation occurs. Thus, the input of $\delta^{18}O$ and δ^2H into the MBL is higher compared to the SWI input from ocean evaporation. The effect of sea spray evaporation on the atmospheric moisture budget is still an open question (Veron, 2015). From SWI measurements in the Mediterranean Sea, Gat et al. (2003) estimated that up to 50% of the marine boundary layer moisture can originate from sea spray evaporation.

The isotopic composition of the water vapour in an air mass can be altered during transport due to the formation of clouds (⑤), precipitation in the form of rain (⑥) and snow (⑦), mixing with other air masses (②), below-cloud processes, such as equilibration with rain droplets, rain evaporation and snow sublimation (⑧), and new moisture input from surface evaporation (①) (Dütsch et al., 2018). Isotopic fractionation during condensation and deposition of water vapour to liquid and solid precipitation decreases $\delta^{18}O$ and δ^2H of the remaining atmospheric water vapour. This process can occur repeatedly to an air mass and can be described by the Rayleigh distillation model (Dansgaard (1964), as explained in Sec. 1.1.2 and 3.1.3). Further processes, that deplete the vapour phase of heavy isotopes are equilibration with falling precipitation, or its evaporation and sublimation in an undersaturated environment. Hydrometeors, originating
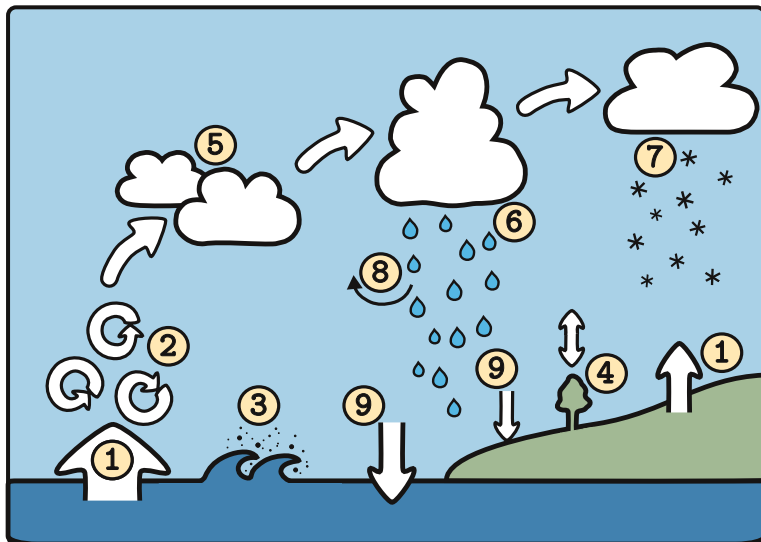
Figure 1.4: Schematic of the atmospheric water cycle with processes during which isotopic fractionation occurs: ① surface evaporation, ② turbulent mixing, ③ sea spray evaporation, ④ evapotranspiration, ⑤ cloud formation, ⑥ rain formation, ⑦ snow formation, ⑧ below-cloud processes, and ⑨ dew deposition.

from higher, more isotopically depleted altitudes, introduce low δ-values at lower altitudes. To differ between these processes, that lead to low δ-values in water vapour, the simultaneous measurements of SWIs in water vapour and precipitation and the changes in d during these processes can give further insight (Aemisegger et al., 2015; Graf et al., 2019). For example, the influence of below-cloud processes such as rain equilibration and rain evaporation can be identified from the difference in d and δ-values between rain and water vapour in high resolution measurements (Graf et al., 2019). Mixing with air masses of different isotopic compositions from different altitude and latitudes, for example the mixing of freshly evaporated water vapour with more depleted water vapour in the MBL, can further change the isotopic composition of an air mass (Benetti et al., 2018).

Finally, water leaves the atmosphere by various sinks. Precipitation is an efficient way of water removal and leaves behind atmospheric water vapour with low δ^{18}O and δ^2H. Next to precipitation, dew formation (⑨) in supersaturated environments is a sink for atmospheric water vapour. This process is especially important in arid regions (Jacobs et al., 1999). In oceanic regions, dew formation is only observed in humid environments in the warm sector of extratropical cyclones (Neiman et al., 1990). The importance of dew formation on the ocean surface for the SWIs in the marine boundary layer water vapour is investigated in Chapter 4.

The isotopic composition of MBL moisture provides an accumulated fingerprint of all phase change processes encountered by the water from the source location to the sink. The large number of different processes influencing water vapour during its cycling in the atmosphere, poses difficulties for the interpretation of its isotopic composition. For the interpretation of ship-based water vapour measurements, knowledge of the processes controlling the isotopic composition of MBL moisture is crucial. These processes are described in the following.

1.2.2 The marine boundary layer

Stull (2009) defines the boundary layer *'as that part of the troposphere that is directly influenced by the presence of the earth's surface, and responds to surface forcings with a timescale of about an hour or less.'* The boundary layer is bound by the Earth's surface and the boundary layer top, which often appears in the form of a temperature inversion. The marine boundary layer (MBL) is defined as the boundary layer which is bound by the ocean surface. The net surface radiation at the ocean surface $I_{ocean,net}$ is balanced by the surface H_g, sensible H_s and latent H_l heat flux. The energy budget at the surface can be expressed as follows:

$$I_{ocean,net} + H_g = H_s + H_l. \tag{1.8}$$

Equation 1.8 holds if it is assumed that the ocean surface is an infinitesimally thin layer and no changes in temperature, for example due to the horizontal advection of air masses, occur at the surface. Ocean evaporation, expressed as latent heating, is an important component of the air-sea heat fluxes and influences the sea surface temperature as well as MBL humidity and turbulence. For example, in environments with low relative humidity with respect to sea surface temperature (h_s), enhanced ocean evaporation tends to destabilise the MBL, favouring turbulent mixing with the free troposphere. Enhanced entrainment in turn leads to an increase in the MBL's vertical extent.

The MBL consists of three sublayers (Lewis and Schwartz, 2013): a laminar sublayer above the ocean surface with a thickness of a few mm, where moisture transport is dominated by molecular diffusion. A surface layer of several tens of meters extends above the laminar layer and is characterised by turbulent transport and an increase in wind speed with height. Between the surface layer and the MBL top, the Ekman layer is situated

in which Coriolis effects gain in importance next to turbulence. Hence, the vertical transport of moisture through the MBL is prone to different transport processes, which influence the isotopic composition of the water vapour differently. To describe the isotopic fractionation during ocean evaporation and the isotopic composition of the evaporative flux, Craig and Gordon (1965) adapted the described separation of diffusive and turbulent transport into two layers in their ocean evaporation model (Fig. 1.5, left). They proposed a distinction into a lower laminar layer above the air-sea interface, which is dominated by diffusive transport, and an upper turbulent layer, which is dominated by turbulent transport. Assuming a steady flux rate through all atmospheric layers, the isotopic composition of the evaporative flux R_{evap} is given by

$$R_{evap} = \frac{\alpha_k \cdot (R_{MBL} \cdot h_s - R_{oc} \cdot \alpha_e)}{h_s - 1},$$
(1.9)

where R_{MBL} is the isotopic ratio of MBL water vapour and R_{oc} the isotopic ratio of the ocean. This formulation of the evaporative flux depends on the isotopic composition of the marine boundary layer, which is not always known. Merlivat and Jouzel (1979) introduced the "closure assumption" which assumes that the only source for MBL water vapour is ocean evaporation and, thus, $R_{evap,clos}=R_{MBL}$ (Fig. 1.5, middle). This assumption yields a simplified expression of the isotopic composition of the evaporative flux:

$$R_{evap,clos} = R_{MBL} = \frac{\alpha_k \cdot \alpha_e \cdot R_{oc}}{h_s \cdot (1 - \alpha_k) - 1}$$
(1.10)

While equation 1.9 provides a value for the isotopic composition of the evaporation flux, equation 1.10 allows for the actual calculation of the isotopic composition of MBL water vapour. The evolution of the SWI
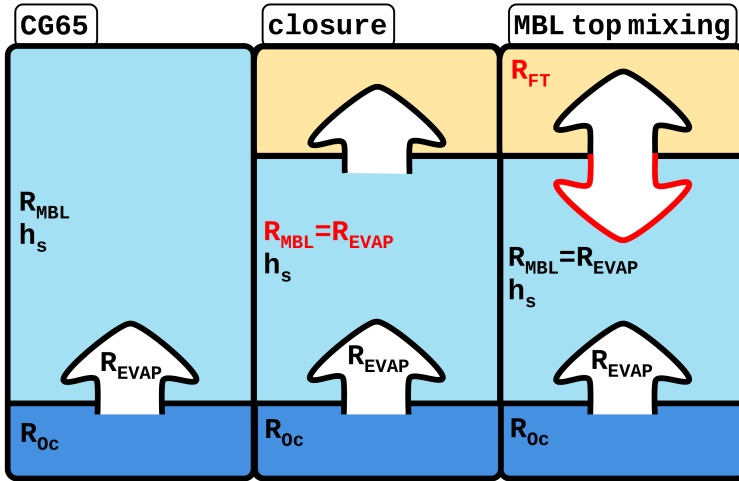
Figure 1.5: Schematic of ocean evaporation models describing the iso-topic composition of the evaporative flux (R_{evap}) and the MBL (R_{MBL}). CG65 describes the Craig and Gordon (1965) model, closure the model by Merlivat and Jouzel (1979) using the closure assumption and MBL top mixing the MBL framework by Benetti et al. (2018). For details see text.

composition of the MBL due to continuous input from ocean evaporation using the Craig and Gordon (1965) model is discussed and applied to an air parcel moving over an SST-gradient in Sec. 3.1.1.

The "closure assumption" does not include situations where other processes than ocean evaporation, such as vertical mixing and horizontal advection, affect the isotopic composition of the MBL water vapour. In the absence of horizontal advection, the isotopic composition of the MBL can be approximated by the mixing of free tropospheric air masses (i.e. air masses

above the MBL) with the evaporated water vapour. The continuous mixing of dry free tropospheric air masses into the MBL counteracts the moistening of the MBL due to ocean evaporation and, thus, preserves a low h_s-environment which favours ocean evaporation. Without such a ventilation process, either from vertical mixing or horizontal advection, h_s in the MBL will increase until an equilibrium with the ocean is reached at h_s=1, at which ocean evaporation is stopped. A framework for vertical mixing in the MBL, which includes the mixing of water vapour from ocean evaporation with free tropospheric air masses at the MBL top, has been developed by Benetti et al. (2018) (Fig. 1.5, right). In their framework, the isotopic composition of the MBL (expressed in δ-notation) is

$$\delta_{MBL} = (1 - b) \cdot \delta_{evap,clos} + b \cdot \delta_{LFT} \qquad (1.11)$$

$$\text{where } b = \frac{r \cdot \alpha_k \cdot (1 - h_s)}{(1 - r) \cdot h_s + \alpha_k \cdot (1 - h_s)}. \qquad (1.12)$$

$\delta_{flux,clos}$ is the isotopic composition of the evaporative flux under the closure assumption in δ-notation, $_{LFT}$ denotes properties of air masses from the lower free troposphere, $_{MBL}$ properties of air masses from the MBL, and $r = \frac{q_{LFT}}{q_{MBL}}$ with q being the specific humidity. Here, $h_s = \frac{q_{LFT}}{r \cdot q_s}$ is a function of q_{LFT}, showing that h_s in the MBL depends on the mixed-in free tropospheric air masses. This formulation of the isotopic composition of the MBL accurately reproduces variations in SWI measurements of MBL water vapour in the absence of frequent variations due to horizontal advection (Benetti et al., 2018).

More elaborate models simulating the MBL isotopic composition during ocean evaporation have been developed. Feng et al. (2019) used a 1-D steady state MBL model including height-dependent diffusion and mixing,

which means that no separation in a laminar and turbulent layer is needed, and horizontal and vertical advection to simulate vertical SWI gradients in the MBL. δ^{18}O and δ^{2}H decrease and d increases with height in their simulations. The strongest increase in d is seen in the lowest few centimeters, where non-equilibrium effects are strongest. Few studies have investigated vertical SWI profiles from measurements and showed that a wide range of vertical SWI profiles, including negative d-gradients, occurs in the MBL (Uemura et al., 2008; Sodemann et al., 2017; Salmon et al., 2019). Negative vertical d-gradients cannot be explained by the discussed vertical mixing model for the MBL. Processes related to cloud droplet evaporation at the MBL top or precipitation evaporation could lead to negative d in the upper MBL inducing a negative vertical d-gradient (Sodemann et al., 2017; Salmon et al., 2019). Vertical SWI gradients in the MBL are further discussed in Chapter 2.

The discussed processes affecting the MBL isotopic composition neglect the influence of the large-scale atmospheric flow. Especially, the passage of cyclones strongly changes the properties of the MBL. The effect of extratropical cyclones on the MBL isotopic composition is discussed in the next section.

1.2.3 Extratropical cyclones

The MBL moisture budget is strongly influence on the synoptic time scale by the passage of extratropical cyclones. The large-scale advection of air masses within an extratropical cyclone leads to contrasting properties of the MBL (Neiman et al., 1990; Persson et al., 2005; Beare, 2007; Boutle et al., 2010): The cold sector, which is dominated by equatorwards transport of air masses, has low h_s, low air temperature and high H_s and

H_l leading to unstable conditions in the MBL. In the warm sector, air masses are tranported polewards and high h_s, high air temperature and low or negative H_s and H_l are observed together with stable MBL conditions. Furthermore, the formation of clouds and precipitation along the frontal zones between the sectors strongly impacts the MBL moisture budget.

In the extratropics, the variations of SWIs within the MBL water vapour are shaped by various processes related to extratropical cyclones with strongest variations observed during frontal passages. The passage of a cold front leads to a decrease in δ-values (Gedzelman and Lawrence, 1990), which is caused by below-cloud processes, such as rain evaporation, equilibration of rain and water vapour, and by the horizontal advection of air masses with low δ-values behind the cold front (Pfahl et al., 2012; Aemisegger et al., 2015; Graf et al., 2019). Fewer studies are available on the isotopic variability in water vapour during a warm front passage. Gedzelman and Lawrence (1990) showed, that $\delta^{18}O$ increases across the warm front due to the advection of isotopically enriched air masses in the warm sector.

The strong changes in SWIs due to a frontal passage reflect, on the one hand, the precipitation-related processes along the fronts and, on the other hand, the contrasting properties of air in the cold and warm sector of extratropical cyclones. An idealised model study by Dütsch et al. (2016) showed, that horizontal advection is the most important process in shaping the large-scale isotopic composition of water vapour within an extratropical cyclone due to the large-scale flow patterns associated with the cold and warm sectors. Therefore, high (low) δ-values are observed in the warm (cold) sector. Due to the idealised model setup in their study, isotopic fractionation due to air-sea moisture fluxes are not represented and the influence relative to the large-scale horizontal advection is not quantified. Ocean evaporation can be identified by investigating d, which increases with increasing evaporation. Uemura et al. (2008) showed in measurements

from the Southern Ocean that high d and low δ-values occured in a period of low h during a cold air outbreak. On a wider perspective, high d can be linked to strong large-scale ocean evaporation (Aemisegger and Sjolte, 2018). Only limited measurements of SWIs in warm sectors are available. Uemura et al. (2008) observed negative d in MBL water vapour during a warm air advection event, which might be due to decreasing strength in ocean evaporation. The drivers of the variability of SWIs in water vapour within the warm sector of extratropical cyclones have not been studied in detail so far. In Chapter 4, an analysis of the drivers of the isotopic variability in water vapour in the cold and warm sector of extratropical cyclones are presented.

1.3 Objectives and outline

Former studies have shown that the large-scale atmospheric flow impacts air-sea moisture fluxes and influences the moisture budget of the marine boundary layer. Thus, they are expected to affect the SWI variability of the MBL. The aim of this dissertation is to investigate the SWI variability in MBL water vapour and assess the role of weather systems in shaping the SWI composition of the MBL. For this thesis, five-month ship-based SWI data in water vapour was collected during the Antarctic Circumnavigation Expedition from November 2016 to April 2017. These measurements are combined with further meteorological and environmental measurements during the cruise. The isotope-enabled numerical weather prediction model COSMO$_{\text{iso}}$ is used for the detailed analysis of the measured timeseries and for the calculation of trajectories and moisture sources of MBL water vapour. Furthermore, single-process air parcel models are developed and applied to understand the Lagrangian evolution of the isotopic composition in the MBL. The drivers of the SWI variability in MBL water

vapour are investigated on various spatial and temporal scales focusing on the following questions:

1. How does the large-scale atmospheric flow influence the MBL isotopic composition in different climate zones?

2. Which environmental factors determine near-surface vertical SWI gradients in the MBL?

3. How does warm and cold temperature advection affect air-sea moisture fluxes?

4. What are the drivers of the SWI variability within the cold and warm sectors of extratropical cyclones?

The thesis is structured in the following way: The calibration of the SWI measurements from ACE is described in Chapter 2 and the measurements are analysed to identify the main drivers of the meridional and vertical SWI variability. The effect of phase change processes on the SWI composition of water vapour is analysed using single-process air parcel models, which are introduced in Chapter 3. In Chapter 4, the SWI composition of water vapour in the MBL is studied in the context of cold and warm temperature advection by combining measurements and model simulations with single-process air parcel models and COSMO$_{iso}$. Finally, the main findings are summarised and the broader implications of these finding are discussed (Chapter 5).

Chapter 2

Meridional and vertical variations of the water vapour isotopic composition in the marine boundary layer over the Atlantic and Southern Ocean

2.1 Introduction

The atmospheric branch of the water cycle is an essential component of the Earth's climate system. Its short-term variability is directly linked to our daily weather, including the occurrence of clouds and precipitation. The main source for atmospheric water in oceanic regions is ocean evaporation which is strongly influenced by the large-scale atmospheric flow (Simmonds and King, 2004; Papritz et al., 2014) as well as small-scale turbulent and convective mixing (Jabouille et al., 1996; Sherwood et al., 2010). Ocean evaporation feeds moisture into the marine boundary layer (MBL), where the evaporated ocean water undergoes convective and turbulent mixing. The measurement of surface evaporation fluxes over the ocean is difficult and moisture source attribution of MBL water vapour cannot be done by traditional atmospheric humidity measurements. A useful tool to investigate the influence of dynamical processes on the MBL water budget at various spatial and temporal scales are stable water isotopologues (SWIs, hereafter referred to as isotopes for simplicity). In this study, we investigate synoptic driving mechanisms of SWI signals in the MBL at different latitudes in the Atlantic and the Southern Ocean.

SWIs are usually quantified by the δ-notation (Craig, 1961): $\delta[‰] = (\frac{R}{R_{\text{VSMOW2}}} - 1) \cdot 1000$, where R is the isotopic ratio of either $H_2^{18}O$ or $^2H^1H^{16}O$ (with R representing the ratio of the concentration of the heavy molecule to the concentration of $H_2^{16}O$). The δ-notation expresses the relative deviation of the isotopic ratios R from the internationally accepted primary water isotope standard, that is, the Vienna standard mean ocean water (VSMOW2; with $^2R_{\text{VSMOW2}}$=1.5576$\cdot$10^{-4} and $^{18}R_{\text{VSMOW2}}$=2.0052$\cdot$10^{-3}; $^2R_{\text{VSMOW2}}$ is multiplied by two to account for the two possible positions of ^2H within the water molecule). SWIs are tracers of atmospheric processes involving phase changes of water. Whenever a phase change occurs, the rel-

ative abundance of SWIs is altered by isotopic fractionation. The difference in saturation vapour pressure between heavy and light isotopes causes one type of isotopic fractionation, referred to as equilibrium fractionation, the strength of which is inversely related to temperature. A second type of fractionation, the non-equilibrium fractionation (Dansgaard, 1964; Craig and Gordon, 1965), occurs additionally to equilibrium fractionation if the two phases are not in equilibrium. This is the case, for example, during ocean evaporation. During non-equilibrium conditions, a net transfer of water molecules occurs, whereby diffusion effects alter the relative abundance of SWIs due to the different diffusion velocity of the different water molecules. The secondary isotope variable deuterium excess ($d = \delta^2$H - 8$\cdot\delta^{18}$O; Dansgaard 1964) provides a measure of non-equilibrium fractionation. d is close to zero in the absence of non-equilibrium effects at temperatures of around 20 °C. The mean global d of water evaporated from the ocean is approximately 10 ‰, which indicates that, on average, non-equilibrium conditions are expected during evaporation (Craig, 1961).

Isotopic fractionation and the distribution of SWIs in the hydrological cycle have been studied since the early 1950s using measurements and modelling of SWIs (Epstein and Mayeda, 1953; Dansgaard, 1954; Craig, 1961, see also reviews of Gat, 1996, Galewsky et al., 2016). Commercially available cavity ring-down laser spectrometers have enabled an increasing amount of field studies measuring SWIs during the past decade. These continuous, high-resolution measurements of SWIs in water vapour provide the necessary precision and accuracy to study short-term variability of moist processes at the timescale of typical weather systems (Aemisegger et al., 2012). Ship-based measurements of SWIs in water vapour have proven to be useful to identify governing processes that define the MBL moisture budget such as the influence of the advection of terrestrial air masses (Gat et al., 2003), the organisation of convective systems in the

tropics (Kurita, 2013), mixing with the free troposphere in the subtropics (Benetti et al., 2014), the movement of atmospheric fronts in extratropical and polar regions (Kurita et al., 2016), the sublimation of snow on sea ice in polar regions (Bonne et al., 2019) and the influence of relative humidity and sea surface temperature at diverse latitudes (Uemura et al., 2008; Bonne et al., 2019). Recent studies of SWI measurements in the atmospheric water cycle identified the importance of these processes mainly for specific regions. In extratropical and polar regions, the passage of atmospheric fronts leads to abrupt changes in air masses and strongly contrasting isotopic signatures ahead and behind the front in precipitation (Gedzelman and Lawrence, 1990) and water vapour (Aemisegger et al., 2015; Kurita et al., 2016). Furthermore, moisture source locations and moisture transport paths are highly variable and depend strongly on the observation location in extratropical and polar regions (Steen-Larsen et al., 2013, 2015). In the subtropics, MBL air masses are prone to mixing between descending mid- to upper tropospheric air masses and water vapour from ocean evaporation, which leads to MBL isotope signals that are more depleted than the water vapour formed from ocean evaporation (Noone et al., 2011; Benetti et al., 2014, 2015). In the tropics, convection exerts a strong control on moist atmospheric processes and leaves distinct isotopic signals in tropical precipitation depending on the degree of organisation of convective systems, convective downdrafts and cloud top height (Lawrence et al., 2004; Bony et al., 2008; Torri et al., 2017). Below-cloud interaction of isotopically depleted rain droplets with MBL water vapour also affects the SWI composition of the MBL. Deep convective rainfall in the tropics leads to a depletion of SWIs in MBL water vapour compared to the isotopic signal from only ocean evaporation (Lawrence et al., 2004; Kurita, 2013). Even though different processes have been identified at different latitudes, the relative importance of these processes for the isotopic composition in

the MBL at different latitudes and in different large-scale flow configurations has not been assessed so far.

The MBL has been described by Brutsaert (1965) with a three-layer model. A viscous sublayer of a height of several millimetres that is in equilibrium with the sea surface is overlaid by a surface layer with tens of meters height, which is dominated by turbulence, and, above, the well-mixed Ekman layer spans to the top of the MBL (Lewis and Schwartz, 2013). A similar view of the lower MBL, dividing it into a thin laminar layer close to the ocean surface and a turbulent layer above, was used by Craig and Gordon (1965) to calculate the isotopic composition of the evaporative flux from the ocean surface. The Craig and Gordon (1965) model has been applied and refined in various studies and has been shown to adequately simulate the isotopic composition of the MBL water vapour under evaporative conditions (e.g. Merlivat and Jouzel, 1979; Gat, 2008; Horita et al., 2008; Pfahl and Wernli, 2009; Benetti et al., 2018; Feng et al., 2019).

Ship-based measurements are normally situated in the surface layer of the MBL and thus directly influenced by turbulent conditions. Atmospheric turbulence in the vicinity of the ocean surface is induced by momentum fluxes that depend on the sea state and wind speed. The sea state can be described by the dimensionless wave age, which is the ratio of the phase speed of the dominant wave component of the sea state to wind speed (Young, 1999). The wave age describes the ability of waves to absorb energy from the wind and hence represents stages of their development process. On the one hand, when waves are young (wave age $\sim$<1.0), waves travel slower than wind and thus are strongly forced by the atmosphere. As a result, waves absorb energy from the wind, grow rapidly and eventually break, generating sea spray (see e.g. Toffoli et al., 2017). When the sea state is mature (wave age >1.0), on the other hand, waves travel faster than the wind and no longer absorb energy from it. Under these circumstances, waves

are independent from the wind and assume a gently sloping profile, which makes them less prone to breaking and spray generation. The sea state does not only affect turbulence but also sea spray production. Sea spray is produced by breaking waves and bubble bursts which mainly occur during rough sea states at high wind speeds (Monahan et al., 1986) and young wave age. The production and subsequent evaporation of water from sea spray particles introduces isotopically enriched water vapour into the lower MBL if the water from sea spray particles evaporates nearly completely. This process of water evaporating from sea spray particles will be referred to as sea spray evaporation in the following. Gat et al. (2003) estimated that up to 50% of the measured humidity in the Mediterranean MBL can originate from sea spray evaporation. It is difficult to directly measure sea spray evaporation and, therefore, it is still an open question to what extent sea spray evaporation affects moisture in the MBL (Veron, 2015) in different wind forcing conditions. Due to the specific isotopic signature of sea spray evaporation, SWI measurements near the ocean surface might give further insight into the moisture contribution of this process.

In summary, ship-based measurements of SWIs in water vapour are influenced by processes acting at various spatio-temporal scales. To investigate these processes, recent studies focused mainly on specific regions and have not compared the relative importance of these processes at different latitudes. Furthermore, there is still a lack of measurements to study small-scale turbulent processes close to the ocean surface that could influence MBL moisture significantly, e.g. by sea spray evaporation. The objectives of this study are to investigate 1) the variability of SWIs in the oceanic MBL at different latitudes, 2) the large-scale circulation drivers of SWI signals in different climate zones, and 3) the local small-scale drivers of SWI signals such as turbulent mixing and sea spray evaporation. This
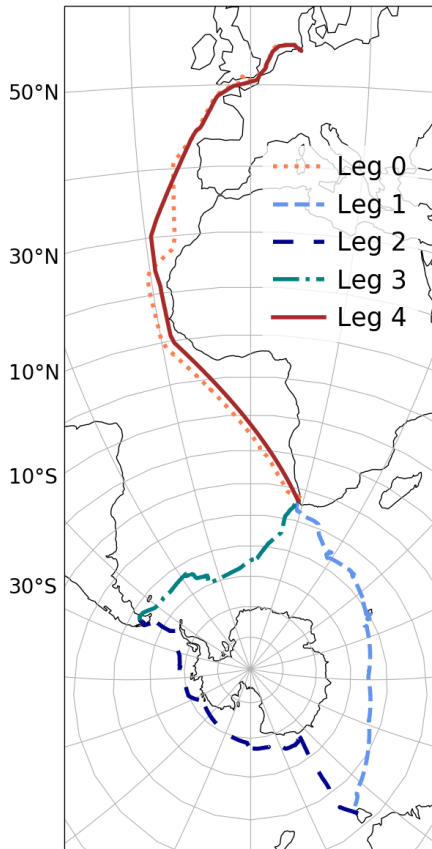
Figure 2.1: Overview of the ACE cruise from November 2016 - April 2017. The five legs (coloured lines) took place from 21 Nov - 15 Dec 2016 (Leg 0), 21 Dec 2017 - 18 Jan 2017 (Leg 1), 22 Jan - 22 Feb 2017 (Leg 2), 26 Feb - 19 Mar 2017 (Leg 3) and 22 Mar - 11 Apr 2017 (Leg 4).

study combines the water vapour measurements from three cavity ring-down spectrometers at two different heights on a research vessel during the Antarctic Circumnavigation Expedition (ACE) in the Atlantic and the Southern Ocean in 2016/2017 to analyse the meridional and vertical SWI variations in this five-month dataset. The drivers of SWI variability in the MBL are identified with a special focus on the diagnosed Lagrangian moisture sources (Sodemann et al., 2008). The Lagrangian perspective allows to study the conditions in the "catchment area" of MBL moisture and, thus, to compare local and remote drivers of SWI variability in the MBL. The study is structured in the following way: First, the measurement setup and calibration procedures are described (Section 2.2). Second, a detailed analysis of the difference between the datasets is given to assess possible measurement errors and calibration uncertainties (Section 2.3). Third, the variability of the SWI time series is analysed by presenting and discussing the dominant drivers for meridional and vertical SWI variations (Section 2.4).

2.2   Methods and Data

In this section, measurements conducted during the Antarctic Circum-navigation Expedition (ACE, see Section 2.2.1) are described. The main dataset of this study are the ship-based measurements of SWIs in water vapour at two elevations on the research vessel with different measurement setups and independent calibration and post-processing procedures (Sections 2.2.2 and 2.2.3). Thereafter, the additional measurements, model datasets and methods used in this study are described (Section 2.2.4).

2.2.1 Expedition

The Antarctic Circumnavigation Expedition (ACE) took place between 21 November 2016 and 11 April 2017 on the RV *Akademik Tryoshnikov* (Walton and Thomas, 2018). The expedition was divided into three main legs covering the circumnavigation of Antarctica in the Southern Ocean [legs 1-3] and two additional legs with Atlantic Ocean transects from Bremerhaven (Germany) to Cape Town (South Africa) [leg 0] and back [leg 4] (see cruise track in Fig. 2.1). Amongst the wide range of observations during ACE, a comprehensive set of atmospheric in situ measurements of aerosol characteristics (Schmale et al., 2019) and SWIs were conducted. Two instrumentation setups for measuring SWIs in water vapour using Picarro laser spectrometers were installed on the RV *Akademik Tryoshnikov* (Fig. 2.2). One setup was installed approximately 8 m a.s.l. (hereafter referred to as SWI-8) and was measuring with two instruments on both sides of the vessel (port side (ps) and starboard side (sb)). The second setup was situated at a height of approximately 13.5 m a.s.l. (hereafter referred to as SWI-13). Further atmospheric and oceanographic measurements were conducted during ACE on-board the RV *Akademik Tryoshnikov* providing the following datasets used in this study: atmospheric chemistry measurements next to the SWI-13, automated meteorological measurements, and remote sensing of wave activity (see Section 2.2.4). In the following, 1-hourly means of the measured datasets are shown with the 1-hourly standard deviations of the 1-second resolution time series, if not mentioned otherwise.

2.2.2 SWI-13

The SWI-13 measurements were conducted in the atmospheric measurement container on deck 2 of RV *Akademik Tryoshnikov*, approximately
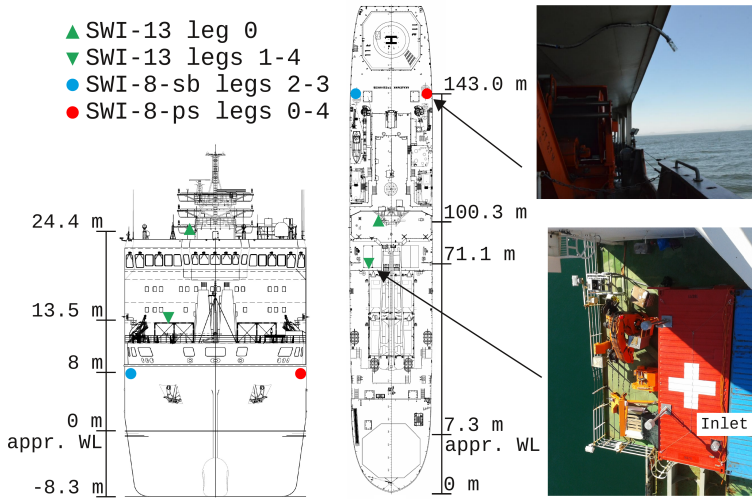
Figure 2.2: Inlet positions on RV Akademik Tryoshnikov *(adjusted vessel plans from the Arctic and Antarctic Research Institute). Distances are given relative to the approximate water line (appr. WL, [m]) for the front view and relative to the front for the top view. Pictures of the mounted inlets for SWI-8-ps (top) and SWI-13 during legs 1-4 (bottom) are shown to the right.*

13.5 m a.s.l. during legs 1 to 4 (Fig. 2.2). A custom-made plexiglass inlet was mounted on top of the container (see supplementary Fig. S1). Three layers of perforated plexiglass surrounded the inlet line to prohibit sea spray from reaching the line. The outermost layer was heated with a self-limiting heating band to avoid icing on the plexiglass surface of the inlet and to hold the inlet temperature above ambient temperature to avoid condensation. A 1.5 m long heated PFA tube with 10 mm inner diameter connected the inlet with the laser spectrometer inside the container. A filter ($0.2\,\mu$m PTFE vent filter) was used to prevent particles from entering the line. The heated PFA inlet line had a constant temperature of $50\,^{\circ}$C and was flushed with a KNF pump at a pumping rate of $9\,\ell\,\text{min}^{-1}$ leading to a total renewal of the air in the inlet line every second. A Picarro cavity ring-down spectrometer L2130-i was connected to the inlet line and operated continuously inside the container with a flow rate through the cavity of $300\,\text{m}\ell\,\text{min}^{-1}$.

Due to power issues, the SWI-13 measurement system had to be moved to the upper bridge at a height of 24.4 m a.s.l. during leg 0 (see Fig. 2.2, green triangle). Less sea spray was expected due to the increased height, and therefore a downward facing teflon funnel, instead of the plexiglass inlet, was mounted to the inlet line.

During legs 1-4, the temperature inside the measurement container was regulated to $20\pm5\,^{\circ}$C. In the tropics on legs 0 and 4, the temperature in the atmospheric measurement container and the room on the upper bridge exceeded $40\,^{\circ}$C, potentially affecting the measurements (see Section 2.3.1). Furthermore, some precipitate remained on the container roof after precipitation events and short-term contributions of isotopically depleted moisture from precipitation evaporation to the measured air cannot be ruled out after such events. The inlet was inspected frequently and snow around the inlet was removed on a few occasions during leg 2.

Measurements with a known standard (calibration runs) were performed

with an automated schedule using a standard delivery module (SDM) from Picarro. The L2130-i raw measurements were calibrated using the SDM calibration runs following a similar procedure as described in Aemisegger et al. (2012): First, the data was corrected for the humidity dependent isotope bias (referred to as isotope-humidity dependency, e.g. Schmidt et al., 2010; Aemisegger et al., 2012; Steen-Larsen et al., 2013) for all measurements with a water vapour mixing ratio below 12000 ppmv. A few recent studies (Bailey et al., 2015; Bonne et al., 2019) showed that the isotope-humidity dependency of their instrument is additionally sensitive to the isotopic composition of the used standard. No such impact was found for our L2130-i optimised for higher flow rates (see supplementary Fig. S5). Second, a two-point slope correction and normalisation to VSMOW2-SLAP2 using a 10-day running mean of the calibration runs was applied to correct for the drift of the instrument during the cruise. The calibration protocol and the isotope-humidity dependency correction are discussed in more detail in the supplementary material.

The water vapour mixing ratio w measured by L2130-i was calibrated using a dew point generator (LI-COR LI 610). Before and after the cruise, calibration measurements were conducted in the lab with controlled mixing ratios between 5'000 and 32'000 ppmv.

2.2.3 SWI-8

The second set of SWI measurements in water vapour were conducted in the hydrological lab on the main deck. Two inlet lines were installed to measure on both sides of the research vessel at a height of approximately 8 m a.s.l. A Picarro cavity ring-down spectrometer L2120 was connected to the portside inlet line (SWI-8-ps) during legs 0 to 4. For legs 2 and 3,

a second Picarro laser spectrometer L2130-i was installed to measure on the starboard side (SWI-8-sb). The inlet lines were made of a ¼" copper tubing, which was isolated and constantly heated to 50 °C in order to avoid the condensation of water vapour. The inlets were protected with a plastic bottle (see Fig. 2.2) and inspected several times per day.

Two types of calibration devices were used. A self-made device described in Steen-Larsen et al. (2014) was used on all legs while a Picarro SDM was additionally used during legs 2-3. The SDM was used for the L2130-i calibration runs and the self-made device for both laser spectrometers. The same calibration routines were used as described for SWI-13 (see supplementary material) by applying a correction for the isotope-humidity dependency for all measurements with a water vapour mixing ratio below 15'000 ppmv and by correcting the instrument's drift with a two-point slope correction and normalisation to VSMOW2-SLAP2 using 10-day running means of the calibration runs for L2120 and 14-day running means for L2130-i, because the calibration runs are available at a lower frequency for L2130-i. As the SDM was only used during two of the five legs, the dataset was calibrated using the self-made device, while the SDM outputs were used for comparison.

We tested the sensitivity of the final SWI-13 and SWI-8 time series to the calibration procedure. Different calibration versions were calculated by altering the calibration procedure. A detailed description and comparison of these different calibration versions is given in Section 2.3.

2.2.4   Additional measurements and model datasets

2.2.4.1   Atmospheric microphysical and chemical measurements: Sea spray concentration and exhaust mask

A sea spray proxy was calculated from the particle number size distribution obtained by an aerodynamic particle sizer (APS, TSI Model 3321), which was operated inside the atmospheric measurement container (Schmale et al., 2019). Here, we define the sea spray proxy as particles with a diameter larger than 700 nm (N700) for legs 1-3. In the Southern Ocean along the ACE cruise track, other sources of particles larger than 700 nm are negligible (Schmale et al., 2019). The sea spray proxy strongly underestimates the total number of particles originating from sea spray, since most of them are smaller. However, for our purposes, N700 is a good indicator to identify the influence of sea spray on the SWI measurements. No sea spray proxy was calculated for leg 4 where mineral dust and soot from forest fires also influenced the measurements and interfered with the identification of sea spray using just a particle diameter and no chemical information. No measurements are available for leg 0. The particle number size distribution measurements were influenced by the vessel's exhaust plume, depending on wind direction, wind speed and vertical atmospheric stability. The CO_2 mixing ratio, black carbon mass concentration and particle number concentrations show distinct signals during exhaust influence and were used to generate an exhaust mask, with which the sea spray proxy is cleansed. No influence by the exhaust plume on the SWI measurements was observed (see Section 2.3.2). Therefore the exhaust mask is not applied to the SWI time series.

2.2.4.2 Ocean surface state measurements

The sea state was continuously monitored using the wave and surface current monitoring system (WaMoS-II, Ziemer and Günther, 1994; Dittmer, 1995)). WaMoS-II is composed of an analog-to-digital converter and a processing software to acquire and analyse video signals from the marine X-band radar on board of the RV *Akademik Tryoshnikov*. Standard image processing techniques based on Fourier transforms are used to extract the wave energy spectrum from which wave characteristics are derived to calculate the wave age (for details see supplementary material).

2.2.4.3 Meteorological measurements

An automated weather station (model: AWS420, Vaisala) was operated on the RV *Akademik Tryoshnikov* during ACE delivering measurements of air pressure at 20 m a.s.l., air temperature, dew point temperature and relative humidity at 23.7 m a.s.l., and relative and absolute wind speed and direction at 30 m a.s.l. The recorded measurements were processed automatically by the Vaisala system. Dew point temperature, air temperature, and atmospheric pressure are used to calculate the specific humidity q. The relative humidity with respect to sea surface temperature (h_{SST}) is defined as $h_{\mathrm{SST}} = \frac{q}{q_{sat,SST}}$, where $q_{sat,SST}$ is the saturation specific humidity at sea surface temperature. Calibrated sea surface temperature (SST) measurements from ACE using a thermosalinograph (Aqualine FerryBox by Chelsea Technologies Group Ltd.) are not yet available. Therefore, the SST from the European Centre for Medium Range Weather Forecasts (ECMWF) operational data (see Section 2.2.4.4) is interpolated along the ship track and used to calculate h_{SST}. In order to quantify the bias caused by airflow distortion due to the ship's superstructure, the observed relative

wind speed was compared to the expected relative wind speed based on ECMWF analysis data (as described in Section 2.2.4.4) and a corrected true wind speed at 10 m above sea level was derived (for details on the wind speed correction, see Landwehr et al. (2019) and supplementary material).

2.2.4.4 Model data and Lagrangian methods

The Lagrangian analysis tool LAGRANTO (Wernli and Davies, 1997; Sprenger and Wernli, 2015) was used to calculate 10-day air parcel backward trajectories using the three-dimensional wind fields from the six-hourly global operational analysis data of the ECMWF and short-term forecasts in between the analysis time steps, i.e. at 03, 09, 15, 21 UTC. The ECMWF fields were interpolated on a regular horizontal grid of $0.5°$ horizontal spacing on 137 vertical levels. Up to 56 trajectories were launched every hour from the surface to 500 hPa in steps of 10 hPa, and with increased vertical resolution in the lowest 20 hPa above sea level, starting trajectories at 1, 2, 3, 4, 5, 10, 15 and 20 hPa above sea level.

The moisture sources of the MBL water vapour along the ACE ship track were calculated hourly using the Lagrangian moisture source diagnostic by Sodemann et al. (2008), adapted for identifying the sources of water vapour instead of precipitation (Pfahl and Wernli, 2008) based on the 10-day backward trajectories. The mean global atmospheric moisture residence time is 4-5 days with maximum residence time up to 8 days in polar regions and the eastern tropical Atlantic ocean (Läderach and Sodemann, 2016). Therefore, 10-day backward trajectories are expected to cover the moisture source areas along the ACE track. The mean source conditions (latitude, longitude, air temperature, and specific humidity) are calculated and weighted by the amount of moisture uptake. For each hour along the ACE track, the 75 % moisture source area is calculated. This area represents

the source region of 75% of the total moisture at the measurement position neglecting the 25 % sources with the lowest moisture contributions. A moisture uptake-to-loss ratio (following Suess et al. (2019), adapted for water vapour in the MBL) is used as a measure to compare the cumulative moisture uptake to the cumulative rainout of air parcels in the MBL at the measurement location. Changes in the specific humidity q for each timestep during the 5 days prior to arrival along the backward trajectories starting within the MBL are used to calculate the ratio. An increase in q within a timestep is interpreted as an uptake of moisture by the air parcel, decreasing q as a loss of moisture. A high uptake-to-loss ratio represents low moisture loss relative to moisture uptake during the 5 days before arrival and, thus, minor influence by rainout on the measured SWI composition is expected.

Cyclone frequencies were calculated by applying a 2D cyclone detection algorithm, which identifies the outermost closed sea level pressure contour that encloses a pressure minimum (Wernli and Schwierz, 2006; Sprenger et al., 2017) using the ECMWF operational analysis data. Accordingly, anticyclone frequencies were calculated using the outermost closed sea level pressure contour that encloses a pressure maximum.

2.3 Uncertainties from the SWI post-processing procedure

To identify robust deviations between the measured SWI time series from different locations on the ship, uncertainties due to the measurement and post-processing procedure are assessed. This allows for a quality check of the SWI time series to identify robust small-scale horizontal and vertical differences in SWIs in the lowermost MBL. The comparison of SWI-8-

ps and SWI-8-sb provides a measure of horizontal variations in SWIs around the research vessel, whereas the comparison of SWI-8 with SWI-13 gives an estimate of vertical variations in SWIs (compare Fig. 2.2). The difference between SWI-8-sb and SWI-8-ps has a mean value of $0.8\,[-1.6\ldots3.2]\,‰$ for δ^2H (numbers in brackets denote the 65% percentile range), $-0.04\,[-0.41\ldots0.38]\,‰$ for δ^{18}O and $1.2\,[-0.2\ldots2.4]\,‰$ for d (see also Appendix Fig. A.1) and are smaller than the vertical differences (Fig. 2.3). Large horizontal differences between SWI-8-sb and SWI-8-ps are observed only during short time periods, most likely due to sea spray influence on one of the two sides. The horizontal differences can be interpreted as the expected noise due to small differences in the measurement setup (e.g. length of inlet line, angle of inlet towards the ocean surface, ship's structure at inlet position). In the following, we will use SWI-8-ps to represent the measurements at 8 m a.s.l. because these measurements are available during the entire expedition. The vertical differences between SWI-13 and SWI-8-ps (Δ_{13-8}) over all legs are up to an order of magnitude larger than the horizontal differences for the δ-values, with $-2.6\,[-4.8\ldots-0.2]\,‰$ for δ^2H (numbers in brackets denote the 65% percentile range), $-0.55\,[-0.90\ldots-0.14]\,‰$ for δ^{18}O and $1.8\,[0.5\ldots3.2]\,‰$ for d (for details see also Appendix Fig. A.1). The robustness of these vertical differences is assessed in the following uncertainty analysis, which focuses on the effects of instrument properties, pollution by the ship's exhaust and the calibration procedure.

2.3.1   Instrument properties

High quality laser spectrometric measurements rely on a precise regulation of temperature and pressure within the instrument's cavity. The

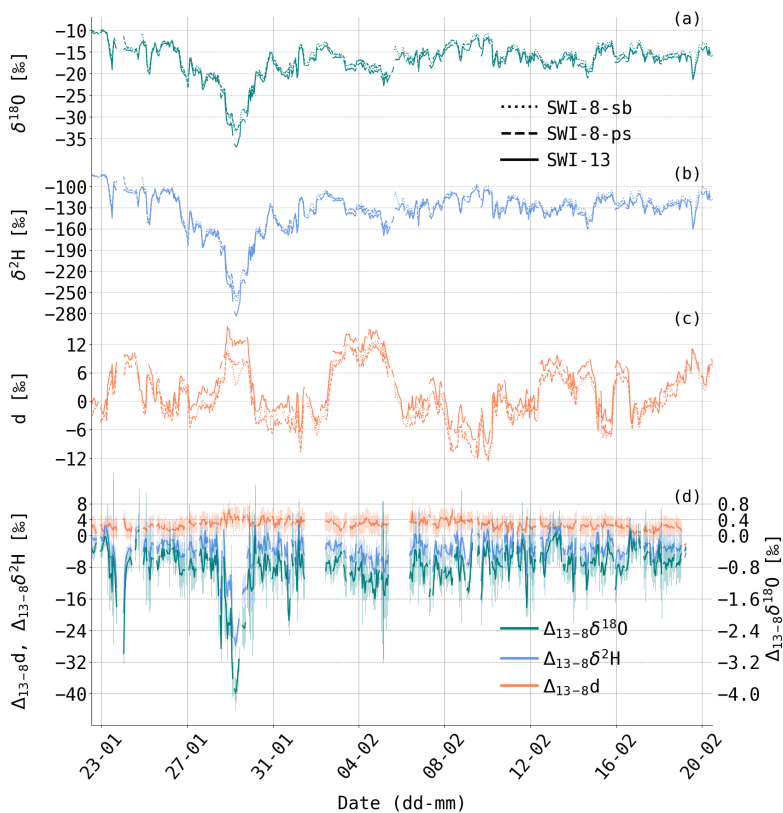*Figure 2.3: Time series of hourly means of (a) $\delta^{18}O$, (b) δ^2H, (c) d, and (d) Δ_{13-8} for leg 2 from SWI-13, SWI-8-ps, and SWI-8-sb measurements. Δ_{13-8} is the difference between SWI-13 and SWI-8-ps. The errorbars in panel (d) denote hourly standard deviations of the 1s data.*

target cavity pressure (CP) is regulated to 50 ± 0.02 and 35 ± 0.03 Torr, for SWI-13 and SWI-8-ps, respectively, and the cavity temperature (CT) to $80 \pm 0.002\,°C$. To exclude differences in the SWI signal due to an unstable cavity environment, data points were excluded if the cavity pressure and temperature deviated by more than 0.2 Torr and $0.02\,°C$, respectively, from the target cavity pressure and temperature (0.2 % of all data points for SWI-13 and 0.6% for SWI-8-ps). The remaining data points are analysed for a potential dependency of Δ_{13-8} on the cavity properties. The vertical differences in δ-values between SWI-13 and SWI-8-ps, $\Delta_{13-8}\delta^2H$ and $\Delta_{13-8}\delta^{18}O$, do not show any correlation with deviations from the target cavity properties of the respective instruments, with a Pearson correlation coefficient smaller than 0.1 for $\Delta_{13-8}\delta^2H$ resp. $\Delta_{13-8}\delta^{18}O$ correlated with CP or CT of each SWI-13 and SWI-8-ps. Also during the high temperatures at the measurement location in the tropics, the cavity environment does not show any irregularities. Thus, variations in the cavity environment do not contribute to the differences between SWI-13 and SWI-8-ps. A detailed analysis of the observed variations in cavity properties is given in the supplementary material.

2.3.2 Influence of exhaust air

Chemical measurements at the inlet site of SWI-13 showed episodic pollution by the vessel's exhaust air (see section 2.2.4.1). Exhaust air might affect the SWI measurements in water vapour by altering the ambient air's gas mixture, and by the presence of e.g. hydrocarbons impacting the spectroscopic baseline (Aemisegger et al., 2012; Johnson and Rella, 2017). A possible exhaust impact on the SWI measurements was analysed by studying Δ_{13-8} during exhaust and no exhaust periods. The medians of

the Δ_{13-8} distributions for δ^2H, δ^{18}O, and d are shifted towards zero by 1.6‰, 0.3‰ and 0.7‰, respectively, for periods with exhaust influence relative to periods without (see Appendix Fig. A.2a-c). The periods with exhaust influence are dominated by westerly winds (Appendix Fig. A.2d) and, thus, the measurements during exhaust influence are mainly associated with zonal advection. The dominance of this large-scale advection situation for the exhaust periods could be the main reason for the observed difference in the Δ_{13-8} distributions for periods with and without exhaust influence. Furthermore, large vertical SWI differences occurred more often during periods without exhaust influence and are thus unlikely to be caused by pollution from the ship's exhaust. Therefore, the exhaust influence on the SWI measurements is considered to be negligible and the exhaust masked is not applied to the SWI-13 time series.

2.3.3   Uncertainties in the calibration procedure

The influence of the various steps in the calibration protocol of SWI-13 and SWI-8-ps is assessed with sensitivity tests by varying one of the following steps and measuring the impact on the calibrated time series:

1. To correct the data for the isotope-humidity dependency, isotope-humidity dependency correction curves are derived using least-square fits to the standard measurements at different water vapour mixing ratios. To estimate the uncertainty of these fitted correction curves, different isotope-humidity dependency correction curves are applied: The correction curves from ACE ($\mathcal{H}_1$ and $\mathcal{H}_3$), a minimum and maximum correction curve ($\mathcal{H}_{1,\min}$, $\mathcal{H}_{3,\min}$ and $\mathcal{H}_{1,\max}$, $\mathcal{H}_{3,\max}$) for the ACE data representing the best fit to the calibration runs ± 1 standard deviation in δ-values of the calibration runs, the

correction curve from Sodemann et al. (2017) ($\mathcal{H}_2$) or no humidity correction ($\mathcal{H}_c$).

2. To correct for drifts between calibration runs, either a 10-day running mean is calculated from the runs or, for each leg, the average over all runs is used.

The calibration versions are summarised in Table A.1 in the Appendix. In the following, the versions are compared to the final versions that are calibrated using $\mathcal{H}_1$ and $\mathcal{H}_3$ for SWI-13 and SWI-8-ps, respectively, and a 10-day running mean for the drift correction between calibration runs. The isotope-humidity dependency correction (step 1) has the strongest impact on the calibration procedure. The uncertainty of the isotope-humidity dependency correction function, estimated by the minimum ($\mathcal{H}_{1,\mathrm{min}}$, $\mathcal{H}_{3,\mathrm{min}}$) and maximum ($\mathcal{H}_{1,\mathrm{max}}$, $\mathcal{H}_{3,\mathrm{max}}$) correction functions, leads to an uncertainty in the calibrated time series smaller than the mean 1-hourly standard deviation of 0.3 ‰, 2.3 ‰ and 2.8 ‰ for δ^{18}O, δ^2H and d, respectively, except for δ^2H and δ^{18}O at $w <$3'000 ppmv. Varying the handling of the calibration runs (step 2) introduces small differences on the order of 0.2 ‰ and 0.1 ‰ for δ^2H and δ^{18}O, respectively. Comparing the variations due to different calibration procedures with the vertical variations in SWIs, we find that Δ_{13-8} is larger than the difference between the calibration versions, except for δ^2H using the calibration of SWI-8-ps with $\mathcal{H}_c$ (no isotope-humidity dependency correction). However, for the other variables, the differences between the final versions and the versions without isotope-humidity dependency correction of SWI-8-ps correspond to less than 50% of Δ_{13-8}. Adding the effect of the uncertainty of the isotope-humidity dependency correction curves (calculated from the minimum and maximum correction curves) of both SWI-13 and SWI-8-ps, changes in the calibrated time series amount to 53%, 75% and 39% of Δ_{13-8} for δ^{18}O,

δ^2H and d, respectively. Even though, the isotope-humidity dependency correction introduces some uncertainty into the calibrated data, it remains distinctly smaller than Δ_{13-8} and, based on our current knowledge of factors influencing the calibration procedure, cannot fully explain the vertical differences in the SWI measurements. For more details on the calibration versions, see supplementary material.

We conclude, that measurement-related factors, which could influence the SWI time series, such as instrument settings, exhaust influence and the calibration procedure, cannot explain the observed vertical differences between the two time series, Δ_{13-8}. Thus, they are considered to be robust and the natural processes driving them are further discussed in Section 2.4.2.

2.4 Results and Discussion

The five-month time series of SWIs in water vapour provide the unique opportunity to assess the effect of moisture source and transport processes on SWIs in the MBL on various time scales and under diverse climatic conditions. In this section, the meridional and vertical variations of the SWI composition of the MBL are analysed. First, the time series are interpreted in their climatic context and meteorological processes responsible for the SWI variations along the meridional transect from 60 °N to 80°S are analysed. Second, it is illustrated how simultaneous SWI measurements at different heights can be used to study vertical isotope gradients and to estimate sea spray influence in the lowermost MBL.

The time series of SWI-13 and SWI-8-sb/ps correlate well with a Pearson correlation coefficient larger than 0.95 for all legs, instruments and variables, except for d which shows a Pearson correlation coefficient between

SWI-13 and SWI-8-ps of 0.9 for leg 0. δ^{18}O and δ^2H are lower and d is higher in SWI-13 than in SWI-8-sb/ps for most of the time except for the tropics and parts of leg 3. Due to the high correlation between the times series, only SWI-13 is discussed in the following section. SWI-13 is chosen because calibrated measurements of w are available for this dataset (see Section 2.2.2) and less sea spray influence is expected at the higher inlet location.

2.4.1 Meridional SWI variations

The diverse climate zones from the tropics to polar regions, traversed during the expedition, provide the possibility to probe a variety of different environmental conditions in various large-scale atmospheric forcing situations. The SWI measurements in Figs. 2.4 and 2.5 show a high event-to-event variability overlaid by a meridional gradient. The SWI values spread from $-8.6\,‰$, $-65.6\,‰$ and $20.3\,‰$ during leg 0 and 4 to $-37.1\,‰$, $-291.0\,‰$ and $-9.0\,‰$ during leg 2 and 3 for δ^{18}O, δ^2H and d, respectively. Here, we investigate the drivers of these meridional SWI variations and aim to disentangle the effect of short-term synoptic events on SWI variability from the effect of varying climatic conditions.

2.4.1.1 Imprint of varying climatic conditions on SWI signals

To investigate the meridional SWI variations, the data were grouped into bins of 10° latitudinal width. Figure 2.6 shows boxplots of these bins for measured SWI and meteorological variables. Furthermore, boxplots of the weighted mean moisture source conditions (Figs. 2.6d-f) are shown. Even though the number of points per bin differs strongly between the extratropics in the Northern and Southern hemisphere (not shown), the

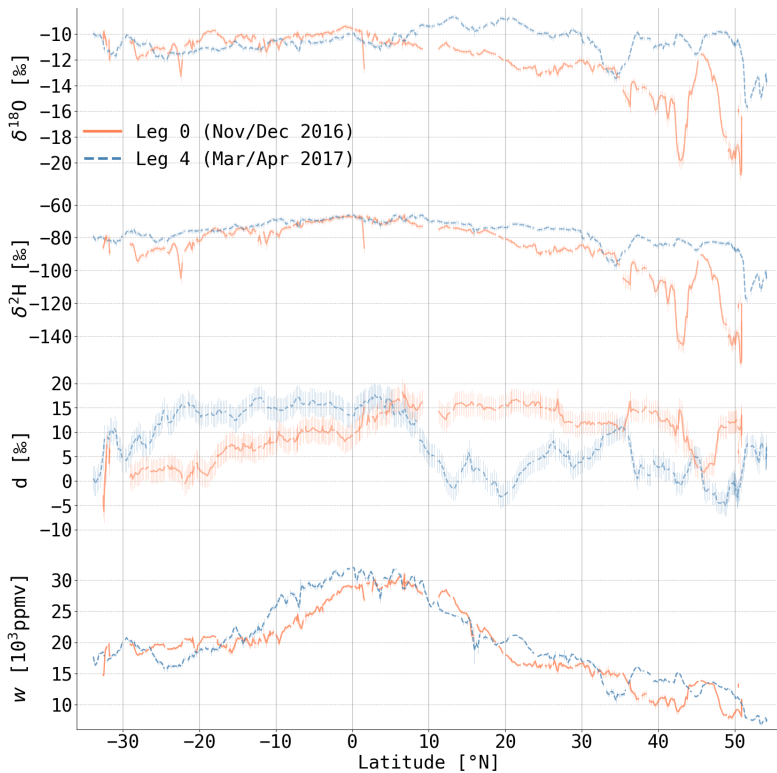*Figure 2.4: Hourly time series of $\delta^{18}O$, δ^2H, d, and w during legs 0 and 4 from SWI-13 versus latitude along the ship track. The errorbars denote hourly standard deviations of the 1s data.*
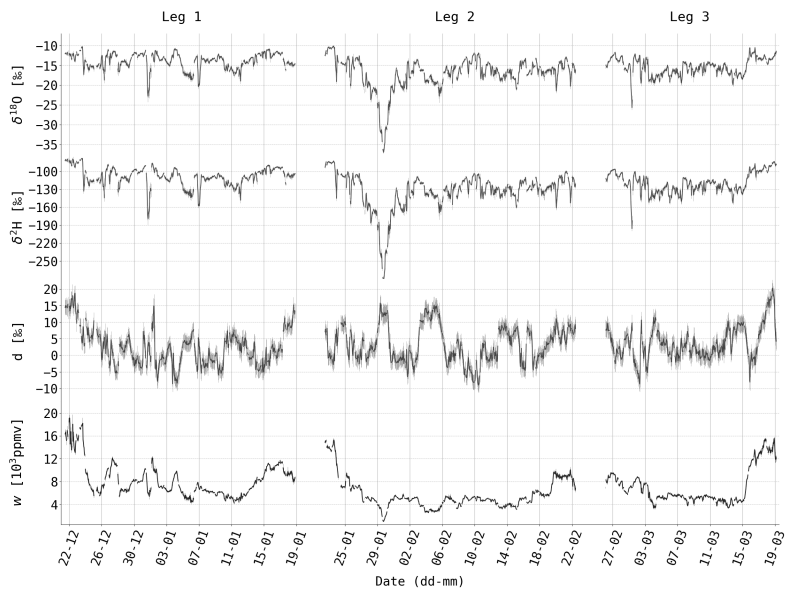
Figure 2.5: Time series of hourly $\delta^{18}O$, δ^2H, d, and water vapour mixing ratio w for legs 1-3 from SWI-13. The errorbars denote hourly standard deviations of the 1s data.

corresponding latitudinal bins of the two hemispheres cover a similar range of values for SWI and meteorological values.

The binned median δ^2H and δ^{18}O values show distinct meridional distributions with on average isotopically enriched air masses in the tropics and depleted air masses in polar regions (Figs. 2.6a,b). Note that the bin representing measurements closest to Antarctica shows an increase in median δ-values compared to the adjacent bin to the North. The measurements between 80°S and 70°S contain only observations from four continuous days, and therefore are strongly influenced by one weather situation.

A meridional gradient is also visible for the bins' interquartile ranges (referred to as IQR, and labeled by the subscript $_{\mathrm{IQR}}$ in the following). The enriched environments in the tropics and subtropics show small IQRs in SWI variables, whereas the depleted extratropical to polar regions show large IQRs. In both hemispheres, δ^2H$_{\mathrm{IQR}}$ and δ^{18}O$_{\mathrm{IQR}}$ increase from 20° to 70° latitude. The variability of SWIs is especially high in the $40 - 50°$ latitude band in both hemispheres. In this band, the [5,95]-percentile range extends over a similar range as the meridional gradient in median δ-values between the extratropics and the tropics. The very large [5,95]-percentile range of SWI measurements in the band $60 - 70°$S is due to very low δ-values measured at the Mertz glacier on 29 January 2017 (see Fig. 2.5), which leads to a strongly skewed distribution of measurements in this latitudinal band.

 The binned environmental conditions at the measurement site give insight into potential reasons for the meridional SWI variations described above. Higher temperature (T) and specific humidity (q) at the ship's position and averaged over the moisture sources are observed in the tropics compared to higher latitudes (Figs. 2.6d,e). Both the median T and q show similar meridional distributions as the median δ^2H and δ^{18}O. The distribution of T is asymmetric with higher temperatures in the $30 - 40°$S band compared
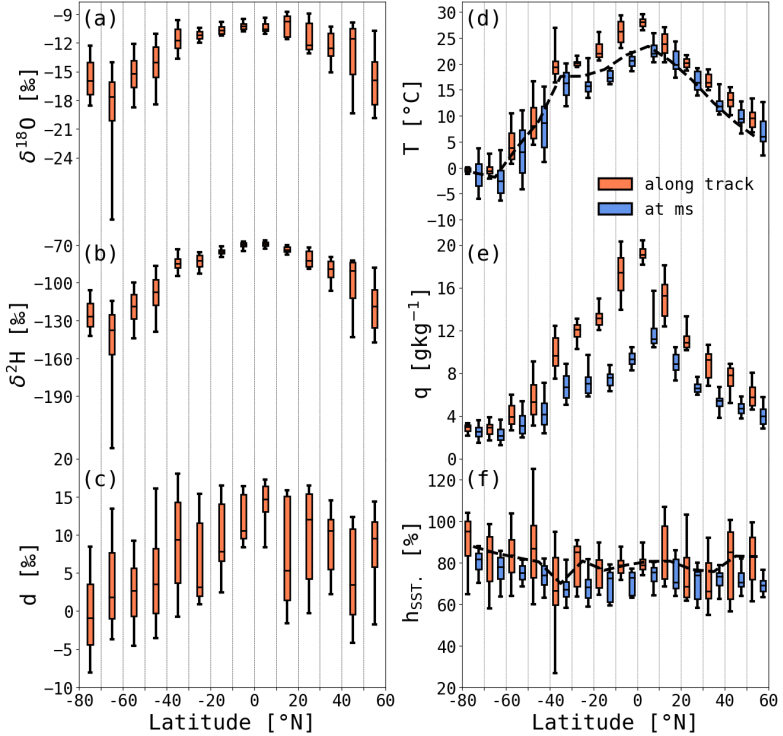
Figure 2.6: Box plots of meridional variations in SWIs and environmental variables for all legs showing mean (black horizontal line in box), interquartile range (boxes) and [5,95]-percentile range (whiskers) of variables in bins of 10° latitudinal width. (a) $\delta^{18}O$, (b) δ^2H, (c) d, (d) air temperature (T), (e) specific humidity (q), and (f) the relative humidity with respect to sea surface temperature (h_{SST}) at the measurement location are shown. Additionally, for T, q and h_{SST} the weighted mean at the moisture sources (ms) is shown (d-f). The black, dashed lines show sea surface temperature from operational ECMWF analysis data (d) and the relative humidity at the measurement location (f).

to the same latitude in the Northern Hemisphere. This asymmetry in the T distribution is reflected in the median δ^2H distribution and expresses the seasonal contrast between the winter and the summer hemispheres. T and q are lower at the moisture source compared to the measurement location, which reflects properties of air masses that experience moistening due to ocean evaporation and warming due to heat exchange with the ocean. They are initially cold and dry, and are advected over a relatively warmer ocean, thereby triggering ocean evaporation by a strong humidity gradient between the ocean and the atmosphere (Aemisegger and Papritz, 2018). For the southernmost bin, the higher T at the moisture source compared to the adjacent bin to the North hints towards more equatorwards sources and transport within the warm sector of an extratropical cyclone, which can explain the relatively enriched SWI composition in this bin closest to Antarctica.

Similar meridional variations, as seen here for $\delta^{18}O$ and δ^2H in water vapour, have been observed for SWIs in precipitation (Araguás-Araguás et al., 2000; Feng et al., 2009). These meridional SWI variations are interpreted traditionally as the isotopic depletion of air masses due to rainout and were described by Dansgaard (1964) as the "temperature effect". Previous measurements of SWIs in water vapour in the Atlantic Ocean show a similar meridional gradient with highest values in the tropics (around -10 ‰ for $\delta^{18}O$) and lowest in polar regions (around -35 ‰ for $\delta^{18}O$, Bonne et al., 2019). Close to the equator, Liu et al. (2014) observed slightly different patterns of meridional variations in their measurements of SWIs in water vapour from the Indian Ocean. They showed a depletion in SWIs in water vapour in the tropics compared to the subtropics. This is probably due to the proximity of the southeast Asian land masses and the influence of deep convective precipitation systems in the tropics, conditions that were not encountered during the SWI measurements in the Atlantic ocean. There

are a few periods of depleted $\delta^{18}O$ in the tropics in the measurements by Bonne et al. (2019) (see their Fig. 1), similar to the precipitation event in the tropics during ACE, which led to a strong short-term isotopic depletion of the MBL by 12 ‰ in $\delta^{18}O$ due to convective downdrafts and below-cloud interaction of hydrometeors with MBL vapour (see leg 0 at 2°N in Fig. 2.4). Due to the rare occurrence of tropical rainfall along the ACE track, the direct SWI imprint of isotopically depleted rainfall in the tropics might be underestimated compared to climatological conditions.

The meridional distribution of d (Fig. 2.6c) with a peak in the tropics at median values of ∼15 ‰ and minima around 0 ‰ close to Antarctica is in line with the d predicted from local h_{SST} and SST conditions using reanalysis data in Aemisegger and Sjolte (2018) based on the closure assumption of Merlivat and Jouzel (1979). Meridional variations in h_{SST} at the measurement location are weak with larger $h_{SST,IQR}$ at higher latitudes (Fig. 2.6f). The local h_{SST} measurements are anti-correlated with d, as shown in Fig. 2.7 as expected from detailed analyse of h_{SST} versus d in water vapour from the Mediterranean (Pfahl and Wernli, 2008), the Southern Ocean (Uemura et al., 2008), and the Atlantic Ocean (Bonne et al., 2019). The SST-d relationship from ACE is illustrated in Fig. 2.7. The meridional gradient observed in d is partly due to the dependency of d on SST during equilibrium fractionation and also reflects the meridional SST gradient as discussed in Aemisegger and Sjolte (2018). The linear relations between d and its environmental controls based on ACE data for evaporative conditions ($h_{SST} < 100\%$) are -0.4 ‰ %$^{-1}$ and 0.4 ‰ K^{-1} for h_{SST} and SST, respectively. These values are consistent with previous ship-based studies (e.g. Uemura et al., 2008; Bonne et al., 2019). Several transient periods of high d concurrent with low h_{SST} were observed along the Agulhas warm ocean current in the Southern Ocean (21 - 25 December 2016; "x" in Fig. 2.7) and along the sea ice edge albeit with lower
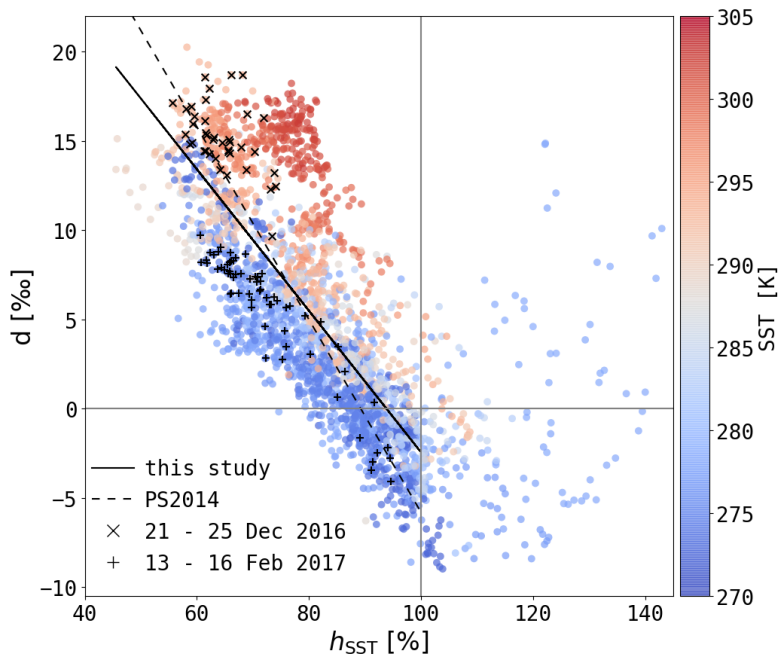
Figure 2.7: *Scatterplot of* d *vs.* h_{SST} *coloured by SST. The linear fit to all points with* h_{SST} *<100% (black line) has a Pearson correlation coefficient of -0.73 with the following fitting function:* $d(h_{\mathrm{SST}}) = -0.4\text{‰}\,\%^{-1} \cdot h_{\mathrm{SST}} + 36.8\text{‰}$. *The dashed line shows the linear relationship between* d *and* h_{SST} *from Pfahl and Sodemann (2014). Two time periods with low* h_{SST} *are marked: 21 - 25 Dec 2016 (x) and 13 -16 Feb 2017 (+).*

peak d values for the same h_{SST} over regions with colder SSTs (13 - 16 February 2017; "+" in Fig. 2.7). In contrast to the observed positive linear correlation of d and SST during ACE, results by Pfahl and Wernli (2008) and Steen-Larsen et al. (2015) showed only weak SST-d-correlations. This discrepancy might be due to the different spatio-temporal focus of these studies, which both used measurements from a fixed station, at the synoptic time scale, in an environment with weak SST gradients. The SST influence on d was also questioned by Pfahl and Sodemann (2014). Their spatial d distribution predicted using a combination of datasets from the South Indian Ocean and the Mediterranean shows several marked differences to our results. In particular, d measured during ACE is 5-10 ‰ smaller along the sea ice edge over low SST and 5-10 ‰ larger in the tropics over high SSTs than the DJF mean predicted by Pfahl and Sodemann (2014). The only exception in the decreasing meridional trend in d during ACE are the elevated values in the northernmost bin, which groups measurements from the British Channel region. In this region, confined by land masses, we expect some influence of higher d vapour from continental air masses, which have been moistened by evapotranspiration (Aemisegger et al., 2014). A few events with supersaturated conditions (h_{SST}>100%) are associated with a moisture flux from the atmosphere into the ocean during warm air advection. These will be discussed in more detail in a follow-up study.

In summary, the meridional distribution of the δ^{18}O, δ^2H and d signals can be linked to the varying climatic conditions, such as T, q, and h_{SST}, along the ACE track, which are reflected in the median isotopic signature in the MBL water vapour. In the next section, the large-scale dynamical drivers of the SWI signals from ACE are described.

2.4.1.2 Imprint of large-scale atmospheric weather systems on SWI signals

The meridional distribution of $\delta^{18}O_{IQR}$, δ^2H_{IQR}, and d_{IQR} (Fig. 2.6a,b,c) is strongly linked to the type of weather systems involved in shaping the isotope signals on synoptic timescales. The drivers of the SWI variability at different latitudes are discussed in this section based on the moisture source properties and the frequency of occurrence of weather systems typical for the traversed regions.

The meridional distribution of the weighted mean moisture source latitude (see supplementary material) shows larger IQRs at higher latitudes. The large spread of moisture source locations in extratropical and polar regions is illustrated by the hourly 75% moisture source regions for the MBL water vapour along the cruise track (Fig. 2.8). The coloured contours in Fig. 2.8 represent the 75% moisture source region for locations in the same colour along the ACE track - the yellow contours in Fig. 2.8b, for example, correspond to locations around 80°E on the ACE track. For legs 1-3 (Fig. 2.8b-d), the moisture source regions cover nearly the whole Southern Ocean. The high temporal variability of the extratropical and polar moisture source areas is due to the high frequency of high and low pressure systems at these latitudes. The frequent passage of extratropical cyclones (Fig. 2.9) and their associated cold and warm sectors leads to an alternating SWI pattern by cold and warm advection (Dütsch et al., 2016; Aemisegger, 2018). A further common feature of the extratropics are the westerly moisture source regions relative to the ship's position, which are due to the mean westerly winds and the eastward movement of extratropical cyclones within the storm track.

In contrast to the widespread moisture source areas in the extratropics, the source areas in the subtropics and tropics are narrowly confined. They
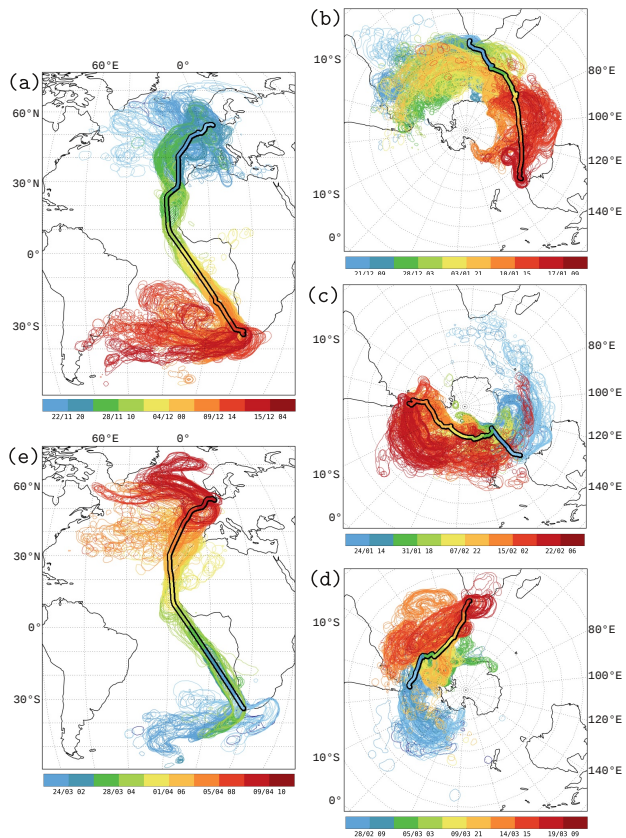
Figure 2.8: Contour plots of hourly 75% moisture source regions of water vapour along the ship track for legs 0 - 4 (a-e) coloured by time. The colours assign the source regions to the corresponding water vapour along the ship track (black framed line).

extend in the direction of the trade winds (Fig. 2.8 a,e) and are located to the east and on the poleward side of the ship's position. The small δ^2H_{IQR} and $\delta^{18}O_{IQR}$ reflect the steady environmental conditions associated with these well-defined, narrow moisture source bands of the slowly subsiding subtropical air masses. In the tropics and subtropics, the SWI variability in the MBL is dominated by vertical transport such as shallow and deep convection, turbulent mixing, and the influence of large-scale descending air masses in the subtropics (Lee et al., 2011; Brown et al., 2013; Benetti et al., 2015). During ACE, the flow conditions in the subtropics are dominated by low-level anticyclones, which lead to large-scale subsidence of air masses (Fig. 2.9b). These descending air masses are transported equatorward and experience extensive moistening due to ocean evaporation and shallow convection in the MBL. Due to the relatively stationary anticyclones and persistent trade winds in the subtropics during ACE, the moisture is transported along a north-east to south-western pathway with small temporal variability from the subtropics into the tropics. This persistent large-scale flow situation leads to similar moisture source locations for a given latitude throughout the tropics and subtropics and similar isotopic compositions of the evaporative flux at the moisture source. Therefore, small IQRs of SWIs have been observed in the tropics and subtropics. One exception is the influence of North African air masses on d which will be discussed later in this section.

In addition to the important role played by moisture source conditions, the measured SWI variations in water vapour can be further influenced by moisture removal and precipitation-vapour interactions during transport, both in the tropics (Lawrence and Gedzelman, 1996; Lawrence et al., 2004; Bony et al., 2008) and extratropics (Graf et al., 2019). These interactions modify the SWI composition of air masses during transport such that the measured isotopic composition deviates from the isotopic composition of
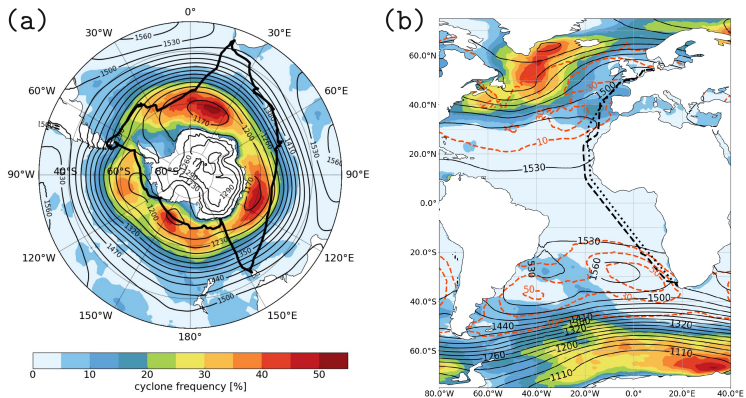
*Figure 2.9: Mean cyclone frequencies (coloured contours, [%]) and geopotential height at 850 hPa (black contours, [m]) are shown for legs 1-3 (**a**) and legs 0 and 4 (**b**). The mean anticyclone frequencies (orange, dashed contours, [%]) for legs 0 and 4 are additionally plotted in panel (**b**). The thick black line shows the ship tracks for legs 1-3. The dashed and dotted black lines show the ship track of legs 0 and 4, respectively. ECMWF operational analysis data was used to produce this figure.*

water vapour from ocean evaporation at the moisture source. The uptake-to-loss ratio, a measure of moisture uptake relative to moisture loss during transport (see Section 2.2.4.4), was 2-4 times larger in the subtropics and tropics than in the extratropics and polar regions (see Appendix Fig. A.3). This implies that polar and extratropical air masses are more strongly affected by precipitation during transport than suptropical and tropical air masses, which reflects the highly dynamical nature of the atmospheric water cycle in the extratropics. Consequently, the high SWI variability of the MBL water vapour in the extratropics is not only due to the strongly varying transport pathways and moisture sources, but also due to larger variability in the precipitation along these pathways. Note, that the fact that we did not encounter deep convective systems during this cruise leads to a high uptake-to-loss ratio in the tropics compared to what we expect in typical tropical deep convective regions.

The meridional variations of d_{IQR} (Fig. 2.6c) are more complex than the ones of $\delta^2\mathrm{H}_{\mathrm{IQR}}$ and $\delta^{18}\mathrm{O}_{\mathrm{IQR}}$. The smallest d_{IQR} are also found in the tropics, however a d_{IQR} maximum in the $10° - 20°$N band along the North African coast coincides with large $h_{\mathrm{SST,IQR}}$ (see Fig. 2.6c,f and d for the corresponding latitudes in Fig. 2.4). These large $h_{\mathrm{SST,IQR}}$ and d_{IQR} reflect the strongly varying importance of African moisture source contributions and the contrasts in source locations between leg 0 and 4 (compare Figs. 2.8a and d). Except for the special case of the $10° - 20°$N band along the African coast, d_{IQR} is on average higher in the extratropics compared to the tropics with two local minima in regions of cold ocean surface currents at $50° - 60°$S in the region of the polar front and at $30° - 40°$N along the cold Canary surface ocean current.

The meridional distribution of SWI signals and their synoptic-timescale variability reveal the different driving processes at different latitudes. The

meridional gradient of the median SWI composition in the MBL reflects the climatic conditions at the measurement and moisture source location, specifically T, q, and h_{SST}. Dynamical drivers such as extratropical cyclones and persistent anticyclones control the variability of the MBL SWI composition at a given latitude. The measured SWI signals, thus, show an imprint of the environmental conditions in the MBL. The variability of these environmental controls and the measured SWI signals is driven by the dynamics of the large-scale circulation.

2.4.2 Vertical SWI variations

An estimate of the vertical SWI gradients in the near-surface layer is given by the difference between SWI-13 and SWI-8-ps signals (Δ_{13-8}). Here, only the isotope variables $\delta^{18}O$, δ^2H and d are discussed, since calibrated specific humidity measurements are only available from SWI-13. More depleted water vapour was systematically measured at the 13.5 m site compared to the 8 m site on the research vessel. The influence of measurement uncertainties has been analysed in Section 2.3 and it has been shown that, to the best of our knowledge, they cannot explain the observed vertical differences. Therefore, physical reasons to explain the vertical SWI variations are discussed in this section. Only legs 1-3 are analysed because ocean surface state measures and sea salt concentrations are available solely for the Southern Ocean part of the cruise and because we expect different processes to affect the near-surface isotopic composition in the tropics compared to the extratropics. The data is shown in 5 min resolution in this section, because turbulence varies on sub-hourly timescales.

The vertical gradients sampled during ACE between the two measurement points at 13.5 m and 8 m a.s.l. amount to $-0.5\,[-0.9\,...\;\;0.0]\,‰\,m^{-1}$ for δ^2H (numbers in brackets denote the 65% percentile range), $-0.10\,[-0.16\,...$

$-0.02]\,\text{‰}\,\text{m}^{-1}$ for $\delta^{18}\text{O}$, and $0.3\,[0.1\,...\,0.6]\,\text{‰}\,\text{m}^{-1}$ for d (Fig. 2.10) with overall more depleted vapour and higher d at the higher elevation than closer to the sea surface. These gradients are approximately twice as large for $\delta^{18}\text{O}$ and about the same order of magnitude for $\delta^{2}\text{H}$ as the ones obtained from aircraft-based measurements in the MBL in the Mediterranean (Sodemann et al., 2017). Since the measurements during ACE were performed much closer to the surface, different vertical gradients can be expected. The vertical gradient in d of this study is opposite to the one observed by Sodemann et al. (2017) and to several profiles by Salmon et al. (2019). For the profiles in the aforementioned studies, cloud processes might have played an important role in shaping the negative vertical d gradient. Such processes can be neglected for near-surface measurements in the absence of fog. Vertical SWI gradients measured in the Mediterranean between 20.35 and 27.9 m a.s.l. on a research vessel (Gat et al., 2003) are an order of magnitude smaller for $\delta^{18}\text{O}$ and about the same order of magnitude for d with large positive gradients in d ($0.6\,\text{‰}\,\text{m}^{-1}$) in the Eastern Mediterranean during conditions with high stability of the air column. Furthermore, the best representation of the vertical SWI gradients in idealized box models was achieved if the box models included sea spray evaporation (Gat et al., 2003). We will study the influence of vertical atmospheric stablity and sea spray evaporation on vertical SWI gradients further by considering in situ measurements of sea spray and wave age.

2.4.2.1 Sea spray and wave age

The dependence of Δ_{13-8} on local environmental conditions is examined to identify the processes that shape the vertical SWI gradients. The observed vertical gradients show a wind dependency with larger negative $\Delta_{13-8}\delta^{2}\text{H}$ and $\Delta_{13-8}\delta^{18}\text{O}$ for high wind speeds and, to a smaller extent, for very low
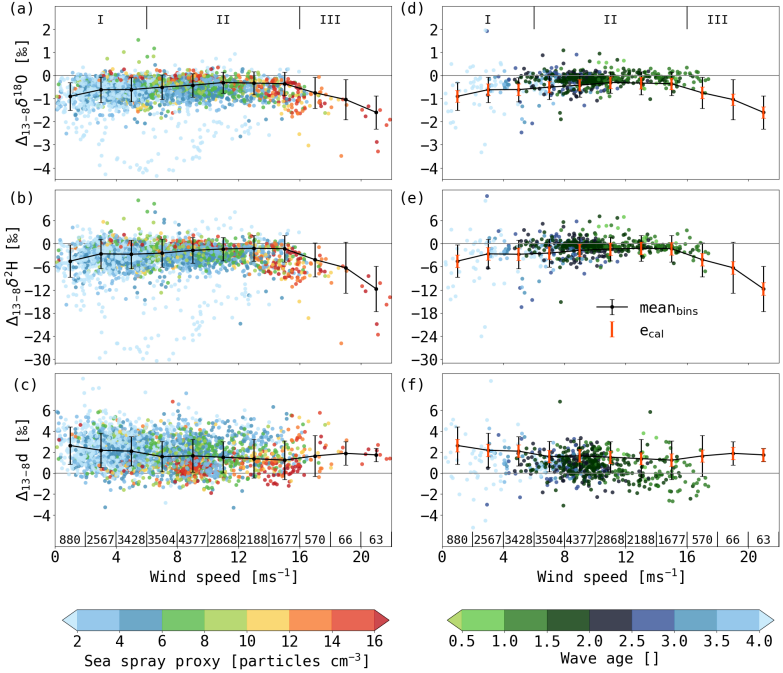
*Figure 2.10: Scatter plots of the vertical differences between SWI-13 and SWI-8-ps for **(a,d)** $\delta^{18}O$ ($\Delta_{13-8}\delta^{18}$), **(b,e)** δ^2H ($\Delta_{13-8}\delta^2H$) and **(c,f)** d ($\Delta_{13-8}d$) versus wind speed for legs 1-3. The colours show the sea spray proxy **(a-c)** or wave age **(d-f)**. The black line represents the mean and standard deviations of the vertical differences in $2\,m\,s^{-1}$-bins. Orange error bars in **(d-f)** show the averaged uncertainty e_{cal} due to the post-processing (as presented in section 2.3) which amounts to 0.25 for $\delta^{18}O$, 1.63 for δ^2H and 0.59 for d. The vertical lines at the bottom indicate the $2\,m\,s^{-1}$-bins labelled by the number of measurement points per bin. The labels (I, II, III) at the top correspond to the wind regimes (see text and Fig. 2.11). Fewer points are shown in **(d-f)** than in **(a-c)**, because less wave age than sea spray data is available. The data is shown in 5 min resolution and only every third time step is plotted in the scatter plots.*

wind speeds compared to intermediate wind speeds (Fig. 2.10). d shows a weaker wind dependency than $\delta^{18}O$ and δ^2H with largest positive $\Delta_{13-8}d$ for low wind speeds. According to this dependency, three wind regimes are defined: [I] low wind speed $< 6\,\mathrm{m\,s^{-1}}$, [II] intermediate wind speed between $6\,\mathrm{m\,s^{-1}}$ and $16\,\mathrm{m\,s^{-1}}$, [III] high wind speed $> 16\,\mathrm{m\,s^{-1}}$. Regime III shows the most extreme vertical SWI gradients, except for $\Delta_{13-8}d$, for which regime I shows the largest vertical gradients (see Appendix Table A.2). The large Δ_{13-8} of the δ-values in regime III coincide with high sea spray concentrations at the upper inlet (Fig. 2.10a-c). Sea spray influences SWIs by sea spray evaporation. Under the assumption that water from sea spray droplets evaporates nearly completely, part of the moisture input into the MBL occurs through a non-fractionating process with signals close to the ocean surface isotope composition. A stronger influence of sea spray evaporation at the lower compared to the upper inlet could lead to a more enriched isotopic composition of water vapour at the lower inlet and thus large negative $\Delta_{13-8}\delta^2H$ and $\Delta_{13-8}\delta^{18}O$ at high wind speed. Because ocean water has a d close to zero, the evaporation signal from sea spray introduces a low d at the lower level and, thus, an increased positive $\Delta_{13-8}d$ is expected. There is a weak tendency to larger positive $\Delta_{13-8}d$ in regime III, but the median d-values are close to the median values in regime II. It cannot be ruled out, that sea spray droplets were deposited on the inlet filter of the lower inlet, where they evaporated and enhanced the isotopic signal induced by sea spray evaporation.

As a measure of sea surface roughness and the production of sea spray from wave breaking, wave age is shown in Figs 2.10d-f. Wave age decreases with increasing wind speed. There are very few wave age measurements available at very high wind speeds during ACE. The available wave age data suggest that the large negative $\Delta_{13-8}\delta^{18}O$ and $\Delta_{13-8}\delta^2H$ in regime III with high sea spray concentrations occurred during breaking wave con-

ditions at low wave age ($\sim< 1.0$). Thus, the large vertical SWI differences in regime III can be explained by sea spray influence, which is stronger at the lower inlet site. For regime I at low wind speed, wave age is high and a much weaker influence of sea spray evaporation is expected. During these calm conditions, there is again a tendency for larger negative Δ_{13-8} in δ-values and larger positive $\Delta_{13-8}d$ compared to regime II. These increased vertical SWI differences in regime I are likely caused by weaker vertical turbulent mixing at low wind speed. This hypothesis is elaborated in more detail in section 2.4.2.2.

2.4.2.2 Effects of marine boundary layer turbulence

Here, an attempt is made to explain the observed near-surface vertical SWI gradients in particular in weak wind conditions. Our analysis focuses again on the atmospheric layer close to the ocean surface with a width of several tens of meters. Note that, in contrast, the vertical mixing model introduced by Benetti et al. (2018) focused on vertical moisture mixing across the MBL top. We propose a qualitative interpretation framework based on the near-surface wind speed and the roughness of the sea surface (Fig. 2.11). Two main processes are taken into account in this framework: (1) vertical turbulent mixing, which increases with wind speed, leads to a well-mixed atmospheric layer close to the ocean surface and, thus, weakens the vertical SWI gradients; and (2) the sea state determines the production of sea spray and the influence of sea spray evaporation on the SWI composition. The proposed framework considers the three wind regimes introduced in section 2.4.2.1, in which these two processes are expected to differ in strength. As a consequence, vertical turbulent mixing and sea spray evaporation exert a varying influence on the vertical SWI gradient in the lowermost MBL.
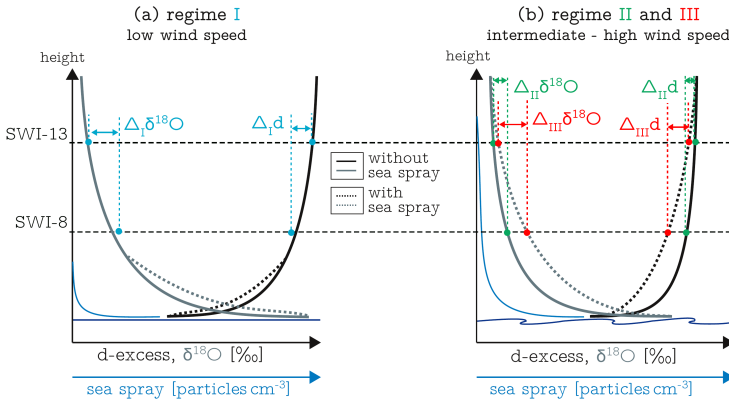
*Figure 2.11: Schematic showing the vertical SWI gradient under low (a)
and intermediate to high (b) wind speed conditions illustrating the three
boundary layer turbulence regimes (I,II,III). Δ_I, Δ_{II} and Δ_{III} represent
the vertical differences between SWI-13 and SWI-8 for the three regimes.
For details see text.*

For low wind speed conditions with high wave age in regime I (Fig. 2.11a),
weak vertical turbulent moisture transport is expected. If the MBL vertical
moisture gradient results from linear mixing of freshly evaporated water
vapour from the ocean surface with moisture from the free troposphere,
which likely experienced condensation previously, then lower layers are
expected to have higher δ-values than upper layers. In such a scenario,
weak vertical mixing leads to strong vertical gradients of specific humidity
and δ-values. Non-equilibrium fractionation at the ocean surface during
evaporation strongly impacts d in the ocean evaporation flux. Therefore,
the vertical d-gradient in the lower MBL depends on the strength of non-

equilibrium fractionation at the ocean surface. If we assume a simple "two end-member"-mixing process in the MBL of freshly evaporated water vapour with free tropospheric air masses that have undergone substantial rainout, the vertical gradient in d is defined by the difference in d between these two end-members. Air masses, which have lost a major fraction of their water vapour during rainout, show a d in water vapour that closely follows a Rayleigh distillation process (Samuels-Crow et al., 2014) and are expected to have high d by the definition of d (see e.g. Dütsch et al., 2017). d in freshly evaporated water vapour is therefore expected to remain below d of free tropospheric air masses that have undergone substantial rainout previously. An effect by sea spray evaporation is not expected in this wind regime as only little sea spray is produced at low wind speeds. This simple interpretation framework could explain the observed conditions with enhanced gradients in $\delta^{18}O$, δ^2H and d at low wind speeds (regime I) compared to medium wind speeds (regime II). However, recent studies (e.g. Sodemann et al., 2017; Salmon et al., 2019) showed that the vertical gradients in particular of d rarely follow a simple two end-member mixing model. Differential transport processes in the boundary layer as well as convective plumes with enriched water vapour (and lower d) are probably responsible for the large variability in the observed vertical isotope profiles. Therefore, further analysis, which goes beyond the scope of this study, is needed to quantify the wind dependency of non-equilibrium fractionation and its effect on the vertical d-gradient in the MBL. For intermediate wind speeds in regime II (Fig. 2.11b), turbulent mixing is stronger, which leads to a well-mixed surface layer. In this regime, the influence by sea spray evaporation is still considered small. Therefore, small vertical SWI differences are measured. Other studies also showed an increasingly well-mixed lower MBL for lower wave age using vertical wind profiles in conditions representative of regime II (e.g. Smedman et al., 2009). For high wind

speeds in regime III (Fig. 2.11b), strong turbulent mixing is assumed in the lower MBL and sea spray production is enhanced, which increases the vertical gradient in SWIs as shown in the previous section.

Even though this qualitative framework can explain the observed vertical SWI differences, it remains difficult to quantify the relative importance of enhanced turbulence and sea spray evaporation from two vertical point measurements. In particular, regime I with weak vertical turbulence at low wind speeds needs to be assessed in more detail including vertical profiles of specific humidity measurements. Therefore, more high-resolution vertical profiles of the SWI composition and environmental parameters such as temperature, specific and relative humidity, sea salt concentrations, and 3D wind speed in the lowermost MBL are needed to verify the proposed mechanisms. Furthermore, modelling the isotopic composition in the MBL with various approaches spanning from simple mixing models to large-eddy simulations could help to understand the measured profiles. Despite these open questions, this study shows that the comparison of measurements at different heights on a research vessel can give new insight into turbulent moisture fluxes during air-sea interaction and may be helpful in the future to estimate the moisture input into the atmosphere from sea spray evaporation.

2.5   Summary and conclusions

In this study, we compared three time series of SWI measurements in water vapour derived from laser spectrometric measurements onboard the RV *Akademik Tryoshnikov* during the Antarctic Circumnavigation Expedition from November 2016 to April 2017. The time series were calibrated and post-processed following a protocol similar to Aemisegger et al. (2012)

and Steen-Larsen et al. (2014), as described in Section 2.2.

These unique five-month time series cover a variety of MBL conditions in different synoptic weather situations and for different small-scale mixing states across the Atlantic and Southern Ocean. We analysed the meridional variations of SWIs in water vapour and their link to meteorological parameters. Overall, the SWI composition in water vapour from the tropics to polar regions reveal distributions similar to the ones known from precipitation measurements at different latitudes. On average, a gradual depletion of heavy isotopes from the tropics to polar regions can be observed, following the evolution of decreasing temperature and specific humidity. The climatic conditions at the measurement and moisture source locations are reflected in the median meridional SWI distribution. The synoptic-timescale variability of SWI signals (interquartile range of meridionally binned hourly measurements) is highest in extratropical and polar regions. Results from a Lagrangian moisture source analysis reveal that the range of SWI compositions at a specific latitude is strongly linked to the variability in moisture source location and conditions. The MBL water vapour in tropical and subtropical regions has narrow, well-defined moisture source regions aligned with the trade winds. The water vapour sampled in these regions typically originates from the progressive moistening of subsiding mid-tropospheric air masses within anticyclones. In contrast, moisture sources in the extratropics are highly variable as a result of the strong meridional moisture transport typical for the extratropics and generally associated with extratropical cyclones. Cyclone passages lead to alternating moisture transport pathways with equatorward sources in the warm sector and poleward sources in the cold sector. Furthermore, moisture loss during transport, which affects the SWI composition of water vapour, is more variable in the extratropics than in subtropical and tropical regions. The range of hourly SWI $\delta-$values in the extratropics under the influence

of cyclone passages is larger by an order of magnitude compared to the subtropics and tropics during persistent weather situations. Whether this extratropical SWI variability in the MBL is mainly due to the advection of air masses with different moisture sources and transport characteristics or rather the result of local air-sea fluxes induced by the large-scale advection of air masses is a question that we will address in a future study based on the ACE dataset. Note that we did not encounter tropical deep convective systems in the equatorial Atlantic Ocean during this cruise and, thus, the SWI variability in the equatorial Atlantic Ocean might be lower during ACE than expected during more convective conditions.

We conducted a thorough quality assessment of the SWI time series, which revealed that the differences between the time series observed at different heights above the ocean is larger than any uncertainty introduced by variations in the instruments' cavity properties, exhaust influence or the calibration procedure. The mean vertical gradients [with 65% percentile range] found in the near-surface layer in the extratropics are $-0.5\,[-0.9\ldots0.0]\,\%_0\,\mathrm{m}^{-1}$ for $\delta^2\mathrm{H}$, $-0.10\,[-0.16\ldots-0.02]\,\%_0\,\mathrm{m}^{-1}$ for $\delta^{18}\mathrm{O}$, and $0.3\,[0.1\ldots0.6]\,\%_0\,\mathrm{m}^{-1}$ for d.

The vertical SWI differences depend on surface wind speed with larger differences for very high and very low wind speeds compared to intermediate wind speeds. This wind speed dependency is qualitatively interpreted in a framework of different influencing factors, including vertical turbulent mixing and sea spray evaporation. Low wind speeds are generally associated with high wave age and low concentrations of sea spray. Therefore, the tendency for larger SWI differences between 8 and 13.5 m a.s.l. at low wind speed can be interpreted as a gradient due to weak vertical mixing of moisture. The small vertical SWI differences at intermediate wind speeds are associated with a lower wave age and might be due to stronger turbulent mixing, which leads to a more homogeneous SWI distribution in the

lowermost MBL. The large vertical SWI differences at high wind speeds are most likely due to a rough sea, breaking waves (low wave age) and an increased enrichment of the lowermost layers from water evaporation of sea spray droplets.

The study of vertical SWI variations in MBL water vapour shows the potential of SWIs as tracers for vertical mixing in the lowermost MBL and as an indicator of atmospheric moisture input by sea spray evaporation. For an in-depth understanding and verification of the proposed mechanisms leading to the observed vertical SWI variations, SWI profiles at higher vertical resolution than the two point measurements in this study should be conducted in future studies. Such a setup could provide a framework to better quantify the contribution of sea spray evaporation to MBL moisture. Overall, the presented measurements from the Atlantic and Southern Ocean highlight the large variety of processes at different scales that shape the short-term variability of SWI signals. The interaction of large-scale atmospheric flow features at different latitudes with small-scale turbulent and convective mixing processes is a topic on which SWI measurements from ACE can provide helpful insights in future research.

Chapter 3

Frameworks for modelling the isotopic composition of atmospheric water vapour

The modelling of SWIs helps to understand the short-term variability of SWIs in the atmospheric water cycle. There are various complexities of SWI models. Single process models, such as the Craig and Gordon (1965) model for ocean evaporation or the Rayleigh model (Dansgaard, 1964), are designed to understand the influence of one process on the isotopic composition of the studied water reservoir. More complex, isotope-enabled numerical models are able to simulate the spatial and temporal evolution of the atmospheric isotopic composition on a global to regional scale. These simulations incorporate a variety of processes, which influence SWIs in the atmospheric water cycle and can, e.g., be used to evaluate the relative importance of these processes for the SWI variaiblity. In this chapter, different SWI models are introduced. First, single-process air

parcel models are described and the influence of these single processes on the isotopic composition of water vapour is discussed (Section 3.1). Second, the isotope-enabled numerical weather prediction model COSMO$_{iso}$ is introduced (Section 3.2) and its most important features for the study of cold and warm temperature advection in Chapter 4 are discussed.

3.1 Single-process air parcel models

To better understand the SWI variability of the MBL, single processes, which influence the isotopic composition of an air parcel in the MBL, are modelled. Especially, the evolution of d in water vapour is investigated to compare to variations in d in the ACE measurements. These single-process air parcel models are used to interpret the SWI evolution of the MBL water vapour in Chapter 4.

3.1.1 Moisture uptake by ocean evaporation

Ship-based measurements of SWIs in water vapour are strongly influenced by ocean evaporation. Air masses, which were exposed to ocean evaporation, can be identified by their high d (Aemisegger and Sjolte, 2018). The continuous moistening of an air parcel due to ocean evaporation increases h_s in the air parcel (if entrainment from above is neglected) and, thereby, changes the environmental conditions during ocean evaporation. The effect of changes in the environmental condition on the SWI composition of an air parcel, which is affected by ocean evaporation, will be studied with an air parcel model which experiences moisture uptake induced by ocean evaporation.

Model setup   The specific humidity q_a of an air parcel with an initial

isotopic composition of $^2R_0$ and $^{18}R_0$ is increased stepwise by a fixed amount Δq. The isotopic composition $^2R_{evap}$ and $^{18}R_{evap}$ of Δq is calculated using the model by Craig and Gordon (1965) (see Equ. 1.9). The evolution of the isotopic composition of the air parcel is calculated iteratively by linear mixing of q of the air parcel and Δq. This results in the following formulation of the isotopic composition $R_{a,i+1}$ at time i+1

$$R_{a,i+1} = \frac{R_{a,i} \cdot q_{a,i} + R_{evap} \cdot \Delta q}{q_{a,i+1}}. \tag{3.1}$$

$R_{evap} = \frac{\alpha_k \cdot (R_{MBL} \cdot h_s - R_{Oc} \cdot \alpha_e)}{h_s - 1}$ is the isotopic composition of the evaporation flux, $R_{a,i}$ the isotopic composition of the air parcel at time i and $q_{a,i+1} = q_{a,i} + \Delta q$. This stepwise increase in q is continued until $q_a = q_s$, which corresponds to saturated conditions ($h_s = 1.0$).

The formulation by Horita and Wesolowski (1994) for the equilibrium fractionation factors and the formulation by Merlivat and Jouzel (1979) without wind-dependency for the non-equilibrium fractionation factors are used. The isotopic composition of the ocean is assumed to correspond to R_{VSMOW}. The SST is predefined and constant during the simulation. In this model, changes in SST and R_{Oc} due to ocean evaporation are neglected. The model is initiated with different q_a, $^2R_0$ and $^{18}R_0$ to simulate ocean evaporation under different environmental conditions.

Results A simulation initiated with 285 K sea surface temperature, 2.7 g kg^{-1} specific humidity (and, thus, h_s=0.31), $-160\,‰$ in δ^2H and $-20.5\,‰$ in δ^{18}O is shown in Fig. 3.1. Next to the isotopic composition of the water vapour and evaporation flux, the equilibrium vapour composition is shown, which represents the isotopic composition of water vapour in thermodynamical equilibrium with the ocean surface. The equilibrium vapour composition is equal to $\alpha_e \cdot R_{oc}$. During the simulation, δ^{18}O and
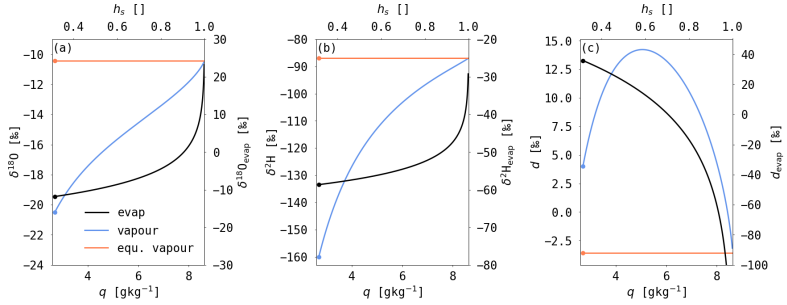
Figure 3.1: Evolution of $\delta^{18}O$ (a), δ^2H (b) and d (c) in an ocean evaporation model run with $SST_0=285\,K$, $q_{a,0}=2.7\,g\,kg^{-1}$, $\delta^2H_0=-160\,‰$ and $\delta^{18}O_0=-20.5\,‰$. The blue line shows the isotopic composition of the water vapour in the air parcel, the orange line of the equilibrium vapour (equ. evap) and the black line of the evaporation flux (evap).

δ^2H in the vapour phase increase towards the equilibrium vapour composition (Figs 3.1b,d). d shows a maximum of 14.2 ‰ at h_s=0.6 and decreases afterwards until it reaches the equilibrium composition of $-3.6\,‰$ (Fig. 3.1c). The isotopic composition of the evaporation flux is more depleted in heavy isotopes than the equilibrium vapour from ocean surface water and more enriched in heavy isotopes than the starting vapour of the air parcel. The δ-values of the evaporation flux increase strongly for h_s close to 1.0. This is due to the strong vertical gradient towards more depleted values in the air parcel compared to the equilibrium vapour over the ocean surface. This large difference in heavy SWIs between the air parcel and equilibrium water vapour leads to an increased flux of heavy isotopes from the ocean surface to the air, which is seen in the increase in δ-values of the evaporation flux. This increase in the evaporation flux leads to the changes in the water vapour δ-values for h_s close to 1.0. This single simulation shows, that continuous ocean evaporation into an air parcel leads to an

increase in d if h_s is low. When the air parcel approaches saturation, d decreases rapidly.

Sensitivity runs were conducted to test the influence of the initial conditions on the isotopic composition of water vapour during the simulation (Fig. 3.3a-d). The shape of the SWI evolution in the the vapour phase is similar for all runs and shows a continuous increase in $\delta^{18}O$ and δ^2H, while d shows a maximum before a continuous decrease towards the equilibrium composition. SST is the main factor influencing the evolution and final isotopic composition of the vapour. Increasing initial SST leads to a higher maximum value of d, and higher final $\delta^{18}O$, δ^2H, d and q. The maximum in d occurs at h_s between 0.6 and 0.75.

SST-gradient The advection of cold air masses in the cold sector of extratropical cyclones transports cold and dry air masses towards low latitudes, thereby inducing strong ocean evaporation (Aemisegger and Papritz, 2018). Due to the equatorward movement, these air masses are transported over an SST gradient. For the North Atlantic region, latent heat fluxes are associated with north-westerly winds perpendicular to the SST gradient (Ogawa and Spengler, 2019), while air masses in the warm sector arrive from south-westerly direction and thus encounter decreasing SST during the transport (Sinclair, 2013). SST influences h_s because q_s increases with increasing SST. Therefore, non-equilibrium fractionation as a function of h_s changes its strength depending on the SST during evaporation. The effect of an SST-gradient on the isotopic composition of the evaporation flux and the MBL isotopic composition is tested with a model simulating the isotopic composition of an air parcel which encounters ocean evaporation while it is transported over an SST gradient.
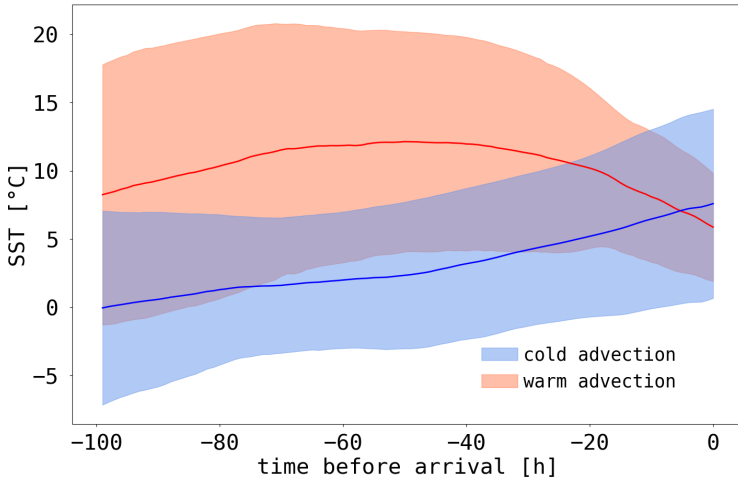
Figure 3.2: Averages of SST along all trajectories arriving at the ACE track in the cold sector (blue) and warm sector (red) within the MBL over open ocean (no sea ice, land fraction <0.1 in the COSMO$_{\text{iso}}$ simulations). Solid lines show the mean values, shaded areas the standard deviation for all trajectories arriving in each sector. These trajectories are calculated using COSMO$_{\text{iso}}$ simulations (see Sec. 4.2.2.2).

The ocean evaporation model setup is adjusted to allow for a prescribed SST-gradient during the simulation. Fig. 3.2 shows the evolution of the SST along trajectories arriving in the MBL along the ACE track in the cold and warm sector of extratropical cyclones. The trajectories were calculated using the COSMO$_{\text{iso}}$ simulations as described in Section 4.2.2.2 and are discussed in detail in Section 4.5. In the cold sector, the trajectories experience a continuous increase in SST. In the warm sector, the trajectories first experience also an increase in SST, but approximately 2 days before

arrival at the ACE track, SST starts decreasing. In accordance with these SST-evolutions along trajectories, SST in the model is defined to increase from an initial SST_0 to a maximum $SST_{max} = SST_0 + 15°C$ (representing the increase in SST during cold advection) and decreases afterwards to a final $SST_{final} = SST_0$ (corresponding to the SST evolution during warm advection).

The increase in q due to ocean evaporation is incorporated in two ways:

1. q increases linearly from $q_{a,0}$ to q_s at SST_{final}. In this scenario, q of the air parcel increases monotonically. This method does not take into account the changing strength in ocean evaporation due to changing h_s. Therefore, the air parcel might have biased low h_s while SST is increasing. Nonetheless, this scenario illustrates the effect of solely changing the SST compared to the first scenario of constant SST.

2. To account for changes in evaporation strength, q is defined to increase proportionally to the evaporation flux $E \propto (q_{SST} - q)$. Δq is scaled by the evaporation flux such that the air parcel is saturated after it has reached SST_{max}.

The main differences between model runs with constant and varying SST is seen in d and q (Fig. 3.3a,e,i). For varying SST, the final q is higher because SST_{final} (and thus q_s) is higher compared to the constant SST runs. Furthermore, in the simulation with Δq proportional to the evaporation rate, q is highest. This is caused by the saturation of the air parcel before SST reaches $SST_{final} < SST_{max}$. In the simulations with an SST-gradient, the maximum in d reaches values up to $20\,‰$, which is caused by the lower h_s compared to the simulations with constant SST. Due to the increasing SST, h_s increases slower with increasing q than in the constant

SST simulation. For linearly increasing q, h_s even decreases, in the beginning. This is due to the small Δq-steps relative to the increase in SST. This means, q increases slower than q_s and, therefore, h_s decreases.
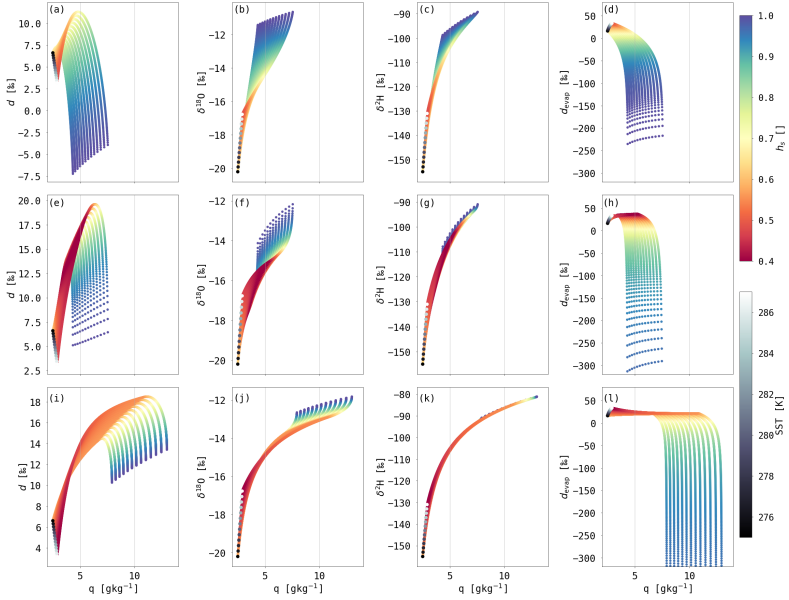
*Figure 3.3: Ocean evaporation model runs with different implementations of the SST and q evolution during the runs: constant SST (**a-d**), varying SST with linearly increasing q (**e-h**) and varying SST with q increasing proportionally to the evaporation flux (**i-l**). The model outputs d (a,e,i), $\delta^{18}O$ (**b,f,j**), δ^2H (**c,g,k**) and the d composition of the evaporation flux d_{evap} (**d,h,l**) are shown for runs with varying initial SST and isotopic compositions (coloured dots). The initial isotopic composition of each model run is indicated with grey dots, coloured by SST_0.*

In all three model setups, a characteristic evolution of d in water vapour

is seen. d increases in the beginning until it reaches a maximum and decreases, when h_s approaches 1.0. Therefore, an air parcel, which experienced moistening by ocean evaporation is expected to have high δ^2H and δ^{18}O, while the value of d is more variable depending on the evolution of undersaturation of the air parcel with respect to SST. Compared to the box model approach by Benetti et al. (2018), this simple Lagrangian model of boundary layer SWIs explicitly simulates the transformation of an air mass.

The described model assumes that each air parcel takes up moisture until it is saturated. Such a continuous moistening of the air masses due to ocean evaporation might not occur in reality. The impact of ocean evaporation can be progressively weakened due to lifting of the air masses or because the air masses move over land. The isotope signals will reflect the integral history of conditions during uptake over the moistening phase of the air parcel. Furthermore, in this model, ocean evaporation is the only process affecting the isotopic composition of the air parcel. Other processes, such as below cloud processes or moisture exchange with the environment due to entrainment at the MBL top by turbulent mixing and convective up and downwards drafts could change the isotopic evolution of the air parcel which is not taken into account in the idealised simulations presented here. The evolution of SWIs in an air parcel as simulated using this ocean evaporation model will be compared to COSMO$_{iso}$ backward trajectories in Section 4.6.3, where it is shown that the ocean evaporation model adequately simulates the SWI evolution along trajectories arriving in the cold sector. These cold sector trajectories are mainly influenced by ocean evaporation. For trajectories arriving in the warm sector, more diverse processes influence the air masses. Therefore, a dew position and a cloud formation air parcel model are introduced in the following to describe further processes influencing SWIs in the MBL.
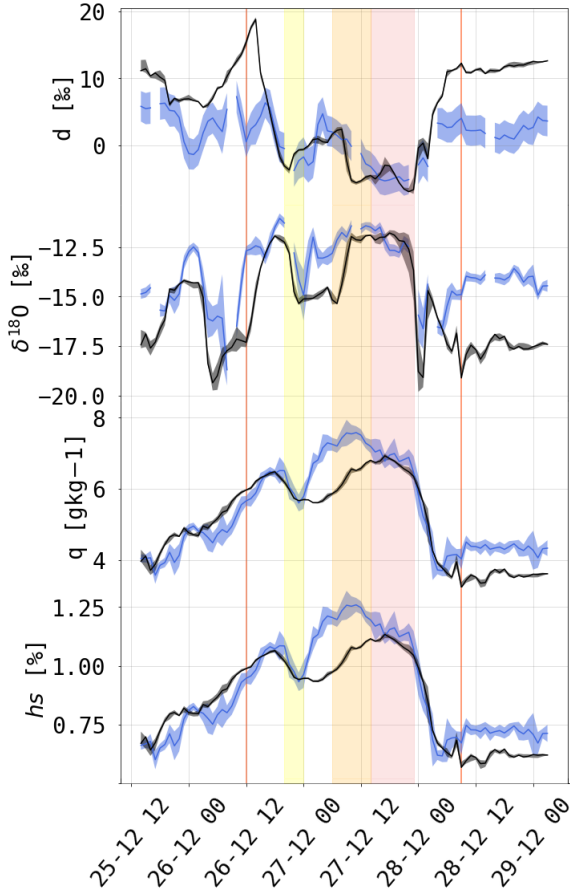
Figure 3.4: Time evolution of d, $\delta^{18}O$, q and h_s from ACE measurements and COSMO$_{\mathrm{iso}}$ simulations during a warm temperature advection event at Marion Island. The blue lines are ACE measurements, the black lines are COSMO$_{\mathrm{iso}}$ simulations interpolated to the ACE track.

3.1.2 Moisture loss by dew deposition on the ocean surface

Measurements of SWIs during ACE show low or negative d in combination with high δ-values during periods of warm temperature advection, i.e. $T_{2m} >$SST and positive anomalies in specific humidity (Fig. 3.4). In these situations, the atmosphere is often oversaturated with respect to the ocean surface temperature such that there is a moisture flux from the atmosphere to the ocean (*dew deposition*). To model the evolution of the SWI composition of the atmospheric water vapour during such a dew deposition event, a simple mass balance approach is chosen. In the following, the model setup and results from model runs are shown.

Model setup   We initiate an air parcel with a specific humidity $q_a > q_s$ and a supersaturation of $h_s = \frac{q_a}{q_s}$, where q_s is the saturation specific humidity at SST. We assume that this air parcel only interacts with the ocean surface and does not exchange water vapour with its atmospheric environment. We let this air parcel equilibrate with the ocean surface by iteratively removing its excess water vapour compared to q_s through dew deposition. Using the traditional aerodynamic formulation, the depositional fluxes for the light water vapour $^l E$ and the heavy water vapour $^h E$ can be formulated as follows:

$$^l E = \Psi \cdot (q_a - q_s) \tag{3.2}$$

$$^h E = \Psi \cdot \alpha_k \cdot (^h q_a - ^h q_s) \tag{3.3}$$

where $\Psi = \rho \lambda C_e U$, with ρ the air density, λ the latent heat of vaporisation, C_e a non-dimensional transfer coefficient, U the wind speed at 10 m a.s.l.), $\alpha_k < 1$ the non-equilibrium fractionation factor, $^h q_a$ the specific humidity

of the heavy water molecules and $^h q_s$ the saturation specific humidity of
the heavy water molecules.

Equations 3.2 and 3.3 can be combined to get an expression of the isotopic
ratio of the depositional flux R_{dew} . Including the boundary condition, that
$^h q_s$ is equal to the saturation specific humidity at SST: $^h q_s = R_{Oc} \cdot \alpha_e \cdot q_s$,
where $\alpha_e < 1$ is the equilibrium fractionation factor, and replacing $^h q_a$ by
$R_a \cdot q_a$, we get the following equation

$$
\begin{aligned}
R_{dew} =^h E/^l E &= \frac{\alpha_k \cdot (R_a \cdot q_a - R_{Oc} \cdot \alpha_e \cdot q_s)}{q_a - q_s} \\
&= \frac{\alpha_k \cdot (R_a \cdot h_s - R_{Oc} \cdot \alpha_e)}{(h_s - 1)}
\end{aligned}
\tag{3.4}
$$

Equation 3.4 corresponds to the equation for the isotopic ratio of the evap-
oration flux of the Craig-Gordon model (Craig and Gordon, 1965). We
use the formulation by Horita and Wesolowski (1994) for the equilibrium
fractionation factors and the formulation by Merlivat and Jouzel (1979)
without wind-dependency for the non-equilibrium fractionation factors.

To model the evolution of the isotopic composition in an air parcel during
dew deposition as a function of specific humidity, the following assump-
tions are made:

- The air parcel looses continuously water vapour by deposition on the
  ocean surface. To simulate this loss with time, the specific humidity
  q_a is continuously decreased by a small amount Δq until $q_a = q_s$.
  Thus, during each step, there is a depositional flux Δq with the
  isotopic ratio R_{dew}.

- The ocean surface isotopic ratio stays constant at R_{VSMOW} and it
  is not altered by the small amount of deposited dew.

- Temperature variations due to equilibration or phase changes are ne-

glected. The temperature difference between ocean and atmosphere is on the order of a few degrees, which does not have a large impact on isotopic fractionation.

Using these assumptions, the isotopic composition of the water vapor can be iteratively calculated with:

$$R_{a,i+1} \cdot q_{a,i+1} = R_{a,i} \cdot q_{a,i} - \Delta q \cdot R_{dew}, \tag{3.5}$$

$$\text{with } q_{a,i+1} = q_{a,i} - \Delta q \tag{3.6}$$

And thus the isotope ratio of the vapour in the air parcel can be calculated iteratively:

$$R_{a,i+1} = \frac{R_{a,i} \cdot q_{a,i} - R_{dew} \cdot \Delta q}{q_{a,i+1}} \tag{3.7}$$

Results   Figure 3.5 shows the evolution of the isotopic composition of the water vapour and the depositional flux as a function of h_s with the initial conditions: $T_{a,0}$=6°C (thus q_s=5.8 g kg^{-1}), δ^2H=-100‰, δ^{18}O=-12.5‰, q_a=7.0 g kg^{-1} and $h_s = \frac{q_a}{q_s}$=121%. These values are chose to represent typical environmental conditions during dew deposition in the Southern Ocean (compare Fig. 3.4).

The evolution of the water vapour d during dew deposition can be divided into two regimes. Regime I for $h_s \gtrsim 1.05$ is dominated by non-equilibrium fractionation (high supersaturation of the air mass). In this strongly supersaturated regime, the initial values of the isotopic composition of the water vapour also play an important role. The depositional flux is most depleted in this regime and has a positive d which leads to an enrichment of the water vapour and a decrease in d. Notice, that the depositional flux represents a flux from the atmosphere to the ocean surface. Therefore, if the depositional flux is isotopically depleted, the remaining water vapour

becomes enriched in SWIs. In Regime II in the range $1.0 < h_s \lesssim 1.05$, there is a non-linear increase in δ-values and a negative d in the depositional fluxes. The water vapour isotopic composition in this regime approaches the isotopic composition of the equilibrium vapour from the ocean surface water and the isotope gradients between the ocean and atmosphere become very small.
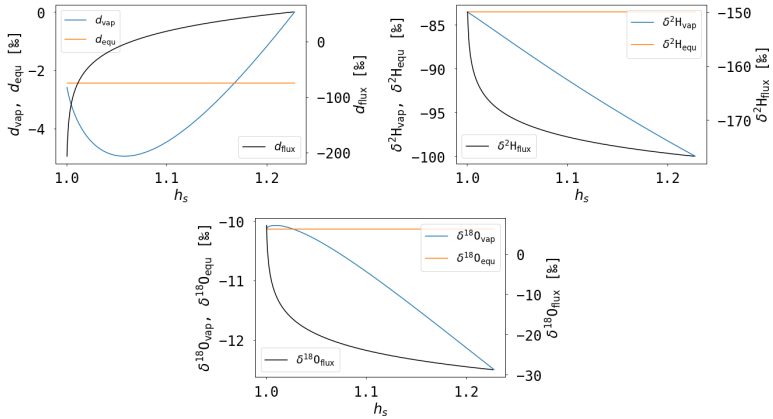
Figure 3.5: Modelled (a) d, (b) δ^2H and (c) $\delta^{18}O$ of water vapour (vap) and depositional flux (flux) during dew deposition on the ocean surface with initial conditions $SST_0=6.0\,°C$, $\delta^2H_0=-100.0\,‰$, $\delta^{18}O_0=-12.5\,‰$ and $q_0=7.0\,g\,kg^{-1}$. The orange line shows the isotopic composition of the water vapour, which is in equilibrium with the ocean surface (equ).

For $\delta^{18}O$, an *overshooting* occurs close to $h_s = 1.0$, which means that $\delta^{18}O$ in water vapour is higher than $\delta^{18}O$ in the equilibrium vapour. The reason for this overshooting is investigated using sensitivity runs in the following.

Model outputs for varying starting conditions are shown in Fig. **??**. Two sets of sensitivity runs at $T_{a,0}$ =6.0°C were conducted. First, the initial specific humidity q_0 was kept constant, while $\delta^{18}O_0$ and δ^2H_0 were varied (Fig. **??**a-c). Second, q_0 was varied, which means that different initial supersaturations are assumed, while the isotopic composition was kept constant (Fig. **??**d-f). For all starting conditions, a decrease in d is seen at high h_s. Depending on the initial isotopic composition and q_0, d shows a minimum and an increase afterwards or decreases directly towards the equilibrium vapour composition (Fig. **??**a,b). The higher the initial h_s and the lower the initial d, the lower is the minimum in d. $\delta^{18}O$ increases with varying rates towards the equilibrium composition depending on the initial values. For high $\delta^{18}O_0$ and q_0, the rate of change in $\delta^{18}O$ as a function of h_s is lower than for lower initial values and the "overshooting" of $\delta^{18}O$ close to h_s=1.0 is more likely to occur. Since this overshooting for $\delta^{18}O$ is not very large in amplitude it is not investigated further. It seems to be a physically plausible signal, which is due to the very depleted dew deposition flux. The continuous removal of a depleted water vapour flux from the ambient vapour leads to a remaining vapour that gets more enriched than the equilibrium vapour from ocean water. The low $\delta^{18}O$ and δ^2H of the dew deposition flux is due to the large gradient in δ-values towards the equilibrium vapour from ocean water. In the case of $\delta^{18}O$, this effect is enhanced by the small diffusivity of $H_2^{18}O$ in air, which leads to a much more pronounced non-equilibrium fractionation effect than for $^1H^2H^{16}O$. For $\delta^{18}O$, the continuous removal of depleted water vapour leads to a remaining water vapour that can become more enriched than equilibrium ocean vapour depending on the chosen initial conditions.
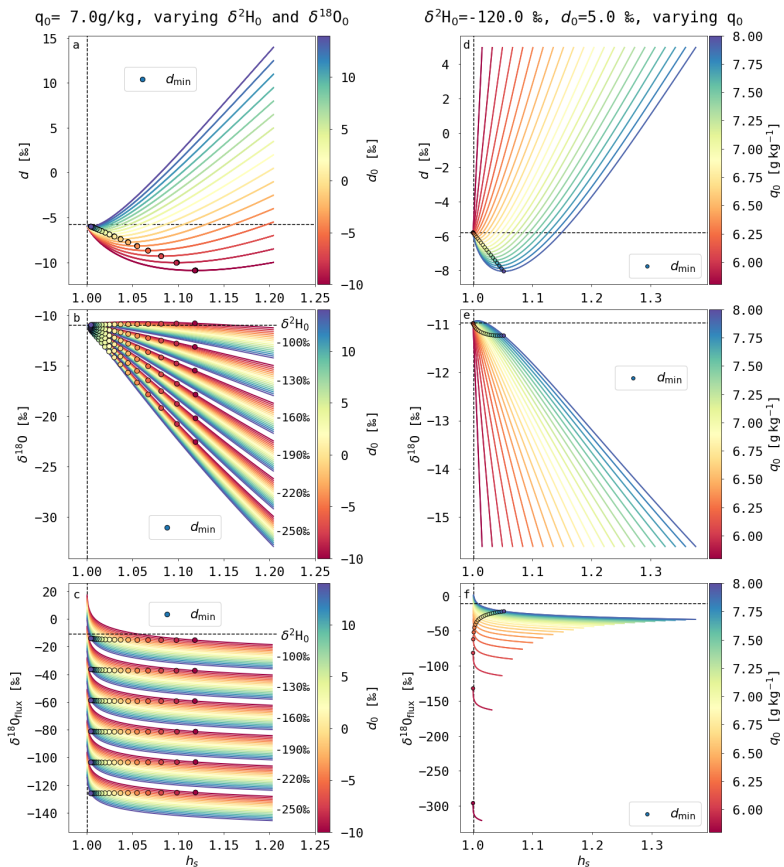
*Figure 3.5: Modelled isotopic composition of water vapour and the depositional flux during dew deposition on the ocean surface for model runs at $6.0\,°C$ and varying initial conditions. The evolution of d (**a,d**) and $\delta^{18}O$ (**b,e**) in water vapour and $\delta^{18}O$ in the depositional flux (**c,f**) are shown as a function of h_s. The runs are coloured by the initial d-excess d_0 (**a-c**) and the initial specific humidity q_0 (**d-f**). The coloured dots mark the position of the minimal d during each run. The vertical dashed black line marks $h_s = 1.0$ and the horizontal line d (**a,d**) and $\delta^{18}O$ (**b,c,e,f**) of the water vapour in equilibrium with the sea surface. Note that different combinations of $\delta^{18}O$ and δ^2H can lead to the same d and, thus, the same evolution of d relative to h_s (see different "batches" of coloured lines in the left panels). In (**b,c**) δ^2H_0 is denoted for each "batch".*

3.1.3   Rayleigh fractionation during cloud formation

The condensation of water vapour in an ascending air parcel leads to the formation of cloud droplets, which changes the isotopic composition of the remaining atmospheric water vapour. This process can be modelled using a Rayleigh fractionation model based on the temperature and moisture evolution of a moist-adiabatic ascent of an air parcel. Thereby it is assumed, that the condensed cloud droplets do not interact anymore with the surrounding water vapour after condensation and are immediately removed. This is a simplification of processes occuring during cloud formation, but it provides a first order understanding of isotopic variations in clouds.

Model setup   A Rayleigh model (Dansgaard, 1964) is used including the temperature dependency of α_e (Horita and Wesolowski, 1994) and the transition from liquid to ice clouds. The temperature and humidity evolution is approximated by the evolution during a moist-adiabatic ascent

starting with $T_{a,0} =6.0\,°C$ and $p_0= 1000\,hPa$ and is modelled in a similar way as in Dütsch et al. (2017). The isotopic ratio of the water vapour during Rayleigh fractionation at step $i+1$ is defined in the following, iterative way:

$$R_{a,i+1} = f^{(\alpha_{eff}-1)} \cdot R_{a,i}, \qquad (3.8)$$

where $f = \frac{q_{a,i+1}}{q_{a,i}}$ is the remaining fraction of moisture in the vapour phase. The change in q from i to $i+1$ corresponds to the excess moisture at step i relative to q_s along a moist-adiabatic ascent. R_a is the isotopic ratio of the water vapour in the air parcel. $\alpha_{eff} > 1$ is the isotopic fractionation factor depending on temperature and the relative fractions of liquid and solid condensate during the moist-adiabatic ascent:

$$\alpha_{eff} = \alpha_e(T) \cdot f_{liq} + \alpha_{ice} \cdot (1 - f_{liq}) \qquad (3.9)$$

f_{liq} is 0 for $T < 250.15\,K$ and 1 for $T > 273.15\,K$ and a quadratic interpolation is used in between these temperatures to represent mixed phase clouds. $\alpha_{ice} > 1$ is the equilibrium fractionation factor in vapour with respect to ice (Majoube, 1971), adjusted for supersaturation over ice (Jouzel and Merlivat, 1984).

Results   Figure 3.6 shows the Rayleigh fractionation model for moist-adiabatic ascent with $T_{a,0} =6.0\,°C$, $p_0 =1000\,hPa$ and initial isotopic composition $\delta^2H_0=-90.0\,‰$ and $\delta^{18}O_0=-12.0\,‰$. Four different scenarios are modelled:

1. Rayleigh fractionation with constant temperature and a step-wise loss of moisture.

2. Rayleigh fractionation along a moist-adiabatic ascent, i.e. with temperature variations, assuming only liquid clouds.

3. same as 2., including ice cloud formation and the fractionation factor for vapour over ice.

4. same as 3., including an adjustment of the ice fractionation factor due to ice supersaturation.

All of these four scenarios show a depletion of δ^{18}O and δ^2H in water vapour with ongoing moisture loss. d in water vapour decreases in the beginning for all scenarios. The decrease in d is small of a value around 1‰ for scenario 1 with constant temperature and increases to values above the start value after the condensation of 75% of the humidity. In the other three scenarios, there is a stronger decrease in d with minimum values of more than 6‰ below the starting value. This stronger decrease in d is due to the temperature-dependency of the equilibrium fractionation factor. α_{eff} increases more rapidly with decreasing temperature for ^{2}H than for ^{18}O (see Fig. 3.6d). Thus, d in the condensate increases and d in the remaining vapour decreases with decreasing temperature. Scenario 3, which includes the equilibrium fractionation effects of the ice phase but neglects non-equilibrium effects due to supersaturation, shows a weaker decrease in d. When including ice supersaturation, the evolution of d follows a similar pattern as scenario 2 with only liquid cloud formation. Once, the amount of heavy isotopes in the vapour phase becomes very small, d increases by definition (due to the non-linearity of the δ-scale, see also Dütsch et al., 2017) for all scenarios.

In a sensitivity experiment using scenario 4 with a moist adiabatic ascent and ice supersaturation, the effect of different initial
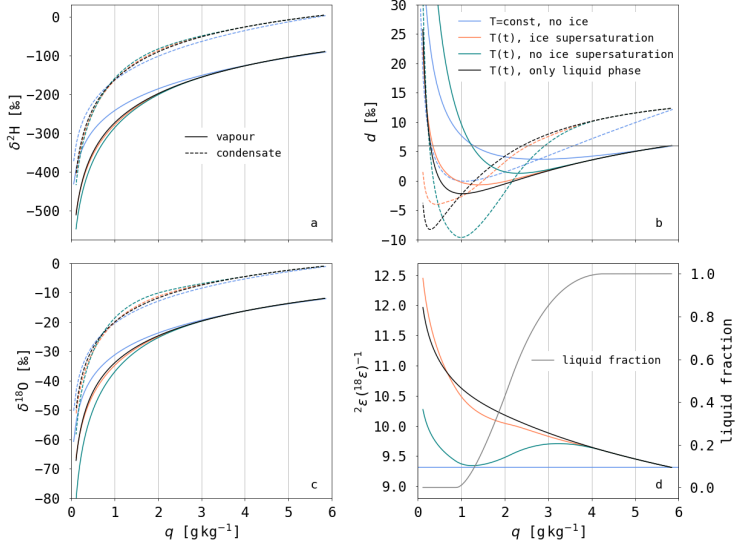
Figure 3.6: Modelled specific humidity q versus (a) δ^2H, (b) d and (c) $\delta^{18}O$ of water vapour (solid lines) and condensate (dashed lines) during Rayleigh fractionation with different model setups (see text for details). Furthermore, the liquid fraction for the two setups with ice cloud formation is shown in (d). The ratio of $^2\epsilon$ and $^{18}\epsilon$ as a measure of the temperature dependency of α_{eff} is shown for each model setup as a function of q. All model runs are initiated at a temperature of 6.0 °C and a pressure of 1000 hPa.

temperatures is shown (Fig. 3.7). The temperature dependency of α_{eff} is stronger for lower temperatures and, therefore, the decrease in d is strongest for low initial temperatures and becomes negative for very low starting
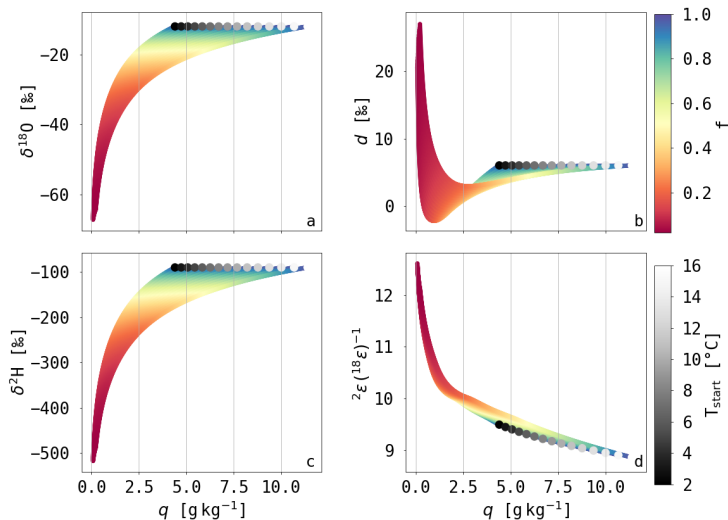
Figure 3.7: Same as Fig. 3.6, but only showing the isotopic composition of the vapour phase for the model setup with ice cloud formation and ice supersaturation with varying initial temperatures from 2 - 16 °C. The model runs are coloured by the remaining fraction of moisture in the air parcel f and the starting position of each model run is indicated with grey dots, coloured by the initial air temperature T_{start}.

temperatures. d starts increasing once only 20% of the water vapour is remaining in the air parcel.

This example illustrates that the condensation of cloud water is a possible process which decreases d-excess in water vapour. In contrast to dew formation, decreasing d is accompanied by decreasing δ-values during cloud formation. Therefore, by combining the evolution of d and δ-values, the effect of dew deposition and cloud formation on the isotopic composition

of water vapour can be separated.

The effects of the three air parcel models on the isotopic composition of water vapour can be separated using phase-space diagrams (Fig. 3.8). In a d-δ^{18}O-phase space (Fig. 3.8a), each model shows a specific evolution. The dew deposition and the Rayleigh fractionation model both show a decrease in d during the first part of their evolution, but they show a different behaviour with respect to δ^{18}O. During dew deposition, δ^{18}O increases in this first half of the simulation, while δ^{18}O in the Rayleigh fractionation model decreases continuously. In the ocean evaporation model, d increases during the first part of the simulation and decreases during the second part. This decrease in d can be separated from the d-decrease during dew deposition and Rayleigh fractionation in the d-q-phase space. While q decreases during dew deposition and cloud formation, q increases during ocean evaporation. Therefore, in the d-δ^{18}O- and the d-q-phase space, each model has a unique evolution. These different behaviours in the phase spaces will be used in Section 4.6.3 to separate the effects of these moist processes in the cold and warm sector of extratropical cyclones.
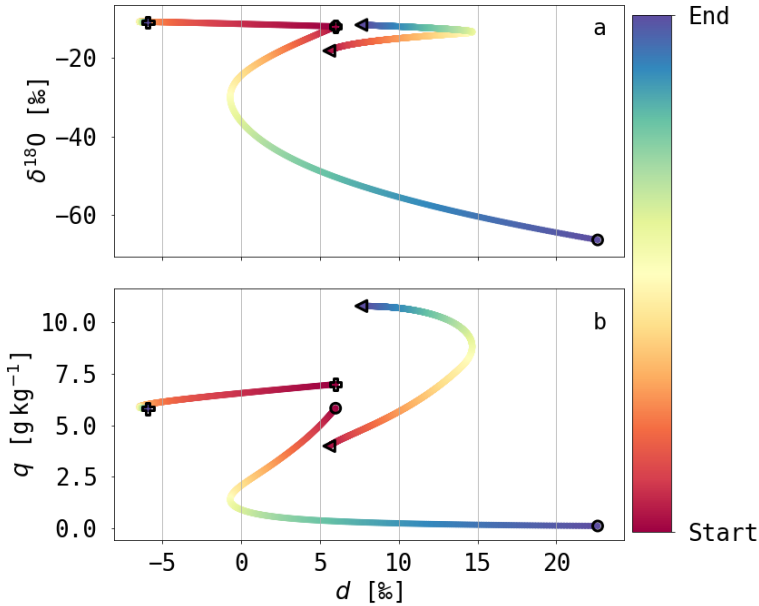
Figure 3.8: *Phase space diagrams of* d *versus* $\delta^{18}O$ *(**a**) and* d *versus* q *(**b**) showing a model run of each air parcel model. All models are initiated with* $T_{\text{start}} = 6\,°C$, *while the specific humidity and isotopic composition is adjusted to respresent typical environmental conditions for the simulated moist processes. For dew deposition (+) initial conditions of* $q_0 == 7\,g\,kg^{-1}$, $\delta^{18}O_0 = -12\,‰$ *and* $\delta^2H_0 = -90\,‰$ *are chosen. The Rayleigh fractionation model (o) is initiated with the same* $\delta^{18}O_0$ *and* δ^2H_0 *as the dew deposition model (which leads to* $q_0 = 5.84\,g\,kg^{-1}$). *The ocean evaporation model (◁) with* Δq *proportional to the evaporation flux and varying SST is initiated with* $\delta^{18}O_0 = -18.2\,‰$, $\delta^2H_0 = -140\,‰$ *and* $q_0 = 4\,g\,kg^{-1}$. *The lines are coloured from the start to the end position.*

3.2   COSMO$_{iso}$

Unlike the simple single-process air parcel models presented in the previous section, an isotope-enabled numerical weather prediction model allows to simulate the processes involved in the atmospheric water cycle in their full complexity. In particular the non-linear interaction of these different processes is mirrored in such a modelling framework. The regional non-hydrostatic weather prediction Consortium for Small-Scale Modelling (COSMO) model (Steppeler et al., 2003) is used operationally by several European weather services. COSMO is based on the primitive thermodynamical equations for compressible flow in a moist atmosphere and can be used for simulations from a horizontal resolution of 50 km to less than 1 km. The COSMO model has been extended by two parallel water cycles for the heavy water molecules $H_2^{18}O$ and $^1H^2H^{16}O$, which mirror the water cycling in COSMO (Pfahl et al., 2012). These additional water cycles are affected by the same physical processes as the light water molecule, except for phase change processes, during which they experience isotopic fractionation. The isotope-enabled COSMO model (COSMO$_{iso}$) has been used to study various aspects of the regional atmospheric water cycle over Europe and the USA (Pfahl et al., 2012; Aemisegger et al., 2015; Dütsch et al., 2018; Christner et al., 2018; Lee et al., 2019). In the following, the formulations of isotopic fractionation used in COSMO$_{iso}$ and TERRAiso, the isotope-enabled land surface module of COSMO, are described.

3.2.1   Boundary data and nudging

Since COSMO$_{iso}$ is a limited-area model, boundary and initial data is needed for all prognostic variables, including the isotope variables. For the COSMO prognostic variables, global reanalysis data (e.g. ERA-Interim

reanalysis data) is used. Furthermore, isotope-enabled global climate models provide the boundary and initial data for the isotope variables. So far, e.g. IsoGSM (Yoshimura et al., 2008) and ECHAM5-wiso (Werner et al., 2011) simulations have been used as isotope boundary and initial data. For measurement comparison studies, nudging of the COSMO$_{iso}$ horizontal wind fields above 850 hPa (von Storch et al., 2000) can be used to assure a close agreement of the atmospheric dynamics with observations, i.e., reanalysis.

3.2.2 Surface fluxes

Ocean surface evaporation is parametrised using the Craig and Gordon (1965) model. Three parametrisations of the non-equilibrium fractionation factors are implemented in COSMO$_{iso}$: The wind-dependent non-equilibrium fractionation factor as defined by Merlivat and Jouzel (1979), the wind-independent non-equilibrium fractionation factor by Pfahl and Wernli (2009) and a wind-independent version based on the smooth regime of the parametrisation by Merlivat and Jouzel (1979). The latter parametrisation was found to match best with existing monthly water vapour isotope data from the marine boundary layer (Aemisegger and Sjolte, 2018) and was therefore chosen for the simulations conducted in Chapter 4. Land surface fluxes are either implemented as all non-fractionating, as in most atmospheric isotope-enabled models (e.g. Yoshimura et al., 2008; Werner et al., 2011). Or for the detailed treatment of land surface fluxes, there is the isotope-enabled version of the mulit-layer soil and land surface module TERRA, which will be described in Sec. 3.2.5. No isotope interaction is implemented for sea ice. A simple sea ice scheme is used, which defines sea ice to occur at SST below $-1.6\,°C$. In these environments, surface fluxes are minimised, which means that heavy and light water molecules

evaporate very weakly and without isotopic fractionation and assuming a
sea ice composition to be equivalent to sea surface isotope signals.

3.2.3   Cloud microphysics

Isotopic fractionation in clouds is only implemented for physical interac-
tions, which involved the vapour phase. In liquid clouds, thermodynamic
equilibrium between the vapour and liquid phase is assumed and the equi-
librium fractionation factor with respect to liquid water (Majoube, 1971)
is applied. In ice clouds, the parametrisation of isotopic fractionation
between ice and vapour follows Jouzel and Merlivat (1984). The equi-
librium fractionation factor with respect to ice (Merlivat and Nief, 1967)
is used. Non-equilibrium fractionation can occur during supersaturation
of the water vapour with respect to ice. Because COSMO predicts su-
persaturation in a prognostic way (as in iCAM5, Dütsch et al., 2019), no
saturation adjustment is used over ice in contrast to other isotope mod-
els (e.g. Blossey et al., 2010). The isotopic fractionation due to ice su-
persaturation is parametrised using a combined effective (equilibrium and
non-equilibrium) fractionation factor (Jouzel and Merlivat, 1984). For rain
droplets, equilibrium between vapour and liquid cannot be assumed due
to non-equilibrium effects in undersaturated environments below the cloud
and a semi-empirical approach based on Stewart (1975) is used to simulate
the isotopic fractionation between rain droplets and the surrounding water
vapour.

3.2.4   Moist convection

A modified version of the Tiedtke mass flux scheme (Tiedtke, 1989) is used
in COSMO for the parametrisation of convection. Three parallel cycles for
the $^1H_2^{16}O$, $^1H_2^{18}O$, $^1H^2H^{16}O$ isotopes are implemented in the convection

scheme. All physical processes are simulated in the same way for heavy and light isotopes, except for phase change processes, where isotopic fractionation is implemented. For ice supersaturation, a temperature-dependent function is used (Risi et al., 2010). This moist convection scheme can be switched off at high spatial resolution such that convection and isotopic fractionation during convection is modelled explicitly. Several recent publications have shown that the performance of COSMO simulations with explicit convection is at least equivalent to a setup with parametrised convection for many aspects of the hydrological cycle and even at relatively coarse horizontal resolution (Hentgen et al., 2019; Vergara-Temprado et al., 2019; Hentgen et al., 2020). Therefore, in this thesis all simulations were preformed in setups with explicit convection.

3.2.5 TERRAiso

The land surface module TERRA (Doms et al., 2011) of the COSMO model simulates surface temperature and specific humidity using the surface energy and water budget. TERRA predicts the water content of the land surface reservoirs, which are vegetation interception, surface liquid water reservoirs, snow and soil water. The isotope-enabled version of TERRA includes diagnostically computed water budgets of the heavy isotopes. Thereby, fractionating fluxes between the reservoirs are bare soil evaporation (from the top soil layer), evaporation from the interception reservoir and dew formation, rime formation and plant transpiration. The surface snow reservoir consists of one snow layer and the soil of 7 layers with liquid transport between the layer being treated as non-fractionating. Vapour transport in the snow and soil is not represented. The isotopic composition of the snow layer is computed as the weighted mean of the accumulated precipitation isotope signal from the falling snow and equi-

librium fractionation during snow sublimation. The isotopic fractionation during surface snow sublimation is implemented assuming equilibrium fractionation using the equilibrium fractionation factor over ice (Merlivat and Nief, 1967) and Majoube (1971). Using this setup, it has been shown that the measured isotopic composition of MBL SWIs is better represented in COSMO$_{iso}$ simulation than using non-fractionating snow sublimation (Jansing, 2019). A detailed summary of the TERRAiso module is given in Aemisegger (2015), Dütsch (2016), and in the supplement of Christner et al. (2018).

Chapter 4

The role of air-sea fluxes for the water vapour isotope signals in cold and warm sectors of extratropical cyclones

4.1   Introduction

Air-sea latent heat flux is the most important source of atmospheric water vapour and impacts mid-latitude and polar atmospheric and ocean dynamics. Strong latent heat fluxes can lead to the intensification of cyclones (e.g. Yau and Jean, 1989; Uotila et al., 2011; Kuwano-Yoshida and Minobe, 2016) and polar lows (Rasmussen and Turner, 2003), to changes in the atmospheric (Neiman et al., 1990; Sinclair et al., 2010) and ocean stability, for example in cyclone-induced cold ocean wakes (Chen et al., 2010) or by leading to deep water formation at high latitudes (Condron et al., 2006; Condron and Renfrew, 2013). In turn, the strength of latent heat fluxes in the extratropics is strongly modulated by the large-scale atmospheric flow. The mean latent heat flux in extratropical cyclones is similar to the mean latent heat flux in the Atlantic Ocean (Rudeva and Gulev, 2010) and the Southern Ocean (Papritz et al., 2014), but shows large differences in latent heat fluxes between the cold and warm sectors of extratropical cyclones. The advection of dry and cold air masses over a warmer ocean surface in the cold sector of extratropical cyclones leads to s strong air-sea moisture gradient and strong large-scale ocean evaporation (Aemisegger and Papritz, 2018), while weak ocean evaporation or even moisture fluxes from the atmosphere to the ocean are observed in the warm sector (Persson et al., 2005; Bharti et al., 2019). In polar regions close to the sea ice edge, cyclones induce the advection of cold and dry air masses over the ocean leading to cold air outbreaks and induce strong latent heat fluxes (Papritz et al., 2015). Thus, large-scale advection of air masses modulates air-sea interactions, especially in regions of frequent passage of extratropical cyclones.

The opposite moisture fluxes in the cold and warm sector of extratropical cyclones impact the MBL stability and moisture budget. In the cold sector,

the positive latent heat fluxes (positive latent heat fluxes are here defined as fluxes from the ocean to the atmosphere) lead to decreasing atmospheric stability and a high marine boundary layer height (Beare, 2007; Sinclair et al., 2010). In idealised model simulations, the strongest ocean evaporation is seen directly behind the cold front in the region of subsiding dry air masses (Boutle et al., 2010). Negative latent heat fluxes, i.e. dew deposition on the ocean surface, has been observed in front of the cold front (Persson et al., 2005) and in warm sectors during the movement of extratropical cyclones over cold ocean regions (Neiman et al., 1990). Dew deposition in the warm sector leads to increasing boundary layer stability and shallow boundary layers (Beare, 2007; Sinclair et al., 2010). The warm sector's freshwater fluxes are further influenced by precipitation in the region of the warm conveyor belt - a coherent, ascending airstream in front of the cold front (Boutle et al., 2010; Madonna et al., 2013). Frontal precipitation can affect the surface freshwater fluxes in both sectors of extratropical cyclones (Catto et al., 2012).

The characteristic surface moisture fluxes of the cold and warm sector of extratropical cyclones are schematically summarised in Fig. 4.1. Latent heat fluxes are caused by a dis-equilibrium between the ocean and atmosphere, which can be expressed by the relative humidity with respect to sea surface temperature $h_s = \frac{q_a}{q_s}$, where q_a is the specific humidity of the atmosphere and q_s the saturation specific temperature at sea surface temperature (SST). q_s is temperature-dependent and increases with increasing temperature. In the cold sector, where dry and cold air masses are advected over a relatively warm ocean surface, the atmosphere-ocean temperature gradient ΔT_{ao} is negative and h_s is low due to a low q_a and relatively a high q_s. Therefore, the air masses in the cold sector are generally undersaturated with respect to the ocean and, thus, positive latent heat fluxes are expected (Fig. 4.1a). Negative surface freshwater fluxes can be observed

in the cold sector due to precipitation. This horizontal air mass advection regime in the cold sector is referred to as cold temperature advection in the following. In the warm sector, warm air masses are advected over a relatively colder ocean surface (referred to as warm temperature advection in the following). Under these environmental conditions, ΔT_{ao} is positive and h_s is high due to a high q_a and a relatively low q_s at low SST. Therefore, the near-surface air masses in the warm sector are likely oversaturated with respect to the ocean surface and negative latent heat fluxes are expected in the warm sector (Fig. 4.1b). Furthermore, precipitation associated with the warm conveyor belt and along the fronts leads to freshwater fluxes from the atmosphere to the ocean.

Despite their important role in the atmospheric moisture budget, only few and regionally limited measurements of surface latent heat fluxes are available, because of the extensive set of measurements needed (Holt and Raman, 1990; Pollard et al., 1983; Fleagle and Nuss, 1985; Neiman et al., 1990; Persson et al., 2005; Bharti et al., 2019). Many studies on surface latent heat fluxes within extratropical cyclones rely on model simulations (e.g. Nuss, 1989; Beare, 2007; Sinclair et al., 2010; Boutle et al., 2011). Further insights into the strength of surface latent heat fluxes can be gained by ship-based measurements of SWIs in water vapour, which provide near-surface water vapour characteristics. SWI measurements can be used to better understand the importance of various moist processes such as ocean evaporation, dew deposition and precipitation for the MBL moisture budget. Air-sea moisture fluxes occur due to non-equilibrium conditions at the atmosphere-ocean interface and, therefore, d can be used as a tracer of such air-sea interactions. The relative abundance of heavy and light isotopes in the different water reservoirs is altered during phase-change processes due to isotopic fractionation. The abundance of the heavy isotopologues
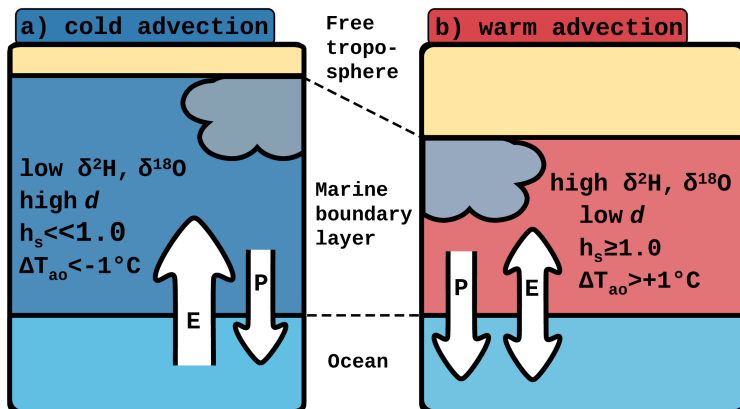
Figure 4.1: Schematic of cold and warm temperature advection and air-sea interaction. E denotes ocean evaporation and P precipitation. ΔT_{ao} is the difference between the air and sea surface temperature. h_s is the relative humidity with respect to sea surface temperature. δ^2H, $\delta^{18}O$ and d refer to the isotopic composition of water vapour. For details see text.

$^2H^1H^{16}O$ and $^1H_2^{18}O$ is expressed by the δ-notation (i.e. δ^2H and $\delta^{18}O$, respectively) (Dansgaard, 1964), which is defined as the isotopic ratio of the concentration of the heavy isotopologue to the concentration of the light isotopologue $^1H_2^{16}O$ relative to an internationally accepted standard isotopic ratio (the Vienna standard mean ocean water, VMSMOW2). There are two types of isotopic fractionation: equilibrium fractionation, which is caused by the difference in saturation vapour pressure of different isotopes, and non-equilibrium fractionation, which occurs due to molecular diffusion, e.g. during ocean evaporation. A measure of non-equilibrium fractionation and, thus, diffusive processes such as evaporation or dew deposition is the second-order isotope variable deuterium excess d, defined

as $d = \delta^2\text{H} - 8 \cdot \delta^{18}\text{O}$. During a diffusive process, a positive anomaly in d develops in the moisture sink (e.g. the atmosphere during ocean evaporation), while a negative d anomaly can be observed in the moisture source reservoir (e.g. rain droplets during below-cloud evaporation).

d in MBL water vapour negatively correlates with the relative humidity with respect to sea surface temperature h_s (Uemura et al., 2008; Pfahl and Wernli, 2008; Bonne et al., 2019; Thurnherr et al., 2020), which reflects the differing strength of ocean evaporation and, thus, non-equilibrium fractionation in different h_s-environments. So far, studies focused on environments with low h_s, where positive d in atmospheric water vapour has been observed due to strong ocean evaporation at low h_s (Uemura et al., 2008; Gat, 2008; Pfahl and Wernli, 2008; Aemisegger and Sjolte, 2018). In an extratropcial cyclones, such low h_s-environments with high d are expected in the cold sector, corresponding to areas of strong large-scale ocean evaporation (Aemisegger and Sjolte (2018) and Fig. 4.1). An opposite signal in d, i.e. d close to or below 0, is expected in the warm sector, where dew deposition or weak ocean evaporation occurs (Fig. 4.1). Only few occurrences of negative d in atmospheric water vapour have been reported (Uemura et al., 2008; Bonne et al., 2019; Thurnherr et al., 2020), which have been related to low ocean evaporation (Uemura et al., 2008) and deposition of water vapour on sea ice (Bonne et al., 2019). However, to our current knowledge there is no study which investigates the dynamical drivers of the d-h_s relationship in high h_s-environments.

Modelling of SWIs in the atmospheric branch of the water cycle helps to identify which moist processes influence the isotopic composition of water vapour. SWI-enabled models of various complexity have been developed. Single-process models, such as the ocean evaporation model by Craig and Gordon (1965) or the Rayleigh model simulating continous moisture loss of a finite water reservoir by condensation (Dansgaard, 1964), describe sin-

gle phase change processes and their impact on SWIs in the atmosphere. These models have been extended in various detail to show, for example, that mixing at the marine boundary layer top is also important for the MBL moisture budget (Benetti et al., 2017). The MBL water vapour isotopic composition has been simulated by extending the Craig and Gordon (1965)-model with a *closure assumption*, which assumes that ocean evaporation is the only source of MBL water vapour and the moisture export flux across the MBL top into the free troposphere the only sink of MBL water vapour (Merlivat and Jouzel, 1979). Other studies incorporated mixing at the MBL top (Benetti et al., 2017) or height-dependent mixing and horizontal diffusion (Feng et al., 2019) into the closure-assumption model. Furthermore, 1-D isotopic models are used to simulate the evolution of rain droplets during their path below clouds to the surface (Stewart, 1975; Graf et al., 2019). The incorporation of SWIs into numerical climate and weather models (Joussaume et al., 1984; Yoshimura et al., 2008; Blossey et al., 2010; Werner et al., 2011; Pfahl et al., 2012) gives the opportunity to study the combined impact of diverse moist atmospheric processes on the SWI-evolution of atmospheric water vapour. Such models also allow for the application of various Eulerian and Lagrangian diagnostics. Detailed insight into the interaction of weather systems and SWIs can be obtained from the isotope-enabled Consortium for Small-Scale Modelling model COSMO$_{iso}$ with spatially and temporally high-resolution simulations (Pfahl et al., 2012). Lagrangian studies based on COSMO$_{iso}$ simulations have shown, that δ^2H and d in near-surface water vapour are strongly influenced by ocean evaporation and, over land, by evapotranspiration and mixing with moist air, while liquid and mixed phase contribute to the δ^2H- and d-variability (Dütsch et al., 2018). The importance of different air mass origins and pathways of air streams for the SWI evolution during frontal passages has been illustrated using COSMO$_{iso}$ simulation in the

Mediterranean Sea (Lee et al., 2019).

Here, we aim to address the following questions (objectives 3 and 4 in Sec. 1.3) by the analysis of 3-months ship-based SWI measurements in the Southern Ocean and COSMO$_{iso}$ simulations of the measurement period:

1. What is the occurrence frequency of different temperature advection regimes in the Southern Ocean?

2. How is the isotopic variability of the MBL water vapour related to air-sea interaction in the cold and warm sectors of extratropical cyclones?

3. What are the driving processes of the SWI variability of MBL in the cold and warm sectors of extratropical cyclones?

This chapter is structured in the following way: In Section 4.2, the dataset and Eulerian and Lagrangian methods are described. In the following, the temperature advection climatology is discussed (Sec. 4.3), the measured SWI signals are related to the cold and warm temperature advection in the cold and warm sector of extratropical cyclones (Sec. 4.4) and the evolution of the isotope signals along COSMO$_{iso}$ trajectories are analysed for the cold and warm sector (Sec. 4.5). Finally, the driving processes of the SWI variability for two case studies of a cold and a warm advection event are identified and single-process air parcel models are used to provide quantitative estimates of the relative importance of the different processes (Sec. 4.6).

4.2 Data and methods

This study combines meteorological and SWI measurements from the Antarctic Circumnavigation Expedition (ACE), which took place from December 2016 to March 2017 in the Southern Ocean (Walton and Thomas (2018), Section 4.2.1), with COSMO$_{iso}$ model data and ERA-Interim reanalysis data (Section 4.2.2). A Eulerian identification scheme of cold and warm temperature advection is introduced in section 4.2.3. Thereafter, the Lagrangian methods used for the analysis are described in section 4.2.4.

4.2.1 Measurement data

During the ACE expedition in the Southern Ocean, continuous measurements of SWIs using a Picarro cavity ring-down laser spectrometer were conducted at a height of 13.5 m a.s.l. above the ocean surface on board of the Russian research vessel *Akademik Tryoshnikov* from 21 Dec 2016 to 19 March 2017. A detailed characterisation of the dataset can be found in Chapter 2. Further measurements from ACE are used here including air temperature, air pressure, relative humidity, a sea spray proxy and wave age (for details see Chapter 2 and Schmale et al., 2019). Sea surface temperatures (SST) are not yet available for the ACE period, therefore, the daily optimum interpolation SST satellite product from the Advanced Very High Resolution Radiometer (AVHRR) infrared sensor (version 2; AVHRR-Only; Reynolds et al. (2007)) are used along the ACE ship track. All data is used at an hourly time resolution in this chapter.

4.2.2   Model data

4.2.2.1   ERA-Interim reanalysis data

Six-hourly data from the ERA-Interim reanalysis dataset (Dee et al., 2011) spanning the time period from 1979 to 2018 is used for the climatological analysis of warm and cold temperature advection (see Section 4.2.3) in the Southern Ocean. The data is interpolated to a $1°$ horizontal grid and 60 vertical levels. Due to fewer observational data in the Southern hemisphere compared to the Northern hemisphere, the model fields are expected to have a higher uncertainty in the Southern hemisphere. Nonetheless, the 4D-var data assimilation system used in the ERA-Interim reanalysis shows good performance in the Southern hemisphere (Dee et al., 2011; Nicolas and Bromwich, 2011) and the uncertainties due to assimilation errors have been shown to be minor (Nicolas and Bromwich, 2011).

Based on the ERA-Interim reanalysis, cyclone frequencies were calculated using a 2D cyclone detection algorithm (Wernli and Schwierz, 2006; Sprenger et al., 2017). Furthermore, surface fronts were detected following Schemm et al. (2015) using the following criteria: (i) the horizontal equivalent potential temperature gradient at 850 hPa has to be at least $3.8\,\mathrm{K}\,(100\,\mathrm{km})^{-1}$, and (ii) the fronts need to have a minimum length of 500 km.

4.2.2.2   COSMO$_{\mathrm{iso}}$ simulations

Model simulations with the limited-area isotope-enabled regional numerical weather prediction model COSMO$_{\mathrm{iso}}$ are highly valuable for the analysis of stable water isotopes measurements in their large-scale flow context at high spatial and temporal resolution.

Table 4.1: Specifications of COSMO$_{iso}$ model runs

Run	start [at 0 UTC]	end [at 0 UTC]	domain center [°S, °E]	domain width [°lat, °lon]	time window start end
leg1_run1	13 Dec 2016	12 Jan 2017	47, 18	50, 50	21 Dec 2016 7 UTC / 1 Jan 2017 23 UTC
leg1_run2	24 Dec 2016	23 Jan 2017	47, 73	50, 50	2 Jan 2017 0 UTC / 13 Jan 2017 0 UTC
leg1_run3	3 Jan 2017	2 Feb 2017	52, 130	50, 50	13 Jan 2017 1 UTC / 27 Jan 2017 0 UTC
leg2_run1	12 Jan 2017	11 Feb 2017	61, 151	50, 50	27 Jan 2017 1 UTC / 9 Feb 2017 0 UTC
leg2_run2	28 Jan 2017	27 Feb 2017	61, -154.4	50, 50	9 Feb 2017 1 UTC / 14 Feb 2017 12 UTC
leg2_run3	1 Feb 2017	3 March 2017	61, -100	50, 50	14 Feb 2017 13 UTC / 24 Feb 2017 6 UTC
leg3_run1	16 Feb 2017	18 March 2017	52, -80	47.5, 56.25	24 Feb 2017 7 UTC / 2 March 2017 0 UTC
leg3_run2	21 Feb 2017	23 March 2017	62, -25	50, 50	2 March 2017 1 UTC / 13 March 2017 12 UTC
leg3_run3	1 March 2017	31 March 2017	47, -5	50, 50	13 March 2017 13 UTC / 23 March 2017 1 UTC
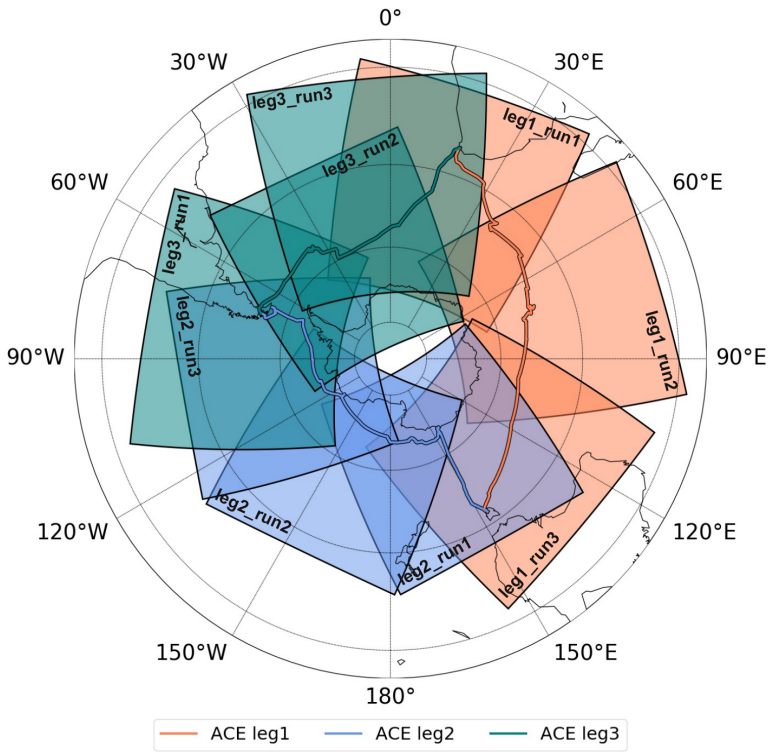
*Figure 4.2: Domains of the nine COSMO*_{iso} *runs as summarised in Table 4.1. The ACE track is indicated by lines coloured by the three legs of the expedition.*

A detailed description of the COSMO$_{iso}$ model is given in Chapter 3. Here, nine COSMO$_{iso}$ simulations were conducted covering the ACE measurement time period in the Southern Ocean. The simulations were initialised and driven at the lateral boundaries by ECHAM5-wiso data (Werner

et al., 2011). The wind in the COSMO domain was spectrally nudged to the ECHAM5-wiso above 850 hPa to keep the meteorology within the COSMO$_{iso}$ domain as close as possible to the reanalysis.The ECHAM5-wiso fields are available 6-hourly with a spectral resolution of T106 and 31 vertical levels and were nudged 6-hourly to temperature, surface pressure, divergence and vorticity of ERA-Interim reanalysis data. The COSMO$_{iso}$ simulations were performed at a horizontal resolution of 0.125° with 40 vertical levels and explicit convection. Hourly outputs of the COSMO$_{iso}$ simulations are used for the analysis. The model domains have an area of approximately 50° x 50° and were shifted along the ACE track, such that the entire expedition route was covered by the 9 simulations in space and time (see Fig. 4.2). The specifications of each model run are summarised in Table 4.1. The first week of each run is used as spin-up time and is not included in the analysis. For comparison with the ACE measurements, the lowest model level of the different variables is interpolated along the ACE track. This corresponds approximately to the height of the inlet on the ship. To account for strong horizontal gradients and spatial shifts in the modelled fields, the ACE track was shifted by ± 10 km in meridional direction and the data was also interpolated along these shifted tracks. This procedure yields an uncertainty of the interpolated model time series. During time periods, when two model runs overlap in time and space, one of the runs is chosen in such a way that cold and warm temperature advection events during ACE are extracted as a whole from one single model run.

4.2.3   Cold and warm temperature advection scheme

To identify cold and warm temperature advection within the cold and warm sector of extratropical cyclones, a temperature advection identi-

fication scheme, which is based on the atmosphere-ocean temperature difference ΔT_{ao}, is used. A threshold of ΔT_{ao} has to be chosen to define cold and warm temperature advection. To neglect regions of small differences in oceanic and atmospheric temperature, where meridional transport of air masses is not dominant, cold temperature advection is defined as time periods when $\Delta T_{ao} < -1.0\,°\text{C}$ and warm temperature advection when $\Delta T_{ao} > 1.0\,°\text{C}$. A zonal advection regimes is defined for $-1.0\,°\text{C} < \Delta T_{ao} < 1.0\,°\text{C}$. Different temperature- thresholds to define the temperature advection regimes are discussed in Hartmuth (2019).
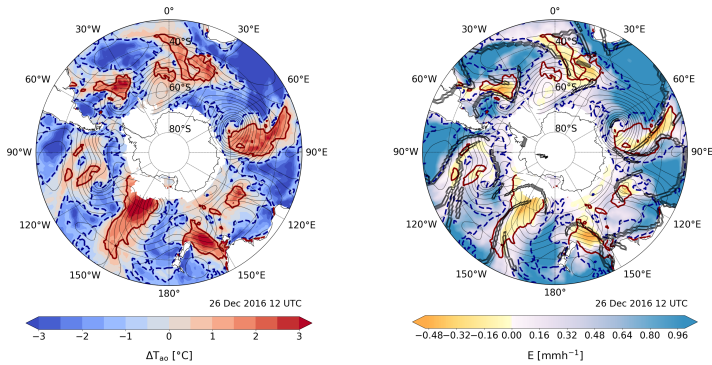
Figure 4.3: Horizontal cross section at 12 UTC on 26 Dec 2016 from ERA-Interim fields. **(a)** *ΔT_{ao} using temperature at 10 m a.s.l. and sea surface temperature. Land masses and areas covered by sea ice are blanked. The black contours show the sea level pressure in 5 hPa intervals. $\Delta T_{ao}=-1.0$ is highlighted in blue, dashed contours, $\Delta T_{ao}=1.0$ in red contours.* **(b)** *Same as* **(a)** *but for ocean evaporation. Additionally, surface fronts are show in black, thick contours.*

The features of cold and warm temperature advection as identified by the proposed scheme are shown for one simulation time step in Fig. 4.3. The warm temperature advection mask covers areas to the north-east of low pressure systems (indicated by sea level pressure in black contours), which correspond to the warm sectors of extratropical cyclones in the Southern Ocean (Fig. 4.3a). To the west of the low pressure system, cold temperature advection in the cold sectors can be seen. For example around 60 °E, the cold and warm sector of a large low pressure system are indicated by the cold and warm temperature advection masks. In this snapshot of cold and warm temperature advection, areas of cold (warm) temperature advection coincide with positive (negative) ocean evaporation (Fig. 4.3b). Cold temperature advection is associated with strong ocean evaporation. Low ocean evaporation occurs mainly between the advection masks, and very small or negative moisture fluxes indicate dew deposition occurring in the warm sectors (see for example at 40 °W in Fig. 4.3b). The surface fronts, which mark the boundaries between the cold and warm sectors and, thus, of the cold and warm temperature advection masks, lie mostly in the areas between cold and warm temperature advection denoting the cold and warm fronts of extratropical cyclones. The warm and and cold fronts of the cyclone at 40 °W delimit the warm sector along its Southern edge following closely the temperature advection mask. In other cases, the surface fronts are not aligned with the temperature advection mask. This is the case for the cyclone at 60 °E, where the cold front lies within the warm temperature advection mask and negative ocean evaporation is seen behind the cold front. This discrepancy between the surface fronts and the temperature advection masks could be caused by differences in the identification schemes. The surface fronts are identified using horizontal gradients in equivalent potential temperature at 850 hPa, while the advection mask is based on the temperature contrast between 10 m a.s.l and surface tempera-

ture. The focus on air-sea interactions in this study justifies the choice of an identification scheme based on surface fields. Ocean evaporation aligns well with the temperature advection masks confirming that the proposed identification scheme is useful for the investigation of air-sea fluxes.

With the proposed identification scheme, we aim for a simple objective method to delimit cold and warm temperature advection in the extratropics, which is adaptable to model simulations as well as measurement data. Other Eulerian features of extratropical cyclones, such as the cyclone centre or fronts, have been identified using automated identification schemes (e.g. Lambert, 1988; Hewson, 1998; Wernli and Schwierz, 2006; Jenkner et al., 2010) and used to characterise the impact of extratropical cyclones on air-sea interaction (Papritz et al., 2014; Aemisegger and Papritz, 2018). The temperature advection scheme presented here, provides the possibility to study the contrasting behaviour of air-sea interactions in the cold and warm sectors of extratropical cyclones.

In this study, the cold and warm temperature advection scheme was applied to the ACE measurements using the measured air temperature and SST satellite products, to the ERA-Interim reanalysis using the temperature difference between the air temperature at 10 m a.s.l. and SST and to the COSMO$_{iso}$ dataset using the temperature difference between the air temperature at 2 m a.s.l. and SST. The low reference air temperature used for the calculation of the COSMO$_{iso}$ advection frequencies might lead to slightly lower advection frequencies in COSMO$_{iso}$ compared to ERA-Interim and the ACE measurements, because larger temperature gradients are expected across larger vertical distances. Nonetheless, the difference between 10 m and 2 m a.s.l. air temperature is expected to be small and that the advection frequencies in COSMO$_{iso}$ are similar to the advection frequencies in ERA-Interim.

4.2.4   Backward trajectories and moisture sources

Seven-days air parcel backward trajectories are calculated using the La-
grangian analysis tool LAGRANTO (Wernli and Davies, 1997; Sprenger
and Wernli, 2015) based on the three-dimensional 1-hourly wind fields
from the COSMO$_{iso}$ simulations. The trajectories were launched every
hour along the ACE track and the 10 km-shifted ACE tracks at pressure
levels between 1000 and 500 hPa in 10 hPa-steps. Trajectories were anal-
ysed until they left the model domain and for the time windows of each
model run as indicated in Table 4.1. Environmental variables were traced
along the trajectories, notably the stable water isotope concentrations such
that the evolution of the SWI composition during the air mass transport
can be analysed.
Moisture sources of the marine boundary layer water vapour along the
ACE track were calculated using the moisture source diagnostic developed
by Sodemann et al. (2008) adjusted to identify the moisture sources of
water vapour (Pfahl and Wernli, 2008) using the seven-days COSMO$_{iso}$
backward trajectories.

In the following, the influence of the large-scale flow on the variability of
SWIs in MBL water vapour in the Southern Ocean is analysed in the con-
text of cold temperature advection, warm temperature advection, and zonal
flow. This analysis is based on the ACE measurements and COSMO$_{iso}$
simulations along the ACE track. The climatological occurrence frequen-
cies of the three large-scale flow categories and associated air-sea moisture
fluxes are discussed and compared to those during the ACE measurement
period in Section 4.3. In Section 4.4, the isotopic composition of the mea-
sured water vapour is analysed with respect to the temperature advection
regimes and the evolution of the isotopic signature of air masses during cold

and warm temperature advection is further investigated using $COSMO_{iso}$ simulations and backward trajectories from the ship's position. In Section 4.5, two case studies for the cold and the warm temperature advection regime are presented to illustrate how the dominant phase-change processes influence the isotopic composition of the near-surface water vapour.

4.3   Frequencies of occurrence of cold advection, warm advection and zonal flow in the Southern Ocean

In order to characterise the temperature advection regimes in their climatological context, the occurrence frequency and associated air-sea moisture fluxes of the three temperature advection regimes in the Southern Ocean are analysed for the period from December to March 1979 - 2018. All occurrence frequencies of temperature advection and associated air-sea fluxes discussed in the following refer to oceanic regions south of 30°S. Cold temperature advection, warm temperature advection and zonal flow are associated with different climatological occurrence frequencies (Fig. 4.4). Zonal flow is the most frequently occurring advection regime (49 %). Cold and warm temperature advection account for 39% and 12 %, respectively. Each temperature advection regime, thus, occurs frequently and represents an important large-scale flow situation of the Southern Ocean atmospheric dynamics. In the following, the environmental conditions during cold temperature advection, warm temperature advection and zonal flow are discussed separately.

Cold temperature advection occurs during the meridional transport of cold air masses over a relatively warmer ocean surface associated with the equatorward movement of cold sector air in extratropical cyclones. A latitudinal
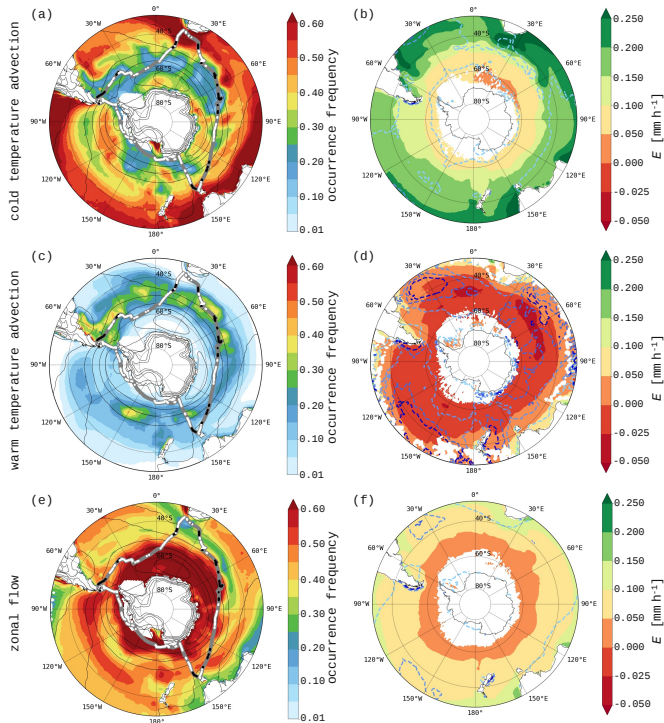
*Figure 4.4: Climatological occurrence frequency of cold temperature advection, warm temperature advection and zonal flow (**a,c,e**) and the associated ocean evaporation (**b,d,f**) for December to March 1979-2018 using ERA-Interim fields. Black contours show cyclone frequencies of 10, 20, 30 and 40 %. The grey thick line shows the ACE ship track with the observed occurrences of cold (white points) and warm (black points) temperature advection events during ACE. Light blue to dark blue dashed lines show mean surface precipitation at levels of 0.06, 0.18, 0.24, and 0.3 mm h^{-1}, respectively.*

band north of 40 °S of high occurrence frequency of cold temperature
advection of up to 60% can be observed north of regions with high cy-
clone frequencies in all three ocean basins (Fig. 4.4a). In these areas,
the cold sectors of extratropical cyclones pass over regions with anoma-
lously warm SSTs, that are larger than the zonal mean SST (Fig. 4.5).
For instance in the southeastern Indian Ocean, the two zonal SST maxima
at 20 ° and 60 °E north of 40°S overlap with the maxima in occurrence
frequency of cold temperature advection. In these regions, hot spots of
large-scale ocean evaporation occur frequently and are associated with the
warm ocean western boundary currents along the continents (Moore and
Renfrew, 2002; Aemisegger and Papritz, 2018). Cold temperature ad-
vection also frequently occurs along the Antarctic coast in the Ross Sea,
Weddell Sea and across the Amery Ice shelf. These areas corresponds to
regions of frequent cold air outbreaks in summer (Papritz et al., 2015).
During cold air outbreaks, which are often induced by extratropical cy-
clones, cold and dry air masses are advected over a relatively warm ocean.
In the same regions along the Antarctic coast, strong large-scale ocean
evaporation events occur, of which more than 80% are driven by extrat-
ropical cyclones (Aemisegger and Papritz, 2018). Strong evaporation is
therefore expected to occur during cold temperature advection and surface
evaporation during cold temperature advection is found to be positive with
a mean value of $0.13 \pm 0.06 \, \mathrm{mm \, h^{-1}}$ (Fig. 4.4b) and increases from South
to North due to the SST-dependence of surface latent heat fluxes. Small
amounts of rainfall are associated with cold temperature advection (mean
value of $0.07 \pm 0.03 \, \mathrm{mm \, h^{-1}}$) and mainly due to shallow convective clouds
behind the cold front. The net air-sea moisture flux during cold tempera-
ture advection is from the ocean into the atmosphere (Fig. 4.4b).
Warm temperature advection frequently occurs in a few areas in the South-
ern Ocean, where warm air masses are transported over a relatively
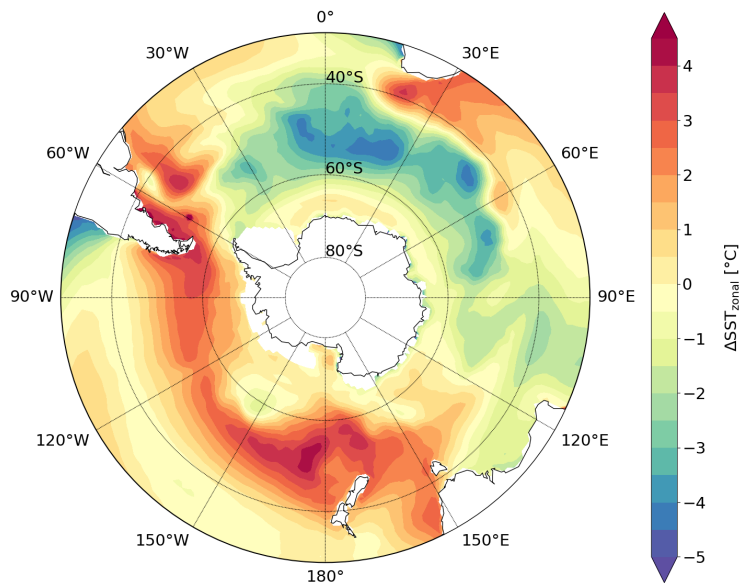
Figure 4.5: Deviations of the climatological sea surface temperature from the zonal means for the months December to March in 1979-2018 using ERA-Interim.

colder ocean. Warm temperature advection hot spots of up to 50% occurrence frequency can be observed north of the region with highest cyclone frequency and to the south of the band of high cold temperature advection occurrence frequency (Fig. 4.4c). These regions are associated with the warm sectors of extratropical cyclones, in which warm and moist air masses are advected polewards. Furthermore, warm temperature advection occurs along the eastern coast of South America and at 150°W in the Pacific, which are regions of anomalously cold ocean waters (Fig. 4.5). The singular hot spot in the Pacific ocean is connected to the location of

the oceanic polar front, which has its most northward position in the Pacific Ocean between $55\,°$S and $60\,°$S around $150\,°$W (Moore et al., 1999). The advection of terrestrial and/or subtropical air masses over the cold Malvinas current along the Argentinian coast leads to frequent warm temperature advection along the east coast of South America. During warm temperature advection, surface evaporation is low or negative with a climatological mean of $0.00 \pm 0.03\,\mathrm{mm\,h^{-1}}$ (Fig. 4.4d). Furthermore, warm temperature advection is accompanied by precipitation with a climatological mean of $0.19 \pm 0.8\,\mathrm{mm\,h^{-1}}$. Thus, there is a net flux of moisture from the atmosphere into the ocean during warm temperature advection.

Zonal flow represents situations when air masses are advected zonally and ocean surface and air temperature differ by less than 1°C. The highest occurrence frequency of zonal advection is seen south of 60°S (Fig. 4.4e), where synoptic-scale fronts are rare (Simmonds et al., 2011). Furthermore, high occurrence frequency of zonal flow can be observed at the equatorward edge of the highest cyclone frequency, where air masses are transported zonally. In the South Pacific, this band of high occurrence frequency between $60\,°$S and $40\,°$S spans particularly far north due to the northward shift of the storm track in the Pacific compared to other ocean basins (Wernli and Schwierz, 2006). The composite mean ocean evaporation is low during zonal advection and has a mean value of $0.06 \pm 0.03\,\mathrm{mm\,h^{-1}}$ between the mean values of ocean evaporation during cold and warm temperature advection (Fig. 4.4f). The mean value of surface precipitation during zonal flow is $0.10 \pm 0.03\,\mathrm{mm\,h^{-1}}$ and, therefore, the net moisture flux is slightly negative during zonal flow. Because the net moisture flux during zonal flow is close to zero and such flow situation do not describe situations of important meridional air mass advection, we will mostly focus on cold and warm temperature advection in the following.

The spatial patterns of occurrence frequencies south of $30\,°$S of cold tem-

perature advection, warm temperature advection, and zonal flow in the ACE summer (Dec 2016 - March 2017, see also Appendix Fig. B.1) are overall similar to the December - March climatology over the period 1979-2018 (Fig. 4.4a,c,e). Notable differences include generally more frequent cold temperature advection events and especially a high occurrence frequency of cold temperature advection across the Amery ice shelf during the ACE period. In summary, the advection frequencies in the Southern Ocean during ACE represent conditions that are representative of the Southern Hemisphere summer conditions. Specifically along the ACE track, occurrence frequencies of the three flow regimes differ from the climatological occurrence frequencies in the Southern Ocean. In the ACE measurements, 59% of all advection events were zonal, 27% cold and 14% warm temperature advection events. The frequency of cold temperature advection events is nearly 20% lower than climatologically expected in the region south of 30 °S. The ACE track was close to Antarctica only in the Pacific, which means that cold air outbreaks in the Atlantic and Indian Ocean, where the ACE track stayed mostly in areas with zonal and warm temperature advection, are undersampled (see also Fig. 4.4). Warm temperature advection events were mainly encountered in the South Indian and Atlantic Ocean. Therefore, the insight from the ACE data set on warm temperature advection are representative for these two ocean basins around Antarctic. Although the majority of temperature advection events during ACE were zonal flow events, in total 32% were cold or warm temperature advection events corresponding to in total one month of measurement time, which provides a large measurement data set to study cold and warm temperature advection.

In the next Sections, we will discuss the isotopic signature during cold temperature advection, warm temperature advection and zonal flow (Sect. 4.4) and the processes shaping the isotopic signature of MBL water vapour

during cold and warm temperature advection (Sect. 4.5).

4.4   Observed SWI composition in the different advection regimes

To test the hypothesis stated in Section 4.2 that high d together with negative δ^2H- and δ^{18}O anomalies occur during cold temperature advection events and low d together with positive δ^2H- and δ^{18}O anomalies during warm temperature advection events, the measured isotope and environmental variables during ACE are analysed with respect to the different temperature advection regimes.

The distributions of δ^2H, δ^{18}O and d during warm temperature advection, cold temperature advection and zonal flow are shown in Fig. 4.6. For all isotope variables, the distributions associated with the cold and the warm temperature advection regime are significantly different when applying a Wilcoxon rank-sum test (p <0.01). The mode of the d distribution during cold advection is 10 ‰ higher than during warm advection. The median d during cold advection is 6.5 ‰ compared to -0.4 ‰ during warm advection. The d distribution during warm advection is bimodal with maxima at -1.2 ‰ and 3.7 ‰. These two modes correspond to two different types of warm advection events. The events with negative d are associated with dew deposition and h_s >100%, whereas the events with positive d are associated with a small net evaporation flux at high h_s (compare distribution of warm advection events in Fig. 4.7). The distribution of δ^2H and δ^{18}O are similar with higher δ-values during warm compared to cold temperature advection. The mode of the distributions is higher by 20 ‰ for δ^2H and 4 ‰ for δ^{18}O during warm than during cold temperature advection. The mode of the zonal flow lies in between the

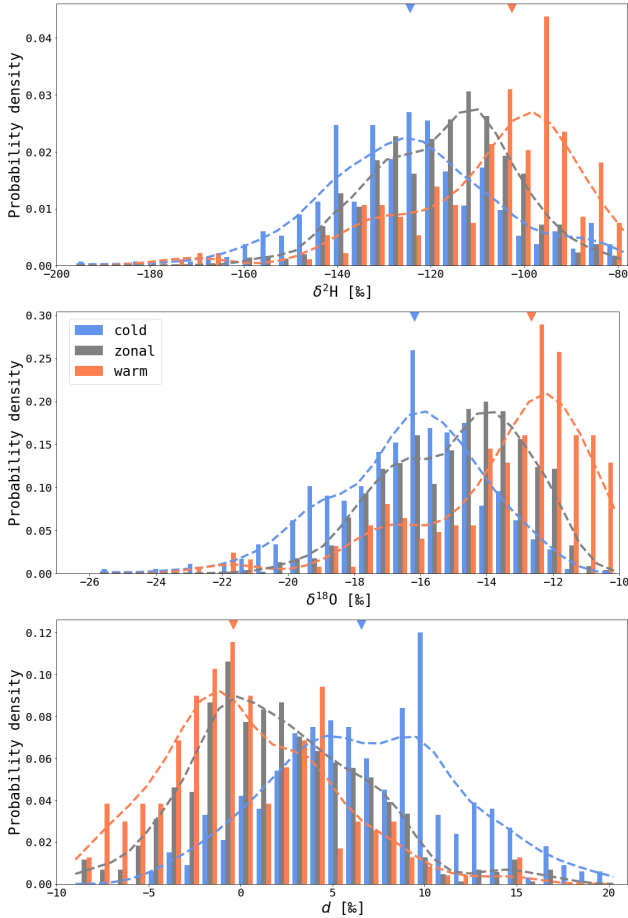*Figure 4.6: Histograms of measured δ^2H (top), $\delta^{18}O$ (middle) and d (bottom) with non-parametric estimates of the distributions (dashed lines) during cold temperature advection (blue), warm temperature advection (orange) and zonal flow (grey). The triangles at the top denote the medians of the cold and warm temperature advection distributions.*

mode of the cold and warm temperature advection distributions for all
isotope variables.

The distinctively different d signal during cold and warm temperature
advection is also visible in the $d - h_s-$phase space (Fig. 4.7). As already
shown in previous studies (Uemura et al., 2008; Steen-Larsen et al., 2014;
Pfahl and Sodemann, 2014; Benetti et al., 2015; Thurnherr et al., 2020),
d in the MBL is anti-correlated with the near-surface relative humidity.
In the ACE measurements, d and h_s negatively correlate with a Pearson
correlation of -0.73. During cold temperature advection, the atmosphere
is under-saturated (low h_s), and during warm advection close to saturation
or over-saturated ($h_s \geq 1$). Thus, contrasting atmosphere-ocean moisture
gradients, which can even be of opposite sign, are associated with cold
and warm temperature advection. Different events in the same temperature
advection regime can be associated with a different evolution in the $d -$
h_s-phase space (see Fig. 4.7). The cold temperature advection event in
January occurs during the passage of the cold sector of an extratropical
cyclone over an area of relatively high sea surface temperature and the
two events in February occur during cold air outbreaks in the Ross Sea
in the cold sector of an extratropical cyclone. All three cold temperature
advection events shown here have a negative correlation of d and h_s and
follow the same slope as the linear interpolation of all cold temperature
advection events during ACE (pointed black line in Fig. 4.7).

The warm advection events in Fig. 4.7 show different temporal evolutions
in the $d - h_s-$phase space for each of the warm temperature advection
events. All of these events occurred near Marion Island and the Crozet
Archipelago in the South Indian Ocean. Two events show an anticorrelation
of d and h_s, whereas the third event on 1 Jan 2017 shows a different
behaviour with high d occurring together with high h_s. This event at
Possession Island in the Indian Ocean in the warm sector of an extratropical

cyclone, is the only occasion, where d and h_s are weakly correlated during ACE. In contrast to the other warm temperature advection events during ACE, the relative humidity during the event on 1 Jan 2017 was below 80% while h_s was higher than 1.2 due to the high specific humidity in the
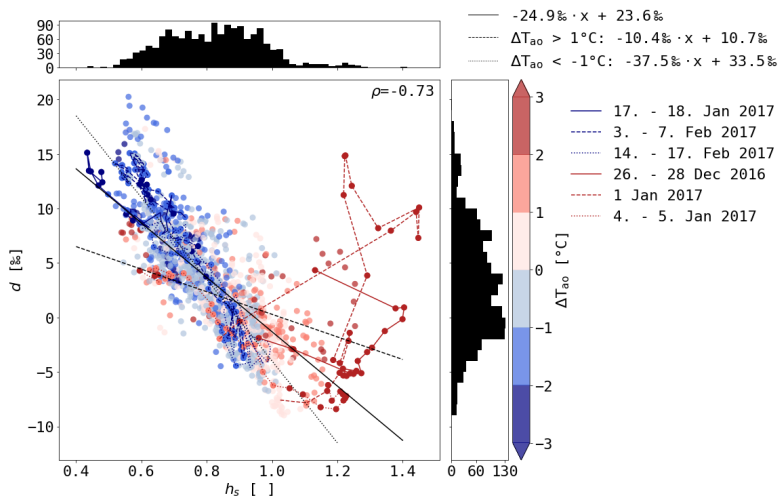
Figure 4.7: Scatterplots of 1-hourly measurements of h_s versus d for ACE legs 1-3 coloured by the temperature difference between the ocean and the atmosphere ($\Delta T_{ao} = T_a - SST$). The black lines show the linear interpolations to all measurements (solid line), to the measurements in the warm sector ($\Delta T_{ao} > 1.0\,°C$, dashed line) and to the measurements in the cold sector ($\Delta T_{ao} < -1.0\,°C$, dotted line). The Pearson correlation coefficient (ρ) of d and h_s has a value of -0.73. The histograms show the distribution of h_s (top) and d (right). Three cold and three warm temperature advection events are indicated with blue and red lines, respectively (for details see text).

warm sector of the extratropical cyclone. Most likely, the nearby island
influenced the air masses around the island leading to higher temperature
and lower relative humidity than further away from the land masses. Due
this special setting of the event, it does not show the typically observed
negative correlation between d and h_s observed in all other warm and cold
advection events.

The ACE measurements confirm the expected contrasts in the isotopic
signature and the close link of d and h_s indicating the opposite air-sea
fluxes of cold and warm temperature advection. From the air-sea fluxes
associated with the different temperature advection regimes, we expect the
MBL to be strongly influenced by ocean evaporation during cold advection
whereas dew deposition on the ocean surface plays a major role in shaping
the observed isotopic composition of water vapour during warm advection.
To identify the driving processes of the contrasting SWI signal during cold
and warm temperature advection, COSMO$_{\text{iso}}$ simulations are used and the
SWI evolution along backward trajectories is studied in the next section.

4.5   Formation of isotope anomalies in different temperature advection regimes

To better understand how the observed anomalies in the isotope signals form
during cold and warm temperature advection, the isotopic composition as
well as other environmental variables were analysed along the ACE track
using COSMO$_{\text{iso}}$ simulations. The simulated isotope variability is in
agreement with the measurements with a Pearson correlation coefficient ρ
of 0.76 for δ^2H, 0.69 for δ^{18}O and 0.69 for d (Fig. 4.8). There is a positive
bias of 5.0 ‰ in the simulated d in the MBL, which could be caused by
lower specific and relative humidity in the simulation compared to the
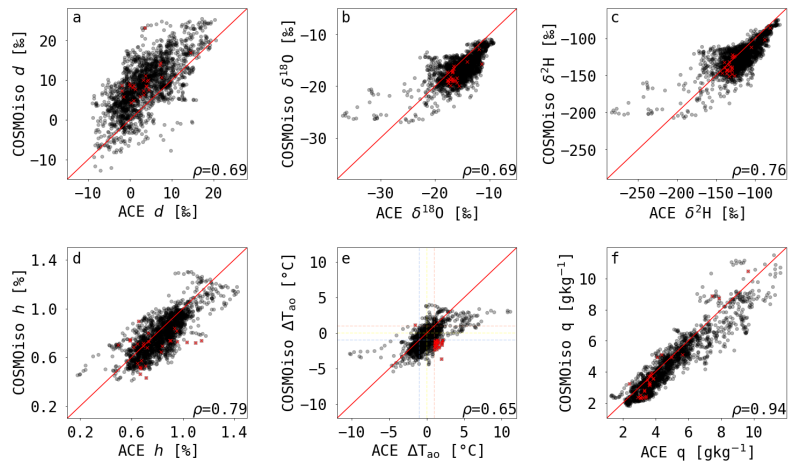
Figure 4.8: Scatterplot of 1-hourly ACE measurements versus interpolated COSMO$_{iso}$ simulations along the ACE track of (a) d, (b) $\delta^{18}O$, (c) δ^2H, (d) relative humidity h, (e) air-sea temperature difference ΔT_{ao} and (f) specific humidity q. Points with contradicting cold and warm temperature advection classification between the measurements and simulations are marked in red.

measurements. For only 1% of all 1-hourly measurement points of legs 1-3, the classification of cold/warm advection according to the COSMO$_{iso}$ simulations disagreed with the observed classification (see also red crosses in Fig. 4.8). These measurement points and their associated trajectories are excluded from the following analysis. The same qualitative distribution of the SWI signal during cold and warm temperature advection is seen with a shift in δ^2H and $\delta^{18}O$ towards negative values and a shift in d towards positive values during cold temperature advection and zonal flow compared to the measured composition during ACE (Fig. B.2 in the Appendix). This difference specifically during conditions with important

contributions of water vapour to the MBL by ocean evaporation could be caused by too strong vertical mixing in the COSMO$_{iso}$ simulations. A further reason for the differences between the measurements and simulations could originate from the formulation of non-equilibrium isotopic fractionation in COSMO$_{iso}$. Using the formulation of the non-equilibrium fractionation factor by Merlivat and Jouzel (1979) instead of the currently used formulation by Pfahl and Wernli (2009) in the COSMO$_{iso}$ simulations leads to a decrease of d by, on average, $2\,\text{\textperthousand}$, on the lowest model level over the ocean surface (Jansing, 2019). However, the simulations using the formulation by Merlivat and Jouzel (1979) also show a decrease in d variability above oceanic areas. As we are interested into processes shaping the SWI variability in the MBL, the formulation by Pfahl and Wernli (2009) is more adequate to use here as the SWI variability in the measurements and simulations agree well. Even though simulated and measured isotope signals do not agree everywhere, the COSMO$_{iso}$ simulations capture the observed variability of the isotopic composition and provide similar distributions of isotope variables as the observations in the three advection categories. These simulations can thus be used for an assessment of the relevant processes shaping the isotopic composition of water vapour in the MBL during cold and warm temperature advection, and for the analysis of the temporal evolution of isotope and other variables during a cold and warm advection case study for which the isotopic values of model data and measurements agree well (see Section 4.6).

During transport, the specific humidity of the air mass varies due to different moist atmospheric processes such as cloud formation, ocean evaporation, dew deposition, and below-cloud evaporation. These processes also affect the air mass' water vapour isotopic composition. A measure to identify such moist processes, which affect the SWI composition of the air mass during transport, is the comparison of the air mass' properties
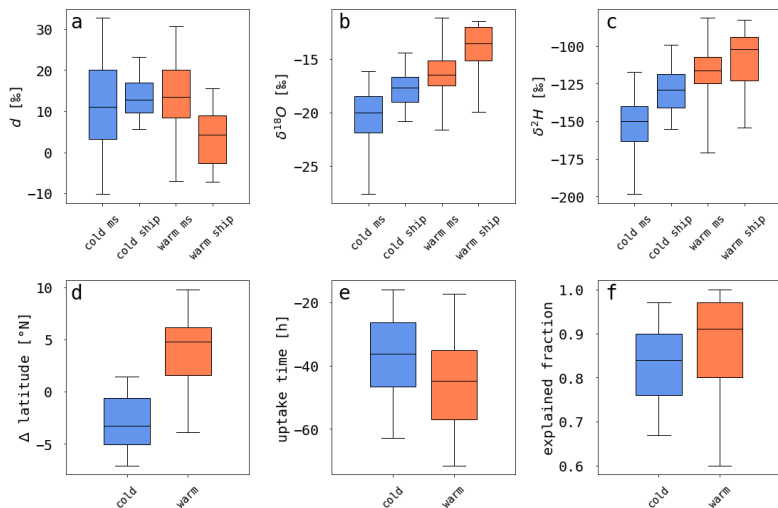
Figure 4.9: Box plots showing mean (black horizontal line in box), interquartile range (boxes) and [5,95]-percentile range (whiskers) of (a) d, (b) $\delta^{18}O$, (c) δ^2H at the moisture source site [ms] and ship location [ship], (d) the difference between the weighted mean moisture source latitude and the latitude upon arrival (Δlat), (e) the weighted mean moisture uptake time before arrival and (f) the explained fraction of specific humidity by the moisture source attribution for cold (blue) and warm (orange) temperature advection.

at the moisture source and at a specific time during transport. The mean weighted moisture sources along the ACE track are computed using 7-day backward trajectories. Furthermore, composites of trajectories starting in the MBL over all cold and warm temperature advection events were calculated and compared with the properties of the air masses at the measurement location. For cold temperature advection, the moisture uptake

took place -37 ± 18 h before the air masses arrived at the measurement
site (Fig.   4.9).   The air masses enter the cold sector -30 ± 31 h before
arrival and, thus, the bulk of the moisture of cold air masses is taken up in
or shortly before entering the cold sector. This means that the air masses
stay in a similar environment, representative of ocean evaporation, from
the moisture source until arrival.   Therefore, similar processes affect the
isotopic composition of the air masses from the moisture source until ar-
rival, which is also reflected in the small changes in d between the moisture
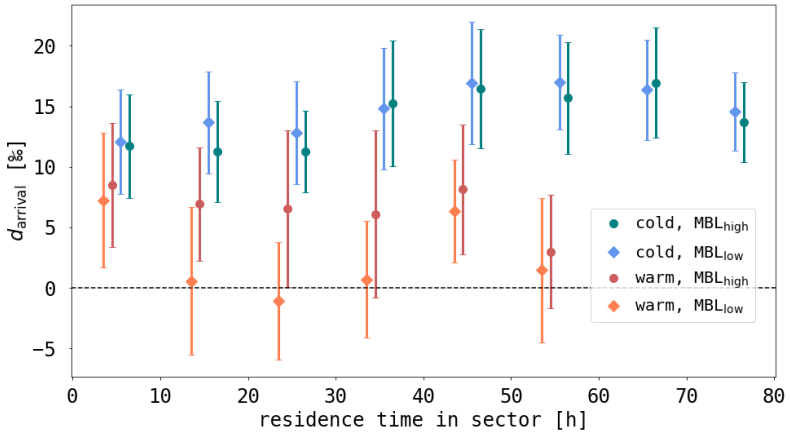source and the arrival (Fig. 4.9a).

*Figure 4.10: Mean d upon arrival at measurement site as a function of the
residence time in the cold or warm sector. For each 10 h-bin of residence
time in the sector, mean values with standard deviation of d upon arrival in
the cold sector (blue,green) and warm sector (red and orange) are shown
for the lower (circle) and upper (diamond) half of the MBL.*

Furthermore, a longer residence time in the cold sector correlates positively with a higher d upon arrival at the measurement site (Fig. 4.10). The δ-values increase from the moisture source until arrival, while the air masses move equatorwards. This isotopic enrichment can be explained by the weaker equilibrium fractionation at higher SST closer to the arrival, which leads to higher $\delta^{18}O$ and δ^2H in the evaporated water vapour. For warm temperature advection, the moisture uptake happens -45 ± 27 h before arrival, while the air masses enter the warm sector much later at -16 ± 14 h before arrival. Therefore, the air masses take up moisture upstream of the warm sector of an extratropical cyclone, and in general in a region with cold advection (Fig. 4.9). The isotopic composition of the water vapour can be strongly modified in the warm sector due to cloud formation and precipitation or dew deposition. This is reflected in the change in d of $-5‰$ from the moisture source to arrival. The strength in d-decrease between moisture source and measurement location depends on the residence time in the warm sector. The strongest decrease in d is seen for air masses in the lower MBL with a residence time of 20-30 h in the warm sector (Fig 4.10). During warm temperature advection, the air masses move polewards from the moisture source and show an increase in δ-values from the moisture source to the point of measurements along the ship track. The increase in $\delta^{18}O$ is stronger in relative terms than for δ^2H. This relative difference in increase of the δ-values co-occurs with the decrease in d between the moisture source and the ACE track. To better understand these changes between the isotopic composition at the moisture source and the point of measurement, the temporal evolution of the isotopic composition and other environmental variables are analysed along the backward trajectories for the 4 days before arrival.

The temporal evolution of d, $\delta^{18}O$ and δ^2H along the trajectories in the cold sector shows a continuous increase towards the arrival (Fig. 4.11, top
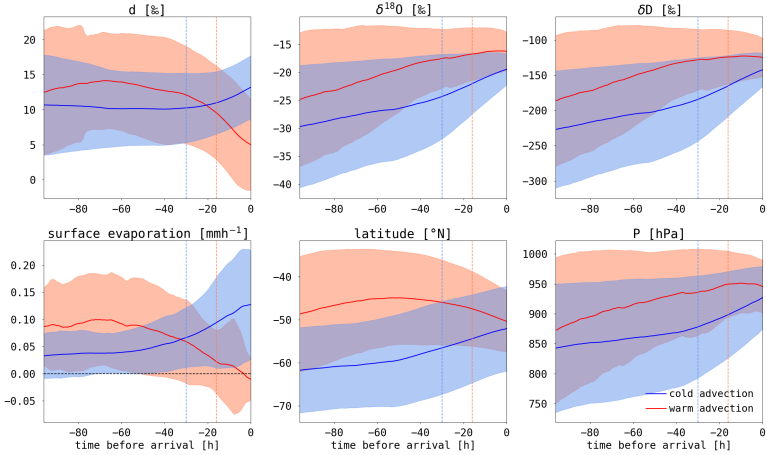
Figure 4.11: Averages of d, $\delta^{18}O$, δ^2H, surface evaporation, latitude and pressure along all trajectories arriving in the cold sector (blue) and warm sector (red) within the MBL over open ocean (no sea ice, land fraction <0.1 in the COSMO$_{\mathrm{iso}}$ simulations). Solid lines show the mean values, shaded areas the standard deviation for all trajectories arriving in each sector. The vertical lines denote the average time step when the trajectories enter the cold (blue line) and the warm sector (red line).

panels). These changes occur simultaneously with an increase in ocean evaporation, an equatorward movement of the air masses and a decrease in height (Fig. 4.11, bottom panels). The strongest changes in d occur during the last 24 hours before arrival, when the air masses are closest to the ocean surface, the ocean evaporation rate strongly increases and the specific humidity reaches its highest mean value of $3.6\,\mathrm{g\,kg^{-1}}$ upon arrival (Fig. 4.12a). The δ-values increase continuously during their residence in the cold sector, with a slightly higher rate during the last 48 hours.

This agrees with the increased ocean evaporation during the last two days from continuously more equatorward regions with increasing SST, and with the descent of the air masses that take up more moisture closer to the surface. The air masses in the cold sector are only weakly influenced by cloud and precipitation-related processes (Fig. 4.12). On average, there is an increase in snow and ice water content in the last 24 hours before arrival. Due to this weak influence of precipitation and clouds along the trajectories, the isotopic composition of the water vapour is only weakly modified between moisture source and point of arrival along the ACE track and the isotopic composition of MBL water vapour is mainly influenced by ocean evaporation.

For warm temperature advection, δ-values increase while the air masses have not yet arrived in the warm sector. Within the warm sector, in the last 18 hours before arrival, the δ-values start to decrease. d already starts decreasing about 70 h before arrival. During the decrease in d outside of the warm sector, the air masses descend and ocean evaporation decreases. Furthermore, the movement of the air masses changes from equatorward to poleward advection. Therefore, this first episode of decreasing d could be due to less non-equilibrium fractionation with a weakening of ocean evaporation. During the d-decrease within the warm sector, the air parcels stay at the same height or ascend, while the ocean evaporation is close to zero or changes sign implying dew formation. During the last 18 hours before arrival, there is a strong increase in rain and cloud water content in the warm air masses. Furthermore, specific humidity decreases after a steady increase before the arrival of the air mass in the warm sector. The arriving air masses during warm advection are thus influenced by more diverse processes than during cold advection. During the last day before arrival when the air masses are in the warm sector, there are three main process influencing the air masses: 1) low ocean evaporation or dew
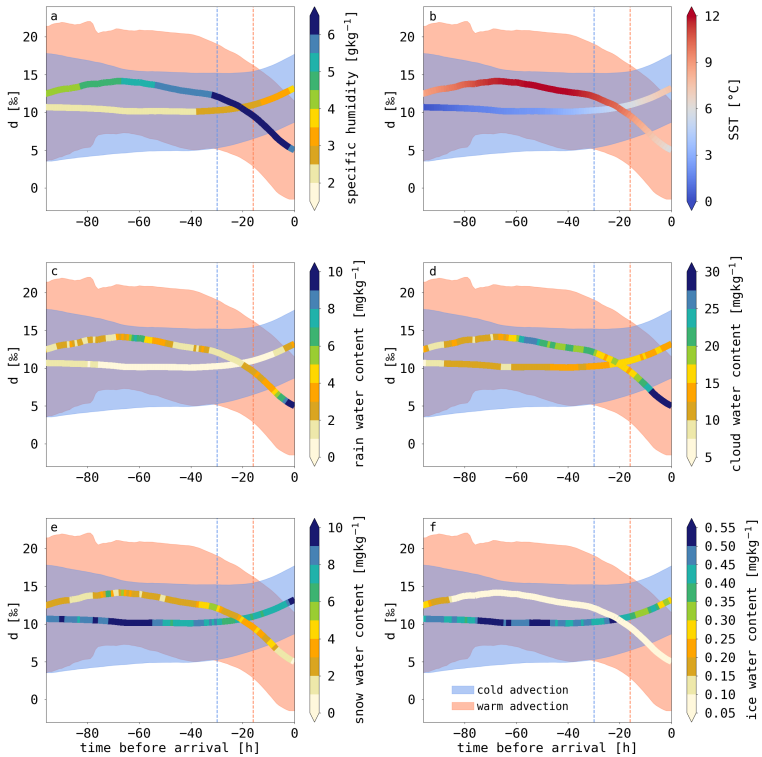
Figure 4.12: Same as Fig. 4.11, but only for d. *The mean trajectories are coloured by the mean values of (a) specific humidity, (b) SST and (c) rain, (d) cloud, (e) snow and (f) ice water content along the trajectories in each sector.*

deposition, 2) cloud formation leading to a strong increase in cloud water
content, 3) precipitation shown by the increase in rain water content and
decrease in specific humidity. How these processes influence the isotopic
composition of water vapour is illustrated in a case study in the next section.

4.6 Temporal SWI evolution in water vapour during a cold and a warm temperature advection event

In this section, a cold and a warm temperature advection event are char-
acterised in detail to illustrate the typical features and the temporal SWI
evolution associated with both meridional flow configurations as well as to
identify the relevant processes shaping the evolution of the MBL isotopic
composition during such events. First, a cold temperature advection event
during a cold air outbreak (CAO) in the Ross Sea is described (Section
4.6.1). Second, a warm temperature advection event is discussed, during
which the warm sector of an extratropical cyclone passes over the research
vessel in the Indian Ocean (Section 4.6.2). These two events are selected
because the modelled and observed isotopic composition agree well. This
allows us to use the model to provide the large-scale flow context and to
investigate the evolution of the SWI signals along backward trajectories.

4.6.1 Enhanced ocean evaporation and positive d anomalies during a cold advection event

On 1 Feb 2017, a low pressure system intensifies in the eastern Ross Sea
and moves southward in the following days, thereby inducing the advection
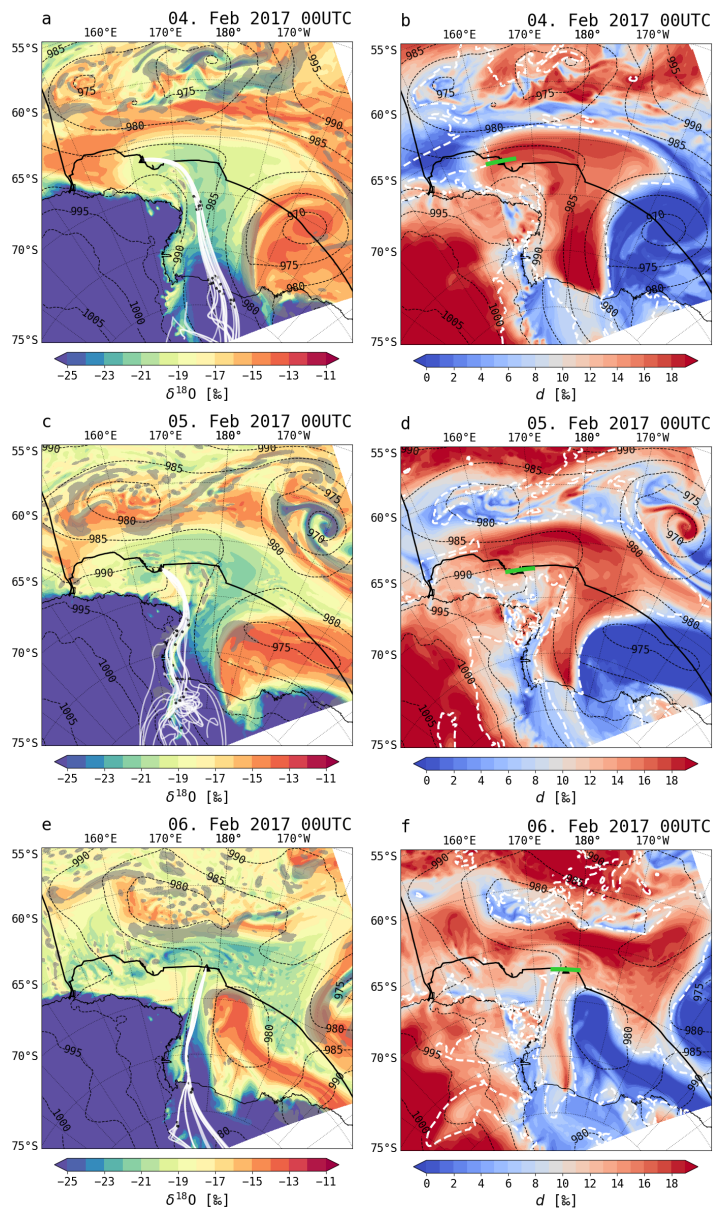of cold and dry Antarctic air masses over the western Ross Sea (Fig. 4.13).

Figure 4.13: (Next page.)

Figure 4.13: $\delta^{18}O$ *(a,c,e) and* d *(b,d,f) on the lowest model level in* COSMO$_{iso}$ *simulation leg2-run1 including the ACE track (black, solid line) with sea level pressure (hPa, dashed black lines). 4-days backward trajectories arriving in the MBL (white lines with every 24 h marked with black dots) and the surface precipitation > 0.1 mm h^{-1} (grey areas) are shown in panel **a,c** and **e**. The position of the vertical cross sections shown in Fig. 4.16 (green thick lines) and the cold temperature advection mask* $(\Delta T_{ao} < -1.0)$ *are shown in white dashed contours in panels **b,d,f**.*

This leads to the development of a CAO in the Ross Sea, which lasts for 5 days from 1 to 6 Feb 2017. The cold front at the northern edge of the cold air mass reaches as far north as 63 °S. The ACE ship measurements are affected by the CAO from 3 to 6 Feb 2017. During these days, q and h_s decrease rapidly and stay at values of $2\,\mathrm{g\,kg^{-1}}$ and 0.6, respectively (Fig. 4.14). The model diagnosed boundary layer height increases from 500 to 1400 m, simultaneously with an increase in ocean evaporation. Elevated ocean evaporation fluxes are dominant over the western Ross Sea leading to the injection of a plume of freshly evaporated ocean water into the MBL, which is bounded by the cold air advection mask (Fig. 4.13). Precipitation amounts are low during this CAO. On 6 Feb 2017, the warm sector of the extratropical cyclone replaces the cold air masses and leads to an increase in q and h_s and a decrease in the boundary layer height and in the ocean evaporation flux. Furthermore, precipitation increases during the decay of the CAO and in the approaching warm sector.

The temporal evolution of q and h_s in the measurements and the simulation agree well from 3 to 5 Feb (Fig. 4.14). In the COSMO$_{iso}$ simulation, the CAO influence at the measurement location weakens 12 h later than in the measurements, as can be seen by the shift in increasing q and h_s between
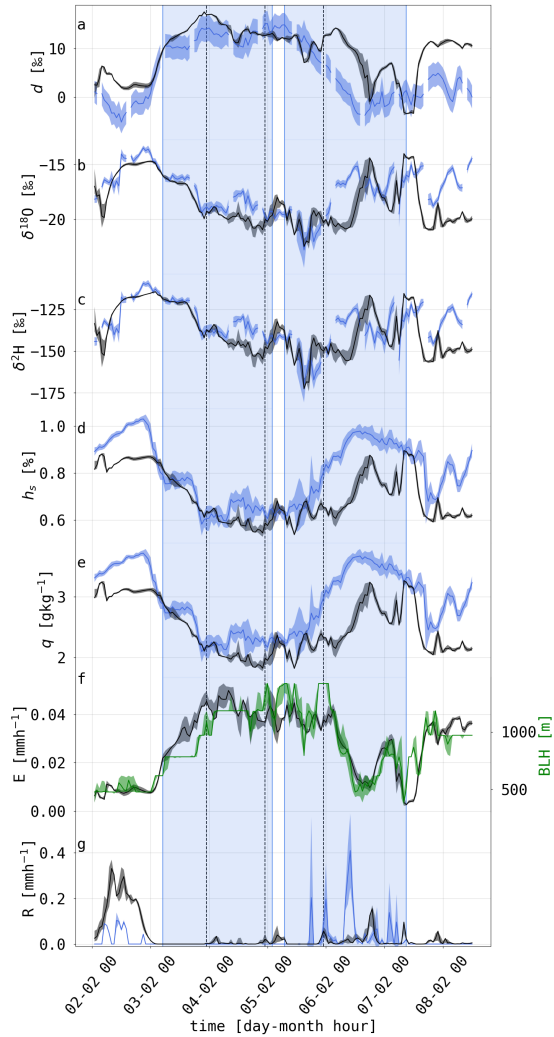
Figure 4.14: (Next page.)

*Figure 4.14: Time evolution of 1-hourly (**a**) d, (**b**) $\delta^{18}O$, (**c**) δ^2H (**d**) h_s, (**e**) specific humidity q, (**f**) ocean evaporation E and boundary layer height BLH, and (**g**) precipitation rate R from ACE measurements and COSMO$_{\text{iso}}$ simulations interpolated along the ship track during the cold temperature advection event in the Ross Sea from 00 UTC 2 Feb to 06 UTC 8 Feb 2017. The blue lines show the measurements with standard deviation, the black and green lines the simulated values including the variability from 10°-shifts of the ACE track (black and green areas). The blue shaded areas denote the two periods discussed in the text. The black dashed vertical lines are the time steps of the horizontal cross sections in Fig. 4.13.*

the time series. Furthermore, there are disagreements in precipitation rates and timing during the decaying phase of the CAO. These disagreements are caused by a temporal shift in the arrival of the warm front of the subsequent cyclone between simulation and measurements. The observed precipitation intensities are affected by large uncertainties because no snow crystal characterisations are available for the calculation of snowfall rates from the ACE micro rain radar measurements. Therefore, the conversion formula from MRR measurements at Dumont D'Urville is used (Grazioli et al., 2017), which provides a rough estimate of the true snowfall rates. In the COSMO$_{\text{iso}}$ simulation, the representation of shallow cumulus clouds over the Southern Ocean is a challenge and is strongly dependent on the model resolution (Papritz and Sodemann, 2018; Possner et al., 2016).

The temporal evolution of the SWI composition is similar in the measurements and the simulation (Fig. 4.14) and shows the same shift between measurements and simulation towards the end of the event as seen in h_s and q. $\delta^{18}O$ and δ^2H decrease during 3 Feb 2017, stay around -20 and -150 ‰, respectively, from 4 to 5 Feb 2017 and increase relatively fast

at the end of the CAO. d increases strongly by 10-15 ‰ with the onset
of the CAO and stays at around 10 ‰ for three continuous days until it
decreases to negative values with the arrival of the warm sector. High d
and low $\delta^{18}O$ and δ^2H overlap with periods of high ocean evaporation and
boundary layer height and low h_s and q under the influence of the CAO.
The event can be divided into two periods. In the first period from 6 UTC
3 Feb to 3 UTC 5 Feb 2017, the SWI signals are relatively constant and
measurements and model agree well. In the second period from 8 UTC 5
Feb to 10 UTC 7 Feb 2017, the CAO decays and a temporal shift between
model and measurements can be observed.

During the first period, d reaches up to 13‰ and $\delta^{18}O$ and δ^2H show low
values of -20‰ and -145‰ (Fig. 4.14a-c). Surface heat fluxes and in
particular ocean evaporation increase and stay at high values during this
period, leading to a deepening of the MBL (Fig. 4.14f). Enhanced ocean
evaporation and associated low h_s during the CAO introduces water vapour
with high d into the MBL. To understand the origin of the characteristic
SWI signal during cold temperature advection, the evolution of the isotopic
composition along backward trajectories is analysed. Backward trajecto-

*Figure 4.15: COSMO_{iso} parameters interpolated along three-day back-
ward trajectories started at 00 UTC 4 Feb 2017 in the MBL from the
ship's position: (a) d (coloured by relative humidity h), (b) $\delta^{18}O$, (c) δ^2H
(coloured by specific humidity), (d) surface evaporation, and (e) height
(coloured by snow water content). The red diamonds note the time when
the trajectory moved over open ocean. The blue cross denotes the last
time the trajectory is above the MBL before arrival. The different bars for
surface evaporation show the values for each trajectory below 500 m a.s.l.*
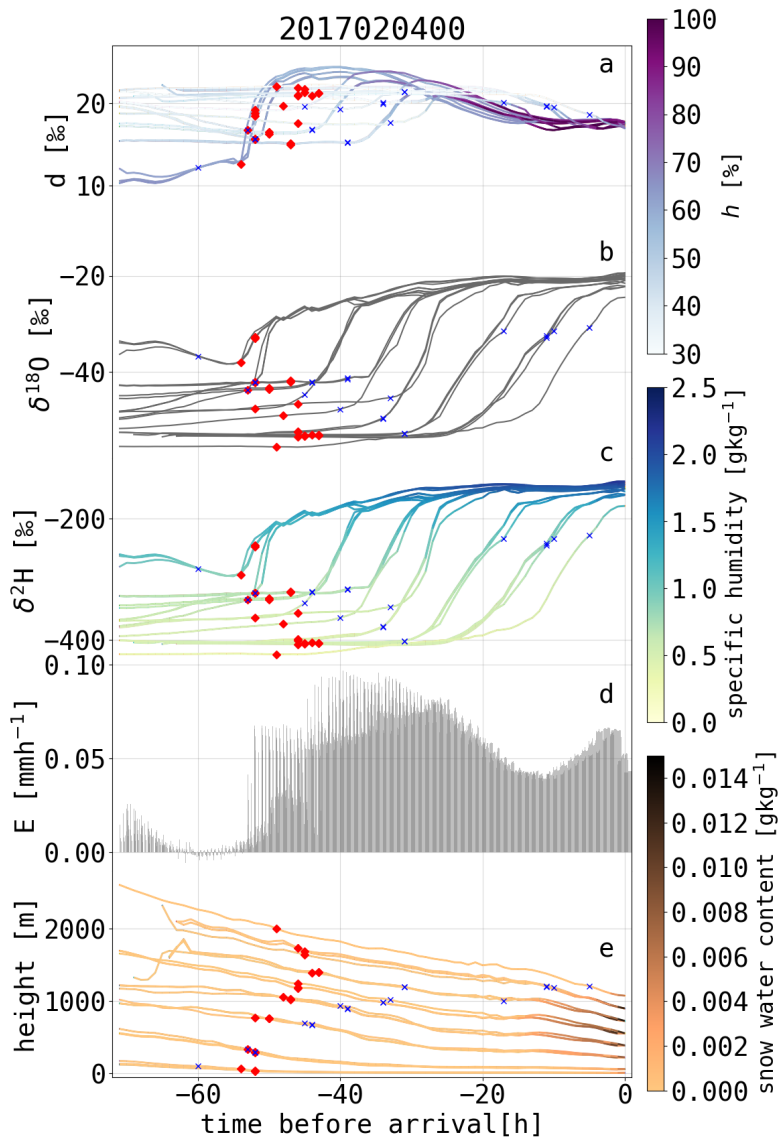
Figure 4.15: (Previous page.)

ries started at 00 UTC 4 Feb 2017 from the ship track move northwestwards from Antarctica over the Ross Sea (Fig. 4.13). During their movement over the Ross Sea towards the ship track, d, $\delta^{18}O$ and δ^2H increase along the trajectories. Depending on their arrival height, the trajectories show different changes in the SWI composition during their movement over the Ross Sea (Fig. 4.15). Trajectories arriving below 500 m a.s.l. are already situated within the MBL when they leave the ice covered areas of the Ross Sea. They are immediately affected by surface evaporation induced by the advection of the dry air masses from the ice sheet over the ocean, which leads to increasing $\delta^{18}O$, δ^2H and d along the transport path. In contrast, trajectories arriving above 500 m a.s.l, do not show a strong change in SWIs when they move over the open ocean. During the movement from Antarctica across the Ross Sea, SWI values stay constant until (or shortly before) the air parcels enter the MBL, when they show a strong increase in d and δ-values due to the influence of surface evaporation and vertical mixing with air from the MBL. The vertical cross section at the ship's position at 00 UTC 4 Feb 2017 shows a strong vertical SWI gradient with very low δ-values above the boundary layer and higher values within the deep boundary layer, which illustrates the contrasting SWI compositions above and in the MBL (Fig. 4.16). d decreases along most trajectories just before arriving at the ship after the strong increase due to enhanced surface evaporation. The decrease in d co-occurs with an increase in h and decrease in surface evaporation (Fig. 4.15). Due to weaker non-equilibrium isotopic fractionation during decreased ocean evaporation at high h, water vapour from ocean evaporation has a lower d. The input of water vapour into the MBL by ocean evaporation accounts for a large fraction of q at the measurement site, which is seen by an increase of q by a factor of 3-4 from the Antarctic coast until arrival (Fig. 4.15c). Small amounts of snowfall at the ship's position and along the trajectories only
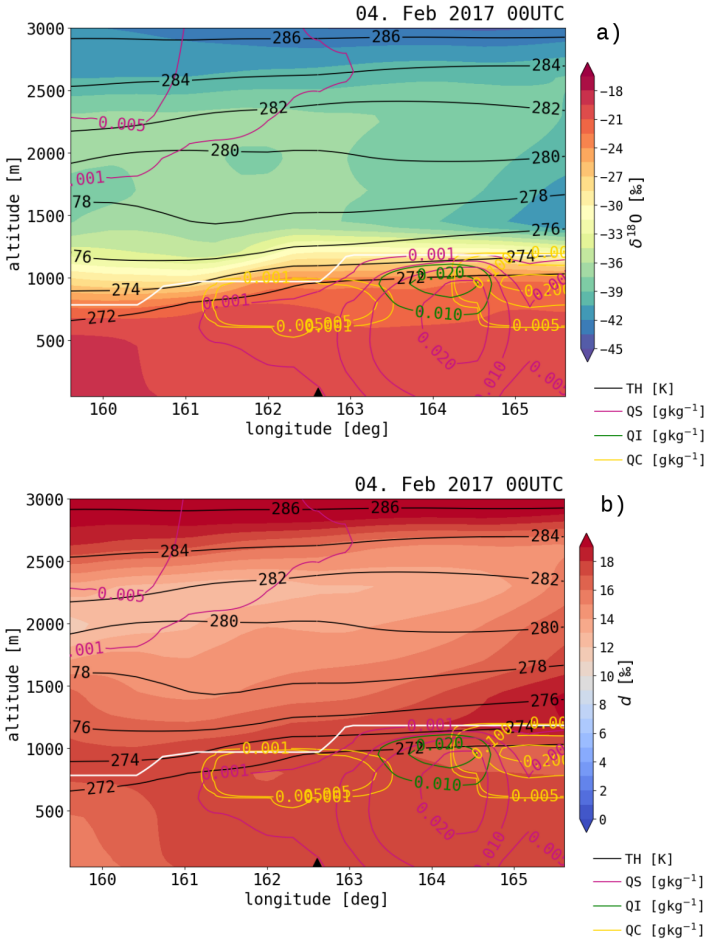
*Figure 4.16: Vertical cross sections along the latitude of the ship's position
at 00 UTC 4 Feb 2017 showing (a) $\delta^{18}O$ and (b) d in COSMO$_{iso}$ simulation
leg2-run1. Also shown are contours of potential temperature (TH) and
cloud (QC), snow (QS) and ice (QI) water content (in $g\,kg^{-1}$). The white
line is the boundary layer height. The black triangle at the bottom denotes
the longitudinal position of the ACE track. The position of the cross section
is shown in Fig. 4.13.*

weakly influence the SWI composition relative to the changes induced by ocean evaporation. Therefore, the SWI composition of water vapour measured near the ocean surface during the CAO is mainly a signal from ocean evaporation which substantially changes the d, δ^{18}O and δ^2H signature of the originally Antarctic air masses. Towards the end of the first period, the air masses arriving at the ship followed the Antarctic coast line. The evolution of the SWI signal along these trajectories is more complex and the SWI signal does not change as strongly between the Antarctic coast line and the measurement site as in the beginning of this period. These air masses experience evaporation during several periods before they arrive at the ship's position and spend only few continuous hours above the ocean surface (see Appendix Fig. B.3).

In the second period of the cold temperature advection event, during the decay of the CAO, several snowfall events occur and q, h_s, δ^{18}O and δ^2H increase, while d decreases (Fig. 4.14). These changes occur later in COSMO$_{\text{iso}}$ than in the observations probably because the air masses in the simulation follow a narrow pathway across the Ross Sea by which air masses from Antarctica still reach the ACE track. The dry Antarctic air masses take up a lot of humidity due to enhanced ocean evaporation in the simulation (Fig. 4.13) and lead to a later weakening of the CAO influence at the measurement site. The trajectories of the second period show a similar evolution as the trajectories in the first period, with strong changes in the SWI composition after the trajectories cross the Antarctic coast line and enter the MBL (see Appendix Fig. B.4).

The SWI composition of MBL water vapour under the influence of a CAO is dominated by the isotopic signal from ocean evaporation. d is sensitive to the strength of ocean evaporation, increases strongly during enhanced ocean evaporation into very dry air masses and decreases with the weakening of ocean evaporation and progressive moistening of the air masses.

Furthermore, strong ocean evaporation leads to a large vertical gradient in
the isotopic composition between the MBL and the free troposphere. High
d and low δ-values in water vapour measured during cold advection, agree
with observations by Uemura et al. (2008), who measured high d during a
cold air outbreak in the Southern Indian Ocean. Here, we focus on the in-
fluence of ocean evaporation on the measurements of SWIs near the ocean
surface. The datasets used in this study could be further used to have a
closer look at the evolution of the MBL isotopic composition during CAOs
to better understand the development of the strong gradients in δ-values
and d across the MBL top and to quantitatively assess the contributions of
ocean evaporation, advection of air masses and mixing between vertical
layers to the SWI composition of the MBL.

The decrease in d during the decay of the CAO and the arrival of the
warm sector illustrates the sensitivity of d to cold and warm temperature
advection. With the arrival of the warm sector, precipitation increases
and additional moist processes can influence the SWI signal of the MBL.
The contribution of these various processes to SWI variability in the warm
sector of extratropical cylones is analysed in the next subsection in the case
study of a warm temperature advection event.

4.6.2 Dew deposition and cloud formation as drivers of negative d anomalies during warm temperature advection

The warm sector of an extratropical cyclone south of Marion Island in the
Indian Ocean (label *C1* in Appendix Fig. B.5) passes the ship, which was
anchored near the island, from 26 to 28 December 2016 (Fig. 4.17). The
cyclone center was positioned at 55°S. A weak low pressure system (*C1.1*
in Appendix Fig. B.5) developed north of cyclone *C1* three days before
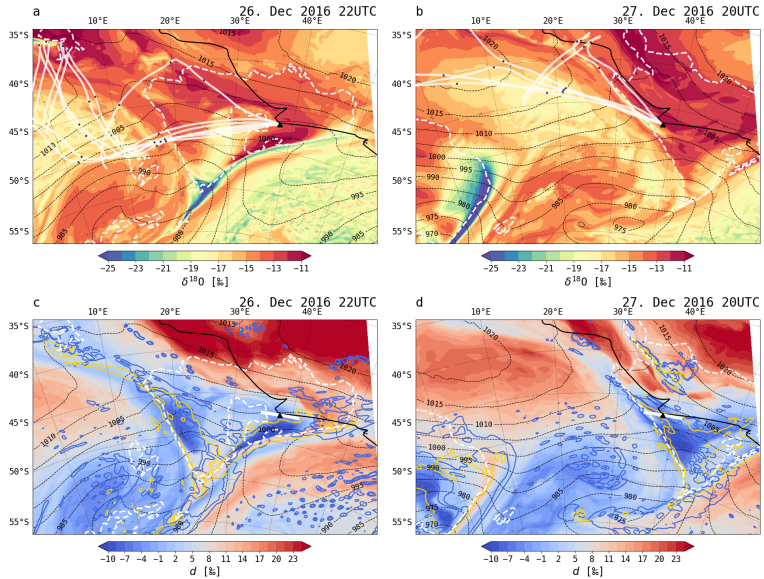
Figure 4.17: $\delta^{18}O$ *(a,b)* and d *(c,d)* on the lowest model level in COSMO$_{\text{iso}}$
simulation leg1-run1 including the ACE track (black solid line) and position
(black triangle) with sea level pressure (hPa, black dashed lines) and the
warm temperature advection mask ($\Delta T_{\text{ao}} > 1.0$, white dashed line). 4-
days backward trajectories arriving in the MBL (white lines with every
*24 h marked with black dots) are shown in panel **a** and **b**. The position of*
the vertical cross sections shown in Fig. 4.19 (white thick lines), surface
precipitation of 0.1 mm h^{-1} (blue lines) and the mean cloud water content
of the 5 lowest model levels of 10 g kg^{-1} (yellow lines) are shown in panels
***c** and **d**.*

arrival of the warm sector at the ship's position and merged with *C1* in
the two days before arrival. The warm temperature advection event at the
measurement site is bounded by precipitation along the warm front in the

beginning and along the cold front at the end. In the beginning of the
event, air masses arrive mainly from the west to south-west and change
to north-western direction during the event. Measured h_s stays above 1.0
for nearly the entire event from 15 UTC 26 Dec to 00 UTC 28 Dec 2016
(Fig. 4.18d). Simultaneously, simulated ocean evaporation is negative,
indicating dew deposition on the ocean surface (Fig. 4.18f). Highest dew
deposition rates coincide with high h_s and q and a very shallow diagnosed
boundary layer height in the model as expected in stable near-surface con-
ditions. There are two peaks in dew deposition rates at the measurement
site, which correspond to two areas of negative ocean evaporation within
the warm sector (black dashed lines in Fig. 4.17c). The first area of dew
deposition lies behind the warm front, the second ahead of the cold front.
In between these two areas, weakly positive ocean evaporation occurs (Fig.
4.18f). This splitting of the warm sector into two areas of dew deposition
is a result of the merging of cyclones *C1.1* and *C1*, whereby two warm
sectors were combined into one larger area (see Fig. B.5 in Appendix).
Measurements and simulation of h_s and q agree well for this event (Fig.
4.18d,e). Precipitation rates along the fronts are captured by the simulation
except for the morning of 27 Dec 2016 when no precipitation is simulated.
Due to the missing rainfall in the simulation, lower q and h_s were simulated
than measured in this time window.

Negative d and high δ^{18}O and δ^2H are measured during the warm tem-
perature advection event. Similar to h_s, there are two maxima in δ-values
and two minima in d. d has two minima of $-3\,‰$ at 18 UTC 26 Dec
2016 and $-5\,‰$ at 16 UTC 27 Dec 2016. They coincide with two periods
of high δ-values up to $-12.5‰$ for δ^{18}O and $-100‰$ for δ^2H during this
warm temperature advection event. These two periods, referred to as warm
period 1 (*WP1*) and 2 (*WP2*), will be compared in the following.

The first period WP1 (from 18 UTC 26 Dec to 02 UTC 27 Dec 2016)

occurs after the passage of the warm front (see Fig. 4.17). The decrease in d is accompanied by high $\delta^{18}O$, δ^2H, q and h_s (Fig. 4.18). There is no precipitation during this period after the warm frontal precipitation, surface evaporation is negative and the diagnosed boundary layer height decreases from 1200 to 700 m. Due to the absence of precipitation and cloud formation (liquid water content shown in Fig 4.19g is zero in this period), the only phase-change process in this period is dew deposition, which most likely causes negative d. The formation of dew can be understood as thermodynamic equilibration of a very moist air parcel that is warmer than the ocean with the ocean surface temperature. If the atmosphere is oversaturated with respect to sea surface temperature, this equilibration implies a dew deposition flux, which leads to an increase in δ-values in vapour, with a simultaneous decrease in d (see section 3.1.2). Therefore, the observed SWI evolution during this period of decreasing d with a simultaneous increase in $\delta^{18}O$ and δ^2H follows the expected evolution induced by dew deposition, which reveals an important process leading to negative d near the ocean surface.

According to the COSMO$_{iso}$ simulation, negative d is not only seen at lower levels but throughout and above the MBL at 22 UTC 26 Dec 2016 (Fig. 4.19). d stays constant or decreases from the ocean surface towards

Figure 4.18: As Fig. 4.14, but for the warm temperature advection event at Marion Island from 26 Dec to 28 Dec 2016. Additionally in (g), mean cloud water content on the five lowest model levels (10-200 m a.s.l.) is shown (QC). The vertical orange lines denote the beginning and end of the warm temperature advection event. The shaded orange areas correspond to the two periods WP1 and WP2 discussed in the text.
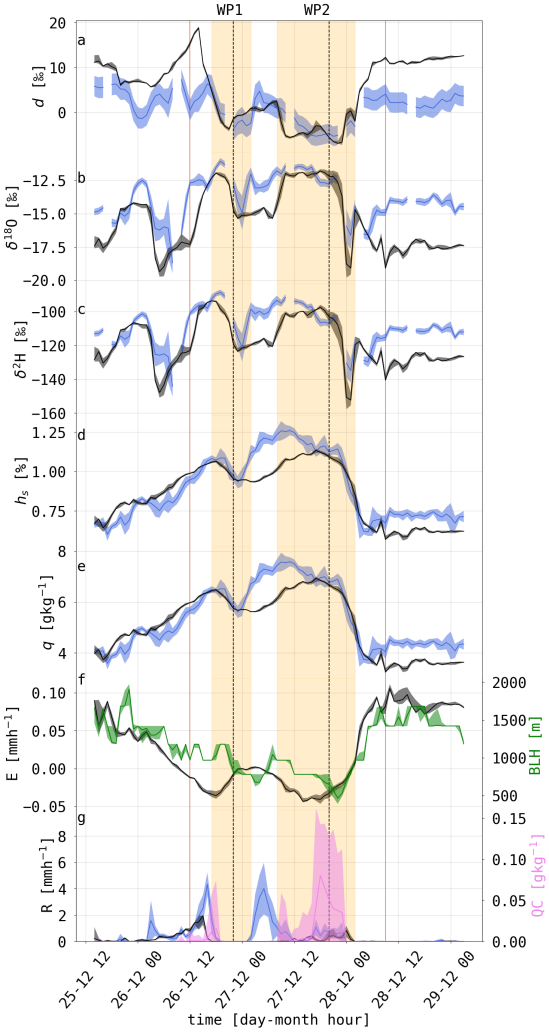
Figure 4.18: (Previous page.)
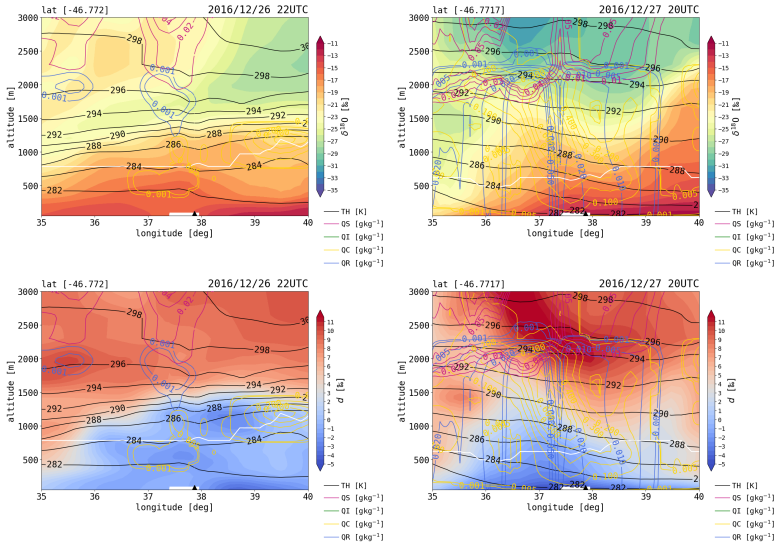
Figure 4.19: As Fig. 4.16, but for COSMO$_{iso}$ *simulation leg1-run1 at 22 UTC 26 Dec 2016 and 20 UTC 27 Dec 2016. Additional, blue contours show rain water content.*

the MBL top and starts to increase well above the MBL. Even though d does not change strongly across the MBL, air masses arriving in the lower and upper MBL encounter different processes during their transport leading to negative d. As illustrated along the 4-day backward trajectories, dew deposition is the main process affecting the air masses in the lower MBL, in which the measurements took place (Fig. 4.20). The trajectories arriving in the lower MBL from a north-western direction stayed close to the surface for the previous two days and show a strong increase in h_s, accompanied by a strong decrease in surface evaporation and in d, after they enter the warm sector. In contrast, air masses in the upper MBL arrive

from west to south-west and show a decrease in d over a longer period
than the trajectories arriving in the lower MBL. The trajectories arriving in
the upper MBL were influenced by cyclone *C1.1* two days before arrival.
They travel along the warm front of *C1.1* within the cold sector towards
the cyclone center, where they ascend two days prior to arrival (see also
Fig. B.5 in Appendix). Before the ascent, d decreases, while δ^{18}O and
δ^2H increase. During the ascent, δ^{18}O and δ^2H start to decrease together
with d. After the ascent, the trajectories change their direction and move
towards Marion Island within the warm sector of *C1.1* that merges with the
warm sector of *C1*. Subsequently, d stays low and decreases further when
the trajectories enter the MBL, while δ^{18}O and δ^2H increase. Therefore,
the negative d in the upper MBL builds up over several days and the
strongest decrease in d occurs before and during the lifting of air masses
in the cyclone center of *C1.1*. The decrease in d along these trajectories
during their movement towards the ship track is the combination of two
processes. First, before the ascent, the same process occurs as seen for
the air mass arriving in the lower MBL. Weak ocean evaporation and dew
deposition leads to an increase in δ^{18}O and δ^2H and a decrease in d.
Second, d is lowered during the ascent with the formation of cloud water.
Rayleigh fractionation during a simulated moist adiabatic ascent induces a
slightly decreasing d due to the temperature-dependency of the equilibrium
fractionation factor in the lower troposphere (see Section 3.1.3 on Rayleigh
fractionation during a moist adiabatic air parcel ascent). In contrast to dew
formation, the δ-values decrease during cloud formation, which agrees
with the evolution of δ^{18}O and δ^2H along the trajectories during their
ascent in the cyclone center. Negative d anomalies at or below the MBL
top during the occurrence of clouds as seen at 22 UTC 26 Dec 2016, can
also be seen during the cold advection event (Fig. 4.16). Therefore, cloud
processes can also play a role in forming negative d in the upper MBL
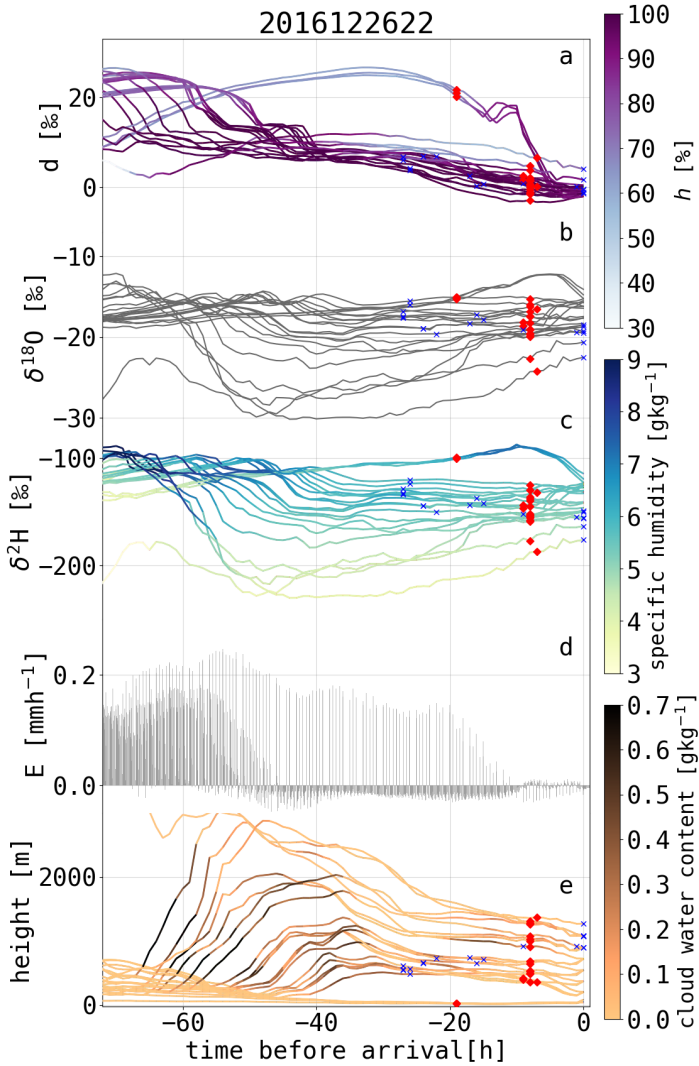
Figure 4.20: As Fig. 4.15, but for 3-day backward trajectories starting
from the ship's position below 1.5· MBL-height at 22 UTC 26 Dec 2016.
Here, the red diamonds show the time, when the trajectories entered the
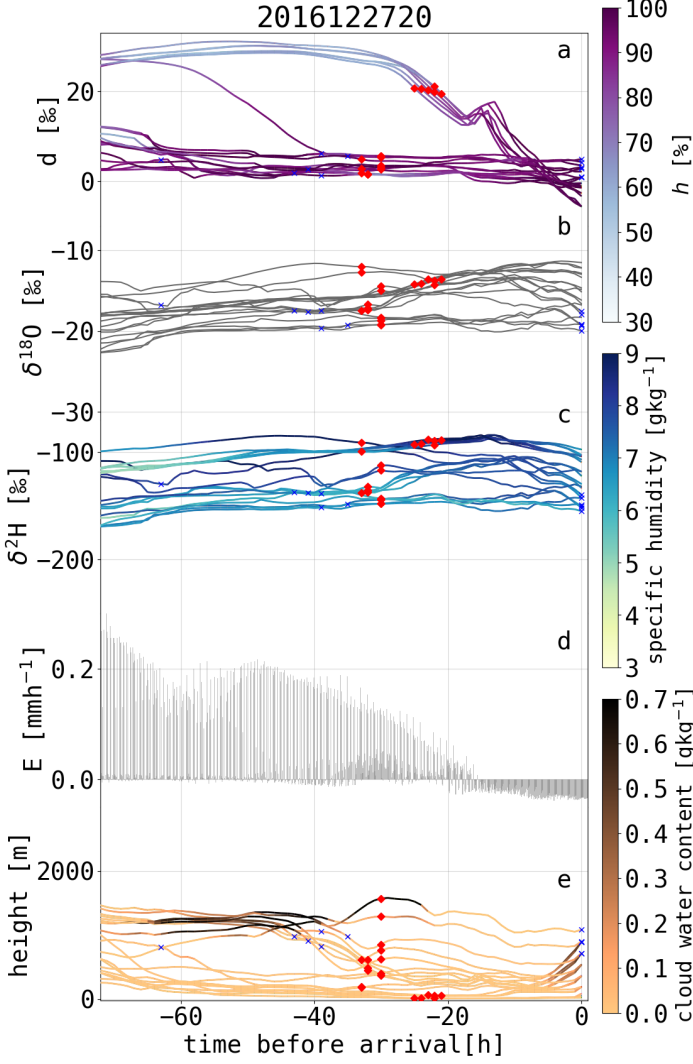warm sector.

Figure 4.21: As Fig. 4.20, but for 20 UTC 27 Dec 2016.

during cold advection.

This example of warm temperature advection shows that understanding, e.g., d-structures in a vertical cross section requires considering the Lagrangian history of air parcels, because accumulated physical processes that occurred along the flow might be responsible for the observed signals (see also Spreitzer et al. (2019); Attinger et al. (2019) for similar findings independent of isotope processes).

The second period WP2 occurs from 09 UTC 27 Dec to 02 UTC 28 Dec 2016, i.e. starting 9 hours after the end of the first period. In this period, d at the ship's position decreases a second time after an intermittent increase (Fig. 4.18a). In the beginning of *WP2*, the simulated and measured signals disagree with more precipitation and higher q and h_s in the measurements as well as a more gentle decrease in d than the simulated values (Fig. 4.18). A peak in precipitation rates at 05 UTC 27 Dec occurs before the decline in d and weaker precipitation prevails into this period of decreasing d, q and h_s. After an increase in δ^{18}O and δ^2H, the SWI composition stays constant in the second half of this period with high dew deposition and high amounts of cloud water on the lowest model levels.

The relative importance of dew deposition and cloud formation for shaping the isotopic composition of the MBL is different during *WP2* compared to *WP1*, which is visible by the SWI evolution along 3-day backward trajectories (Fig. 4.20 and 4.21). Less trajectories have been ascending before arrival in the MBL during *WP2* compared to *WP1*. A characteristic decrease in d due to decreasing surface evaporation rates and dew formation occurs in the last 18 h before arrival, when the trajectories enter the warm sector at low levels. These lower trajectories are further influenced by local cloud formation as they start to ascend along the cold front during the last few hours before arrival. Therefore, the SWI measurements near the ocean surface are not only influenced by dew deposition, as it was

observed during *WP1*, but the near-surface air masses can also be affected by cloud formation near the measurement site. During *WP2*, there is a positive d-gradient in the MBL with height (Fig. 4.19), whereas during *WP1* d stayed low across the MBL and above. Therefore, negative d is more confined to the ocean surface during *WP2*, where cloud formation and dew deposition have a combined impact on d.

Below-cloud evaporation could have played a role during the warm temperature advection event discussed here, especially where low precipitation rates were observed during *WP2*. During the continuous evaporation of rain droplets, $\delta^{18}O$ and δ^2H (d) of the remaining rain droplets increases (decreases) due to isotopic fractionation during evaporation. Therefore, at the lower edge of totally evaporating rainfall (virga) input of water vapour with high δ-values and low d can influence the vertical gradient of SWI variables in the MBL. However, no virgas were detected in the MRR measurements during the event and therefore, evaporation of cloud droplets and precipitation most likely plays a minor role in this case study.

The negative d observed during the warm temperature advection at Marion Island is driven by two main processes: ocean surface dew deposition and cloud formation. For the near-surface d signal, dew deposition is important throughout the warm sector with an increasing influence of low-level cloud formation closer to the cold front. In the upper MBL, d can be built up several hundred km away from the measurement site and be advected over long distances. Therefore, air-sea interaction is an important driver of the SWI composition of the MBL during warm temperature advection and is often accompanied by cloud formation. Cloud processes as drivers of negative d have been mentioned in earlier studies for the interpretation of negative d in SWI measurements in the MBL and across the MBL top and was mainly interpreted as the impact of continuous evaporation of hydrometeors (Aemisegger et al., 2015; Sodemann et al., 2017; Salmon

et al., 2019) or ice-supersaturation conditions in mixed-phase clouds, during which non-equilibrium fractionation effects occur (Bolot et al., 2013; Salmon et al., 2019). The results of this study show that local and upstream formation of clouds can contribute to the observed negative vertical d-gradients across the MBL and the MBL top as observed by Sodemann et al. (2017) and Salmon et al. (2019). Uemura et al. (2008) hypothesized that sea spray evaporation and near equilibrium conditions at high h_s could explain low d values in water vapour near the ocean surface during the passage of an extratropical cyclone. The results of this study show that high h_s is one of the main drivers of low d in the lower MBL. Sea spray evaporation can influence the MBL SWI composition by introducing a low d if the water vapour of the sea spray droplets evaporates nearly fully (Gat et al., 2003). The vertical SWI-gradient in near-surface SWI measurements during ACE increased during high wind speed conditions, which favor sea spray production, and can be used as a sea spray evaporation indicator (Thurnherr et al., 2020). During *WP1* and *WP2*, the near-surface vertical δ^{18}O-gradient stayed within $\pm 0.2\,\text{‰}\,\text{m}^{-1}$ and the sea spray proxy stayed below $5\,\text{particles}\,\text{cm}^{-3}$ for most of the time during the warm temperature advection event (see also Fig. B.6 in the Appendix). For a short period in the beginning of *WP1*, the sea spray proxy showed values above $10\,\text{particles}\,\text{cm}^{-3}$, but no increase in the vertical δ^{18}O-gradient is visible during this period. Therefore, sea spray evaporation has, most likely, not played an important role for the observed negative d during this warm temperature advection event.

4.6.3 Application of single-process air-parcel models to the SWI evolution along trajectories

The SWI evolution during processes such as ocean evaporation, dew deposition and cloud formation can be approximated by the single-process air parcel models described in Chapter 3. In an isotope phase-space diagram, these processes follow specific paths and, thus, such diagrams can be used to identify the aforementioned processes along COSMO$_{iso}$ air parcel trajectories. We simulate the different paths in the phase-space diagram of three single-process air-parcel models:

1. *Moisture uptake due to ocean evaporation of an air parcel advected across a meridional SST gradient:*
   In this model, an air parcel continuously takes up moisture from ocean evaporation. The isotopic composition of the evaporation flux is calculated using the parametrisation by Craig and Gordon (1965). During the simulation, SST increases from a starting SST$_0$ to a maximum value SST$_{max}$ during the first half of the model steps and decreases afterwards to SST$_{final}$ = SST$_0$. The model steps are given by changes in q, which are proportional to the evaporation flux until h_s=1.0. The model is run twice, for a cold and a warm advection environment.

2. *Dew deposition from a supersaturated air parcel that is equilibrating with the ocean surface:*
   The dew depositional flux is prescribed by changes in q, which decreases continuously until $q=q_s$ with a constant SST throughout the model run. The isotopic composition of the depositional flux is calculated using the model by Craig and Gordon (1965).

3. *Moist adiabatic ascent of an air parcel and cloud formation:*
   A moist adiabatic ascent is assumed using prescribed initial values
   for temperature and pressure. In the ascending air parcel, cloud
   condensation and Rayleigh fractionation during condensation is im-
   plemented. q decreases continuously following the moist adiabatic
   profile until q corresponds to less than 1% of the starting value.

The starting parameters of the model runs are summarised in the Appendix
(Table B.1) and are similar to values encountered along the trajectories.
Figure 4.22 illustrates the simulated SWI evolution from the three process
models together with three COSMO$_{iso}$ trajectories from the warm and
cold temperature advection event discussed in the previous sections. The
increase in δ-values and d along the trajectory from the cold temperature
advection event (blue trajectory in Fig. 4.22) after it moved over the open
ocean (blue triangle) until arrival (black diamond) is well reproduced by
ocean evaporation across a meridional transect in a cold environment (thin,
solid lines). Also for the warm temperature advection trajectories (orange
and violet trajectories in Fig. 4.22), a SWI-evolution similar to the ocean
evaporation model (dashed lines) is seen for the first 1-2 days in the upper
and lower MBL. These trajectories start at higher q and SST compared to
the cold temperature advection event, which reflects the more equatorward
starting position of the trajectories. Therefore, the increase in d and δ-
values while the trajectories move equatorward over open ocean can be
simulated using the ocean evaporation air-parcel model.

The decrease in d before arrival along the blue trajectory (Fig. 4.22c) has
a similar magnitude as d in the cold ocean evaporation model runs, but is
seen at lower q along the trajectory. For the warm advection trajectories, the
decrease in d shows different behaviours in the d-q phase-space diagram.
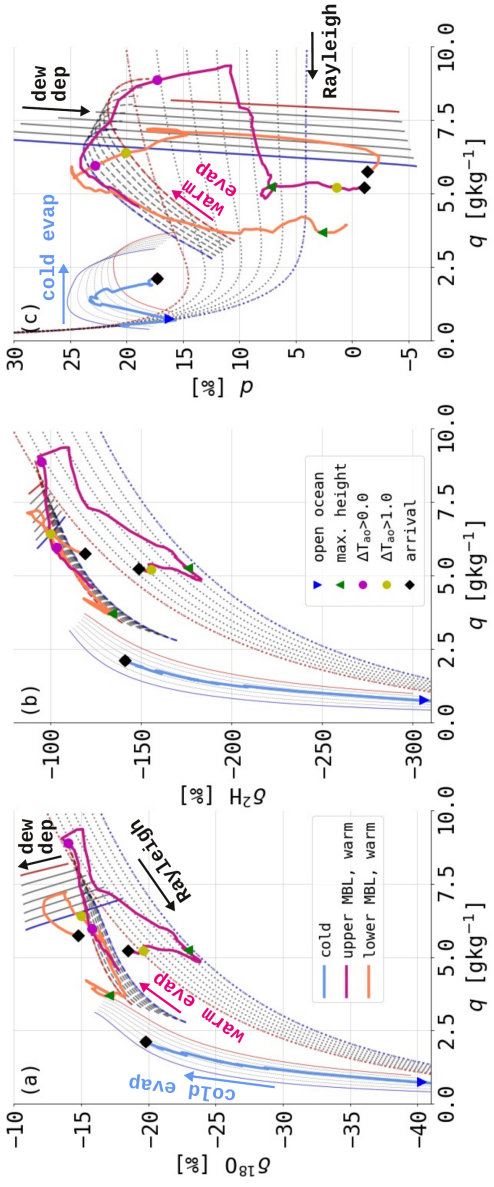Along the upper MBL trajectory (violet trajectory in Fig. 4.22c), a decrease

Figure 4.22: (Next page.)

*Figure 4.22: Phase-space diagrams of q versus **(a)** $\delta^{18}O$, **(b)** $\delta^{2}H$ and **(c)** d along two 4-day backward trajectories started 50 m a.s.l. (orange line) and 900 m a.s.l (violet line) at 22 UTC 26 Dec 2016 during a warm advection event and one 4-day backward trajectory started 60 m a.s.l. (blue line) at 00 UTC 4 Feb 2017 during a cold advection event. Model output from single-process air parcel models are shown for a range of initial values. The black, thick solid lines show the evolution in the isotopic phase-space during dew deposition (dew dep), the dashed and thin solid lines during evaporation over warm (warm evap) and cold (cold evap) ocean temperatures, respectively, and the dotted lines during Rayleigh fractionation (Rayleigh). For details on the model setups, see Appendix Table B.1 and text. Coloured markers denote specific events along the trajectories: when the air-sea temperature gradient along the trajectory increased above 0.0 °C (violet dots) and above 1.0 °C (yellow dots), the time of arrival at the measurement site (black diamond), the last maximum in height before arrival (green triangle) and the time of moving over open ocean (blue triangle). Different coloured model outputs denote the minimum (blue) and maximum initial SST (red) used for the various model runs, except for the moist adiabatic ascent model, where the coloured lines denote increasing initial d from blue to red in the model runs. The arrows in **(a)** and **(c)** denote the direction of the runs for each model.*

in d is seen while q is increasing to its maximum value of $9.4\,\mathrm{g\,kg^{-1}}$. This decrease follows a similar path as the ocean evaporation model, but experiences a stronger decrease in d. The different behaviour of d in the ocean evaporation model runs and along the trajectories might be due to further processes affecting the isotopic composition of the air masses, e.g. mixing with other air masses, or a different magnitude of moisture uptake along the trajectory compared to the air-parcel model runs. The dew deposition model (solid, thick lines) can simulate the isotopic composition

of the lower MBL trajectory (orange trajectory after yellow point). During
dew deposition, d decreases strongly while δ^2H and $\delta^{18}O$ increase for a
few hours. A similar evolution due to dew deposition is not seen for the
upper MBL during the warm temperature advection. In contrast, a weak
decrease in d accompanied by a strong decrease in $\delta^{18}O$, δ^2H and q is
seen for the upper MBL trajectory after the strong decrease in d during
ocean evaporation. This path follows the SWI evolution during a moist
adiabatic ascent during which cloud formation occurs (dotted lines). This
comparison of model outputs and single trajectories in an isotope phase-
space shows that the single-process models can explain the SWI evolution
along single COSMO$_{iso}$ trajectories. Furthermore, the dominant processes
driving the SWI composition along trajectories arriving in the warm and
cold sector of extratropical cyclones as described in the previous sections
are confirmed by the process models.

For the last few hours before arrival of the warm sector trajectories, nei-
ther process model can describe the SWI-evolution along the trajectories.
There is an increase in d with a simultaneous decrease in $\delta^{18}O$ and δ^2H for
the lower MBL in the warm sector after the trajectory reached its minimum
d of $-2.4\,‰$. For the upper MBL trajectory, d decreases strongly after the
trajectory reached the maximum height (green triangle), while $\delta^{18}O$ and
δ^2H increase. A possible mechanism explaining this evolution is a contin-
uous mixing of air masses from the free troposphere (with relatively low
δ-values and high d) with MBL air masses (with relatively high δ-values
and low d). The δ-values of the lower and upper MBL trajectories in the
warm sector approach each other during the last time steps (Fig. 4.22a,b),
which can be interpreted as a mixing process of the lower and upper MBL.
The proposed dominant processes of the SWI evolution in the lower and
upper MBL as seen for two trajectories at 22 UTC 26 Dec 2016, is also
found in the bulk evolution of SWIs along trajectories in the lower and up-

per MBL at 22 UTC 26 Dec 2016 during *WP1* and at 20 UTC 27 Dec 2016
during *WP2* (Fig. 4.23). The trajectories of the lower MBL are defined
as trajectories with $d > 15\,‰$ 24 h before arrival, while trajectories in the
upper MBL have $d < 15\,‰$ 24 h before arrival. At 20 UTC 27 Dec 2016
more trajectories follow the pathway through the upper MBL than at 22
UTC 26 Dec 2016. Therefore, panels a, c and e in Fig. 4.23 are dominated
by trajectories from the first date, whereas panels b, d and f show mainly
trajectories from the latter date. The movement of the trajectories into the
MBL and the warm sector are indicated by differently coloured dots in Fig.
4.23. The trajectories in the lower MBL first enter the MBL (green dots in
panel e), and enter the warm secor afterwards (yellow dots) before arrival
(black squares). For the upper MBL, the different markers are less clearly
separated. Panel f shows that most trajectories first enter an environment
with

*Figure 4.23: Phase-space diagrams of q versus **(a,b)** $\delta^{18}O$, **(c,d)** δ^2H and
(e,f) d along 4-day backward trajectories at 22 UTC 26 Dec 2016 and at
20 UTC 27 Dec 2016 following a pathway in the lower MBL **(a,c,e)** and the
upper MBL **(b,d,f)** shown as dots, which represent hourly time steps along
the trajectories, coloured by ocean evaporation. The black solid lines
show the evolution in the isotopic phase-space during dew deposition, the
dashed lines during ocean evaporation and the dotted lines during Rayleigh
fractionation using the single-process air parcel models. For details on the
model setups, see Appendix Table B.1. Coloured markers denote specific
events along the trajectories: when the air-sea temperature gradient along
the trajectory increased above $0.0\,°C$ (violet dots) and above $1.0\,°C$ (yellow
dots) for the last time before arrival, respectively, the time of arrival at the
measurement site (black diamond), and the time of entrance into the MBL
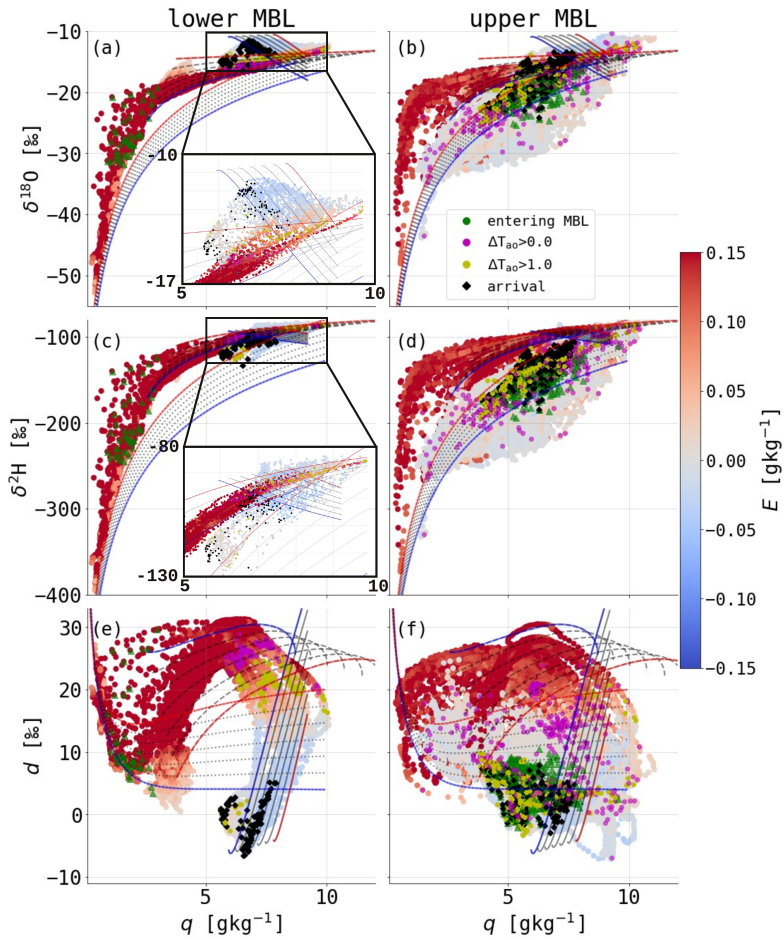(green dots).*

Figure 4.23: (Previous page.)

higher air temperature than SST (violet dots) before they enter the MBL and the warm sector before arrival (all other dots). Model runs of the different air-parcel models overlay the trajectories and help to identify the dominant processes affecting the isotopic composition of the air masses at different stages during the transport. In the lower MBL (Fig. 4.23a,c,e), the trajectories follow the evaporation model evolution until the trajectories enter the warm sector. Subsequently, they follow a path according to the dew deposition model. This is well visible by the clearly separated "point clouds" in Fig. 4.23a,c,e. After the trajectories enter the MBL (green dots), d, δ^{18}O and δ^2H increase while following the evaporation model until they enter a regime with higher air temperature than SST (violet dots). d starts decreasing while q still increases until $\Delta T_{ao} > 1.0\,°C$ (yellow dots), when q starts to decrease with still decreasing d and increasing δ^{18}O (see small window in panel Fig. 4.23a) following the dew deposition model. The arrival point of the trajectories (black dots) lies at the lower end of the dew deposition model. For the upper MBL, the trajectories first follow the evaporation model and some trajectories subsequently experience dew deposition (light blue coloured dots in panels b, d and f). In contrast to the lower MBL, many trajectories experience ascent during which cloud formation affects the isotopic composition of the air parcel. This can be seen in panel f, where a separation of the dots with $\Delta T_{ao} > 0.0\,°C$ (purple) and the remaining dots is visible. The latter are left of the dots marking $\Delta T_{ao} > 0.0\,°C$. In between these dots, the air parcels experience a decrease in q and d. Furthermore, there is no increase in δ^{18}O during this period, but the trajectories rather follow the moist adiabatic ascent (see greyish dots in panels b and d). Therefore, most of the trajectories in the upper MBL experienced cloud formation during a moist adiabatic ascent accompanied by a decrease in d.

The bulk SWI-evolution during two periods in the warm sector follows

unique paths in the isotope phase-space diagram, which represent specific processes such as ocean evaporation, dew deposition and moist adiabatic ascent. The simplified physical frameworks used for the single-process air-parcel models can describe the effect of isotopic fractionation on atmospheric water vapour during these processes.

4.7 Conclusions

An objective identification method for cold and warm temperature advection, based on the air-sea temperature difference is applied on a three-month ship-based measurement dataset in combination with numerical model simulations with the isotope-enabled numerical weather prediction model COSMO$_{\text{iso}}$. The cold and warm sectors of extratropical cyclones are shown to be associated with contrasting isotopic signals in the marine boundary layer. Composite analysis and case studies of cold and warm temperature advection are used to identify the driving processes of the observed variability of the isotopic signal in marine boundary layer water vapour. Negative (positive) δ^{18}O- and δ^{2}H-anomalies and positive (negative) d-anomalies are associated with positive (negative) ocean evaporation induced by the meridional transport of air masses in the cold and warm sector of extratropical cyclones.

For cold advection events, the moisture uptake along the backward trajectories occurs on average 37 hours before arrival at the measurement site. This moisture originates from ocean evaporation within the cold sector, which is the main process shaping the isotopic composition of the measured water vapour. The influence of ocean evaporation is confined to a relatively deep marine boundary layer leading to a strong gradient in the isotopic composition of water vapour between the freshly evaporated water vapour and the free troposphere at the marine boundary layer top.

Processes shaping the water vapour isotopic composition during warm advection are more diverse. On average, the air masses enter the warm sector 18 hours before arrival, which generally occurs after the major part of the moisture uptake. Within the warm sector, the air masses encounter a net loss of moisture due to two main processes leading to the characteristic isotopic signals associated with the warm sector of extratropical cyclones. First, air-sea interaction in the form of dew deposition leads to a negative d anomaly and positive $\delta^{18}O$ and δ^2H anomalies. Second, the formation of clouds in ascending air masses leads to low d in water vapour due to the temperature-dependency of the isotopic equilibrium fractionation occurring in clouds. Negative d in the lower marine boundary layer is mainly shaped by local processes such as dew deposition and cloud formation while the upper marine boundary layer can be influenced by upstream decreasing ocean evaporation, dew deposition and cloud formation several hundred km away. In the warm as well as the cold sector, negative vertical d-gradients were seen in COSMO$_{\text{iso}}$ simulations. Such gradients have been observed in measurements of stable water isotopes in water vapour in the marine boundary layer (Sodemann et al., 2017; Salmon et al., 2019). The results of this study show that negative d anomalies and negative d-gradients in the upper marine boundary layer can be caused by upstream processes and that the d-variability in extratropical cyclones is strongly shaped by the large-scale flow. Therefore, simultaneous anomalies in $\delta^{18}O$, δ^2H and d in marine boundary layer water vapour can be used to identify moist processes experienced by air masses during their transport in extratropical cyclones.

The specific SWI-evolution and strength of changes in the SWI composition of water vapour due to different moist processes have been simulated using single-process air parcel models of dew deposition, ocean evaporation across a meridional SST gradient and Rayleigh fractionation during a

moist adiabatic ascent. These simple process models adequately simulate the SWI-evolution along $COSMO_{iso}$ backward trajectories and confirm the main processes identified in the case studies of cold and warm temperature advection in Southern Ocean extratropical cyclones. Furthermore, these simple single-process models give an estimate of the induced changes in d by different processes. The strongest changes in water vapour d are caused by air-sea moisture fluxes such as the decrease in ocean evaporation during the movement across a meridional SST gradient and dew deposition. Rayleigh fractionation during moist adiabatic ascent can lead to a decrease in water vapour d an order of a magnitude smaller than dew deposition.

The presented observational and modelling datasets are valuable for further analysis of marine boundary layer moisture cycling under the influence of large-scale flow patterns. For example, to quantify the contribution of single processes to the SWI variability in the cold and warm sector or by assessing the lifetime of negative d in the marine boundary layer of the warm sector.

Chapter 5

Conlusions and Outlook

SWIs are passive tracers of moist processes in the atmosphere. The isotopic composition of MBL water vapour records the history of air masses in the MBL and helps in constraining the MBL water budget. In this thesis, ship-based SWI measurements of water vapour from the Atlantic and Southern Ocean were collected to investigate the SWI variability in the marine boundary layer and to study how the SWI variability is driven by the large-scale atmospheric flow. This five-month, high-resolution dataset of SWIs in water vapour provides unique insight into the SWI variability of water vapour in the Southern Ocean and into moist processes on various spatial and temporal scales. Additionally to the SWI measurements, model simulations were conducted using the isotope-enabled numerical weather prediction model COSMO$_{\mathrm{iso}}$ and single-process air parcel models. In this chapter, the conclusions and implications from this thesis for future research are summarised and discussed.

5.1   Ship-based SWI measurements and calibration

The main dataset of this thesis are the five-month ship-based measurements of SWIs in water vapour during the Antarctic Circumnavigation Expedition, which were performed using a cavity ring-down laser spectrometer. As discussed in Chapter 2 and Appendix A.1, ship-based SWI measurements raise several challenges and require careful calibration.

Sea spray can enter the inlet line and evaporate. This leads to a bias in the measurements depending on how much sea spray is introduced into the inlet line. To prevent such contamination, a three-layered inlet was designed specifically for ACE, which successfully prevented sea spray from entering the inlet line. Nonetheless, the influence of sea spray on the measurements and the production of sea spray by the ship's movement is difficult to assess. As shown in Chapter 2, one way of identifying situations of strong sea spray influence are parallel SWI measurements on the research vessel at different heights. The SWI differences between the lower and higher inlet position are enhanced during increased sea spray production and evaporation (see Sec. 2.4.2.1). The qualitative analysis of vertical SWI differences presented in this thesis can be extended in future studies by measuring SWIs as well as further parameters such as sea spray concentration, specific humidity, and air temperature at several heights above sea level under different wind forcing situations. Such a setup could, on the one hand, increase our understanding of the contribution of sea spray evaporation to the MBL moisture budget, and on the other hand, give insight into the vertical SWI gradients in the near-surface MBL. For a systematic analysis of sea spray production and evaporation and its influence on the isotopic composition in the MBL, laboratory experiments using a water tank in a wind channel or a bubble tank could be conducted. The simultaneous

measurements of other chemical substances could further help to better understand biogeochemical cycling of these substance and their linkage to the atmospheric water cycle.

The calibration procedure of SWI measurements using a cavity ring-down laser spectrometer involves several steps, which contribute differently to the final uncertainty of the calibrated SWI time series. A detailed sensitivity analysis showed that the largest uncertainty is introduced by the isotope-humidity correction, which makes up approximately 50% of the total calibration uncertainty. This is in agreement with several previous studies, which showed that a detailed humidity-dependency correction is crucial for high quality laser spectrometric measurements (e.g. Sturm and Knohl, 2010; Aemisegger et al., 2012; Bailey et al., 2015). This uncertainty is minimised by choosing a fit for the isotope humidity correction curves, which represents the isotope-humidity dependency well. Due to the different responses of different instruments, this fit has to be re-examined regularly for each instrument.

Recently is has been shown that the strength of the isotope-humidity dependency of laser spectrometers changes with different isotopic composition of the measured standard water (Bonne et al., 2019; Weng et al., 2020). We showed that this isotope dependency of the isotope-humidity dependency varies with the flow rate of the instrument (see Appendix A.1.1.2). With an increased flow rate, the isotope dependency decreases and lies within the uncertainty of the measurements. This has implications for a potential correction of the isotope dependency and generally supports the usage of a high flow rate through the instrument to minimise memory and response times.

The interpretation of SWI measurements relies on simultaneous environmental measurements. The broad-ranging instrumentation used during ACE included a micro rain radar, frequent radiosonde launches and a me-

teorological measurement station. Furthermore, detailed chemical mea-
surements of the atmosphere were conducted by other projects. Even
though a long catalogue of measurements is available for ACE, some fur-
ther measurements would be useful in future campaigns. For the calibration
of snow measurements with the micro rain radar, detailed knowledge of
the snow size and shape is needed. Therefore, disdrometer measurements
would help to better characterise snow size and snow fall rate. For the
analysis of the effect of strong ocean evaporation on the isotopic composi-
tion of the surface ocean, high precision measurements of δ^{18}O and δ^2H
of ocean water samples are needed to achieve a high-quality time series of
d in ocean water.

5.2   Meridional variations

The SWI measurements from ACE were used to analyse the SWI vari-
ability and its drivers under different climatic conditions (Chapter 2). It
was found that the median meridional distributions of SWIs in the MBL
water vapour are shaped by the environmental conditions at the measure-
ment and moisture source sites, such as air temperature, specific humidity
and relative humidity with respect to saturation at SST. In contrast, the
synoptic-timescale variability of SWIs in water vapour at a given latitude
is driven by the variability in moisture source regions and the frequency
of extratropical cyclones and anticyclones. Therefore, variations of SWIs
in water vapour at a given location depend on the large-scale flow setting.
The identified meridional SWI variations in water vapour are similar to
the observed meridional SWI variations in precipitation reported in pre-
vious studies (Rozanski et al., 1992; Araguás-Araguás et al., 2000; Feng
et al., 2009). An influence of the large-scale atmospheric flow on the SWI
variability of precipitation, as observed for water vapour in this study, has

been seen for Reykjavik (Aemisegger, 2018), where the SWI variability in precipitation is related to the position and intensity of the North Atlantic storm track. How the measured SWI variability in water vapour translates into the isotopic signal of precipitation has still to be investigated further. Analysing the SWI variability in precipitation and the dominant large-scale flow patterns at various locations and, if possible, including SWI measurements of water vapour, could help to improve our understanding of how the large-scale atmospheric flow influences the isotopic composition of precipitation at a given location.

5.3 Vertical variations

With simultaneous measurements of SWIs in water vapour at two different heights above the ocean surface during ACE, the SWI variability at different locations on a research vessel was assessed (Chapter 2). The SWI vertical differences showed a wind dependency with large vertical differences at very high wind speeds due to sea spray evaporation. At low wind speed, enhanced vertical gradients were observed, which might be caused by decreased turbulent mixing in the MBL. For logistic reason, it was not possible to have an instrument comparison or a humidity calibration of the measurements at the lower heights. For future studies, such measurements are possible with a relatively small effort and should be done to have better constraints for assessing near ocean surface vertical moisture gradients. Due to the limitations of the experimental setup in this study with only two measurements at different heights, a thorough uncertainty estimation of the calibration procedure was performed, showing that to the best of our knowledge the calibration uncertainty cannot explain the observed vertical differences between the measurements. The qualitative assessment of the

wind dependency of vertical SWI gradients done here could be extended by studying the dependency of non-equilibrium fractionation on the wind speed. This could be achieved by several approaches. The importance of turbulent versus diffusive transport and their impact on the non-equilibrium fractionation can be assessed. Studies looking at this factor in detail relied on few measurement data points from specific regions (e.g. the Mediterranean in Pfahl and Wernli, 2009) or reanalysis data in combination with monthly SWI observations (Aemisegger and Sjolte, 2018). The large SWI dataset from ACE could, thus, give further insights into the turbulent and diffusive transport during ocean evaporation and their effect on the SWI composition in the MBL. Furthermore, the vertical SWI differences in the tropics have not been studied in detail and might reveal further processes influencing the near-surface SWI gradient. Last but not least, measurement of vertical SWI gradients using more than two measurement points and by including measurements of the water vapour mixing ratio, air temperature and wind speed can give further insight into the near-surface vertical SWI gradients in different large-scale forcing situations.

5.4   SWIs in the cold and warm sectors of extratropical cyclones

Air-sea interactions and their influence on the SWI composition of MBL water vapour had been assessed using the ACE measurements together with single-process air parcel models and COSMO$_{\mathrm{iso}}$ simulations (Chapter 4). Cold and warm advection was identified with an objective identification scheme. Using ERA-Interim reanalysis data and the ACE measurements, a Southern Ocean climatology of cold and warm advection was derived and cold and warm advection events during ACE were identified, respectively.

The cold and warm temperature advection events in the Southern Ocean mostly occur in the cold and warm sector of extratropical cyclones, respectively. Contrasting air-sea moisture fluxes are found in the warm and cold sectors of extratropical cyclones, which affect the SWI composition in the MBL. In the cold sector, positive d and negative $\delta^{18}O$ and δ^2H anomalies are observed together with positive ocean evaporation, while in the warm sector, negative d and positive $\delta^{18}O$ and δ^2H anomalies occur simultaneous with dew deposition. Using seven-day backward trajectories based on the 3D wind fields from COSMO$_{iso}$ simulations, it was shown that the cold sector is strongly influenced by ocean evaporation within the cold sector, which dominates the isotopic signal of the MBL. In the warm sector, moisture uptake along the trajectories occurs before they enter the warm sector and the isotopic signal from ocean evaporation is strongly modified by dew deposition on the ocean surface and cloud formation, that can lead to low or even negative d in water vapour.

The COSMO$_{iso}$ simulations showed that negative d signals in the MBL can be transported over hundreds of kilometres. This implies that for a detailed understanding of the driving processes of the SWI variability in the MBL and vertical SWI gradients, the Lagrangian history of the air masses has to be taken into account. The strength of the Lagrangian perspective to understand the effects of complex physical processes on the atmospheric flow has also been demonstrated by previous studies from a non-isotopic point of view (e.g. Crezee et al., 2017; Spreitzer et al., 2019; Attinger et al., 2019). The lifetime of negative d has not been assessed in this study. The COSMO$_{iso}$ dataset generated in this study can be used to investigate how far negative d is transported in the MBL and if negative d from dew deposition can be transported to higher levels and potentially impact the vertical MBL d gradient.

Effects from below-cloud evaporation have not been investigated in the case

study, but could be of importance in other cases. The dataset used here provides the opportunity to study the evolution of SWIs along trajectories in various meteorological situations and to investigate how the isotopic composition of hydrometeors depends on the frequency of cold and warm temperature advection in future studies.

5.5 Modelling the isotopic composition of the marine boundary layer

5.6 Modelling the isotopic composition of the marine boundary layer

The comparison of SWI measurements in water vapour with COSMO$_{iso}$ simulations shows a good qualitative agreement between measurement and simulation in δ^{18}O, δ^2H and d (Chapter 4). A shift in d to too high values in the simulations might be caused by too low modelled specific humidity in the MBL. Several aspects of the COSMO$_{iso}$ simulations have not been studied in detail here. For example, sea ice in the model is defined by SST below $-1.6\,°C$ and its main impact on the atmosphere is to strongly reduce surface fluxes. There is no air-snow and air-ice interaction included over sea-ice and thus the isotopic composition is not influenced by these processes. As shown by Bonne et al. (2019), the isotopic composition of MBL water vapour in polar regions can be influenced by sublimation of (sea) ice or snow lying on the sea ice. Therefore, differences between modelled and measured SWIs close to Antarctica could be related to poorly represented air-sea-ice interactions in COSMO$_{iso}$. Similarly, TERRA$_{iso}$, the

land module of COSMO$_{iso}$, treats the snow cover with only one snow layer. Therefore, no memory of the vertical snow layering and its isotopic composition is incorporated. Jansing (2019) showed in a sensitivity experiment that SWIs in MBL water vapour agree better with the ACE measurements if isotopic fractionation during snow sublimation from the surface is implemented in TERRA$_{iso}$. Therefore, air-snow interaction can influence the isotopic composition of SWIs in water vapour over the Southern Ocean. The influence of snow sublimation and the isotopic composition of vertical snow layers in TERRA$_{iso}$ could be further investigated using the ACE dataset.

The single-process air parcel models introduced in Chapter 3 represent the Lagrangian evolution of the isotopic composition of MBL water vapour in a realistic way, when comparing them to COSMO$_{iso}$ SWI signals along backward trajectories for individual periods, during which the respective process from the single-process model dominates. A decrease in d as observed during warm advection events, can be induced by various processes in the MBL. First, the SST during ocean evaporation influences the ocean-atmosphere humidity gradient and moisture fluxes and, thus, influences the isotopic composition of the evaporative flux. A decrease in d can therefore be associated with decreased ocean evaporation at high h_s. Second, cloud formation during a moist adiabatic ascent can lower d due to the temperature dependency of equilibrium fractionation along with a strong decrease in q. Third, dew deposition on the ocean surface induces a strong decrease in d with a weaker decrease in q than seen during cloud formation. These different process behaviours in the d-q-phase space can be used to identify and quantify the effect of these processes on the SWI composition of air parcels. This analysis showed that negative d in measurements can have different origins and that the temporal evolution of d is linked to air-sea interaction as well as cloud formation. The Rayleigh distillation air parcel

model showed that the temperature dependency of equilibrium fractiona-
tion impacts the evolution of d in an air mass during cloud formation. It
has been proposed by previous studies (Sodemann et al., 2017; Salmon
et al., 2019) that evaporation of cloud and rain droplets above and below
the cloud can also lead to a negative d in the upper MBL. The mechanism
leading to low d layers is however not fully explained. The near-surface
SWI measurements from ACE do not provide detailed insight into moist
processes at the MBL top. Aircraft campaigns measuring SWIs in water
vapour such as during EUREC4A from Jan to Feb 2020 (Bony et al., 2017)
will be useful in the future to improve the understanding of negative d in the
upper MBL and how the different proposed mechanisms, that potentially
produce low or even negative d, interact.

The SWI evolution in single-process air parcel models showed good agree-
ment with the isotopic evolution along trajectories in COSMO$_{iso}$. As
COSMO$_{iso}$ uses similar assumptions on the isotopic fractionation as the
process models, a good agreement indicates that the Lagrangian SWI
evolution is occasionally dominated by individual processes and that the
final isotopic signature reflects the combined influence of these processes.
Assessing these Lagrangian single process models with measurements is
not straightforward as up- and downstream measurements of the same air
masses would be needed. Furthermore, the output of moisture tenden-
cies from model simulations, which report the processes responsible for
changes in the moisture budget at a given grid point, could be used. Also,
changes in isotopic composition in COSMO$_{iso}$ simulations could be as-
signed to the phase change processes causing the SWI changes and saved
in model outputs. Such studies would give more detailed information on
the processes affecting the isotopic composition in COSMO$_{iso}$. With these
moisture and isotopic tendencies, the main drivers of changes in SWIs in
COSMO$_{iso}$ could be identified and their relative contributions quantified

in the model.

5.7   Limitations of this study

The SWI measurements during ACE are affected by several limitations due to planning issues and unforeseeable parameters, such as the functioning of all instruments, software and material and the occurrence of specific weather situations. The coordination of the SWI measurements in water vapour by different ACE research projects was not planned in advance. This led to the missing instrument comparison and humidity calibration of some instruments and, thus, more uncertainties in the analysis of the vertical SWI differences. High specific humidity in the tropics affected the calibration of the SWI measurements due to unforeseeable power issues. The calibration of the laser spectrometer at ambient humidity was not possible due to the high specific humidity in the tropics and the isotopically depleted standard water often did not reach constant isotopic values during the calibration runs. Furthermore, the standard waters were too depleted for the calibration of the very enriched water vapour in the tropics and the bias correction had to be applied to values lying above the calibrated range of values. Therefore, the measurements in the tropics have higher uncertainties than measurements from the subtropic and extratropics. For security reasons, the research vessel avoided the center of extratropical cyclones and regions of high wind speeds if possible. Therefore, the measurements during ACE are biased towards low wind speeds.

$COSMO_{iso}$ has not been used for the simulation in polar regions so far. Several shortcomings in the representation of air-sea interactions and the parametrisation of isotopic fractionation during air-ice interaction are present as discussed in Sec. 5.6. $COSMO_{iso}$ simulations depend on the representation of the atmospheric flow and the isotopic composition of the

air masses in the initial and boundary data. Only few observations are available over Antarctica, which leads to high uncertainties in the boundary data and, thus, the regional COSMO$_{iso}$ simulations. Furthermore, the ERA-interim reanalysis data used for the simulation of ECHAM5-wiso data is the best knowledge we have of the state of the atmosphere, but does not necessarily represent the reality. The COSMO$_{iso}$ simulations showed biases towards too low specific humidity which led to a bias in the absolute strength of air-sea interactions and d. The Lagrangian analysis relies on the accuracy of the backward trajectories, which were calculated off-line based on hourly model outputs.

The air-parcel models are a selection of processes affecting the isotopic composition of the MBL. Further processes such as the mixing with other air masses and below-cloud effects are not considered in these models. The ocean evaporation model depends on many initial parameters. This leads to many degrees of freedom for choosing the initial values in this model. Furthermore, the ocean evaporation air-parcel model is relatively sensitive to the parametrisation of the moisture uptake. The Rayleigh fractionation air-parcel model neglects the exchange of cloud water and water vapour after cloud formation, which possibly affects the isotopic composition of water vapour derived from the Rayleigh fractionation air-parcel model.

For the interpretation of the SWI variability in the MBL, several aspects are not included in this study. The vertical gradients across the MBL and the MBL top studied in this thesis rely solely on model simulation and, thus, a measurement comparison is needed to confirm the findings. For the interpretation of the SWI measurements, many different measurements are used. Nonetheless, the full potential of some measurements, such as the micro rain radar and the radiosondes, has not been exhausted yet to better understand the effect of below-cloud processes and atmospheric stability, respectively, on the isotopic composition of the MBL. The ACE dataset

has not been directly compared to other ship-based SWI datasets in the
Atlantic (e.g. Benetti et al., 2017) and the Southern Ocean (e.g. Uemura
et al., 2008), which could help to assess the SWI variability observed
during ACE.

5.8   Final remarks

This thesis shows how the high spatial and temporal resolution of the ship-
based SWI measurements in water vapour in combination with a range of
modelling tools spanning from simple theoretical models to sophisticated
numerical weather prediction models, allows for a detailed identification of
the driving processes of SWI variability in the MBL. The detailed knowl-
edge of the processes leading to the observed distribution of isotopes in the
water cycle in the extratropics and polar regions gained by such SWI mea-
surements should be used to improve our knowledge of moist processes in
the atmosphere. The advantage of SWI measurements compared to other
measurements is that they enable detailed inference of physical processes
from a few measured variables. This benefit should be utilised to improve
the understanding of other atmospheric measurements and to better char-
acterise how the atmospheric flow shapes the cycling of other substances
in the atmosphere. This could lead to a more detailed understanding of
biogeochemical cycles and their connection to the atmospheric water cycle
by applying the learnings from SWI meteorology.

Appendix A

Appendix material to Chapter 2

Table A.1: Calibration versions of SWI-13 and SWI-8-ps used in this study. The following isotope-humidity dependency correction functions are used in the calibration versions: $\mathcal{H}_c$ applies a constant factor of 0 as correction term (i.e. no isotope-humidity dependency correction is used). $\mathcal{H}_{1,\min}$ and $\mathcal{H}_{1,\max}$ are the best fit correction curves to the SWI-13 calibration runs -/+ 1 standard deviation to estimate the uncertainty of the best fit ($\mathcal{H}_1$) to the calibration runs. Accordingly, $\mathcal{H}_{3,\min}$, $\mathcal{H}_{3,\max}$ and $\mathcal{H}_3$ are defined for SWI-8. $\mathcal{H}_2$ is the correction curve from Sodemann et al. (2017). The running mean/average column specifies the handling of the times in between calibration runs: run *refers to 10-day running means used for the calibration runs. For* ave*, the calibration runs of each standard are averaged for each legs and this average value is used for the calibration of the corresponding leg. Version 1 for each dataset (SWI-13 and SWI-8-ps) is the final version used in Section 2.4.*

Version	isotope-humidity correction	running mean / average
	SWI-13	
1	$\mathcal{H}_1$	run
2	$\mathcal{H}_c$	run
3	$\mathcal{H}_{1,\min}$	run
4	$\mathcal{H}_{1,\max}$	run
5	$\mathcal{H}_1$	ave
6	$\mathcal{H}_2$	run
	SWI-8-ps	
1	$\mathcal{H}_3$	run
2	$\mathcal{H}_c$	run
3	$\mathcal{H}_{3,\min}$	run
4	$\mathcal{H}_{3,\max}$	run
5	$\mathcal{H}_3$	ave

Table A.2: Vertical SWI gradients for the three wind regimes for legs 1-3: [I] low wind speed $< 6\,m\,s^{-1}$, [II] intermediate wind speed between $6\,m\,s^{-1}$ and $16\,m\,s^{-1}$, [III] high wind speed $> 16\,m\,s^{-1}$. The gradients are given in $\permil\,m^{-1}$. In brackets, the 65 % percentile ranges are noted.

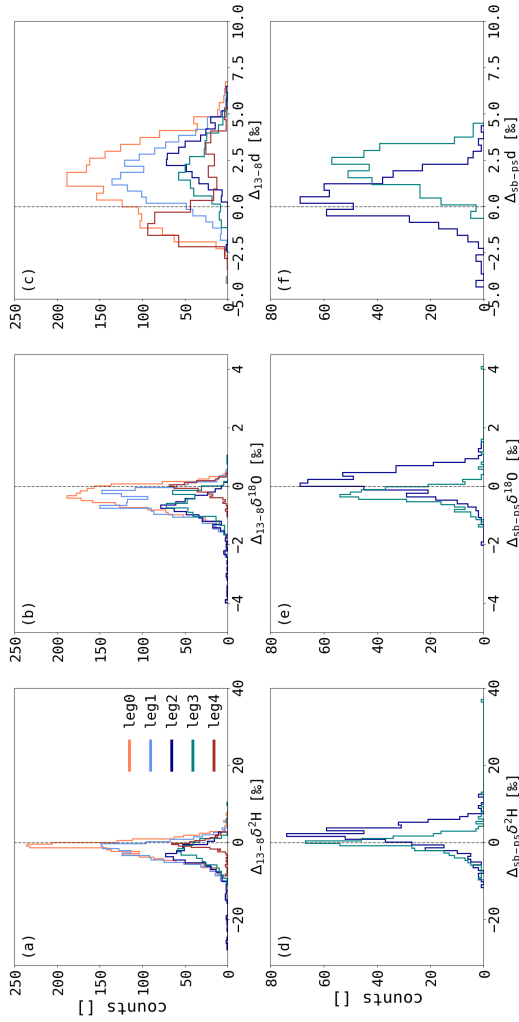| Regime	$\Delta_{13-8}\delta^2H$	$\Delta_{13-8}\delta^{18}O$	$\Delta_{13-8}d$
I-III	$-0.5\,[-0.9\ldots0.0]$	$-0.10\,[-0.16\ldots-0.02]$	$0.3\,[0.1\ldots0.6]$
I	$-0.6\,[-1.0\ldots-0.2]$	$-0.12\,[-0.18\ldots-0.06]$	$0.4\,[0.2\ldots0.6]$
II	$-0.4\,[-0.8\ldots0.0]$	$-0.09\,[-0.15\ldots-0.01]$	$0.3\,[0.1\ldots0.5]$
III	$-1.0\,[-1.5\ldots-0.2]$	$-0.16\,[-0.26\ldots-0.03]$	$0.3\,[0.0\ldots0.6]$

Figure A.1: Histograms of difference between SWI-13 and SWI-8-ps (**a-c**) and SWI-8-sb and SWI-8-ps (**d-f**) for $\delta^2 H$, $\delta^{18} O$ and d. The histograms are coloured by legs. SWI-8-sb is only available for legs 2 and 3.
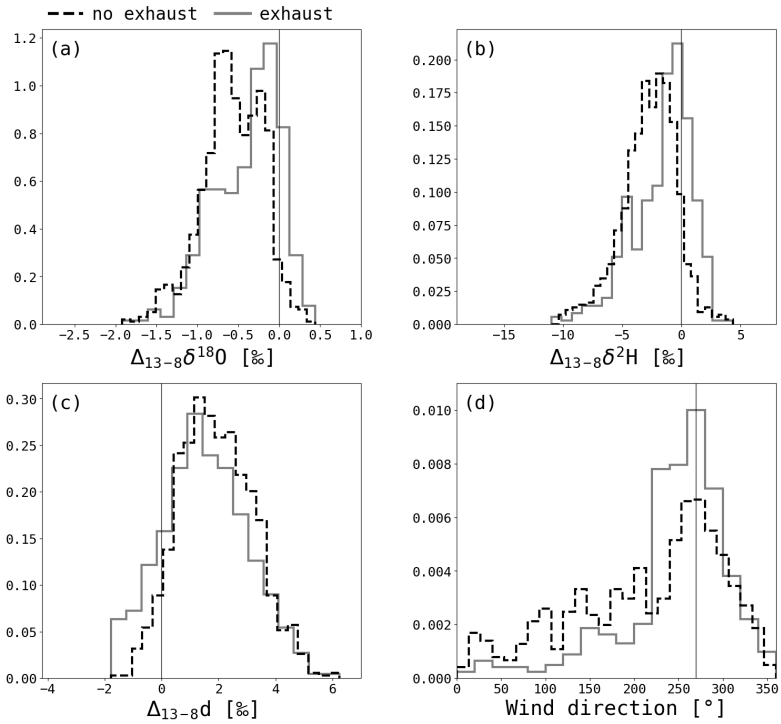
*Figure A.2: Normalized histograms showing distribution of difference between SWI-13 and SWI-8-ps (Δ_{13-8}) for $\delta^{18}O$ **(a)**, δ^2H **(b)**, and d **(c)** and distribution of absolute wind direction **(d)** for periods without [black, dashed line] and with [grey, solid line] exhaust influence. Westerly wind direction is marked in **(d)** with a thin black line at 270°.*
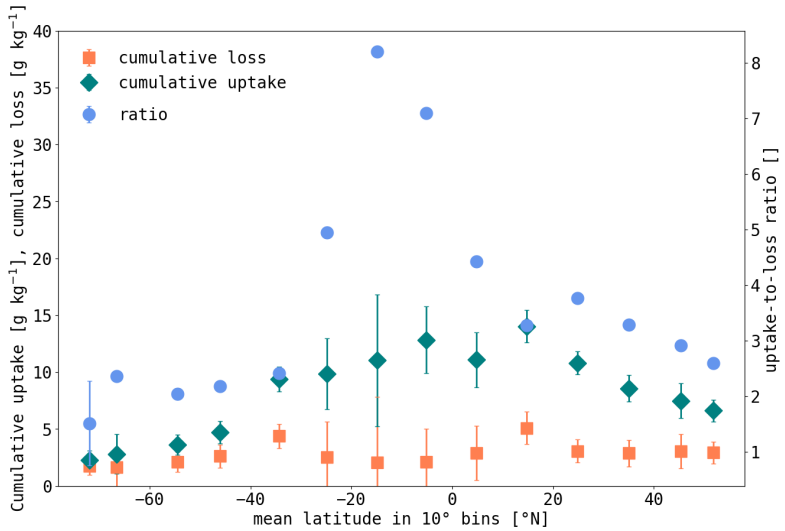
Figure A.3: Meridional variations of uptake-to-loss ratio (blue circles, []), cumulative loss (orange squares, $[g\,kg^{-1}]$) and cumulative uptake (green diamonds, $[g\,kg^{-1}]$) over the 5 days prior to arrival at the measurement locations along backward trajectories for legs 0-4. On the x-axis, the mean latitude of the 10° bins is shown.

A.1 Stable water isotope measurement

In the following, the calibration protocol including the isotope-humidity dependency of the two SWI time series SWI-13 and SWI-8 are documented in detail.

A.1.1 SWI-13

A.1.1.1 Calibration protocol

The L2130-i raw measurements were calibrated using the SDM calibration runs to correct for the humidity dependent isotope bias and the drift of the instrument during the cruise using a similar procedure as described in Aemisegger et al. (2012). Calibration runs with two liquid standards (MP $[-11.42\,‰,\ -82.05\,‰]$ and GRIP $[-34.59\,‰,\ -267.22\,‰]$, for $[\delta^2H, \delta^{18}O]$, respectively) were performed. Ambient air was dried by pumping it through a replaceable 5 Å molecular sieve with indicating drierite (Agilent, volume of $400\,cm^3$) and used as carrier gas in the calibration system. The residual humidity in the system after 5 min was 50-100 ppmv for dry runs in the laboratory and is expected to be 200-300 ppmv in the tropics at high ambient humidity. The two standards were sampled approximately every second week. The liquid sample analysis for $\delta^{18}O$ and δ^2H performed according to routine procedures at FARLAB (UiB) showed that the variations in the liquid standards during the cruise are smaller than the standard deviation of the SDM calibration runs.

The two liquid standards were measured once per day at different hours of the day for 15 min at a mixing ratio of 12'000 ppmv. Calibration runs had to fulfil three criteria during a time window of 5 min: 1) the standard deviation of the 1 Hz signals of δ^2H and $\delta^{18}O$ is below 1.0 ‰ and 0.3 ‰, respectively, 2) the relative standard deviation of the water vapour mixing

ratio w is $\leq 5\,\%$, and 3) no significant trend in δ^2H occurs in the 5 min time window. A total of 225 successful calibration runs were conducted during ACE. There are successful calibration runs available at least every second/third day for MP/GRIP, respectively, except for leg 0 and one occasion each during legs 1 and 2 (see also supplementary Fig. S2). For each successful calibration run, the mean values used for calibration of the raw data were calculated for the last 5 min window that fulfils the above criteria to minimise memory effects. The data post-processing procedure adopted for SWI-13 includes the following three steps:

1) Humidity dependent isotope bias correction: Isotope measurements using laser spectroscopy show a bias that depends on the humidity of the measured air sample [referred to as isotope-humidity dependency (e.g. Schmidt et al., 2010; Aemisegger et al., 2012; Steen-Larsen et al., 2013)]. The isotopic composition of known standards at different mixing ratios was measured in the lab after ACE. The raw δ^{18}O and δ^2H time series were corrected with the isotope-humidity dependency correction terms $\mathcal{H}_{\delta^{18}O}$ and $\mathcal{H}_{\delta^2 H}$, respectively, which are the best fit curves using the method of least squares to the measured standard samples (see also Section A.1.1.2). The uncertainty of the correction curve is estimated with fitted curves to the measurements ± 1 standard deviation. In this study, we observe a slightly stronger isotope-humidity dependency for very low humidity compared to the isotope-humidity correction curve presented in the study by Sodemann et al. (2017), which characterised the same instrument during a campaign in 2013. All measurements below 12'000 ppmv were corrected for the isotope-humidity dependency. Above 12'000 ppmv, the effect was considered negligible.

2) Drift correction: The humidity-corrected SWI time series was then further post-processed to account for the instrument's drift using a two-point slope correction and normalisation to VSMOW2-SLAP2 according to the

IAEA recommendations. A 10-day running mean of the calibration runs was calculated to correct each measurement point using the corresponding running mean standard values. If the isotope-humidity dependency corrected δ^2H was larger than the value of the MP standard, the slope correction was done using a mean over all calibration runs of the corresponding leg for each standard. This was done because successful calibrations with GRIP were rare in the tropics during ACE due to problems with the SDM syringe pump. Because the instrument's drift is small during ACE, a mean value of the calibration runs for each leg should adequately approximate the standard value. In total, 17% of all data are corrected using a mean standard value over the whole leg, which affects the tropics and subtropics on legs 0 and 4 and the measurements close to South Africa on legs 1 and 3.

2) Water vapour mixing ratio: For the calibration of the water vapour mixing ratio with a dew point generator (LI-COR LI 610), the following correction curve was derived using linear interpolation between w_{raw} as measured by the L2130-i system and expected w from the regulated dew point of the LI-COR:

$w_{cal} = a \cdot w_{raw} + b$ with $a = 0.734$ and $b = -1102.37$ ppmv.

A.1.1.2 Isotope-humidity correction curves

The isotope-humidity correction curves were derived using least-square fits to the standard measurements at different water vapour mixing ratio using L2130-i with an SDM. L2130-i has two operational modes: a normal mode with a flow rate of $50\,\text{m}\ell\,\text{min}^{-1}$ and a flight mode, which has an increased flow rate of $300\,\text{m}\ell\,\text{min}^{-1}$. The isotope-humidity dependency shows different properties for the two operational modes of L2130-i. At normal mode flow rate, the isotope-humidity correction curve depends
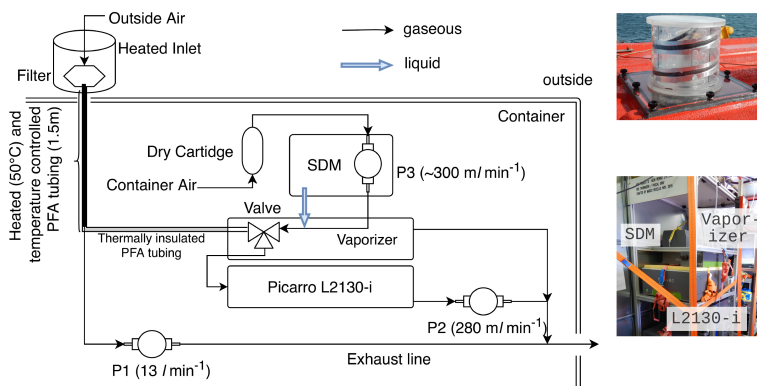
Figure A.4: Flow diagramm of measurement setup of SWI-13. SDM is the standard delivery module from Picarro. P1 and P2 are KNF pumps for L2130-i and for flushing the inlet, respectively. P3 is the internal pump of the SDM. The top right photograph shows the heated, 3-layered inlet which was mounted on the container. The bottom right photograph shows the measurement tower in the container with the SDM, the vaporizer and L2130-i.

on the isotopic composition of the standard sample (supplementary Fig.
A.8b). For more depleted standard compositions, larger deviations from
the reference isotopic composition are recorded at low humidities, whereas
the deviations nearly vanish for the most enriched standard composition
(MP: [-11.42 ‰, -82.05 ‰], for [δ^2H, δ^{18}O], respectively). This isotope-
dependency of the isotope-humidity correction curve is only seen for δ^2H
in normal flow mode. An isotope-dependency of the isotope-humidity
correction curve was also reported by Bonne et al. (2019) for δ^2H (see
supplementary figure 1 in their publication). In flight mode, the isotope-
dependency is negligible as the isotope-humidity correction curves vary
within the standard deviation of the measurements. The cause of these
different isotope-humidity dependency properties for different operational
modes of L2130-i is not evident. There could be several causes such
as memory effects in the tubings and cavity of the laser spectrometer or
background effects due to the chemical composition of the dry air used for
the calibration runs (Aemisegger et al., 2012; Johnson and Rella, 2017).
For the calibration of the ACE SWI-13 data, the isotope-dependency of
the isotope-humidity correction curves is neglected because the instrument
was operated in flight mode. The following isotope-humidity correction
curves ($\mathcal{H}_1$ in supplementary Fig. A.7) were used for SWI-13:

$$\delta^{18}O_{corr} = \delta^{18}O_{raw} + \mathcal{H}_{\delta^{18}O}(w_{raw}) \tag{A.1}$$

$$\text{with } \mathcal{H}_{\delta^{18}O}(w_{raw}) = -a(w_{raw}^b - 12000^b), \tag{A.2}$$

$$\delta^2H_{corr} = \delta^2H_{raw} + \mathcal{H}_{\delta^2H}(w_{raw}) \tag{A.3}$$

$$\text{with } \mathcal{H}_{\delta^2H}(w_{raw}) = -c(w_{raw}^d - 12000^d) \tag{A.4}$$

where w_{raw} is the uncalibrated water vapour mixing ratio in ppmv and
$a = 1.369\text{e}+04$, $b = -1.078$, $c = 5.033\text{e}+04$ and $d = -1.156$.

A.1.2   SWI-8

A.1.2.1   Calibration protocol

For the calibration of SWI-8, calibration runs were conducted with three liquid standards (Bermuda $[-0.25\,‰, 2.1\,‰]$, NEEM $[-33.5\,‰, 257.1\,‰]$ and CPH MilliQ $[-8.9\,‰, -61.7\,‰]$ for $[\delta^2 H, \delta^{18} O]$, respectively). The main standard was CPH MilliQ which was used for the instrument drift calibration. Samples of CPH MilliQ were collected every two weeks to check for possible storage effects. Sample analysis after the expedition showed that the variation of the isotopic composition of the standard samples did not exceed the instrument's precision. Ambient air was dried by pumping it through a drierite (Agilent) drying unit and used as carrier gas in the calibration systems. Calibrations were started when the humidity in the cavity was less than 200 ppmv.

The laser spectrometers were calibrated once a day with two alternating types of calibration: (1) Instrument's drift calibration was performed by measuring each of the three standards for 30 min at a mixing ratio of 15000 ppmv. For further calculations, we used the results of the last 10 min to avoid memory effects. (2) For the isotope-humidity dependency correction, we measured the CPH MilliQ standard at different humidities from 3000 to 30000 ppmv. At every level the standard was measured for 12 min, from which we took only the last 10 min for further calculations. Best fits using the method of least squares are applied to these calibration runs to correct for the isotope-humidity dependency of the SWI. The following isotope-humidity corrections ($\mathcal{H}_3$ and $\mathcal{H}_4$ in supplementary Fig. A.7) are

applied:

$$\delta^{18}O_{corr} = \delta^{18}O_{raw} + \mathcal{H}_{\delta^{18}O}(w_{raw}) \tag{A.5}$$

$$\text{with } \mathcal{H}_{\delta^{18}O}(w_{raw}) = a \cdot \exp(\frac{1}{x^{1.08}}) - b, \tag{A.6}$$

$$\delta^{2}H_{corr} = \delta^{2}H_{raw} + \mathcal{H}_{\delta^{2}H}(w_{raw}) \tag{A.7}$$

$$\text{with } \mathcal{H}_{\delta^{2}H}(w_{raw}) = c \cdot \exp(\frac{1}{x^{1.08}}) - d \tag{A.8}$$

where w_{raw} is the uncalibrated water vapour mixing ratio in ppmv and a = -4294.0, b = 4294.1326, c = -54830.0, d = -54830.6937 for L2120 and a = -16036.0, b = -16036.4954, c = -46986.0, d = -46986.4514 for L2130-i.
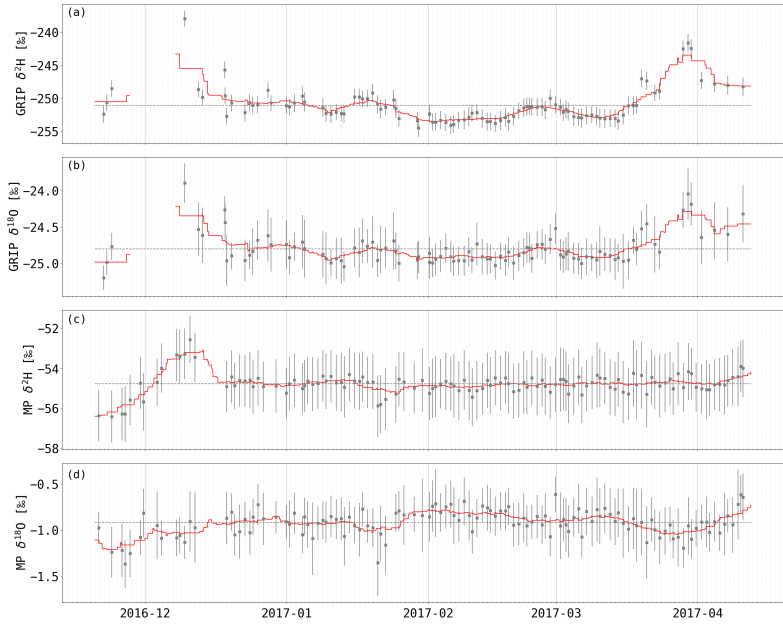
Figure A.5: Time series of successful mean calibration runs with standard deviation of MP and GRIP for SWI-13 during ACE. The red line represents the 10-day running mean of the calibration runs. The instrument was not running on 13:00 - 23:30 UTC 1 Dec 2016 and from 08:00 UTC 14 Dec 2016 - 09:00 UTC 17 Dec 2016 during leg 0.
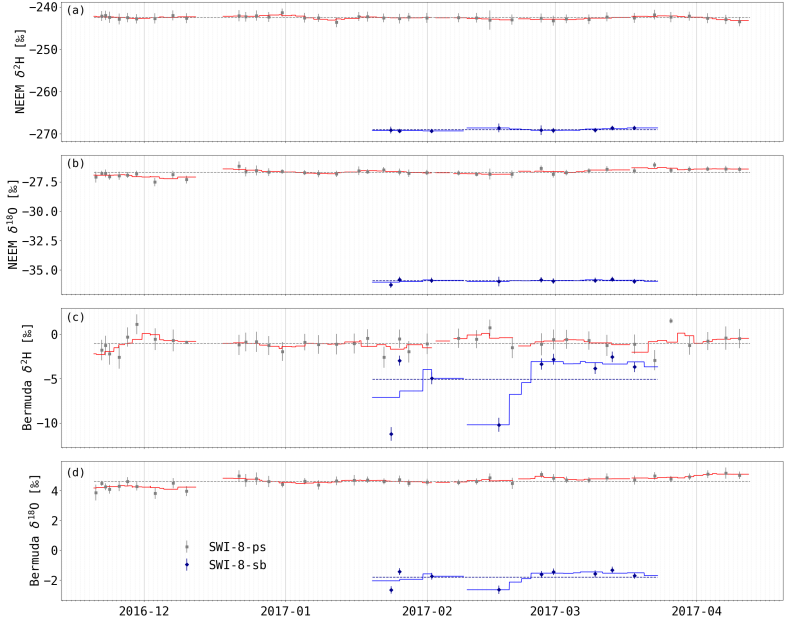
Figure A.6: Time series of successful mean calibration runs with standard deviation of NEEM and Bermuda for SWI-8-ps and SWI-8-sb during ACE. The red line represents the 10-day running mean of the calibration runs for SWI-8-ps, the blue line, the 14-day running mean for SWI-8-sb.
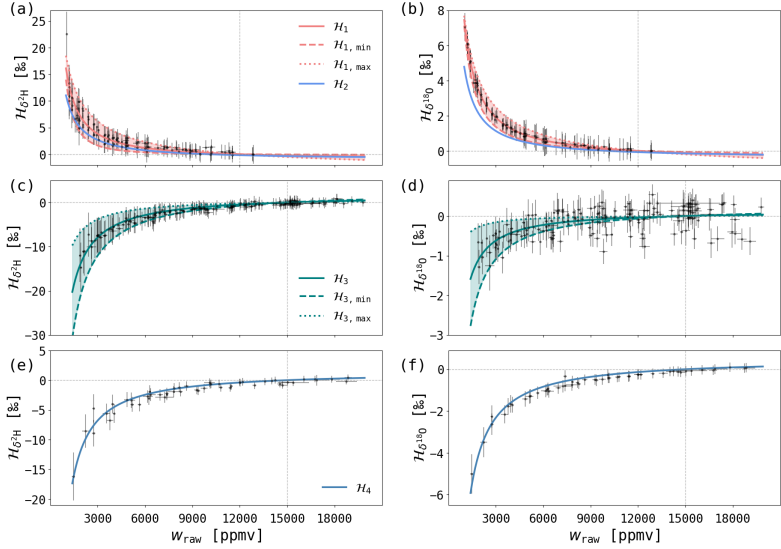
*Figure A.7: Isotope-humidity dependency correction curves $\mathcal{H}_{\delta^2\mathrm{H}}$ and $\mathcal{H}_{\delta^{18}\mathrm{O}}$ for L2130-i (SWI-13) **(a,b)**, L2120 (SWI-8-ps) **(c,d)**, and L2130-i (SWI-8-sb) **(e,f)**. $\mathcal{H}_1$, $\mathcal{H}_3$ and $\mathcal{H}_4$ are the best fit curves to the measured standards of L2130-i (SWI-13), L2120 (SWI-8-ps) and L2130-i (SWI-8-sb), respectively. For L2130-i (SWI-13) and L2120 (SWI-8-ps), the uncertainty of the best fit is shown with maximum ($\mathcal{H}_{1,\max}$,$\mathcal{H}_{3,\max}$) and minimum ($\mathcal{H}_{1,\min}$,$\mathcal{H}_{3,\min}$) curves representing the best fits to the measurements +/- 1 standard deviation. $\mathcal{H}_2$ is the isotope-humidity correction curve for L2130-i (SWI-13) from Sodemann et al. (2017).*
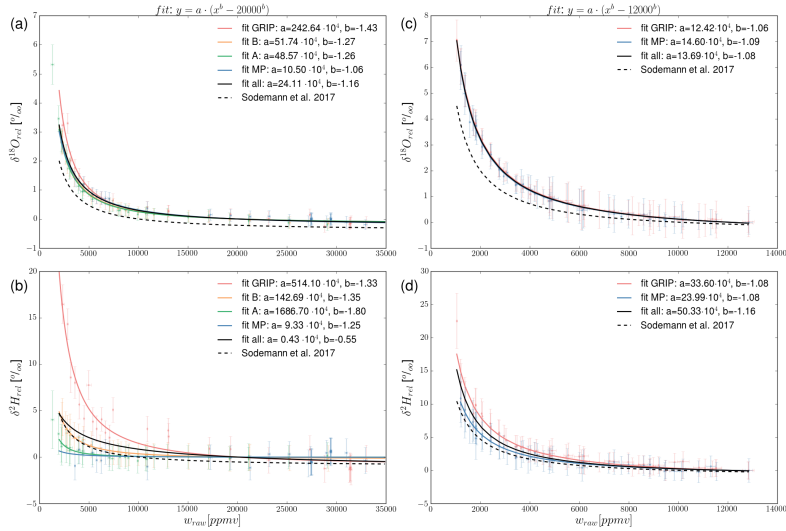
*Figure A.8: Isotope-humidity correction curves in normal **(a,c)** and flight **(b,d)** mode for L2310-i (SWI-13). $\delta^{18}O_{rel}$ and $\delta^2 H_{rel}$ are $\delta^{18}O$ and $\delta^2 H$, respectively, relative to the mean isotopic composition of the standard runs at humidities above 12000 ppmv. The calibration runs are shown with standard deviations and are coloured by the different standards. The correction curves are the best fits of $y = a \cdot (x^b - 12000^b)$ to the calibration runs with a and b for the corresponding values given in the plot legends. The dashed line is the isotope-humidity correction curve for L2130-i from Sodemann et al. (2017). The isotopic composition (in ‰) of the standards are the following: GRIP $(-34.59, -267.33)$, B $(-18.39, -140.07)$, A $(-14.34, -107.81)$, MP $(-11.42, -82.05)$, for $\delta^{18}O$ and $\delta^2 H$ respectively.*

A.2   Variations in cavity properties

Since δ^2H and δ^{18}O show a similar picture, the following analysis focuses on δ^2H. Figure A.9 shows the distributions of $\Delta_{13-8}\delta^2$H against deviations from the regulated value of the CP (Fig. A.9a,c) and CT (Fig. A.9b,d) of SWI-13 and SWI-8-ps, respectively, with additional histograms of the variables separately for each leg (coloured). The shift towards negative values in y-direction (i.e. $\Delta_{13-8}\delta^2$H) illustrates the systematic difference between SWI-13 and SWI-8-ps. A similar shift is not visible in x-direction for the cavity properties. These measurements are distributed symmetrically around the regulated values of CP and CT for all legs and both instruments and variations in CP and CT do not show any correlation with $\Delta_{13-8}\delta^2$H.
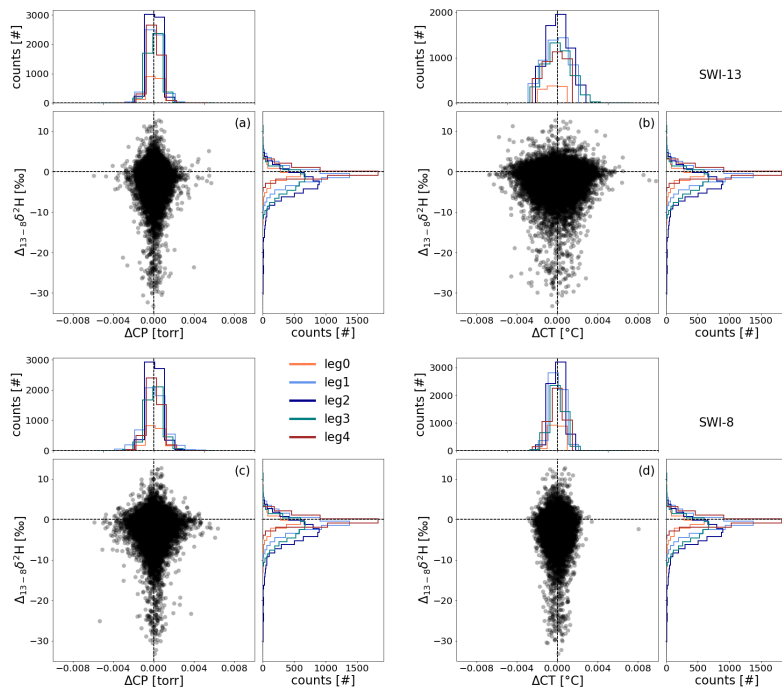
*Figure A.9: Scatter plots of vertical differences in $\delta^2 H$ between SWI-13 and SWI-8 ($\Delta_{13-8}\delta^2 H$) versus the deviations ΔCP **(a,c)** and ΔCT **(b,d)** from the regulated value of the cavity pressure (CP) and cavity temperature (CT), respectively, are shown for SWI-13 and SWI-8 are shown. Here, 5-minute averages are used. Histograms for each leg (coloured) are shown for the variable in each scatter plot.*

A.3   Calibration versions

In Fig. A.10 the difference between SWI-8-ps v1 and SWI-13 v1 (Δ_{8-13}) versus the difference between selected calibration versions and version 1 of SWI-13 (Δ_{cal}) is shown. As a proxy to compare Δ_{8-13} and Δ_{cal}, a weighted median for Δ_{8-13} [m_{8-13}] and Δ_{cal} [m_{cal}] is defined:

$$m_{8-13} \;=\; \mathrm{median}(\Delta_{8-13}(t)), \qquad\qquad (A.9)$$

$$m_{cal} \;=\; \mathrm{median}(\Delta_{cal}(t)) \qquad\qquad (A.10)$$

$\forall\, t$ within the analysed time period with $\Delta_{cal}(t) \neq 0$. m_{8-13} is larger than m_{cal} for all versions. This means that the vertical differences between SWI-8 and SWI-13 are larger than the uncertainties associated with variations in the calibration protocol. Only for d of v2, points tend to fall on the 1:1-line for very depleted water vapour mixing ratios. In other words, for very low humidities the observed difference in SWI with height could be partially diminished by not applying any isotope-humidity correction. Measurements with low humidity need to be interpreted carefully as their value depends strongly on the humidity correction function which shows a steep slope and increased uncertainty for low humidities. Even though, low humidities lie on the 1:1-line for d in v2, m_{8-13} is 2 times larger than m_{ver2} for d (see Fig. A.10g). The uncertainty of the fitted humidity correction curve $\mathcal{H}_1$, visualised with version 3, is small compared to Δ_{8-13}. Δ_{ver2} stays below the standard deviation for most of the measurement points. Version 5 shows only small differences compared to version 1 and affects only points with small Δ_{8-13}.
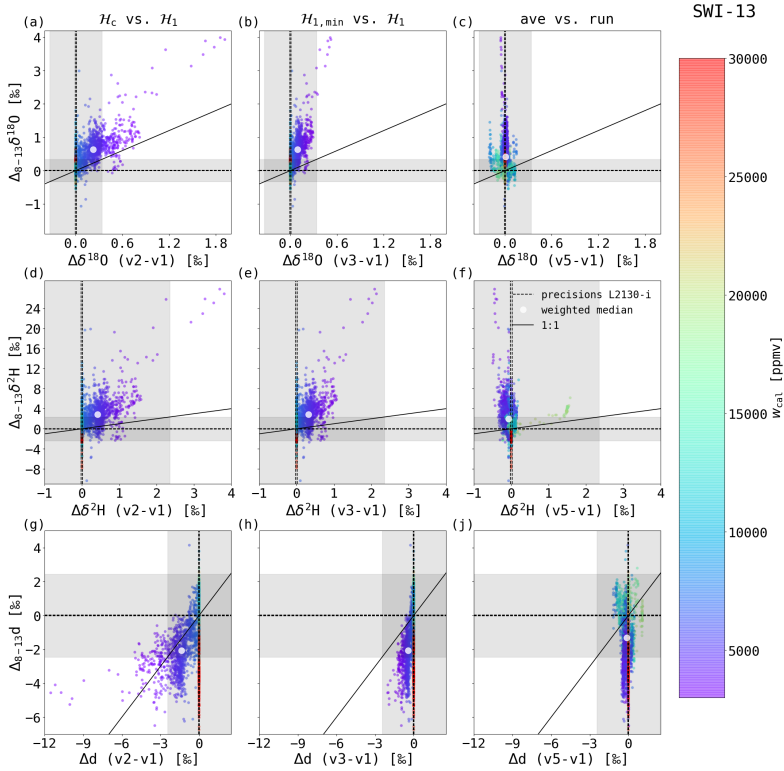
Figure A.10: Scatter plots showing different calibration versions of SWI-13: 1-hourly data of vertical differences between SWI-8-ps and SWI-13 $\Delta_{8-13}\delta^{18}O$ **(a-c)**, $\Delta_{8-13}\delta^2H$ **(d-f)** and $\Delta_{8-13}d$ **(g-j)** are shown versus calibration versions v2 (**[a,d,g]**, $\mathcal{H}_c$, i.e. correction term is zero), v3 (**[b,e,h]**, $\mathcal{H}_{1,\,min}$) and v5 (**[c,f,j]**, average calibration runs) relative to the reference version v1 ($\mathcal{H}_{1,\,run}$). Dashed lines indicate the precision of L2130-i (from Aemisegger et al., 2012). The solid lines show 1:1 lines. Shaded areas lie within the mean 1-hourly standard deviation of the reference version over all legs. The weighted median (white points) represents the median of the vertical differences m_{8-13} and version differences m_{cal} for all points with $\Delta_{ver} \neq 0$ (see text for details).
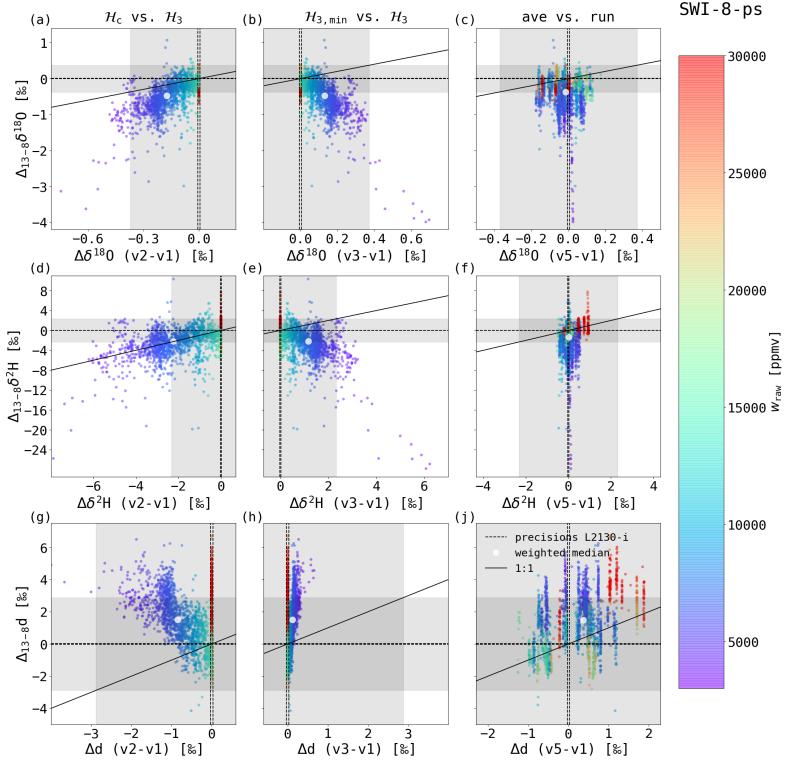
*Figure A.11: Scatter plots showing different calibration versions of SWI-8-ps: 1-hourly data of vertical differences $\Delta_{13-8}\delta^{18}O$ **(a-c)**, $\Delta_{13-8}\delta^2H$ **(d-f)** and $\Delta_{13-8}d$ **(g-j)** are shown versus calibration versions v2 ([a,d,g], $\mathcal{H}_c$, i.e. correction term is zero), v3 ([b,e,h], $\mathcal{H}_{3,\min}$) and v5 ([c,f,j], average calibration runs) relative to the reference version v1 ($\mathcal{H}_3$). $\mathcal{H}_{3,\min}$ and $\mathcal{H}_3$ refer to the isotope-humidity dependency curves as described in Fig. A.7. For the vertical differences, SWI-13 v1 and SWI-8-ps v1 are used. Dashed lines indicate the precision of L2130-i (from Aemisegger et al., 2012). The solid lines show 1:1 lines. Shaded areas lie within the mean 1-hourly standard deviation over all legs. The weighted median (white points) represents the median of the vertical differences m_{13-8} and version differences m_{cal} for all points with $\Delta_{ver} \neq 0$ (see text for details).*

The ratio of $\frac{m_{cal}}{m_{8-13}}$ is used to estimate how much of the vertical differences Δ_{8-13} can be explained by uncertainties in the calibration procedure. The changes due to different calibration versions amounts for 10-30% of Δ_{8-13} for most versions. The scenario of no humidity calibration shows a higher ratio for d of 82%. The difference between calibration versions using $\mathcal{H}_1$ or $\mathcal{H}_{1,\min}$ explains 15%, 10% and 26% of the vertical differences for δ^{18}O, δ^2H, and d, respectively.

The same analysis was done for SWI-8-ps (Fig. A.11). The picture is similar as for SWI-13 with larger m_{8-13} than m_{cal}, except for δ^2H and version 2 without isotopic-humidity correction (Fig. A.11d). For this version, vertical differences are of similar order as the differences to the final calibration version. Note, that this is only the case for δ^2H, whereas δ^{18}O and d have smaller or opposite changes between the calibration version compared to the vertical differences. The difference between calibration versions using $\mathcal{H}_3$ or $\mathcal{H}_{3,\min}$ explains 38%, 65% and 13% of the vertical differences for δ^{18}O, δ^2H, and d, respectively. This version comparison underlines that the largest uncertainties are introduced by the isotope-humidity dependency correction and shows that, based on our best knowledge, Δ_{8-13} cannot be fully explained by uncertainties in the calibration procedure.

A.4   Measurement techniques: Wave age and wind speed

A.4.1   Wave age

The wave age during ACE was derived from the WaMoS-II measurements. WaMoS-II records and stores consecutive series of 32 radar images per minute. During ACE, the radar operated with a range of $\sim$2.5 km and sampled a total area of 20 km^2 around the ship. Standard image processing techniques based on Fourier transforms are used to extract the wave energy spectrum $E(\omega, \theta)$, where ω is the angular frequency and θ the direction of propagation from 32 images (i.e. one spectrum every minute). An average wave spectrum is calculated every 20 min. N-th moments (m_N) of the spectrum are used to compute the significant wave height ($4 \cdot m_o^{1/2}$), mean periods and group velocity. Wave age is calculated from the derived wave group velocity and the wind speed.

A.4.2   Wind speed correction

Wind speed and direction were measured with two 2D-sonic anemometers (models: WS425 and WMT702), which were mounted on vertical poles on the uppermost side arms of the main mast. The anemometers are approximately 7.5 m above the monkey island and 30.5 m above average sea level. The relative wind speed and direction are recorded at a rate of 0.33 Hz together with the ship's heading (compass) by the automated weather station. Averages of the relative wind speed were calculated over 5 min intervals.

The bias caused by airflow distortion was estimated by comparing the

observed relative wind speed with the expected relative wind speed based on ECMWF analysis data. The expected relative wind speed was calculated using the following steps: (1) The wind at 30 m a.s.l. [U30, V30] was estimated from the wind at 10 m a.s.l. assuming a logarithmic wind profile modified by the universal stability function (Fairall et al., 2003; Edson et al., 2013). For this, the Monin-Obukov length scale was estimated from the ECMWF surface fluxes. (2) [U30, V30] was interpolated to 5 min resolution and used to calculate the expected relative wind speed based on the ship's heading and velocity by inverting the equations from Smith et al. (1999). The average ratio of observed and expected wind speed was evaluated as function of the relative wind direction and used to scale the observed wind speeds. True wind speed and direction were calculated using the ship's heading (compass) and velocity (GPS) following Smith et al. (1999). Subsequently, true wind speed at 10 m a.s.l. was estimated using the previously used logarithmic wind profile. A manuscript describing this analysis in detail is in preparation.

Appendix B

Appendix material to Chapter 4
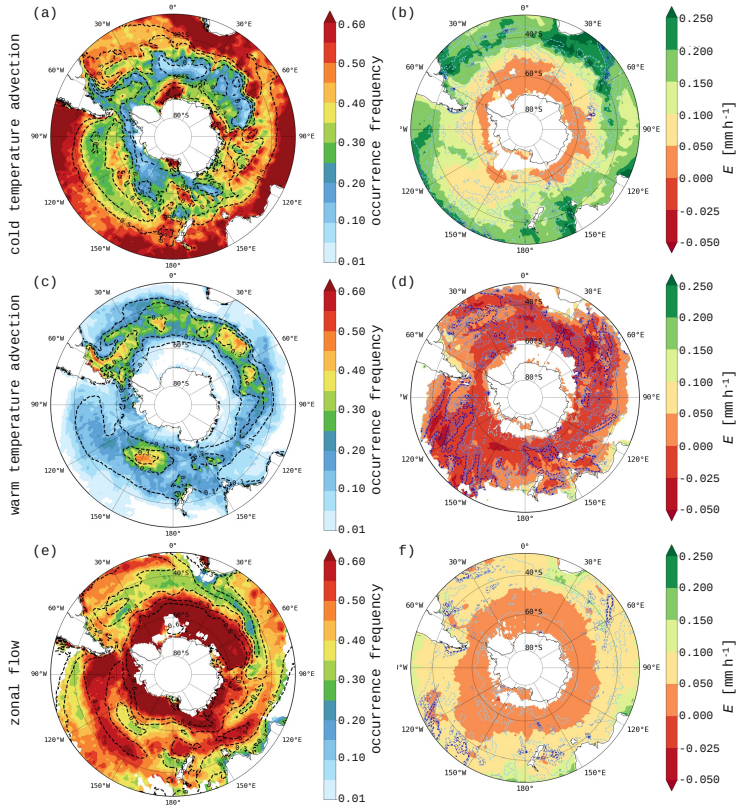
Figure B.1: Mean occurrence frequency of cold temperature advection, warm temperature advection and zonal flow (a,c,e) and the associated ocean evaporation (b,d,f) for December 2016 to March 2017 using ERA-Interim. Blue dashed lines show mean surface precipitation at levels of 0.06, 0.18, 0.24, and 0.3 mm h^{-1}. Black, dashed contours show the climatological occurrence frequency of cold temperature advection (a), warm temperature advection (c) and zonal flow (e) as shown in Fig. 4.4.
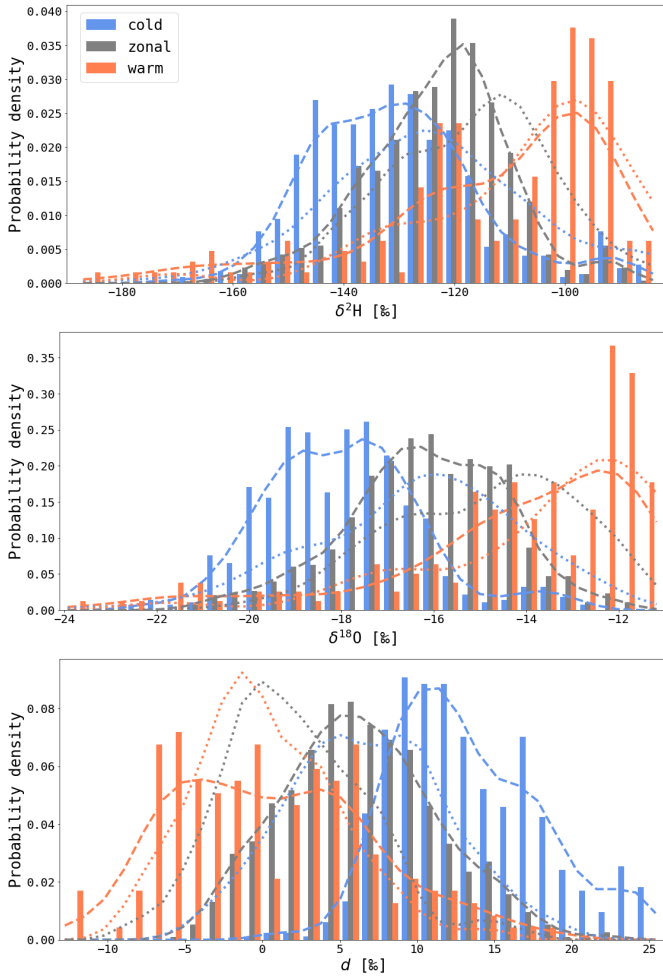
Figure B.2: Same as Fig. 4.6 with isotopic compositions along the ACE track in COSMO$_{\mathrm{iso}}$ simulations. The dotted lines are the distributions from the ACE measurements.
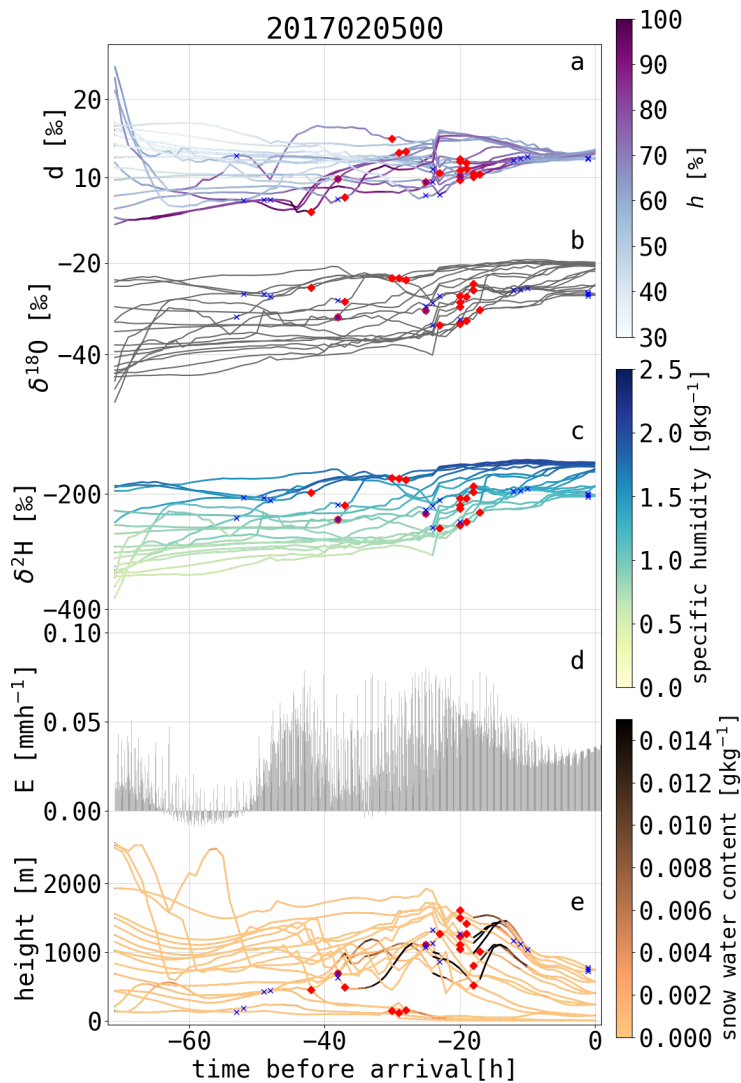
Figure B.3: Same as Fig. 4.15 but at 00 UTC 5 Feb 2017.
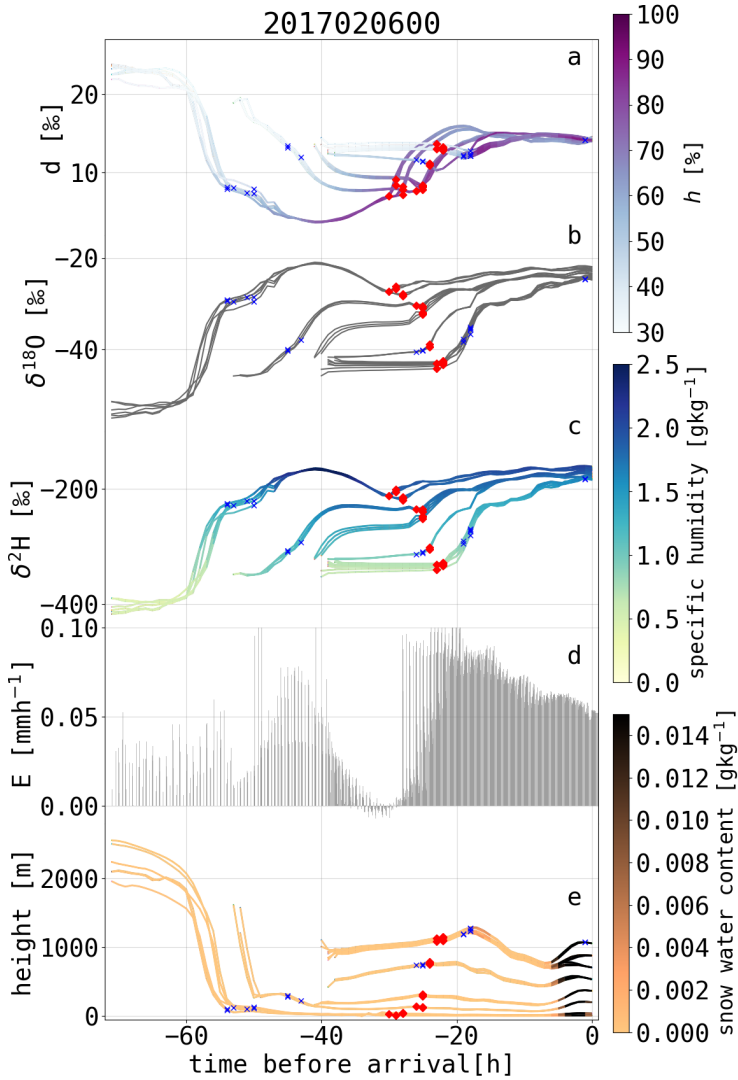
Figure B.4: Same as Fig. 4.15 but at 00 UTC 6 Feb 2017.
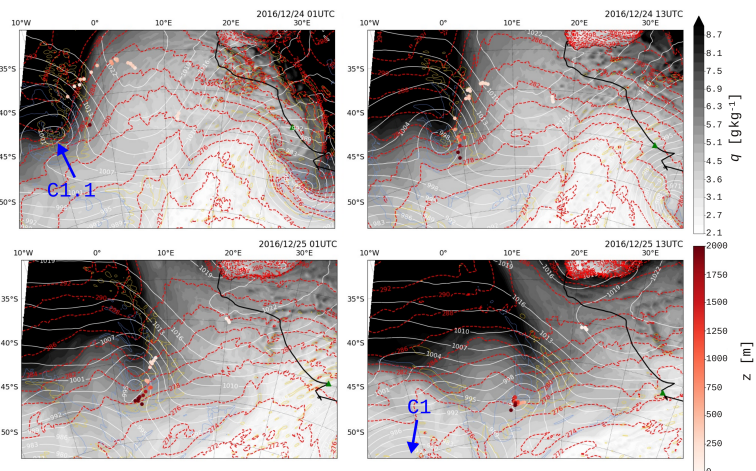
Figure B.5: Horizontal cross sections of specific humidity (q) at four time steps in COSMO$_{\mathrm{iso}}$ simulation leg1-run1. Coloured points show the position of air parcel arriving at 22 UTC 26 Dec 2016 below 1.5·BLH at the ship's position and are coloured by their height (z). Dashed red lines denote potential temperature [K], solid white lines the sea level pressure [hPa]. The mean cloud liquid water content of the five lowest model levels (∼20-200 m) of a value of 0.01 g kg^{-1} is shown in thin, yellow contours, the surface precipitation of 0.01 g kg^{-1} in thin, blue contours.

Table B.1: *Initial conditions of single-process air-parcel model runs in Figs. 4.22 and 4.23. Evaporation (warm) and Evaporation (cold) refer to the ocean evaporation air-parcel model (described in Section 3.1.1) with initial conditions in a warm and cold environment, respectively. Evaporation (cold) is only shown in Fig. 4.22. The dew deposition model is described in Section 3.1.2 and the air-parcel model simulating Rayleigh fractionation during moist-adiabatic ascent in Section 3.1.3.*

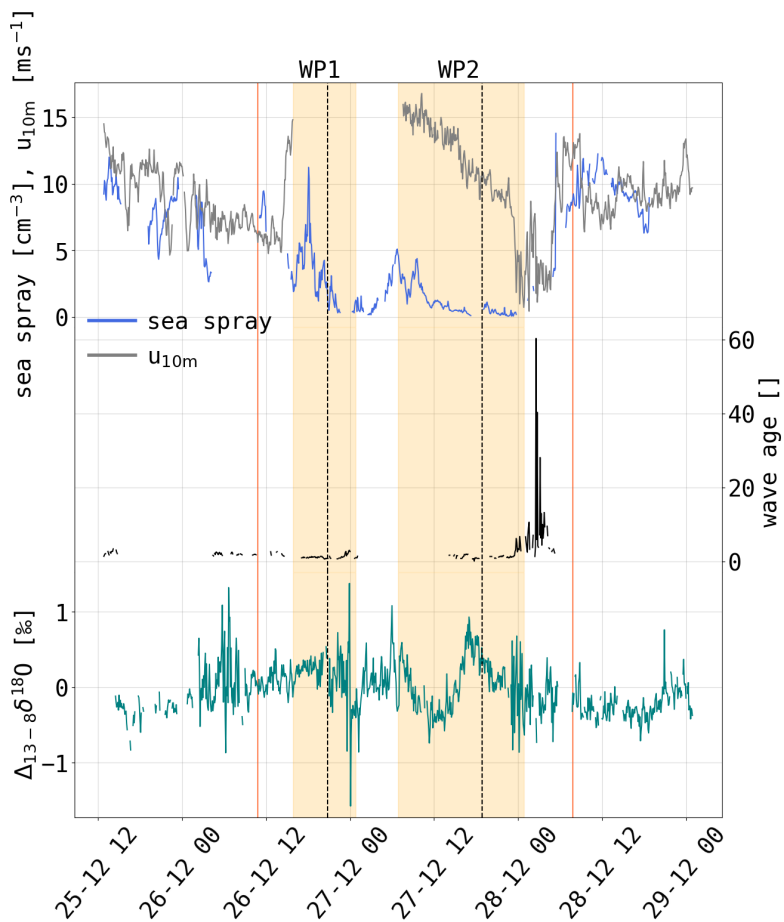| Model	dew deposition			evaporation (warm)			evaporation (cold)			Rayleigh		
	from	to	step	from	to	step	from	to	step	from	to	step
δ^2H [‰]	-108	-96	2	-170	-140	5.0	-330	-300	5	-128	-80	8
δ^{18}O [‰]	-18.0	-14.0	0.67	-22.8	-18.8	0.67	-43.5	-39.5	0.67	-16.5	-12.5	0.67
d [‰]	36.0	16.0	3.33	12.4	10.4	0.33	18.0	16.0	0.33	4.0	20.0	2.67
q_0 [g kg^{-1}]	7.0	8.2	0.2	2.8	3.4	0.1	0.4	1.0	0.1	10.0	10.0	0.0
SST_0 [K]	279.5	283.5	0.67	280.0	283.0	0.5	274.0	275.5	0.25	281	287	1.0
SST_{max} [K]				299.0	298.0	0.17	280.0	281.5	0.25			

Figure B.6: Same as Fig. 4.18, but showing sea spray proxy, wind speed at 10 m a.s.l., wave age and difference in $\delta^{18}O$ between measurements at 8 m and 13.5 m a.s.l. on the research vessel. For details on these time series see section 2.2.

Bibliography

Aemisegger, F., 2015: TERRAiso test case studies using a TERRA stand-alone setup for Riet-holzbach. Unpublished manuscript.

— 2018: On the link between the North Atlantic storm track and precipitation deuterium excess in Reykjavik. *Atmos. Sci. Lett.*, **19**, 19:e865, doi:10.1002/asl.865.

Aemisegger, F. and L. Papritz, 2018: A climatology of strong large-scale ocean evaporation events. Part I: Identification, global distribution, and associated climate conditions. *J. Clim.*, **31**, 7287–7312, doi:10.1175/JCLI-D-17-0591.1.

Aemisegger, F., S. Pfahl, H. Sodemann, I. Lehner, S. I. Seneviratne, and H. Wernli, 2014: Deuterium excess as a proxy for continental moisture recycling and plant transpiration. *Atmos. Chem. Phys.*, **14**, 4029–4054, doi:10.5194/acp-14-4029-2014.

Aemisegger, F. and J. Sjolte, 2018: A climatology of strong large-scale ocean evaporation events. Part II: Relevance for the deuterium excess signature of the evaporation flux. *J. Clim.*, **31**, 7313–7336, doi:10.1175/JCLI-D-17-0592.1.

Aemisegger, F., J. K. Spiegel, S. Pfahl, H. Sodemann, W. Eug-

ster, and H. Wernli, 2015: Isotope meteorology of cold front passages: A case study combining observations and modeling: Water isotopes during cold fronts. *Geophys. Res. Lett.*, **42**, 5652–5660, doi:10.1002/2015GL063988.

Aemisegger, F., P. Sturm, P. Graf, H. Sodemann, S. Pfahl, A. Knohl, and H. Wernli, 2012: Measuring variations of δ^{18}O and δ^{2}H in atmospheric water vapour using two commercial laser-based spectrometers: An instrument characterisation study. *Atmos. Meas. Tech.*, **5**, 1491–1511, doi:10.5194/amt-5-1491-2012.

Araguás-Araguás, L., K. Froehlich, and K. Rozanski, 2000: Deuterium and oxygen-18 isotope composition of precipitation and atmospheric moisture. *Hydrol. Process.*, **14**, 1341–1355, doi:10.1002/1099-1085(20000615)14:8<1341::AID-HYP983>3.0.CO;2-Z.

Attinger, R., E. Spreitzer, M. Boettcher, R. Forbes, H. Wernli, and H. Joos, 2019: Quantifying the role of individual diabatic processes for the formation of PV anomalies in a North Pacific cyclone. *Q. J. R. Meteorol. Soc.*, **145**, 2454–2476, doi:10.1002/qj.3573.

Bailey, A., D. Noone, M. Berkelhammer, H. C. Steen-Larsen, and P. Sato, 2015: The stability and calibration of water vapor isotope ratio measurements during long-term deployments. *Atmos. Meas. Tech.*, **8**, 4521–4538, doi:10.5194/amt-8-4521-2015.

Bailey, A., H. K. A. Singh, and J. Nusbaumer, 2019: Evaluating a moist isentropic framework for poleward moisture transport: Implications for water isotopes over Antarctica. *Geophys. Res. Lett.*, **46**, 7819–7827, doi:10.1029/2019GL082965.

Beare, R. J., 2007: Boundary layer mechanisms in extratropical cyclones. *Q. J. R. Meteorol. Soc.*, **133**, 503–515, doi:10.1002/qj.30, wOS:000245911700017.

Benetti, M., G. Aloisi, G. Reverdin, C. Risi, and G. Sèze, 2015: Importance of boundary layer mixing for the isotopic composition of surface vapor over the subtropical North Atlantic Ocean. *J. Geophys. Res. Atmos.*, **120**, 2190 – 2209, doi:10.1002/2014JD021947.

Benetti, M., J.-L. Lacour, Á. E. Sveinbjörnsdóttir, G. Aloisi, G. Reverdin, C. Risi, A. J. Peters, and H. C. Steen-Larsen, 2018: A framework to study mixing processes in the marine boundary layer using water vapor isotope measurements. *Geophys. Res. Lett.*, **45**, 2524–2532, doi:10.1002/2018GL077167.

Benetti, M., G. Reverdin, C. Pierre, L. Merlivat, C. Risi, H. C. Steen-Larsen, and F. Vimeux, 2014: Deuterium excess in marine water vapor: Dependency on relative humidity and surface wind speed during evaporation. *J. Geophys. Res. Atmos.*, **119**, 584–593, doi:10.1002/2013JD020535.

Benetti, M., H. C. Steen-Larsen, G. Reverdin, Á. E. Sveinbjörnsdóttir, G. Aloisi, M. B. Berkelhammer, B. Bourlès, D. Bourras, G. d. Coetlogon, A. Cosgrove, A.-K. Faber, J. Grelet, S. B. Hansen, R. Johnson, H. Legoff, N. Martin, A. J. Peters, T. J. Popp, T. Reynaud, and M. Winther, 2017: Stable isotopes in the atmospheric marine boundary layer water vapour over the Atlantic Ocean, 2012–2015. *Sci. Data*, **4**, 160128, doi:10.1038/sdata.2016.128.

Bharti, V., C. W. Fairall, B. W. Blomquist, Y. Huang, A. Protat, P. P. Sullivan, S. T. Siems, and M. J. Manton, 2019: Air-sea heat and momentum fluxes in the Southern Ocean. *J. Geophys. Res. Atmos.*, **124**, 12426–12443, doi:10.1029/2018JD029761.

Blossey, P. N., Z. Kuang, and D. M. Romps, 2010: Isotopic composition of water in the tropical tropopause layer in cloud-resolving simulations of an idealized tropical circulation. *J. Geophys. Res. Atmos.*, **115**,

doi:10.1029/2010JD014554.

Bolot, M., B. Legras, and E. J. Moyer, 2013: Modelling and interpreting the isotopic composition of water vapour in convective updrafts. *Atmos. Chem. Phys.*, **13**, 7903–7935, doi:10.5194/acp-13-7903-2013.

Bonne, J.-L., M. Behrens, H. Meyer, S. Kipfstuhl, B. Rabe, L. Schönicke, H. C. Steen-Larsen, and M. Werner, 2019: Resolving the controls of water vapour isotopes in the Atlantic sector. *Nat. Commun.*, **10**, 1632, doi:10.1038/s41467-019-09242-6.

Bonne, J.-L., V. Masson-Delmotte, O. Cattani, M. Delmotte, C. Risi, H. Sodemann, and H. C. Steen-Larsen, 2014: The isotopic composition of water vapour and precipitation in Ivittuut, southern Greenland. *Atmos. Chem. Phys.*, **14**, 4419–4439, doi:10.5194/acp-14-4419-2014.

Bony, S., C. Risi, and F. Vimeux, 2008: Influence of convective processes on the isotopic composition (δ^{18}O and δD) of precipitation and water vapor in the tropics: 1. Radiative-convective equilibrium and Tropical Ocean–Global Atmosphere–Coupled Ocean-Atmosphere Response Experiment (TOGA-COARE) simulations. *J. Geophys. Res.*, **113**, D19305, doi:10.1029/2008JD009942.

Bony, S., B. Stevens, F. Ament, S. Bigorre, P. Chazette, S. Crewell, J. Delanoë, K. Emanuel, D. Farrell, C. Flamant, S. Gross, L. Hirsch, J. Karstensen, B. Mayer, L. Nuijens, J. H. Ruppert, I. Sandu, P. Siebesma, S. Speich, F. Szczap, J. Totems, R. Vogel, M. Wendisch, and M. Wirth, 2017: EUREC4a: A field campaign to elucidate the couplings between clouds, convection and circulation. *Surv. Geophys.*, **38**.
URL https://dspace.mit.edu/handle/1721.1/118193

Boutle, I. A., R. J. Beare, S. E. Belcher, A. R. Brown, and R. S. Plant, 2010: The moist boundary layer under a mid-latitude weather system. *Bound-Layer Meteorol.*, **134**, 367–386, doi:10.1007/s10546-009-9452-

9.

Boutle, I. A., S. E. Belcher, and R. S. Plant, 2011: Moisture transport in midlatitude cyclones. *Q. J. R. Meteorol. Soc.*, **137**, 360–373, doi:10.1002/qj.783.

Brown, D., J. Worden, and D. Noone, 2013: Characteristics of tropical and subtropical atmospheric moistening derived from Lagrangian mass balance constrained by measurements of HDO and H_2O. *J. Geophys. Res. Atmos.*, **118**, 54–72, doi:10.1029/2012JD018507.

Brutsaert, W., 1965: A model for evaporation as a molecular diffusion process into a turbulent atmosphere. *J. Geophys. Res.*, **70**, 5017–5024, doi:10.1029/JZ070i020p05017.

Cappa, C. D., M. B. Hendricks, D. J. DePaolo, and R. C. Cohen, 2003: Isotopic fractionation of water during evaporation. *J. Geophys. Res. Atmos.*, **108**, 4525, doi:10.1029/2003JD003597.

Catto, J. L., C. Jakob, G. Berry, and N. Nicholls, 2012: Relating global precipitation to atmospheric fronts. *Geophys. Res. Lett.*, **39**, L10805, doi:10.1029/2012GL051736.

Chen, S., T. J. Campbell, H. Jin, S. Gaberšek, R. M. Hodur, and P. Martin, 2010: Effect of two-way air-sea coupling in high and low wind speed regimes. *Mon. Weather Rev.*, **138**, 3579–3602, doi:10.1175/2009MWR3119.1.

Christner, E., F. Aemisegger, S. Pfahl, M. Werner, A. Cauquoin, M. Schneider, F. Hase, S. Barthlott, and G. Schädler, 2018: The climatological impacts of continental surface evaporation, rainout, and subcloud processes on δD of water vapor and precipitation in Europe. *J. Geophys. Res. Atmos.*, **123**, 4390–4409, doi:10.1002/2017JD027260.

Condron, A., G. R. Bigg, and I. A. Renfrew, 2006: Polar mesoscale

cyclones in the northeast Atlantic: Comparing climatologies from
ERA-40 and satellite imagery. *Mon. Weather Rev.*, **134**, 1518–1533,
doi:10.1175/MWR3136.1.

Condron, A. and I. A. Renfrew, 2013: The impact of polar mesoscale
storms on northeast Atlantic Ocean circulation. *Nature Geosci.*, **6**, 34–
37, doi:10.1038/ngeo1661.

Craig, H., 1961: Isotopic variations in meteoric waters. *Science*, **133**,
1702–1703, doi:10.1126/science.133.3465.1702.

Craig, H. and L. Gordon, 1965: Deuterium and oxygen 18 variations in the
ocean and the marine atmosphere. *Proceedings of the Stable Isotopes in
Oceanographic Studies and Paleotemperatures*.

Crezee, B., H. Joos, and H. Wernli, 2017: The microphysical building
blocks of low-level potential vorticity anomalies in an idealized extrat-
ropical cyclone. *J. Atmos. Sci.*, **74**, 1403–1416, doi:10.1175/JAS-D-16-
0260.1.

Dansgaard, W., 1954: The O18-abundance in fresh water. *Geochim. Cos-
mochim. Acta*, **6**, 241–260, doi:10.1016/0016-7037(54)90003-4.

— 1964: Stable isotopes in precipitation. *Tellus*, **16:4**, 436–468,
doi:10.3402/tellusa.v16i4.8993.

Dee, D. P., S. M. Uppala, A. J. Simmons, P. Berrisford, P. Poli,
S. Kobayashi, U. Andrae, M. A. Balmaseda, G. Balsamo, P. Bauer,
P. Bechtold, A. C. M. Beljaars, L. v. d. Berg, J. Bidlot, N. Bormann,
C. Delsol, R. Dragani, M. Fuentes, A. J. Geer, L. Haimberger, S. B.
Healy, H. Hersbach, E. V. Hólm, L. Isaksen, P. Kållberg, M. Köhler,
M. Matricardi, A. P. McNally, B. M. Monge-Sanz, J.-J. Morcrette, B.-K.
Park, C. Peubey, P. d. Rosnay, C. Tavolato, J.-N. Thépaut, and F. Vitart,
2011: The ERA-Interim reanalysis: configuration and performance of

the data assimilation system. *Q. J. R. Meteorol. Soc.*, **137**, 553–597, doi:10.1002/qj.828.

Dittmer, J., 1995: Use of marine radars for real time wave field survey and speeding up the transmission process. *Proceedings of the WMO/IOC Workshop on Operational Ocean Monitoring Using Surface Based Radars*, WMO, number 694 in WMO/TD, 133–137.

Doms, G., J. Förstner, E. Heise, H.-J. Herzog, D. Mironov, M. Raschendorfer, T. Reinhardt, B. Ritter, R. Schrodin, J.-P. Schulz, and G. Vogel, 2011: A description of the nonhydrostatic regional COSMO model. Part II: Physical parameterization. *Deutscher Wetterdienst, Offenbach, Germany*.

Dütsch, M., P. N. Blossey, E. J. Steig, and J. M. Nusbaumer, 2019: Nonequilibrium fractionation during ice cloud formation in iCAM5: Evaluating the common parameterization of supersaturation as a linear function of temperature. *J. Adv. Model. Earth Sy.*, **11**, 3777–3793, doi:10.1029/2019MS001764.

Dütsch, M., S. Pfahl, M. Meyer, and H. Wernli, 2018: Lagrangian process attribution of isotopic variations in near-surface water vapour in a 30-year regional climate simulation over Europe. *Atmos. Chem. Phys.*, **18**, 1653–1669, doi:https://doi.org/10.5194/acp-18-1653-2018.

Dütsch, M., S. Pfahl, and H. Sodemann, 2017: The impact of nonequilibrium and equilibrium fractionation on two different deuterium excess definitions. *J. Geophys. Res.: Atmos.*, **122**, 12,732–12,746, doi:10.1002/2017JD027085.

Dütsch, M., S. Pfahl, and H. Wernli, 2016: Drivers of δ^2H variations in an idealized extratropical cyclone. *Geophys. Res. Lett.*, **43**, 5401–5408, doi:10.1002/2016GL068600.

Dütsch, M. L., 2016: *Stable water isotope fractionation processes in weather systems and their influence on isotopic variability on different time scales*. Ph.D. thesis, ETH Zurich, Zurich.

Edson, J. B., V. Jampana, R. A. Weller, S. P. Bigorre, A. J. Plueddemann, C. W. Fairall, S. D. Miller, L. Mahrt, D. Vickers, and H. Hersbach, 2013: On the exchange of momentum over the open ocean. *J. Phys. Oceanogr.*, **43**, 1589–1610, doi:10.1175/JPO-D-12-0173.1.

Epstein, S. and T. Mayeda, 1953: Variation of O18 content of waters from natural sources. *Geochim. Cosmochim. Acta*, **4**, 213–224, doi:10.1016/0016-7037(53)90051-9.

Epstein, S., R. P. Sharp, and A. J. Gow, 1970: Antarctic ice sheet: Stable isotope analyses of Byrd station cores and interhemispheric climatic implications. *Sci.*, **168**, 1570–1572.

Fairall, C. W., E. F. Bradley, J. E. Hare, A. A. Grachev, and J. B. Edson, 2003: Bulk parameterization of air–sea fluxes: Updates and verification for the COARE algorithm. *J. Clim.*, **16**, 571–591, doi:10.1175/1520-0442(2003)016<0571:BPOASF>2.0.CO;2.

Feng, X., A. M. Faiia, and E. S. Posmentier, 2009: Seasonality of isotopes in precipitation: A global perspective. *J. Geophys. Res.*, **114**, D08116, doi:10.1029/2008JD011279.

Feng, X., E. S. Posmentier, L. J. Sonder, and N. Fan, 2019: Rethinking Craig and Gordon's approach to modeling isotopic compositions of marine boundary layer vapor. *Atmos. Chem. Phys.*, **19**, 4005–4024, doi:10.5194/acp-19-4005-2019.

Fleagle, R. G. and W. A. Nuss, 1985: The distribution of surface fluxes and boundary layer divergence in midlatitude ocean storms. *J. Atmos. Sci.*, **42**, 784–799, doi:10.1175/1520-

0469(1985)042<0784:TDOSFA>2.0.CO;2.

Galewsky, J., H. C. Steen-Larsen, R. D. Field, J. Worden, C. Risi, and M. Schneider, 2016: Stable isotopes in atmospheric water vapor and applications to the hydrologic cycle. *Rev. Geophys.*, **54**, 809–865, doi:10.1002/2015RG000512.

Gat, J. R., 1996: Oxygen and hydrogen isotopes in the hydrologic cycle. *Annu. Rev. Earth Planet. Sci.*, **24**, 225–262, doi:10.1146/annurev.earth.24.1.225.

— 2008: The isotopic composition of evaporating waters – review of the historical evolution leading up to the Craig–Gordon model. *Isotopes in Environmental and Health Studies*, **44**, 5–9, doi:10.1080/10256010801887067.

Gat, J. R., B. Klein, Y. Kushnir, W. Roether, H. Wernli, R. Yam, and A. Shemesh, 2003: Isotope composition of air moisture over the Mediterranean Sea: An index of the air–sea interaction pattern. *Tellus B*, **55**, 953–965, doi:10.1034/j.1600-0889.2003.00081.x.

Gedzelman, S. D. and J. R. Lawrence, 1990: The isotopic composition of precipitation from two extratropical cyclones. *Mon. Weather Rev.*, **118**, 495–509, doi:10.1175/1520-0493(1990)118<0495:TICOPF>2.0.CO;2.

Graf, P., H. Wernli, S. Pfahl, and H. Sodemann, 2019: A new interpretative framework for below-cloud effects on stable water isotopes in vapour and rain. *Atmos. Chem. Phys.*, **19**, 747–765, doi:10.5194/acp-19-747-2019.

Grazioli, J., C. Genthon, B. Boudevillain, C. Duran-Alarcon, M. D. Guasta, J.-B. Madeleine, and A. Berne, 2017: Measurements of precipitation in Dumont d'Urville, Adélie Land, East Antarctica. *Cryosphere*, **11**, 1797–1811, doi:10.5194/tc-11-1797-2017.

Hartmuth, K., 2019: The role of cold and warm air advection for the

hydrological cycle in the south indian ocean. *Master thesis, ETH Zurich, Zurich*, doi:10.3929/ethz-b-000437864.

Hastrup, K., 2013: Water and the configuration of social worlds: An anthropological perspective. *J. Water Resource Prot.*, **05**, 59–66, doi:10.4236/jwarp.2013.54A009.

Hentgen, L., N. Ban, N. Kröner, D. Leutwyler, and C. Schär, 2019: Clouds in convection-resolving climate simulations over Europe. *J. Geophys. Res. Atmos.*, **124**, 3849–3870, doi:10.1029/2018JD030150.

Hentgen, L., N. Ban, J. Vergara-Temprado, and C. Schär, 2020: Improving the simulation of tropical clouds in explicit high resolution climate models. *submitted to J. Adv. Model. Earth Sy.*.

Hewson, T. D., 1998: Objective fronts. *Met. Apps*, **5**, 37–65, doi:10.1017/S1350482798000553.

Holt, T. and S. Raman, 1990: Marine boundary-layer structure and circulation in the region of offshore redevelopment of a cyclone during GALE. *Mon. Weather Rev.*, **118**, 392–410, doi:10.1175/1520-0493(1990)118<0392:MBLSAC>2.0.CO;2.

Horita, J., K. Rozanski, and S. Cohen, 2008: Isotope effects in the evaporation of water: A status report of the Craig–Gordon model. *Isotopes Environ. Health. Stud.*, **44**, 23–49, doi:10.1080/10256010801887174.

Horita, J. and D. J. Wesolowski, 1994: Liquid-vapor fractionation of oxygen and hydrogen isotopes of water from the freezing to the critical temperature. *Geochim. Cosmochim. Acta*, **58**, 3425–3437, doi:10.1016/0016-7037(94)90096-5.

Horton, R. E., 1931: The field, scope, and status of the science of hydrology. *Eos. Trans. AGU*, **12**, 189–202, doi:10.1029/TR012i001p00189-2.

Jabouille, P., J. L. Redelsperger, and J. P. Lafore, 1996: Modifi-

cation of surface fluxes by atmospheric convection in the TOGA COARE region. *Mon. Weather Rev.*, **124**, 816–837, doi:10.1175/1520-0493(1996)124<0816:MOSFBA>2.0.CO;2.

Jacobs, A. F. G., B. G. Heusinkveld, and S. M. Berkowicz, 1999: Dew deposition and drying in a desert system: a simple simulation model. *J. Arid Environ.*, **42**, 211–222, doi:10.1006/jare.1999.0523.

Jansing, L., 2019: Marine boundary layer stable water isotope variability in the southern ocean − an investigation using the regional COSMOiso model. *Master thesis, ETH Zurich, Zurich*, doi:10.3929/ethz-b-000438068.

Jenkner, J., M. Sprenger, I. Schwenk, C. Schwierz, S. Dierer, and D. Leuenberger, 2010: Detection and climatology of fronts in a high-resolution model reanalysis over the alps. *Met. Apps*, **17**, 1–8, doi:10.1002/met.142.

Johnsen, S. J., W. Dansgaard, and J. W. C. White, 1989: The origin of Arctic precipitation under present and glacial conditions. *Tellus B*, **41B**, 452–468, doi:10.1111/j.1600-0889.1989.tb00321.x.

Johnson, J. E. and C. W. Rella, 2017: Effects of variation in background mixing ratios of N_2, O_2, and Ar on the measurement of δ^{18}O-H_2O and δ^2H–H_2O values by cavity ring-down spectroscopy. *Atmos. Meas. Tech.*, **10**, 3073–3091, doi:10.5194/amt-10-3073-2017.

Joussaume, S., R. Sadourny, and J. Jouzel, 1984: A general circulation model of water isotope cycles in the atmosphere. *Nature*, **311**, 24–29, doi:10.1038/311024a0.

Jouzel, J., R. B. Alley, K. M. Cuffey, W. Dansgaard, P. Grootes, G. Hoffmann, S. J. Johnsen, R. D. Koster, D. Peel, C. A. Shuman, M. Stievenard, M. Stuiver, and J. White, 1997: Validity of the temperature reconstruction from water isotopes in ice cores. *J. Geophys. Res.: Oceans*, **102**,

26471–26487, doi:10.1029/97JC01283.

Jouzel, J. and L. Merlivat, 1984: Deuterium and oxygen 18 in precipitation: Modeling of the isotopic effects during snow formation. *J. Geophys. Res. Atmos.*, **89**, 11749–11757, doi:10.1029/JD089iD07p11749.

Kurita, N., 2013: Water isotopic variability in response to mesoscale convective system over the tropical ocean. *J. Geophys. Res. Atmos.*, **118**, 10376–10390, doi:10.1002/jgrd.50754.

Kurita, N., N. Hirasawa, S. Koga, J. Matsushita, H. C. Steen-Larsen, V. Masson-Delmotte, and Y. Fujiyoshi, 2016: Influence of large-scale atmospheric circulation on marine air intrusion toward the East Antarctic coast. *Geophys. Res. Lett.*, **43**, 9298–9305, doi:10.1002/2016GL070246.

Kuwano-Yoshida, A. and S. Minobe, 2016: Storm-track response to SST fronts in the northwestern Pacific region in an AGCM. *J. Clim.*, **30**, 1081–1102, doi:10.1175/JCLI-D-16-0331.1.

Läderach, A. and H. Sodemann, 2016: A revised picture of the atmospheric moisture residence time. *Geophys. Res. Lett.*, **43**, 924–933, doi:10.1002/2015GL067449.

Lambert, S. J., 1988: A cyclone climatology of the Canadian Climate Centre general circulation model. *J. Clim.*, **1**, 109–115, doi:10.1175/1520-0442(1988)001<0109:ACCOTC>2.0.CO;2.

Landwehr, S., I. Thurnherr, N. Cassar, M. Gysel-Beer, and J. Schmale, 2019: Using global reanalysis data to quantify and correct airflow distortion bias in shipborne wind speed measurements. *Atmos. Meas. Tech. Discuss.*, **2019**, 1–26, doi:10.5194/amt-2019-366.

Lawrence, J. R., S. D. Gedzelman, D. Dexheimer, H.-K. Cho, G. D. Carrie, R. Gasparini, C. R. Anderson, K. P. Bowman, and M. I. Biggerstaff, 2004: Stable isotopic composition of water vapor in the tropics. *J.*

Geophys. Res. Atmos., **109**, D06115, doi:10.1029/2003JD004046.

Lawrence, R. J. and D. S. Gedzelman, 1996: Low stable isotope ratios of tropical cyclone rains. *Geophys. Res. Lett.*, **23**, 527–530, doi:10.1029/96GL00425.

Lee, J., J. Worden, D. Noone, K. Bowman, A. Eldering, A. LeGrande, J.-L. F. Li, G. Schmidt, and H. Sodemann, 2011: Relating tropical ocean clouds to moist processes using water vapor isotope measurements. *Atmos. Chem. Phys.*, **11**, 741–752.

Lee, K.-O., F. Aemisegger, S. Pfahl, C. Flamant, J.-L. Lacour, and J.-P. Chaboureau, 2019: Contrasting stable water isotope signals from convective and large-scale precipitation phases of a heavy precipitation event in southern Italy during HyMeX IOP 13: A modelling perspective. *Atmos. Chem. Phys.*, **19**, 7487–7506, doi:https://doi.org/10.5194/acp-19-7487-2019.

Lewis, E. R. and S. E. Schwartz, 2013: Fundamentals. *Sea salt aerosol production: Mechanisms, methods, measurements and models*, American Geophysical Union (AGU), 9–99.

Liu, J., C. Xiao, M. Ding, and J. Ren, 2014: Variations in stable hydrogen and oxygen isotopes in atmospheric water vapor in the marine boundary layer across a wide latitude range. *J. Environ. Sci.*, **26**, 2266–2276, doi:10.1016/j.jes.2014.09.007.

Madonna, E., H. Wernli, H. Joos, and O. Martius, 2013: Warm conveyor belts in the ERA-Interim dataset (1979–2010). Part I: Climatology and potential vorticity evolution. *J. Clim.*, **27**, 3–26, doi:10.1175/JCLI-D-12-00720.1.

Majoube, M., 1971: Fractionnement en oxygene 18 et en deuterium entre l'eau et sa vapeur. *J. Chim. Phys.*, **68**, 1423–1436.

Merlivat, L., 1978: Molecular diffusivities of $H_2^{16}O$, $HD^{16}O$, and $H_2^{18}O$ in gases. *The Journal of Chemical Physics*, **69**, 2864, doi:10.1063/1.436884.

Merlivat, L. and J. Jouzel, 1979: Global climatic interpretation of the deuterium-oxygen 18 relationship for precipitation. *J. Geophys. Res. Oceans*, **84**, 5029–5033, doi:10.1029/JC084iC08p05029.

Merlivat, L. and G. Nief, 1967: Fractionnement isotopique lors des changements d'état solide-vapeur et liquide-vapeur de l'eau à des températures inférieures à 0°C. *Tellus*, **19**, 122–127, doi:10.1111/j.2153-3490.1967.tb01465.x.

Monahan, E. C., D. E. Spiel, and K. L. Davidson, 1986: A model of marine aerosol generation via whitecaps and wave disruption. *Oceanic whitecaps: And their role in air-sea exchange processes*, E. C. Monahan and G. M. Niocaill, eds., Springer Netherlands, Dordrecht, Oceanographic Sciences Library, 167–174.

Moore, G. W. K. and I. A. Renfrew, 2002: An assessment of the surface turbulent heat fluxes from the NCEP–NCAR reanalysis over the western boundary currents. *J. Clim.*, **15**, 2020–2037, doi:10.1175/1520-0442(2002)015<2020:AAOTST>2.0.CO;2.

Moore, J. K., M. R. Abbott, and J. G. Richman, 1999: Location and dynamics of the Antarctic Polar Front from satellite sea surface temperature data. *J. Geophys. Res. Oceans*, **104**, 3059–3073, doi:10.1029/1998JC900032.

Neiman, P. J., M. A. Shapiro, E. G. Donall, and C. W. Kreitzberg, 1990: Diabatic modification of an extratropical marine cyclone warm sector by cold underlying water. *Mon. Weather Rev.*, **118**, 1576–1590, doi:10.1175/1520-0493(1990)118<1576:DMOAEM>2.0.CO;2.

Nicolas, J. P. and D. H. Bromwich, 2011: Precipitation changes in high southern latitudes from global reanalyses: A cautionary tale. *Surv. Geophys.*, **32**, 475–494, doi:10.1007/s10712-011-9114-6.

Noone, D., J. Galewsky, Z. D. Sharp, J. Worden, J. Barnes, D. Baer, A. Bailey, D. P. Brown, L. Christensen, E. Crosson, F. Dong, J. V. Hurley, L. R. Johnson, M. Strong, D. Toohey, A. Van Pelt, and J. S. Wright, 2011: Properties of air mass mixing and humidity in the subtropics from measurements of the D/H isotope ratio of water vapor at the Mauna Loa Observatory. *J. Geophys. Res. Atmos.*, **116**, D22113, doi:10.1029/2011JD015773.

Nuss, W. A., 1989: Air-Sea interaction influences on the structure and intensification of an idealized marine cyclone. *Mon. Weather Rev.*, **117**, 351–369, doi:10.1175/1520-0493(1989)117<0351:ASIIOT>2.0.CO;2.

Ogawa, F. and T. Spengler, 2019: Prevailing surface wind direction during air–sea heat exchange. *J. Clim.*, **32**, 5601–5617, doi:10.1175/JCLI-D-18-0752.1.

Papritz, L., S. Pfahl, I. Rudeva, I. Simmonds, H. Sodemann, and H. Wernli, 2014: The role of extratropical cyclones and fronts for Southern Ocean freshwater fluxes. *J. Clim.*, **27**, 6205–6224, doi:10.1175/JCLI-D-13-00409.1.

Papritz, L., S. Pfahl, H. Sodemann, and H. Wernli, 2015: A climatology of cold air outbreaks and their impact on air–sea heat fluxes in the high-latitude South Pacific. *J. Clim.*, **28**, 342–364, doi:10.1175/JCLI-D-14-00482.1.

Papritz, L. and H. Sodemann, 2018: Characterizing the local and intense water cycle during a cold air outbreak in the Nordic Seas. *Mon. Weather Rev.*, **146**, 3567–3588, doi:10.1175/MWR-D-18-0172.1.

Persson, P. O. G., J. E. Hare, C. W. Fairall, and W. D. Otto, 2005: Air–sea interaction processes in warm and cold sectors of extratropical cyclonic storms observed during FASTEX. *Q. J. R. Meteorol. Soc.*, **131**, 877–912, doi:10.1256/qj.03.181.

Pfahl, S., E. Madonna, M. Boettcher, H. Joos, and H. Wernli, 2013: Warm conveyor belts in the ERA-Interim dataset (1979–2010). Part II: Moisture origin and relevance for precipitation. *J. Clim.*, **27**, 27–40, doi:10.1175/JCLI-D-13-00223.1.

Pfahl, S. and H. Sodemann, 2014: What controls deuterium excess in global precipitation? *Clim. Past*, **10**, 771–781, doi:10.5194/cp-10-771-2014.

Pfahl, S. and H. Wernli, 2008: Air parcel trajectory analysis of stable isotopes in water vapor in the eastern Mediterranean. *J. Geophys. Res.*, **113**, D20104, doi:10.1029/2008JD009839.

— 2009: Lagrangian simulations of stable isotopes in water vapor: An evaluation of nonequilibrium fractionation in the Craig-Gordon model. *J. Geophys. Res. Atmos.*, **114**, doi:10.1029/2009JD012054.

Pfahl, S., H. Wernli, and K. Yoshimura, 2012: The isotopic composition of precipitation from a winter storm – a case study with the limited-area model COSMOiso. *Atmos. Chem. Phys.*, **12**, 1629–1648, doi:10.5194/acp-12-1629-2012.

Pollard, R. T., T. H. Guymer, P. K. Taylor, H. Charnock, and R. T. Pollard, 1983: Summary of the JASIN 1978 field experiment. *Philos. Trans. R. Soc. Lond. A*, **308**, 221–230, doi:10.1098/rsta.1983.0001.

Possner, A., E. Zubler, U. Lohmann, and C. Schär, 2016: The resolution dependence of cloud effects and ship-induced aerosol-cloud interactions in marine stratocumulus. *J. Geophys. Res. Atmos.*, **121**, 4810–4829, doi:10.1002/2015JD024685.

Rasmussen, E. A. and J. Turner, 2003: *Polar lows: Mesoscale weather systems in the polar regions*. Cambridge University Press, Cambridge.

Reynolds, R. W., T. M. Smith, C. Liu, D. B. Chelton, K. S. Casey, and M. G. Schlax, 2007: Daily high-resolution-blended snalyses for sea surface temperature. *J. Clim.*, **20**, 5473–5496, doi:10.1175/2007JCLI1824.1.

Risi, C., S. Bony, F. Vimeux, and J. Jouzel, 2010: Water-stable isotopes in the LMDZ4 general circulation model: Model evaluation for present-day and past climates and applications to climatic interpretations of tropical isotopic records. *J. Geophys. Res. Atmos.*, **115**, doi:10.1029/2009JD013255.

Rozanski, K., L. Araguás-Araguás, and R. Gonfiantini, 1992: Relation between long-term trends of oxygen-18 isotope composition of precipitation and climate. *Sci.*, **258**, 981–985, doi:10.1126/science.258.5084.981.

Rudeva, I. and S. K. Gulev, 2010: Composite analysis of North Atlantic extratropical cyclones in NCEP–NCAR reanalysis data. *Mon. Weather Rev.*, **139**, 1419–1446, doi:10.1175/2010MWR3294.1.

Salmon, O. E., L. R. Welp, M. E. Baldwin, K. D. Hajny, B. H. Stirm, and P. B. Shepson, 2019: Vertical profile observations of water vapor deuterium excess in the lower troposphere. *Atmos. Chem. Phys.*, **19**, 11525–11543, doi:10.5194/acp-19-11525-2019.

Samuels-Crow, K. E., J. Galewsky, Z. D. Sharp, and K. J. Dennis, 2014: Deuterium excess in subtropical free troposphere water vapor: Continuous measurements from the Chajnantor Plateau, northern Chile. *Geophys. Res. Lett.*, **41**, 8652–8659, doi:10.1002/2014GL062302.

Schemm, S., I. Rudeva, and I. Simmonds, 2015: Extratropical fronts in the lower troposphere − global perspectives obtained from two automated methods. *Q. J. R. Meteorol. Soc.*, **141**, 1686–1698, doi:10.1002/qj.2471.

Schmale, J., A. Baccarini, I. Thurnherr, S. Henning, A. Efraim, L. Regayre, C. Bolas, M. Hartmann, A. Welti, K. Lehtipalo, F. Aemisegger, C. Tatzelt, S. Landwehr, R. L. Modini, F. Tummon, J. S. Johnson, N. Harris, M. Schnaiter, A. Toffoli, M. Derkani, N. Bukowiecki, F. Stratmann, J. Dommen, U. Baltensperger, H. Wernli, D. Rosenfeld, M. Gysel-Beer, and K. S. Carslaw, 2019: Overview of the Antarctic Circumnavigation Expedition: Study of Preindustrial-like Aerosols and their Climate Effects (ACE-SPACE). *Bull. Am. Meteorol. Soc.*, **100**, 2260–2283, doi:10.1175/BAMS-D-18-0187.1.

Schmidt, M., K. Maseyk, C. Lett, P. Biron, P. Richard, T. Bariac, and U. Seibt, 2010: Concentration effects on laser-based δ^{18}O and δ^2H measurements and implications for the calibration of vapour measurements with liquid standards. *Rapid Commun. Mass Spectrom.*, **24**, 3553–3561, doi:10.1002/rcm.4813.

Sharp, Z., 2007: *Principles of stable isotope geochemistry*. Pearson Prentice Hall, Upper Saddle River, New Jersey.

Sherwood, S. C., R. Roca, T. M. Weckwerth, and N. G. Andronova, 2010: Tropospheric water vapor, convection, and climate. *Rev. Geophys.*, **48**, RG2001, doi:10.1029/2009RG000301.

Simmonds, I., K. Keay, and J. A. Tristram Bye, 2011: Identification and climatology of southern hemisphere mobile fronts in a modern reanalysis. *J. Clim.*, **25**, 1945–1962, doi:10.1175/JCLI-D-11-00100.1.

Simmonds, I. and J. C. King, 2004: Global and hemispheric climate variations affecting the Southern Ocean. *Antarct. Sci.*, **16**, 401–413, doi:10.1017/S0954102004002226.

Sinclair, V. A., 2013: A 6-yr climatology of fronts affecting Helsinki, Finland, and their boundary layer structure. *J. Appl. Meteorol. Climatol.*, **52**, 2106–2124, doi:10.1175/JAMC-D-12-0318.1.

Sinclair, V. A., S. E. Belcher, and S. L. Gray, 2010: Synoptic controls on boundary-layer characteristics. *Bound-Layer Meteorol.*, **134**, 387–409, doi:10.1007/s10546-009-9455-6, wOS:000274013600002.

Smedman, A., U. Högström, E. Sahleé, W. M. Drennan, K. K. Kahma, H. Pettersson, and F. Zhang, 2009: Observational study of marine atmospheric boundary layer characteristics during swell. *J. Atmos. Sci.*, **66**, 2747–2763, doi:10.1175/2009JAS2952.1.

Smith, S. R., M. A. Bourassa, and R. J. Sharp, 1999: Establishing more truth in true winds. *J. Atmos. Ocean. Technol.*, **16**, 939–952, doi:10.1175/1520-0426(1999)016<0939:EMTITW>2.0.CO;2.

Sodemann, H., F. Aemisegger, S. Pfahl, M. Bitter, U. Corsmeier, T. Feuerle, P. Graf, R. Hankers, G. Hsiao, H. Schulz, A. Wieser, and H. Wernli, 2017: The stable isotopic composition of water vapour above Corsica during the HyMeX SOP1 campaign: Insight into vertical mixing processes from lower-tropospheric survey flights. *Atmos. Chem. Phys.*, **17**, 6125–6151, doi:10.5194/acp-17-6125-2017.

Sodemann, H., C. Schwierz, and H. Wernli, 2008: Interannual variability of Greenland winter precipitation sources: Lagrangian moisture diagnostic and North Atlantic Oscillation influence. *J. Geophys. Res.*, **113**, D03107, doi:10.1029/2007JD008503.

Spreitzer, E., R. Attinger, M. Boettcher, R. Forbes, H. Wernli, and H. Joos, 2019: Modification of potential vorticity near the tropopause by nonconservative processes in the ECMWF model. *J. Atmos. Sci.*, **76**, 1709–1726, doi:10.1175/JAS-D-18-0295.1.

Sprenger, M., G. Fragkoulidis, H. Binder, M. Croci-Maspoli, P. Graf, C. M. Grams, P. Knippertz, E. Madonna, S. Schemm, B. Škerlak, and H. Wernli, 2017: Global climatologies of Eulerian and Lagrangian flow features based on ERA-Interim. *Bull. Am. Meteorol. Soc.*, **98**, 1739–

1748, doi:10.1175/BAMS-D-15-00299.1.

Sprenger, M. and H. Wernli, 2015: The LAGRANTO Lagrangian analysis tool – version 2.0. *Geosci. Model Dev.*, **8**, 2569–2586, doi:10.5194/gmd-8-2569-2015.

Steen-Larsen, H. C., S. J. Johnsen, V. Masson-Delmotte, B. Stenni, C. Risi, H. Sodemann, D. Balslev-Clausen, T. Blunier, D. Dahl-Jensen, M. D. Ellehøj, S. Falourd, A. Grindsted, V. Gkinis, J. Jouzel, T. Popp, S. Sheldon, S. B. Simonsen, J. Sjolte, J. P. Steffensen, P. Sperlich, Á. E. Sveinbjörnsdóttir, B. M. Vinther, and J. W. C. White, 2013: Continuous monitoring of summer surface water vapor isotopic composition above the Greenland ice sheet. *Atmos. Chem. Phys.*, **13**, 4815–4828, doi:10.5194/acp-13-4815-2013.

Steen-Larsen, H. C., Á. E. Sveinbjörnsdóttir, T. Jonsson, F. Ritter, J.-L. Bonne, V. Masson-Delmotte, H. Sodemann, T. Blunier, D. Dahl-Jensen, and B. M. Vinther, 2015: Moisture sources and synoptic to seasonal variability of North Atlantic water vapor isotopic composition. *J. Geophys. Res. Atmos.*, **120**, 2015JD023234, doi:10.1002/2015JD023234.

Steen-Larsen, H. C., Á. E. Sveinbjörnsdóttir, A. J. Peters, V. Masson-Delmotte, M. P. Guishard, G. Hsiao, J. Jouzel, D. Noone, J. K. Warren, and J. W. C. White, 2014: Climatic controls on water vapor deuterium excess in the marine boundary layer of the North Atlantic based on 500 days of in situ, continuous measurements. *Atmos. Chem. Phys.*, **14**, 7741–7756, doi:10.5194/acp-14-7741-2014.

Steppeler, J., G. Doms, U. Schättler, H. W. Bitzer, A. Gassmann, U. Damrath, and G. Gregoric, 2003: Meso-gamma scale forecasts using the nonhydrostatic model LM. *Meteorol. Atmos. Phys.,*, **82**, 75–96, doi:10.1007/s00703-001-0592-9.

Stewart, M. K., 1975: Stable isotope fractionation due to evaporation and

isotopic exchange of falling waterdrops: Applications to atmospheric processes and evaporation of lakes. *J. Geophys. Res.*, **80**, 1133–1146, doi:10.1029/JC080i009p01133.

Stull, R. B., 2009: *An introduction to boundary layer meteorology*, volume 13 of *Atmospheric sciences library*. Springer, Dordrecht.

Sturm, P. and A. Knohl, 2010: Water vapor δ^2H and δ^{18}O measurements using off-axis integrated cavity output spectroscopy. *Atmos. Meas. Tech.*, **3**, 67–77, doi:10.5194/amt-3-67-2010.

Suess, E., F. Aemisegger, J. E. Sonke, M. Sprenger, H. Wernli, and L. H. E. Winkel, 2019: Marine versus continental sources of iodine and selenium in rainfall at two European high-atitude locations. *Environ. Sci. Technol.*, **53**, 1905–1917, doi:10.1021/acs.est.8b05533.

Thurnherr, I., A. Kozachek, P. Graf, Y. Weng, D. Bolshiyanov, S. Landwehr, S. Pfahl, J. Schmale, H. Sodemann, H. C. Steen-Larsen, A. Toffoli, H. Wernli, and F. Aemisegger, 2020: Meridional and vertical variations of the water vapour isotopic composition in the marine boundary layer over the atlantic and southern ocean. *Atmos. Chem. Phys.*, **20**, 5811–5835, doi:10.5194/acp-20-5811-2020.

Tiedtke, M., 1989: A comprehensive mass flux scheme for cumulus parameterization in large-scale models. *Mon. Weather Rev.,*, **117**, 1779–1800, doi:10.1175/1520-0493(1989)117<1779:ACMFSF>2.0.CO;2.

Toffoli, A., D. Proment, H. Salman, J. Monbaliu, F. Frascoli, M. Dafilis, E. Stramignoni, R. Forza, M. Manfrin, and M. Onorato, 2017: Wind generated rogue waves in an annular wave flume. *Phys. Rev. Lett.*, **118**, 144503, doi:10.1103/PhysRevLett.118.144503.

Torri, G., D. Ma, and Z. Kuang, 2017: Stable water isotopes and large-scale vertical motions in the tropics. *J. Geophys. Res. Atmos.*, **122**, 3703–3717,

doi:10.1002/2016JD026154.

Uemura, R., Y. Matsui, K. Yoshimura, H. Motoyama, and N. Yoshida, 2008: Evidence of deuterium excess in water vapor as an indicator of ocean surface conditions. *J. Geophys. Res.*, **113**, D19114,, doi:10.1029/2008JD010209.

Uotila, P., T. Vihma, A. B. Pezza, I. Simmonds, K. Keay, and A. H. Lynch, 2011: Relationships between Antarctic cyclones and surface conditions as derived from high-resolution numerical weather prediction data. *J. Geophys. Res. Atmos.*, **116**, doi:10.1029/2010JD015358.

Vergara-Temprado, J., N. Ban, D. Panosetti, L. Schlemmer, and C. Schär, 2019: Climate models permit convection at much coarser resolutions than previously considered. *J. Clim.*, **33**, 1915–1933, doi:10.1175/JCLI-D-19-0286.1.

Veron, F., 2015: Ocean spray. *Annu. Rev. Fluid Mech.*, **47**, 507–538, doi:10.1146/annurev-fluid-010814-014651.

von Storch, H., H. Langenberg, and F. Feser, 2000: A spectral nudging technique for dynamical downscaling purposes. *Mon. Weather Rev.*, **128**, 3664–3673, doi:10.1175/1520-0493(2000)128<3664:ASNTFD>2.0.CO;2.

Walton, D. W. H. and J. Thomas, 2018: Cruise report − Antarctic Circumnavigation Expedition (ACE) 20th December 2016 − 19th March 2017. *Zenodo*, **Version 1**, doi:10.5281/zenodo.1443511.

Weng, Y., A. Touzeau, and H. Sodemann, 2020: Correcting the impact of the isotope composition on the mixing ratio dependency of water vapour isotope measurements with cavity ring-down spectrometers. *Atmos. Meas. Tech.*, **13**, 3167–3190, doi:10.5194/amt-13-3167-2020.

Werner, M., P. M. Langebroek, T. Carlsen, M. Herold, and G. Lohmann,

2011: Stable water isotopes in the ECHAM5 general circulation model: Toward high-resolution isotope modeling on a global scale. *J. Geophys. Res. Atmos.*, **116**, doi:10.1029/2011JD015681.

Wernli, H. and H. C. Davies, 1997: A Lagrangian-based analysis of extratropical cyclones. Part I: The method and some applications. *Q. J. R. Meteorol. Soc.*, **123**, 467–489, doi:10.1002/qj.49712353811.

Wernli, H. and C. Schwierz, 2006: Surface cyclones in the ERA-40 dataset (1958–2001). Part I: Novel identification method and global climatology. *J. Atmos. Sci.*, **63**, 2486–2507, doi:10.1175/JAS3766.1.

Winschall, A., S. Pfahl, H. Sodemann, and H. Wernli, 2012: Impact of North Atlantic evaporation hot spots on southern Alpine heavy precipitation events. *Q. J. R. Meteorol. Soc.*, **138**, 1245–1258, doi:10.1002/qj.987.

Yakir, D. and X.-F. Wang, 1996: Fluxes of CO_2 and water between terrestrial vegetation and the atmosphere estimated from isotope measurements. *Nature*, **380**, 515–517, doi:10.1038/380515a0.

Yau, M. K. and M. Jean, 1989: Synoptic aspects and physical processes in the rapidly intensifying cyclone of 6–8 March 1986. *Atmos.-Ocean*, **27**, 59–86, doi:10.1080/07055900.1989.9649328.

Yepez, E. A., D. G. Williams, R. L. Scott, and G. Lin, 2003: Partitioning overstory and understory evapotranspiration in a semiarid savanna woodland from the isotopic composition of water vapor. *Agric. For. Meteorol.*, **119**, 53–68, doi:10.1016/S0168-1923(03)00116-3.

Yoshimura, K., M. Kanamitsu, D. Noone, and T. Oki, 2008: Historical isotope simulation using reanalysis atmospheric data. *J. Geophys. Res. Atmos.*, **113**, doi:10.1029/2008JD010074.

Young, I., 1999: *Wind generated ocean waves*, volume 2. Elsevier.

Ziemer, F. and H. Günther, 1994: A system to monitor ocean wave fields.

Proceedings of the second international conference on air-sea inter-action and meteorology and oceanography of the coastal zone, Amer. Meteor. Soc., 117–118.

Acknowledgements

I am grateful to everyone, who supported me during my PhD project. Especially, I would like to thank the following persons:

Heini Wernli for the opportunity to conduct a PostDiploma and PhD on stable water isotopes, the trust in sending me on a research cruise in the beginning of my PhD, the many inputs and guidance throughout the PhD.

Franziska Aemisegger for introducing me into and passing on the passion for SWI meteorology during my Bachelor thesis, the great collaboration and the many advices during my PhD, for always finding time to discuss new findings and for interesting discussions on isotope- and not isotope-related topics.

Pascal Graf for the introduction into the SWI measurements during ACE, for being a good companion on our journey around Antarctica and for his inputs on my PhD thesis.

Julia Schmale, Irina Gorodetskaya, Maria Tsukernik, Jasmine Lee, Silvia Henning, "the Rusties" and all the other ACE colleagues for the help and collaboration during ACE with the measurement setup

My gardening companions and the Thursday evening crew for the important leisure times.

My family, friends and Tim Gallusser for being here.

Thanks! (Picture by Pascal Graf)